

Tribodynamic analysis of high-speed rolling element bearings in flexible multi-body environments



**Loughborough
University**

by
Harry Questa

Wolfson School of Mechanical, Electrical, and Manufacturing
Engineering
Loughborough University

A Doctoral Thesis submitted in partial fulfillment of the requirements for
the award of Doctor of Philosophy of Loughborough University

March 2025

Abstract

Roller bearings are critical components in electrified vehicle (EV) powertrains. They are often performance limiting, introducing NVH (Noise, Vibration and Harshness), tribological and wear challenges. With a push towards achieving zero-prototype development, the use of advanced simulation tools to accurately predict their behaviour at both component and system level is becoming more prevalent.

Modern electrified motors and transmissions operate at considerably higher speeds than traditional internal combustion engine powertrains. This leads to much higher lubricant entrainment velocities at the roller-race conjunction in the bearings. Consequently, the elastohydrodynamic (EHL) film can be of the same order of magnitude and even exceed that of the contact deformation predicted by the dry Hertzian assumption. This significantly influences the contact mechanics and hence total bearing stiffness.

This research presents a coupled tribological and dynamic modelling approach for high-speed rolling element bearings. Experimental studies using a novel test rig highlight the influence of the EHL film, with measured bearing motion serving as boundary conditions for tribological analyses. A coupled simulation approach is developed, integrating an implicit lubricated bearing model within a system level, flexible multi-body dynamic model. Results at the contact and system levels are evaluated under high-speed EV operating conditions to compare lubricated and non-lubricated analyses. An artificial neural network (ANN) is trained to predict EHL film thickness across a wide range of bearing geometries, tribological parameters and operating conditions. The ANN is then employed within the coupled simulation as a more accurate alternative to the regressed film thickness equations, with its performance evaluated against numerical and analytical approaches in terms of predictive accuracy and computational efficiency.

This multi-physics approach improves the understanding of the interaction between tribological behaviour and system dynamics. The deeper understanding of these matters is expected to support more objective future developments of these modern powertrains to enhance their efficiency, durability and NVH refinement.

Keywords High-speed; roller bearings; tribodynamics; elastohydrodynamics; EHL; flexible multi-body dynamics; artificial neural network; ANN

Acknowledgements

I would like to thank my primary supervisor, Dr Mahdi Mohammadpour, for his guidance, support, and encouragement throughout this project. His efforts and expertise have helped greatly to progress this work and my understanding of the technical aspects of this field.

I would like to express my gratitude to Professor Stephanos Theodossiades and Professor Colin Garner. Their valuable input has ensured both depth and breadth to the final thesis. I am also grateful to the many colleagues at Loughborough University who have contributed to the development of this work.

Many thanks go to my industrial supervisors at AVL List GmbH, Dr Stephen Bewsher and Professor Günter Offner, for their technical and professional guidance. A special thanks to Mr. Martin Sopouch for assisting with my transition to AVL List GmbH, as well as to my colleagues for their support and advice, both professionally and personally.

Finally, my loving thanks go to my family and friends for the continued support throughout this endeavour. To my parents, I am deeply grateful for your unwavering encouragement and belief in me. To my partner, Kate, your patience, love and support have made the final stages of this work possible.

Table of contents

List of figures	xi
List of tables	xv
Nomenclature	xvii
List of Abbreviations	xxii
Publications	xxv
1 Introduction	1
1.1 Research Aims and Objectives	2
1.2 Contributions to Knowledge	3
1.3 Structure of the Thesis	4
2 Literature Review	7
2.1 Rolling Element Bearing Introduction	7
2.2 Rolling Element Bearing Modelling	9
2.2.1 Quasi-static Bearing Models	9
2.2.2 Dynamic Bearing Models	10
2.2.3 Lubricated Dynamic Bearing Models	11
2.3 Contact Mechanics	13
2.3.1 Hertzian Contact Mechanics	13
2.3.2 Line Contacts	16
2.4 Elastohydrodynamic Lubrication	17
2.4.1 History	17
2.4.2 Numerical Methods	18
2.4.3 Starvation	20
2.4.4 Thermal EHL	20
2.4.5 Elastohydrodynamic Pressure and Film Characteristics	22

2.4.6 Lubrication Regimes	23
2.5 Artifical Neural Networks	24
2.6 Closure	26
3 Investigating the Effect of Lubrication on the Tribodynamic Behaviour of High-Speed Roller Bearings	29
3.1 Introduction	29
3.2 Workflow	30
3.2.1 Operating Principles	31
3.2.2 Lubricated Contact Mechanics	32
3.2.3 Experimental Test Rig	33
3.2.4 Instrumentation	34
3.2.5 Signal Processing	36
3.2.6 Contact Mechanics at the Roller Race Conjunction	37
3.2.7 Implicit Tribological Model	38
3.2.8 Surface Topography Measurements	40
3.3 Numerical EHL Model	40
3.3.1 Reynolds Equation	41
3.3.2 Finite Difference Formulation	43
3.3.3 Effect of Pressure on Lubricant Viscosity	44
3.3.4 Effect of Pressure on Lubricant Density	45
3.3.5 Effect of Temperature on Lubricant Viscosity	46
3.3.6 1D EHL Solution Methodology	46
3.3.7 Numerical EHL Model Validation	48
3.3.8 Experimental Result Verification	48
3.4 Results and Discussion	51
3.4.1 Film Thickness and Load Across Speed Sweep	52
3.4.2 EHL Regimes	53
3.4.3 Dry vs Lubricated Tribodynamic Model	54
3.4.4 Numerical EHL Results	55
3.5 Conclusions	57
4 Modelling Lubricated Bearings in a Flexible Multi-Body Dynamic Environment	61
4.1 Introduction	61
4.2 Methodology	62
4.3 System Level Flexible Model	62
4.3.1 Lubricated Component Level Model	66

4.3.2	Representative Excitation Methodology	71
4.3.3	Co-Simulation of Coupled Models	72
4.4	Results and Discussion	77
4.4.1	Conclusions	81
5	Artificial Neural Networks for EHL Film Thickness Predictions	85
5.1	Introduction	85
5.2	Numerical vs Analytical Film Thickness Values at High Entrainment Velocities	86
5.3	ANN Fundamentals	87
5.3.1	Network Architecture	88
5.3.2	Forward Propagation	89
5.3.3	Backpropagation	89
5.4	Methodology	90
5.4.1	EHL Input Data Generation	92
5.4.2	ANN Structure Evaluation	96
5.4.3	Explicit Bearing Film Thickness Predictions	102
5.4.4	Implicit Bearing Film Thickness Predictions	104
5.5	Results and Discussion	104
5.5.1	ANN Structure Evaluation	104
5.5.2	Explicit Bearing Film Thickness Predictions	108
5.5.3	Implicit Bearing Film Thickness Predictions	110
5.6	Conclusions	111
6	Conclusions and Future Work	115
6.1	Overall Conclusions	115
6.2	Contributions to Knowledge	117
6.3	Addressing the Research Questions	119
6.4	Future Work	119
References		121

List of figures

2.1	Electrified powertrain.	8
2.2	Torque-speed characteristics of permanent magnet synchronous motor (PMSM).	8
2.3	Roller-race model for line contact.	14
2.4	Ball-race model for point contact.	14
2.5	Hertzian contact deflection.	15
2.6	Effect of dimensionless inlet distance on film thickness for starvation modelling.	21
2.7	EHL film and pressure distribution.	23
2.8	Stribeck curve and specific film thickness values.	24
3.1	Experimental tribodynamics methodology overview.	30
3.2	Cylindrical roller bearing in equilibrium position.	31
3.3	Mutual separation and convergence of inner and outer races.	32
3.4	EHL film thickness and pressure distribution at contact.	33
3.5	Experimental rig schematic.	34
3.6	Accelerometer locations on test bracket.	35
3.7	Laser vibrometer locations on shaft.	35
3.8	Validation of dimensionless pressure distribution, present model (solid), Masjedi and Khonsari (dashed).	48
3.9	Validation of dimensionless film thickness distribution, present model (solid), Masjedi and Khonsari (dashed).	49
3.10	Bearing bore displacement frequency spectra.	51
3.11	Shaft displacement frequency spectra.	51
3.12	Contact load and film thickness - Outer race.	52
3.13	Film and load - EHL to hydrodynamic regime.	53
3.14	EHL and hydrodynamic conditions during roller operation. Key: IR = Iso-viscous Rigid, VR = Viscous Rigid, VE = Viscous Elastic, IE = Iso-viscous Elastic.	54

3.15 Contact load difference between dry and lubricated model.	55
3.16 Dry and lubricated model load difference: a) 3 050 rpm, b) 14 135 rpm, c) 14 855 rpm.	56
3.17 Selected points for the numerical EHL model.	57
3.18 EHL pressure and film thickness distributions: a) Node 1, b) Node 2, c) Node 3, d) Node 4, e) Node 5, f) Node 6.	58
4.1 Flowchart of models.	63
4.2 System level model schematic.	64
4.3 Bearing schematic.	66
4.4 Dry vs lubricated roller-race contact.	67
4.5 Contact level validation.	69
4.6 PMSM torque profile and maximum and minimum torque fluctuation. .	72
4.7 Hub motor excitation model.	73
4.8 Communication vector and degrees of freedom.	74
4.9 Output port Demux blocks and degrees of freedom.	75
4.10 Input port Mux blocks and degrees of freedom.	76
4.11 Simulink® model schematic.	76
4.12 Rolling element contact stiffness - Dry vs lubricated maximum values. .	77
4.13 Rolling element contact force - Dry vs lubricated percentage increase. .	78
4.14 Inner race stiffness - Dry vs lubricated operating envelope.	79
4.15 Inner race displacement - Dry vs lubricated operating envelope.	79
4.16 Inner race acceleration - Dry vs lubricated operating envelope.	80
4.17 Rolling element contact stiffness - Dry vs lubricated minimum values. .	80
4.18 Film thickness vs contact force 21 000 rpm.	81
4.19 Film thickness vs contact force 12 500 rpm.	81
5.1 Central film thickness - EHL vs analytical.	87
5.2 ANN schematic.	88
5.3 ANN data flow, models and training flowchart.	91
5.4 Greenwood informed training data vs Marian et al.	94
5.5 Workflow to constrain training input data using Greenwood regimes. .	95
5.6 Greenwood informed training data vs unconstrained data.	97
5.7 ANN structure to predict EHL central film thickness (9 – [14 – 14 – 14]3 – 1).	98
5.8 Normal contact load vs cage angular displacement.	103
5.9 Bearing operating conditions vs Greenwood informed training data. .	103

5.10 R^2 performance of ANN structure ($N=14$, $t=3$) using a Logistic Sigmoid activation function at each hidden layer: a) 600 points, b) 1000 points, c) 2000 points, d) 5000 points.	107
5.11 ANN, numerical and analytical central film thickness comparisons.	108
5.12 Central film thickness - EHL vs ANN vs analytical at increasing shaft rotational speed.	109
5.13 ANN vs analytical film thickness at speed intervals from 5 000 - 20 000 <i>rpm</i>	110
5.14 ANN vs analytical CPU time per simulation.	112

List of tables

3.1	Surface topography data	40
3.2	Bearing specification	50
3.3	Lubricant and material properties	50
3.4	Extrapolated film formulae and numerical model central film thickness comparison	58
4.1	Cylindrical roller bearing specification	71
4.2	Bearing material and rheological properties	71
4.3	Pinion geometry	73
4.4	Gear geometry	74
5.1	Range of ANN film thickness calculation parameters	96
5.2	Sensitivity study of ANN structure	98
5.3	R^2 performance of ANN structures using 600 data points and a LogSig activation function	105
5.4	R^2 performance of ANN structures using 600 data points and a Tanh activation function	106
5.5	R^2 performance of ANN structures using 600 data points and a Tanh activation function	106
5.6	Training time of ANN structures with LogSig activation function and 600 data points	106
5.7	Training time of ANN structures with LogSig activation function and 1000 data points	106
5.8	Training time of ANN structures with LogSig activation function and 2000 data points	106
5.9	Training time of ANN structures with LogSig activation function and 5000 data points	107
5.10	Film thickness computation methodology performance relative to the numerical solution	109

5.11 Implicit central film thickness comparison: ANN vs analytical	111
5.12 Implicit CPU time comparison: ANN vs analytical	111

Nomenclature

The nomenclature of all symbols used in the body of this work is given in the following sections. This work combines concepts from various research domains, including multi-body dynamics, elastohydrodynamic lubrication and computer science. Since each field has its own established notation, overlap for certain symbol invariably occurs. The nomenclature is therefore divided by chapter to maintain convention and reduce potential confusion.

Chapter 3

a	Acceleration ($\text{m} \cdot \text{s}^{-2}$)
b	Half-length of the contact (mm)
C	Radial clearance (μm)
D_r	Diameter of roller (mm)
D_p	Pitch diameter (mm)
E_r	Equivalent (reduced) elastic modulus (Pa)
F_x	Radial load in x-direction (N)
F_y	Radial load in y-direction (N)
f_{bpi}	Ball pass frequency of inner race (Hz)
f_{bpo}	Ball pass frequency of outer race (Hz)
f_{shaft}	Shaft rotational frequency (Hz)
G^*	Dimensionless equivalent geometry (-)
h_c	Central film thickness (m)
k	Stiffness ($\text{N} \cdot \text{m}^{-1}$)
L	Roller length (m)
n	Exponent of localized deflection (-)
N	Number of rolling elements (-)

p	Contact pressure (Pa)
r_{in}	Radius of inner race (m)
R_{zx}	Equivalent radius of contact (m)
u	Speed of entraining motion ($\text{m} \cdot \text{s}^{-1}$)
U^*	Dimensionless speed parameter (-)
v	Velocity ($\text{m} \cdot \text{s}^{-1}$)
W	Contact load (N)
W^*	Dimensionless load parameter (-)
x	Displacement in x-direction (m)
x_c	Conjunction x-coordinate (-)
y	Displacement in y-direction (m)
y_c	Conjunction y-coordinate (-)

Greek Symbols

θ	Angular position (rad)
α	Pressure viscosity coefficient (GPa^{-1})
δ	Contact deflection (m)
λ	Stribeck parameter (-)
η_0	Atmospheric lubricant dynamic viscosity ($\text{Pa} \cdot \text{s}$)
η	Lubricant dynamic viscosity ($\text{Pa} \cdot \text{s}$)
ρ	Lubricant density ($\text{kg} \cdot \text{m}^{-3}$)
ρ_0	Atmospheric lubricant density ($\text{kg} \cdot \text{m}^{-3}$)
σ	Composite surface roughness (m)
ω_c	Angular velocity of cage ($\text{rad} \cdot \text{s}^{-1}$)
ω_{ri}	Angular velocity of inner race ($\text{rad} \cdot \text{s}^{-1}$)
ω_s	Angular velocity of shaft ($\text{rad} \cdot \text{s}^{-1}$)
γ	Relaxation factor (-)

Chapter 4

C	Radial clearance (m)
d	Body material damping ($\text{N} \cdot \text{s m}^{-1}$)
E	Elastic modulus (Pa)
E_r	Equivalent (reduced) elastic modulus (Pa)
F_d	Damping force (N)
f_{damp}	Damping factor (-)
f_F	Force vector (N)
f_M	Moment vector ($\text{N} \cdot \text{m}$)
f	Force on partial mass (N)
f^a	External loads (N)
f^*	Non-linear excitation force (N)
G^*	Dimensionless equivalent geometry (-)
h_c	Central film thickness (m)
I_C	Inertia tensor of partial mass ($\text{kg} \cdot \text{m}^2$)
K	Body stiffness matrix ($\text{N} \cdot \text{m}^{-1}$)
k	Body material stiffness ($\text{N} \cdot \text{m}^{-1}$)
K_c	Contact stiffness ($\text{N} \cdot \text{m}^{-1}$)
K_b	Total bearing stiffness ($\text{N} \cdot \text{m}^{-1}$)
K_{EHL}	EHL film stiffness ($\text{N} \cdot \text{m}^{-1}$)
l_a	Active length of roller (m)
l	Length of roller slice (m)
m	Mass of partial mass (kg)
M	Mass matrix of body (kg)
N	Partial mass number (-)
n	Degree of freedom (-)
p^*	Non-linear inertia terms ($\text{kg} \cdot \text{m}^2$)
q	Displacement (m)
\dot{q}	Velocity ($\text{m} \cdot \text{s}^{-1}$)
\ddot{q}	Acceleration ($\text{m} \cdot \text{s}^{-2}$)
R	Bearing inner race radius (m)

r	Roller radius (m)
R_r	Equivalent radius of contact (m)
s	Slice number (—)
T	Total contact moment (N · m)
u_t	Translational displacement of partial mass (m)
U^*	Dimensionless speed parameter (—)
W	Total contact load (N)
w	Force per unit length (N · m ⁻¹)
x	Displacement in x-direction (m)
x_c	Conjunction x-coordinate (—)
y	Displacement in y-direction (m)
y_c	Conjunction y-coordinate (—)
z	Displacement in z-direction (m)

Greek Symbols

θ	Roller angular displacement (rad)
\emptyset	Rotational displacement of partial mass (rad)
α	Pressure viscosity coefficient (GPa^{-1})
δ	Contact deformation (m)
δ_m	Material deformation (m)
η_0	Atmospheric lubricant dynamic viscosity (Pa · s)
ρ_0	Lubricant inlet density (kg · m ⁻³)
ω	Angular velocity of shaft (rad)

Chapter 5

b	Bias
d	Test field distance
f	Activation function
h	Hidden layer number

N	Number of neurons per hidden layer
N_p	Number of data points
n_f	Number of factors
n_s	Number of simulations
R^2	Coefficient of determination
t	Total number of hidden layers
t_i	Target value
u_l	Lower normalised unit value
u_n	Upper normalised unit value
W	Weighting
X	Input value to neuron
x	Dimensional input value
$x_{i,j,LHS}$	Latin hypercube sampling element
x_{max}	Maximum dimensional value in dataset
x_{min}	Minimum dimensional value in dataset
x_w	Weighted sum of inputs plus bias
\tilde{x}	Normalised input or output parameter
y_i	Predicted value
\bar{y}	Mean of target sample
Z_r	Random number
z	Activated output of a neuron

Greek Symbols

ξ	MaxiMin application factor
γ	Regularisation adjustment factor

List of Abbreviations

ANN	Artificial Neural Network
AI	Artificial Intelligence
EV	Electrified Vehicle
BEVs	Battery Electric Vehicles
CRB	Cylindrical Roller Bearing
CFD	Computational Fluid Dynamics
DOF	Degree of Freedom
EHL	Elastohydrodynamic Lubrication
FEM	Finite Element Method
FMBD	Flexible Multi-Body Dynamics
ICE	Internal Combustion Engine
IE	Isoviscous Elastic
IR	Isoviscous Rigid
LHD	Latin Hypercube Design
LHS	Latin Hypercube Sampling
MBD	Multi-Body Dynamic
ML	Machine Learning
MSE	Mean Squared Error
NVH	Noise, Vibration and Harshness
PE	Piezoviscous Elastic
PHEVs	Plug-In Hybrid Electric Vehicles
PMSM	Permanent Magnet Synchronous Motor
PR	Piezoviscous Rigid
PINNs	Physics Informed Neural Networks

RPM	Revolutions Per Minute
STFFT	Short-Time Fast-Fourier Transform

Publications

The results of this thesis are partially summarised in the following journal papers:

- (i) Questa, H., Mohammadpour, M., Theodossiades, S., Garner, C. P., Bewsher, S. R., & Offner, G. (2021). Tribodynamic analysis of high-speed roller bearings for electrified vehicle powertrains. *Tribology International*, 154 (July 2020), 106675.
<https://doi.org/10.1016/j.triboint.2020.106675>.
- (ii) Questa, H., Mohammadpour, M., Theodossiades, S., Garner, C. P., Bewsher, S. R., & Offner, G. (2023). Tribodynamic modelling of high-speed rolling element bearings in flexible multi-body environments. *Machines*, 11(1), 93.
<https://doi.org/10.3390/machines11010093>.
- (iii) Walker, J., Questa, H., Raman, A., Ahmed, M., Mohammadpour, M., Bewsher, S. R., & Offner, G. (2023). Application of tribological artificial neural networks in machine elements. *Tribology Letters*, 71(1), 3.
<https://doi.org/10.1007/s11249-022-01673-5>.

The results of this thesis are partially summarised in the following conference papers:

- (i) Questa, H., Mohammadpour, M., Theodossiades, S., Garner, C. P., Bewsher, S. R., & Offner, G. (2020). Tribodynamic modelling of high-speed rolling element bearings using experimentally obtained boundary conditions. Paper presented at NAFEMS 2020 UK Conference, United Kingdom.

Editorial features:

- (i) Tysoe, W. T., & Spencer, N. D. (2023, February). Turning simulations into formulae by machine learning. *Tribology and Lubrication Technology*, 86–87.
<https://digitaleditions.walsworth.com/publication/?i=779793&p=88&view=issueViewer>

Chapter 1

Introduction

The automotive industry is transitioning into the next phase of powertrain technology. As automotive manufacturers are forced to meet tightening fleet-wide emissions regulations, the electrified vehicle market share is increasing. The European Union (EU) has established ambitious policy [1] mandating that all new cars and vans sold in Europe be zero-emission by 2035 as part of a broader strategy to achieve climate neutrality by 2050. The EU aims to have electrified vehicles - both Battery Electric Vehicles (BEVs) and Plug-in Hybrid Electric Vehicles (PHEVs) - make up 80 % of its automotive market share by 2030. In China, government subsidies and investment in battery technology is also yielding a rapid advancement in electrified vehicle adoption - primarily in the passenger car segment. Whilst the direction of the industry remains susceptible to geopolitical and market influences, it is clear that many future powertrains will rely on electrification.

To achieve high-efficiency and adhere to packaging constraints, modern electrified powertrains utilize high-speed and low load motors [2]. These motors introduce new challenges regarding NVH (Noise, Vibration and Harshness) and the tribology of interacting conjunctions. The compact, lightweight and efficient powertrains operate under significantly different working conditions to conventional internal combustion engine (ICE) systems. They are subject to different underlying physics; such as regime of lubrication, dynamic response and magneto-mechanical interactions. This style of powertrain architecture therefore involves high-speed rolling element bearing operation in both the motor and transmission.

These bearings are crucial structural components and their dynamic response significantly affects the behaviour of the interconnected structures. The dynamic behaviour of the bearing governs the force transmission from the excitation source to the housing and structure. It also influences the tribological contact conditions between rollers and raceways.

With a trend towards cost saving zero-prototype development, the use of simulation tools in modern powertrain development is growing. Multi-system vehicle powertrain concepts are pushing complexity of simulation models and this requires accurate and robust component level understanding. Performance characteristics of the bearings, such as NVH, friction and wear must be accurately modelled at the development stage to ensure full system success.

1.1 Research Aims and Objectives

The primary aim of this work is to investigate the interaction between tribology and dynamics in rolling element bearings, with particular focus on the significance of this multi-physics interaction in high-speed automotive powertrain applications. With rotational speeds up to 25 000 *rpm*, the entrainment velocity of lubricant into the roller-race contact is significant, and conventional dry analyses may no longer be valid. Specifically, this work examines the influence of the elastohydrodynamic (EHL) film, and assesses the necessity of its implicit inclusion in dynamic bearing modelling within flexible multi-body (FMBD) environments. This research also aims to investigate the contribution of artificial neural networks (ANNs) to tribological modelling, assessing if they can achieve the accuracy of numerical methods at high speeds without the computational limitations. These research points are addressed through the following aims and objectives:

Aims

1. To investigate how the EHL film affects the contact load and stiffness of rolling element bearings at the high speed, low torque operating conditions representative of electrified vehicle powertrains.
2. To assess how implicit modelling of this film affects system dynamics at these operating conditions in a flexible, system-level model.
3. To investigate methods of calculating the central EHL film thickness, and assess if an ANN can be used to predict film thickness across a broad range of rolling element bearing input parameters.
4. To explore the possibility of employing an ANN to model tribological phenomena implicitly at the roller-race contact in an FMBD model.

Objectives

1. Develop a high-speed experimental test rig to measure bearing orbital motion as a kinematic input to tribological models. Use this to identify the required workflows and necessary models for tribodynamic analysis, as well as analyse the influence of the EHL film on contact and component behaviour.
2. Develop a lubricated component bearing model, considering the EHL film implicitly at the contact between rolling elements and raceways.
3. Embed the lubricated bearing model within a flexible multi-body dynamic model to assess the influence of the EHL film on the dynamic response of the system.
4. Develop an artificial neural network, capable of computing central EHL film thickness for a wide range of the required input parameters. Assess the computational viability of integrating this implicitly within the FMBD model.

This work was performed in collaboration with AVL List GmbH in order to disseminate the outcomes of this research in the development of commercial codes: AVL EXCITETM M and AVL EXCITETM Power Unit.

1.2 Contributions to Knowledge



The main novelties and contributions to knowledge from this thesis are summarised below:

1. A novel experimental test rig was designed and constructed to measure the kinematic motion of a bearing at rotational speeds and loads up to 750 N and 15 000 rpm respectively. The bearing orbital motion was measured and used for conjunction and component level tribological analysis. The methodology of coupling experimental test with numerical tribological models has not been previously reported in this manner at these speeds. The outcome of this demonstrated the requirement of implicitly modelling the EHL film in future high-speed applications, since it contributed to a 149% contact load increase at 15 000 rpm when compared to conventional dry analyses.
2. A coupled co-simulation approach was established to implicitly consider the EHL film in roller bearings within a high-speed system-level FMBD model. The model, consisting of a flexible shaft and rigid housing, replicates the operating conditions of a 54 kW permanent magnet synchronous motor (PMSM) coupled to a first

stage gear pair, operating at speeds up to 21 000 *rpm*. This was the first time in open literature that an implicitly lubricated multi-physics bearing model has been considered in the context of electrified powertrain dynamics. The outcome of this demonstrated that the increased contact deflection, due to the lubricant film inclusion, increases total bearing stiffness by 24.9 % at 21 000 rpm. This effectively behaves as a non-linear, speed dependant radial preload on the bearing. The contribution of this stiffness increased the natural frequency of the system, and hence affected NVH response. This proves the requirement to consider the EHL film implicitly for rolling element bearing modelling under the high speed, low load operating conditions of electrified powertrains.

3. An ANN was trained to predict EHL central film thickness with input data calculated using a 1D numerical EHL model. A wide value range of input variables necessary for the EHL calculation were used to train the model. The value range was consistent with common machine element contacts, with its applicability also extending to gear pairs and cam contacts. The novel methodology of constraining the training data using the Greenwood regime ensured high data quality whilst only requiring 2 000 training data points. The ANN achieved an MSE of $7.65 \times 10^{-5} \mu\text{m}^2$ when benchmarked against the numerical solution, whilst reducing calculation time by a factor of 1 570. This methodology will further contribute to the computational efficiency and accuracy of tribological ANNs.
4. The ANN was embedded within an FMBD system-level model to calculate EHL film thickness and consider it implicitly in the evaluation of the bearing and system dynamics. The film thickness evaluation achieves the accuracy of the numerical model without the associated computational limitations. This modelling method of combining a component level tribological ANN within an FMBD system-level model has not been previously reported.

1.3 Structure of the Thesis

The research in this thesis is presented in the following structure:

Chapter 1 introduces the topic of the thesis and provides the specific research questions that the work aims to answer.

Chapter 2 provides a review of the literature pertinent to the thesis topic, as well as covering the necessary principles required to address the research questions.

Chapter 3 presents a high-speed experimental test rig which was used to obtain kinematic boundary conditions for tribological models. The importance of including the lubricant film in high-speed dynamic bearing models is assessed here. The governing equations for the thesis are also introduced in this chapter.

Chapter 4 integrates the tribological models used in Chapter 3 into a system-level FMBD model. Simulations up to 21 000 *rpm* are performed using the dynamic input conditions of a 54 kW PMSM coupled to a first stage gear pair. The EHL film is modelled implicitly at the roller-race conjunction, and its affect on system dynamics is evaluated.

Chapter 5 introduces an ANN to address the shortcomings of the analytical approach when estimating EHL film thickness at high speeds. The ANN is trained using a wide design space of input variables. The accuracy of the model and computational efficiency is assessed. The ANN is embedded within the dynamic system level model from Chapter 4 as an alternative approach to the analytical solution for central film thickness.

Chapter 6 presents the general conclusions of the work, and outlines potential future work that could follow this research.

Chapter 2

Literature Review



This chapter reviews the literature pertinent to this research topic. It covers the development of bearing models, ranging from simple quasi-static to high-degree-of-freedom (DOF) dynamic models. Recent advancements on the implicit coupling of tribological and dynamic bearing models is then reviewed. The fundamentals of contact mechanics, essential to the research questions, are introduced alongside a discussion of contact modelling techniques. An overview of elastohydrodynamic lubrication modelling, including numerical methods, characteristics, regimes of lubrication and empirical formulae is presented. Finally, the application of artificial neural networks (ANNs) in the field of tribology and their impact on future modelling is explored.

2.1 Rolling Element Bearing Introduction

The term rolling element bearing encompasses both ball and roller type bearings. These common machine elements permit motion of, or about, shafts in a wide range of devices; from wheel bearings in bicycles and cars to electric motors and aircraft gas turbines. The general use of rolling element bearings occurred from the start of the Industrial Revolution; however, the origin of what constitutes modern bearing design dates back as far as *ca.*1500. Leonardo Da Vinci, in his Codex Madrid, conceived a thrust ball bearing design consisting of spherical balls with conical separation elements [3]. Prior to the scientific advancements of the atomic age, the design of rolling element bearings was regarded as more an art than a science. Alas, this thesis is not a work of art (hyperbole notwithstanding), but rather an advancement of the scientific knowledge that precedes it.

In automotive transmissions, these bearings support shaft rotation as well as the radial and axial forces applied during gear meshing. Figure 2.1 presents an annotated diagram of 2-speed e-Axle commonly found in electrified vehicles. Single or two-stage gearing in these electrified transmissions mean that bearings in both the electric motors

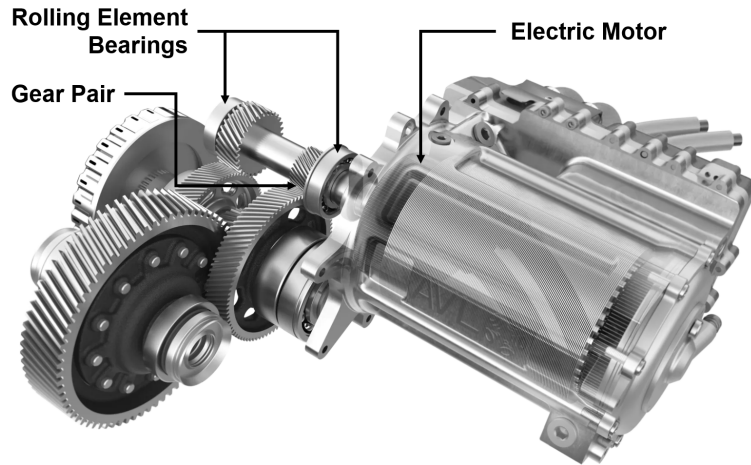


Figure 2.1 Electrified powertrain.

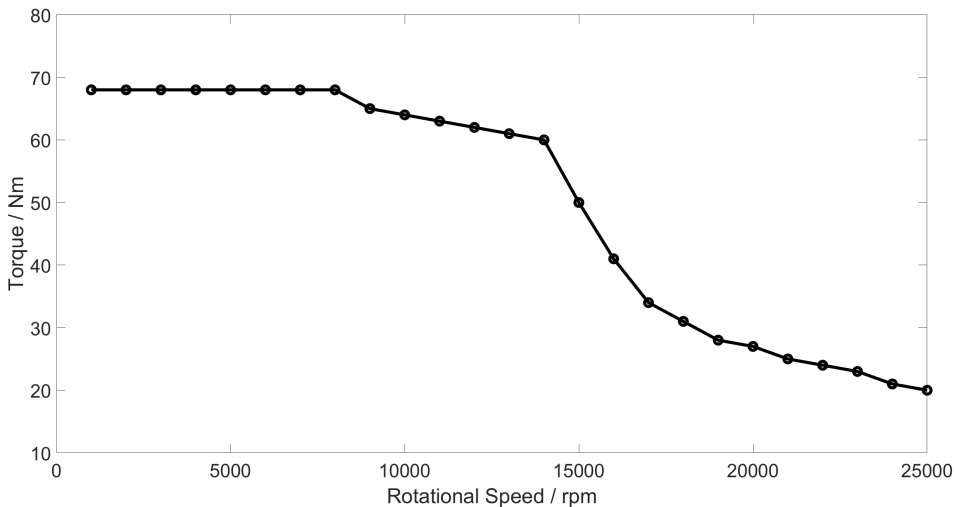


Figure 2.2 Torque-speed characteristics of permanent magnet synchronous motor (PMSM).

and gearbox input shaft operate under high-speeds of up to 25 000 rpm. A typical torque/speed operating range of a 54 kW PMSM used within these electrified drive systems is shown in Figure 2.2.

With such high speeds, these powertrains are able to produce high output power with relatively low torque requirements from the motor [2]. However, these operating characteristics introduce new challenges regarding NVH (Noise, Vibration and Harshness) and the tribology of interacting conjunctions.

2.2 Rolling Element Bearing Modelling

Before the 1960's, bearing studies were primarily conducted experimentally. Empirical formulations were derived to model their performance in early work by Stribeck [4] and Lundberg and Palmgren [5] [6] amongst others. As computer technology improved post-1960, modelling theory and application grew rapidly, pioneered largely by the work of Jones [7] and Harris [8]. In the pursuit of highly efficient and reliable bearings, modelling and the need for accurate representation of the physical phenomena has become important. It is not possible to conduct experimental testing for the large array of design and operational parameters that bearings are required for, therefore experimentally validated numerical analysis is employed.

2.2.1 Quasi-static Bearing Models

Early models predicting load distribution in the rolling elements can calculate bearing stiffness and fatigue life with relative accuracy. These were primarily quasi-static and based on force equilibrium. Studies of static ball bearings under simple radial loading were performed by Stribeck [4] and improved upon by Palmgren [6] for the case of nominal internal clearance. Static models computing radial and axial loads based on a load distribution factor and the angular position of the roller were found using Sjovall's integration model [9], however this was only applicable if the ratio of radial to axial loads is within a particular range. Rumbarger [10] developed a model using Sjovall's integral method for purely axial loading of thrust bearings, capable of calculating moment load due to axial load eccentricity.

It was the work of Jones [7] and his general theory for load deflection analysis of bearings that extended the capability of these models. His work accounted for centrifugal and gyroscopic loading, and unlike previous models, the inner bearing race had 5 degrees of freedom (DOFs); three translational and two rotational displacements that correspond to the external forces in all three Cartesian coordinates and moments applied about two. Bearing equilibrium is obtained at each rolling element by observing the load and corresponding motion of the elements. Jones also included the individual stiffness at the contact between rolling elements and raceways, using the Hertzian contact load-deflection relationship to obtain roller load based on contact deflection. This technique could be applied to both ball and roller bearings by varying the exponent of localised deflection.

Jones' model was considered limited due to the assumption that misalignment effects on the elements are negligible. Harris [8] improved on it by introducing the slicing method along the length of the rollers. This enabled determination of the load distribution

along the contact in roller bearings. This method, known as the Jones-Harris method, was then applicable for highly loaded conditions and able to compute misaligned cases. Vector and matrix methods to analytically solves the quasi-static problem based on the work of Jones and Harris were then presented for tapered roller bearing cases by Andréason [11] and Liu [12]. de Mul *et al.* [13] developed a model for ball and roller bearing equilibrium and stiffness matrix calculations which has the advantage of having load-deflection equations in matrix form. Therefore, implementation of this model was simpler.

Additional functionality has been added to these models such as the effects of thermal expansion on the load-deflection analysis [14]. Numerical models for heat generation based on frictional torque and 3-dimensional transfer through contacting elements was used to account for the expansion. It was found that expansion increased the bearing stiffness and thus natural frequency of the shaft-spindle system due to greater interference of the roller race contact.

Quasi-static models are only applicable under steady-state operating conditions, where time-varying forces and system inertia is negligible. These models do not capture the dynamic behaviour of bearings under changing conditions. However, the static equilibrium solutions [11] [12] [15] are of use to calculate load-deflection and individual element loading within dynamic models.

2.2.2 Dynamic Bearing Models

Transient operating conditions such as acceleration or deceleration of the bearing requires dynamic modelling, particularly important for high-speed applications. In dynamic bearing models, a system of differential equations based on Newton's second law of motion are used. This allows for a time-varying input force such as eccentric rotor unbalances or fluctuating loading conditions present in transmissions. Static equilibrium solutions such as those presented are used within these models to calculate load-deflection and individual element loading.

Hitherto, a multitude of models predicting bearing dynamics have been posed for roller bearings. These investigate the dynamic effect of geometrical and topographical parameters such as surface waviness, surface defects, and the variable compliance affect. This variable compliance effect is caused by time-varying stiffness variations off the inner and outer race bearing contact as rollers change their orbital position and pass through the loaded region. Even with perfect bearing geometry free from any defects, vibration will still occur due to this [16].

Simplified 2 degree of freedom models [17] consider purely in-plane motion of rolling elements in the radial and lateral directions of the bearings for investigation of frequency response to defects [18] and the varying compliance effect [19]. Time varying forces on cutting tool spindles and the effects on radial loading assuming no axial thrust loads or vibration can also be investigated in 2 DOF [20]. These models increase in complexity up to 5-DOF to observe moment loading and centrifugal effects [21] [22] [23]. Most of these models assume the bearing rollers and races are rigid bodies. All of these analyses also assume a dry contact between rolling elements and races which was assumed valid under the elastohydrodynamic regime of lubrication. The fluid film behaves as an amorphous, incompressible solid and generated pressures conform closely to a Hertzian distribution in the loaded region. This, however, neglects the effect of the lubricant film thickness in the contact mechanics and thus underestimates the contact deflection and hence load.

2.2.3 Lubricated Dynamic Bearing Models

Based on the experimental and numerical findings [24] [25] [26], the EHL film at the roller-race conjunction can be shown to increase the bearing stiffness, which continues to rise non-linearly with speed. It is therefore clear that the lubricant film in roller bearings operating at high speeds must be implicitly included in dynamic analyses. As stated by Bizarre *et al.* [27], there are few studies in the open literature that combine the stiffness and damping of an EHL contact with classical bearing dynamics.

Historically the analysis of rolling element bearings has been decoupled into two stages. The first stage is a classic dry Hertzian contact analysis of the roller-raceway contact due to the cyclic variation in geometric bearing centre. The displacement of the bearing centre is obtained through solving equations of motion and roller load is obtained using the Hertzian load-deflection relationship. Extrapolated film thickness equations use the transient load yielded from dry analysis in a second stage study to find central film thickness. This approach does not implicitly consider the effect of the lubricant film on the prevailing bearing motion and load, which is hence underestimated. To overcome these shortcomings, quasi-static analyses employing film thickness formulae in conjunction with Hertzian contact mechanics are required.

Early lubricated bearing models use extrapolated formulae to provide a relationship between the load share and film thickness at each element's contact with the bearing raceways [28]. Aini *et al.* [29] implemented the extrapolated film approach from the work of Rahnejat and Gohar [28] into a five-DOF bearing equilibrium model. The work computes the deformation at each roller-race contact, combining the EHL film

thickness with the elastic deformation of the contacting solids. The force–displacement relationship is shown to follow a non-linear trend.

Mohammadpour *et al.* [30] employed a similar implicit tribodynamic analysis and then utilised a full numerical EHL analysis explicitly for further tribological studies. In their analysis, input shaft speeds of 209 rad/s resulted in much slower entrainment velocities than are applicable for electrified powertrain analyses. Film shape and the elastohydrodynamic pressure profile at the contact could not be calculated in these studies, preventing more detailed analysis such as thermal and sub-surface stress analysis. To determine tribological contact conditions, Mohammadpour *et al.* [30] utilised a full numerical elastohydrodynamic analysis explicitly. Load values on an individual roller at each instantaneous position of the orbit were obtained from the implicit tribodynamic analysis and used within the numerical model.

Sopanen and Mikkola [16] modelled the influence of various surface characteristics on bearing dynamics, including contributions from surface waviness, roughness, localised and distributed effects. Their six-DOF model accounts for the Hertzian contact deformation and the EHL film implicitly within the contact. This model was embedded in a multi-body dynamic (MBD) software to utilise its mathematical capabilities. This work does not, however, demonstrate the effect that the EHL film has on bearing stiffness, and the effect on system dynamics using flexible bodies is not analysed [31]. Sawalhi and Randall [32] used a constant preload approach to imitate the stiffening effect of the film. Whilst this effective preload captures the increased contact stiffness due to the presence of the EHL film, the film thickness does not vary based on the loading conditions.

More recently, Liu and Shao [33] investigated the effects of surface waviness, including the effect of the lubricant film using an equivalent stiffness model. Nonato and Cavalca [34] presented a methodology to model EHL contacts using a set of non-linear springs and viscous dampers. Bizarre *et al.* [27] applied this lubricated non-linear force contact to a five-DOF model of an angular contact ball bearing. This enabled a combined solution scheme for the bearing force equilibrium and the EHL contact. The formulated system of equations was solved, achieving force equilibrium for each rotation of a bearing under constant external load. The authors of this study noted the interest of combining such models within FMBD system level models.

None of the combined models above are embedded within a system level model comprising flexible bodies, and the effect of the change in the contact stiffness due to the lubricant film is not investigated at the system level. Furthermore, the high-speed operation and time-varying loads representative of electrified vehicle transmissions are not considered.

2.3 Contact Mechanics



A critical aspect of this work is the interface between rolling element and race; a field of engineering referred to as Contact Mechanics. The following section gives a brief introduction to the modelling and development of such models. This subject is elaborated further in Section 3.2.6 and Section 4.3.1.

2.3.1 Hertzian Contact Mechanics

Two types of contacts occur in machine elements: conformal and non-conformal. Conformal contacts occur between a concave and a convex body of similar radius, such as in journal bearings. This leads to a relatively large contact area over which load can be distributed and resultant pressures are in the order of MPa. The contact between rolling elements and races is non-conformal in nature as the contacting surfaces are both convex. This type of contact creates a very small contact region over which force is transmitted, leading to very high contact pressures being generated in the order of GPa. Under these pressures, the contact surfaces deform elastically. In the case of a lubricated contact, a lubricant film forms in between the contacting surfaces in the order of microns (typically $< 2 \mu\text{m}$) [35]. Non-conformal contacts are commonly found in rolling element bearings, gear contacts and cam follower pairs.

A fundamental characteristic of these contacts is that the approach of the bodies under external load leads to the deformation of both bodies and the emergence of a contact patch. For two cylinders in contact with their axes parallel, a rectangular or line contact is formed along the length of the cylinders with width $2b$ (see Figure 2.3). An elliptical point contact results from contacting bodies that have different radii along both principal axes [36] (see Figure 2.4). In the case of cylindrical elements, such as those in Needle Roller Bearings (NRBs), Cylindrical Roller Bearings (CRBs) and Tapered Roller Bearings (TRBs), the mutual approach of the roller and race forms a line contact. Spherical elements, such as those found in Deep Groove Ball Bearings (DGBBs) and Angular Contact Ball Bearings (ACBBs), generate an elliptical contact at their conjunction with the raceway.

Two cylinders with radii R_1 and R_2 contacting in a non-conformal manner can be simplified as a rigid cylinder in contact with an elastic half-space. This cylinder, as represented in Figure 2.3, has a radius known as the reduced radius, R' :

$$\frac{1}{R'} = \frac{1}{R_1} + \frac{1}{R_2} \quad (2.1)$$

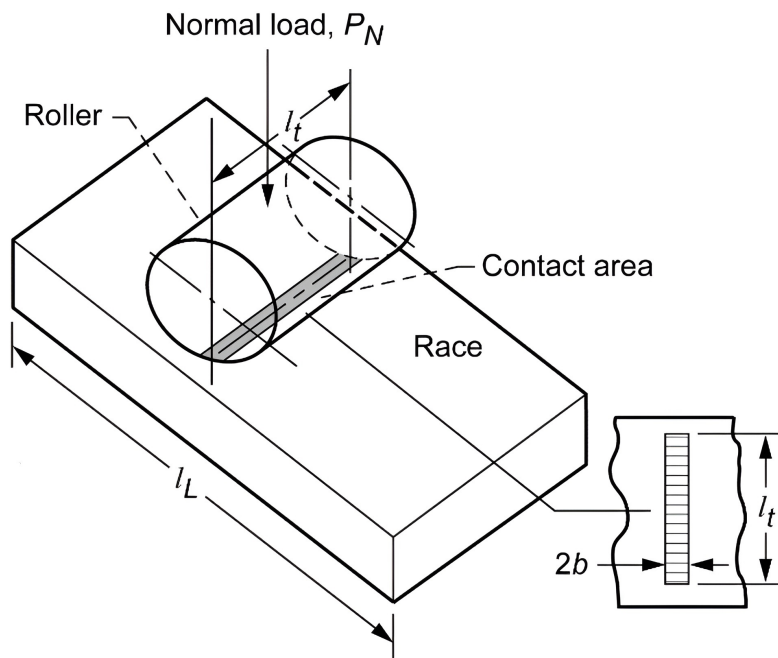


Figure 2.3 Roller-race model for line contact. [37]

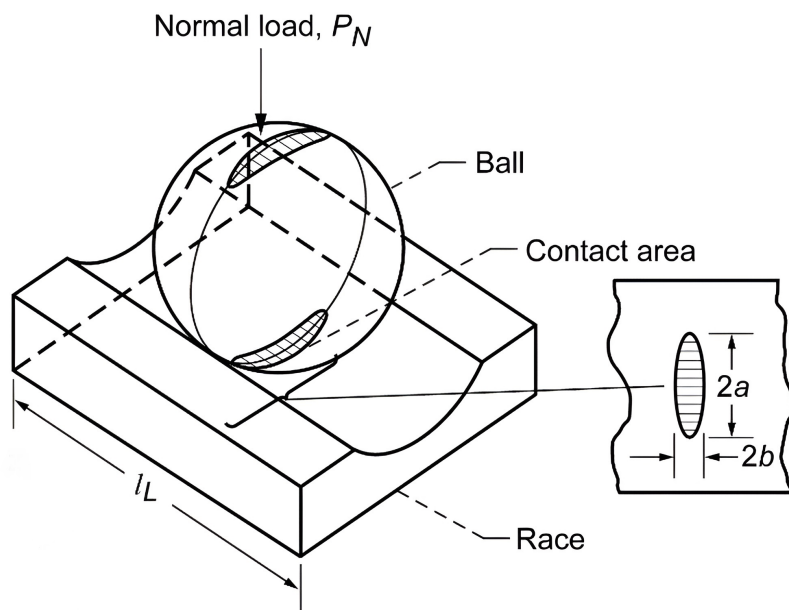


Figure 2.4 Ball-race model for point contact. [37]

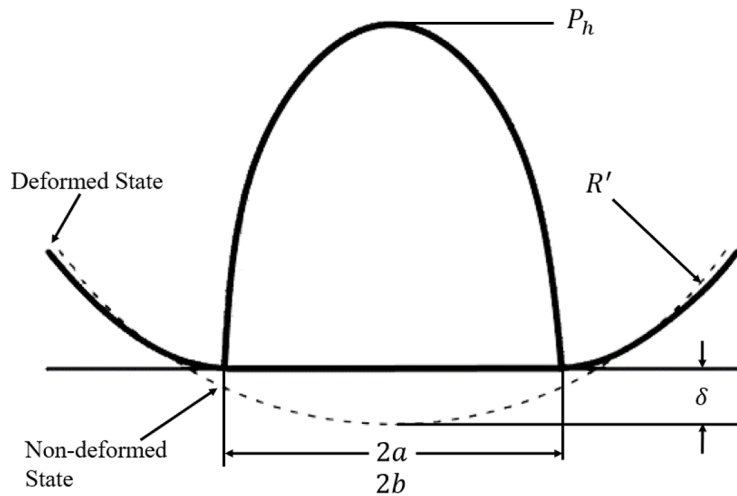


Figure 2.5 Hertzian contact deflection.

The material properties of the two bodies are evaluated in a similar way. The elastic modulus, E and Poisson's ratio, ν , of both bodies are combined to calculate the reduced elastic modulus:

$$\frac{1}{E'} = \frac{1}{2} \left(\frac{1 - \nu_1^2}{E_1} + \frac{1 - \nu_2^2}{E_2} \right) \quad (2.2)$$

According to Hertz's theory of elastostatic solids in contact [38], assuming the contact is frictionless, when load is applied to the cylinder it will experience very small strains. The amount that the cylinder deflects is much smaller than the radius of the cylinder, that is $\delta \ll R'$. The total area of the contact is also much smaller than the radius of the cylinder $a \ll R'$ (exaggerated in Figure 2.5). For example, a cylinder with a radius in order of mm will have a contact width of a few tenths of a mm and deflection a few tenths of a micron ($\delta < a \ll R'$).

The value of the deflection determines the stiffness of the contact and the displacement of the inner bearing race with respect to the outer. The contact area determines the contact pressures and hence maximum sub-surface stresses. Excessive sub-surface stress could lead to inelastic deformation and subsequent fatigue spalling.

Analytical formulae provide a way of calculating the dimensions of the contact patch, b , and the resultant maximum Hertzian pressure, P_h given a known load per unit length, w , material properties and geometry of bodies. For the case of the line contact these are:

$$b = \sqrt{\frac{8wR'}{\pi E'}} \quad (2.3)$$

$$P_h = \sqrt{\frac{2w}{\pi b}} \quad (2.4)$$

2.3.2 Line Contacts

The contact between rolling elements and raceways and the subsequent load and deformation generated at this contact is regarded as one of the most important issues in rolling-element bearing modelling. For a ball bearing, classical Hertzian theory is used to calculate the load-deformation relationship. However, the line contact is more complex.

There exist three methods to determine this relationship for the line contact in roller bearings: the slicing technique, 3D contact method and the alternative slicing technique. The slicing technique [11] divides the roller-race contact region into a finite number of slices, with the total contact forces calculated from the summation of forces of each individual slice. Various formulae have been developed to perform this calculation, all yielding very similar results. A drawback of this method is that the load on each slice does not influence the surrounding slices as they are treated independently. This means that pressure concentrations such as edge stresses on the contact are not captured. The 3D contact method uses the Boussinesq half-space force-displacement relationships and flexibility method of structural analysis. The contact pressure distribution and normal approach between the bodies is found using an iterative scheme, making this a time-consuming method. Kabus *et al.* [39] addressed this in their 6-DOF quasi-static time-domain bearing model by pre-processing a series of contacts at different centreline approaches and roller tilt angles, then interpolating these results in the actual simulations. This negated the need to solve the iterative scheme at each time step. This allowed for bearing misalignment, roller centrifugal forces, flange contact and roller tilt moments to be analysed.

Teutsch and Sauer [40] improved on the slicing technique with their alternative slicing method. Using a matrix of weighted influence coefficients, the effects of force on the deflection of neighbouring slices was captured. It is not too dissimilar in concept to the 3D contact method but with improved computation times. de Mul *et al.* [13] compared the slicing technique with their more complex non-Hertzian model and concluded that the simplicity and accuracy of the slicing method yielded accurate and faster results. Harris and Kotzalas [3] also concluded that the slicing technique, whilst unable to reflect edge stress concentrations, provides a suitably accurate load-displacement result as stresses are only distributed over a small area. For the purpose of load equilibrium, these stresses can be neglected. Misalignment or loading on roller

ends is not captured using this technique, therefore for fatigue life estimates this may produce non-conservative results; for this, the approach by Kabus *et al.* should be used. In general, the slicing technique is the most widely used, owing to its simplicity, speed and sufficient accuracy.



2.4 Elastohydrodynamic Lubrication

2.4.1 History

Under the EHL regime, both the elastic deformation of the solids in contacts as well as hydrodynamic theory are considered. Elastic bodies in contact for the case of ellipsoidal contacts was first investigated by Hertz in 1881 [38], allowing him to obtain the pressure distribution within an ellipsoidal contact. Separate studies on hydrodynamic lubrication were being performed by Reynolds in 1886 [41], based on a simplified version of the Navier-Stokes equation. It took a further 30 years before the two studies would be combined.

Early EHL studies began in 1916 when the pioneering work by Reynolds was applied to a simplified model of a gear-tooth contact by Martin [42]; replicated as two contacting cylinders. This analysis assumed that the solid bodies were rigid and the lubricant to behave with constant viscosity (ie. a hydrodynamic analysis). The resultant pressures were too high and the film thickness so low (1-10 nm) that coverage of asperities (typical order of 100 nm for machined gear teeth) was not possible. This contradicted experimental findings where machining tracks on high-speed gear tooth flanks were still visible after prolonged usage, which could only be explained by the presence of a sufficient lubricant film.

Between the 1930's and 1950's, significant research was performed to include both the elastic deformation of the surfaces and the effect of pressure on viscosity. Peppler [43] and Meldahl [44] both included the effects of surface deformation for non-conformal contacts, with Gatcombe [45] amongst others investigating viscosity increase due to the high pressure in the contact area. Typical EHL pressures are in the range of 0.5-4 GPa and the resulting piezo-viscous properties were found to be partially instrumental to forming the film.

Considered the origin of EHL, Grubin's pioneering work in 1949 [46] combined both elastic deformation and viscosity increase under pressure in film thickness calculations for the first time. In this analysis, he assumed that the deformed surface profiles in a highly loaded lubricated contact matched those produced in a classic dry Hertzian contact of the same materials and loading conditions. Reynolds equation could then

be solved at the inlet region of the contact and a more accurate determination of the separation of the solids in the central region was found. This led to a film thickness in the predicted range (an order higher than Martin's theory) and a more realistic pressure distribution than previous work. This pioneering study formed the basis for future EHL studies.

The first numerical solution of the line contact problem was presented shortly after by Petrusevich [47] which agreed with Grubin's main conclusions. It contained the three main features of an EHL contact: a nearly parallel film in the contact zone with local constriction at the exit, a Hertzian pressure profile, and secondary local maximum pressure or 'spike' at the outlet (see Figure 2.7). In 1959, Dowson and Higginson [48] presented their numerical solution to the isothermal line contact EHL problem. Their iterative inverse method enabled the evaluation of film thickness and pressure distribution for line contact problems for lightly loaded cases. Throughout the 1960s, the authors investigated the effects of variables such as dimensionless surface velocity, materials parameter and load on EHL solutions. The authors then curve fitted their results and generated an empirical formula for isothermal line contacts [49], which was then improved upon by Dowson [50] and Dowson and Toyoda [51]. The formulae predict the minimum film thickness as a function of the rolling velocity, load and material parameters.

Empirical formulae are widely used today for analytical calculations that do not require the computational intensity of a full numerical solution. They are, however, somewhat limited to the operating parameters used in original simulations and do not offer the capabilities of a full numerical solution, such as the modelling of inlet starvation at high speeds.

2.4.2 Numerical Methods

There are two main numerical methods for solving the elastohydrodynamic problem; direct and inverse. Typically, Reynolds equation is solved for pressure based on the lubricant film thickness. Early studies using this direct method suffered from convergence in highly loaded cases.

Inverse Method Ertel [52] introduced the inverse method for the hydrodynamic problem, which was adopted by Dowson and Higginson [48] for the EHL line contact problem. Here, the film thickness profile is found from a given pressure distribution. Solving the elastic deformation equation provides a second film thickness profile that

corresponds to the same pressure distribution. This pressure distribution is then modified manually until the film thickness solutions converge.

This approach has some disadvantages. For low load cases with a non-parallel film shape in the contact region, this method is not suitable since the deviation of the Hertzian starting solution is too large. The film thickness equation is also insensitive to local variations in pressure. Finally, it is only suitable for line contact 1-dimensional cases since the Reynolds equation cannot be integrated for the two-dimensional case. Evans and Snidle [53] overcame the 2-dimensional limitation by using their quasi-static solution where a direct method was applied at the inlet zone and the inverse method in the contact zone. The aim was to overcome the instabilities of the forward iterative method to solve heavily loaded contacts which were limited to 0.5 GPa , whereas common stresses in practice are typically in the order of 1.5 GPa , reaching as high as 4 GPa in some cases. A solution was only found for heavily loaded cases and the approach was limited by the need for an accurate initial estimate for pressure.

Direct Method The direct iterative method is the most common method whereby Reynolds equation is solved to find the pressure with a given film thickness. This pressure distribution is used with the elastic equation to calculate a new film shape. The pressure distribution must also achieve equilibrium with the externally applied load.

Two different direct methods have been used to solve the discretized Reynolds equation. The first is the iterative technique which has been applied to the 1-dimensional line contact problem [54] as well as the two-dimensional point [55] and elliptical [56] contact problem. The Gauss-Seidel scheme was used, solving Reynolds equation for pressure based on film thickness and iterating between the two until convergence was met. Force equilibrium in an outer loop was calculated by integrating pressure across the contact domain and ensuring convergence between the resultant force and the applied external load. The solution comprises of three nested loops that must all converge. Under-relaxation between successive iteration is applied to aid convergence, however this iterative method does not converge for high loads. Furthermore, the number of iterations to achieve convergence is large (ie. of the square of the number of computational points used) and thus excessive computation times result.

The second solution method is the Newton-Raphson method. This was first applied by Okumara [57] and later by Houpert and Hamrock [58], where pressures as high as 4.8 GPa were obtained with low CPU times. These low CPU times are a significant advantage of the Newton-Raphson methodology, with a smaller number of iterations resulting in much faster convergence than Gauss-Seidel.

Further numerical development came in the form of the multi-level method, first used by Lubrecht *et al.* in 1986 [59]. Venner *et al.* [60] used a multilevel multi-integration for point and line contacts in 1990 to reduce the computational cost of solving the film thickness integral. This allowed more nodes in the computational domain to be used for more complex problems with again much faster solution times. Finer grids could therefore be used, yielding faster results than Newton-Raphson for more complex cases. The solution time was proportional to $n \log(n)$, with n being the total number of nodes in the computational domain. This work was mainly focussed on reducing computational time for the point contact problem, with the authors acknowledging the applicability of the Newton-Raphson numerical scheme for the line contact problem.



2.4.3 Starvation

The assumption of a fully flooded inlet region to the contact is not always valid. Starvation may occur if insufficient lubricant is entrained into the contact; significantly affecting EHL characteristics such as film formation and friction coefficient. This starvation is found to be greater at higher speeds, with higher viscosity lubricants and limited lubricant supply [61]. At high speeds, lubricant replenishment can be diminished. For a fully flooded contact, the pressure builds upstream of the contact starting from a pressure gradient close to zero. With insufficient lubricant, the contacting bodies entrain two layers of lubricant, which then merge and form a meniscus at the contact inlet; causing the pressure rise to occur closer to the contact centre with a non-zero pressure gradient and reduced shape of the characteristic pressure distribution [62].

Analytical work on this topic began for the line contact problem by Wolveridge *et al.* [63] and later developed for the elliptical contact problem by Hamrock and Dowson [64]. In these studies, the inlet distance to the centre of the contact domain is varied as an input parameter. As the inlet distance is extended, the flooded condition at the entrance to the contact becomes greater. At a certain inlet distance, the film thickness in the contact is hardly affected (see Figure 2.6), and this is defined as the threshold between starvation and a fully flooded inlet condition. For the case of shorter inlet distances and subsequent starved condition, an equation was presented that could adjust the starved film thickness based on the starvation level and flooded film thickness.

2.4.4 Thermal EHL

Heat is generated in an EHL contact in two ways: due to the viscous shearing of the lubricant and the compressive action of the generated pressures [30]. Classic EHL theory is isothermal and considers a Newtonian fluid with no temperature rise from

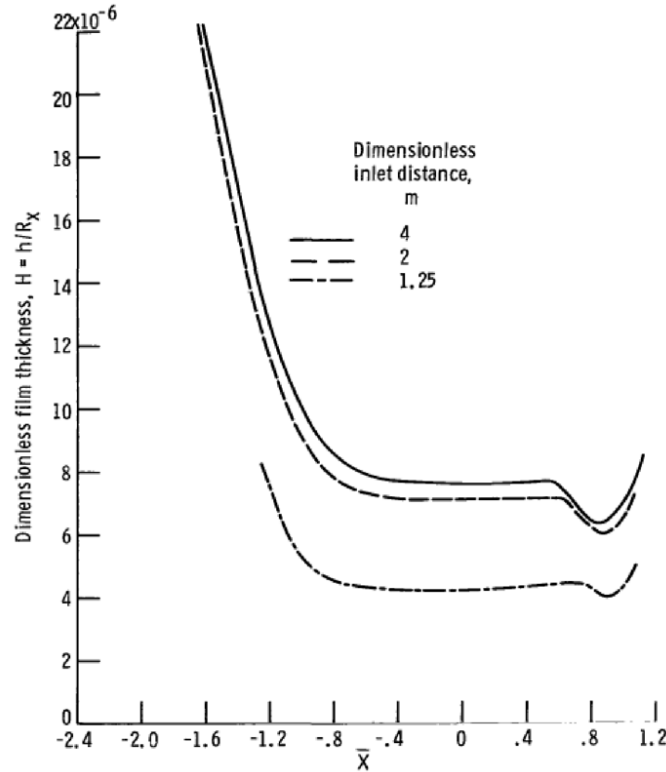


Figure 2.6 Effect of dimensionless inlet distance on film thickness for starvation modelling. [64]

sliding at the conjunction. For the case of pure rolling, this is sufficient to predict film thickness and inlet temperature rise. Rolling element bearings, however, can undergo complex rolling and sliding motions depending on the nature of the loading and contact conditions. The presence of sliding requires a rheological model that considers the viscosity relationship with pressure as well as the use of the energy equation to calculate temperature rise within the lubricant film.

The 3-dimensional energy equation has been solved by various authors for the line contact [65], point contact [66],[67] and finite line contact [68]. The generated heat is carried along the direction of entraining motion, in the direction of side leakage from the contact, and through the bounding surfaces of the contact. This can be reduced to fewer dimensions for the assumption of negligible heat transfer to the contacting bodies in the direction of the film thickness.

It has been found in the case of the point contact under low loads, thermal effects on pressure distribution and film thickness are negligible [69]. However, Kim and Sadeghi [66] concluded that with higher loads, the temperature rise in the film is significant. Under pure rolling conditions, the lubricant film temperature rise was only a moderate 15 °C above ambient and occurred at the inlet zone. As the slide/roll ratio was increased

to 0.2, for the same load and speed conditions a temperature rise of 140 °C above ambient resulted at the contact centre, with the dominant mode of heat transfer being shear heating in the contact. The authors also adjusted the ellipticity parameter of the contact [67], with higher ellipticity parameters bringing the elliptical shape of the contact closer to that of a line. In this study, the load was more moderate, and the temperature rise for pure rolling and a slide/roll ratio of 0.2 was 4.5 °C and 16 °C respectively.

Habchi *et al.* [70] found that even under light loads and moderate speed conditions, thermal effects were still noticeable for Newtonian fluids. For lightly loaded cases, thermal and isothermal results were comparable up to entrainment velocities of $1 \text{ m} \cdot \text{s}^{-1}$ but began to diverge slightly above this: in line with experimental findings. Additionally, as the slide/roll ratio is increased above 0.5, both central and minimum films are found to decrease for the thermal model, whereas the isothermal model remains constant. This is due to shear heating reducing lubricant viscosity. The difference was found to be only 0.015 μm between pure rolling and close to pure sliding for a lightly loaded contact.

Shear thinning of the lubricant also occurs at the inlet region to the contact. EHL films are micron level thickness, and assuming a fully flooded inlet, not all of the lubricant will traverse into the contact. Rejected lubricant will then produce some reverse flows which will shear the lubricant, increasing the inlet temperature and hence reduce the viscosity of the fluid [4].

It is therefore clear that a thermal elastohydrodynamic model is necessary for highly loaded conditions with modest slide/roll ratios. However, under the assumption of light loading and pure rolling, the effects on central film thickness are minimal.

2.4.5 Elastohydrodynamic Pressure and Film Characteristics

If there is relative velocity between two lubricated contacting surfaces, a thin film is formed due to the wedge mechanism and lubricant is entrained into the contact. The pressure profile across the contact deviates from the dry Hertzian parabolic distribution due to the presence of the lubricant.

Figure 2.7 shows the deviation of the film pressure from the dry Hertzian pressure. The main deviation occurs at the outlet of the contact due to the exit conditions. At the entry to the contact, the increasing pressure profile acts to oppose the flow of lubricant into the contact due to the entraining motion. At the outlet, the Couette profile and the pressure differential acts in the same direction to force lubricant out of the contact. For mass flow rate of the lubricant across the contact to be conserved, an outlet constriction is formed to reduce the flow area. The pressure spike at the outlet generates this deformation of the surfaces to maintain this flow balance and is a result of the

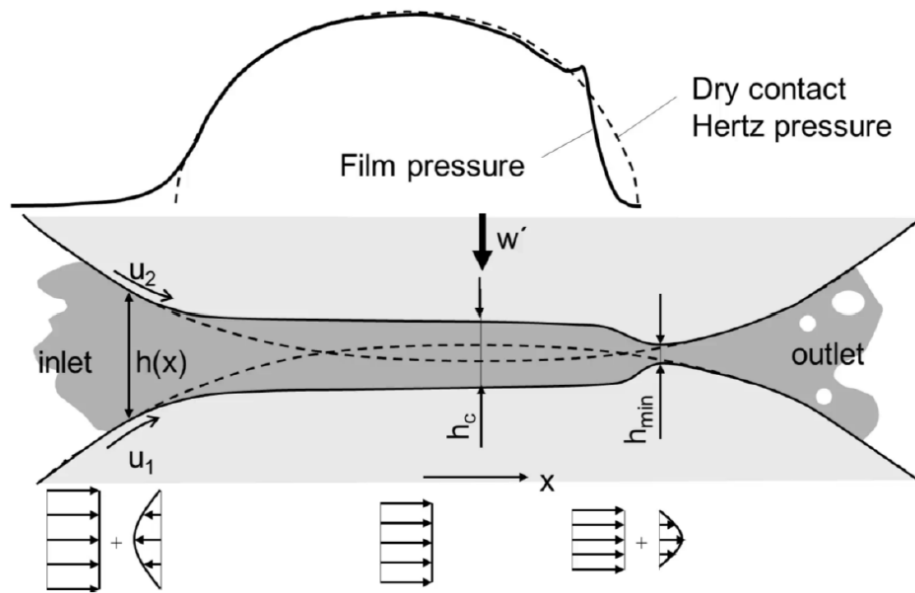


Figure 2.7 EHL film and pressure distribution. [71]

piezo-viscosity of the lubricant. The two laws that must be obeyed are therefore the force equilibrium (the differential of pressure across the contact must equal the applied force), and the flow continuity.

2.4.6 Lubrication Regimes

Lubricated contacts fall into four main regimes; these are:

- **Hydrodynamic:** Contacting surfaces are completely separated by the lubricant film. Load is light, typically several Newtons. The contact surfaces do not experience deformation and resultant pressures are in the region of MPa.
- **Elastohydrodynamic:** Contacting surfaces are completely separated by lubricant film; however, load is medium to heavy. Contact deformation occurs and resultant contact pressures are in the region of GPa.
- **Mixed:** An interrupted oil film separates the two surfaces, ie. some asperity interaction occurs. Mixed lubrication can occur under any load and is dependent on the film thickness and asperity height.
- **Boundary:** The lubricant film is negligible, and surfaces directly interact. This is regarded as a dry contact. At medium and high loads, Hertzian contact conditions can be assumed.

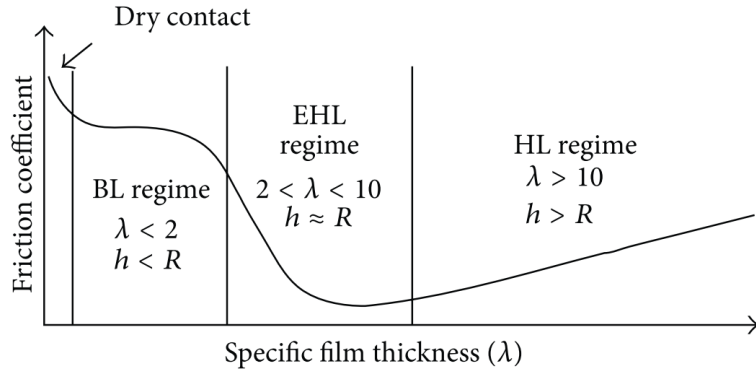


Figure 2.8 Stribeck curve and specific film thickness (λ). [72]

The loaded contact region of bearings are typically in the elastohydrodynamic regime of lubrication. The film thickness to asperity roughness height (lambda ratio, λ) is large enough that the surface features do not typically influence the lubricant thickness and a smooth surface is often assumed. Under operation, emerging clearances result in unloaded regions of the bearing which can cause the roller-to-race contact to deviate from the elastohydrodynamic lubrication regime towards hydrodynamic regime, resulting in sliding and roller-cage collisions [30]. Hence, the contact may go through different regimes of lubrication throughout its rotation.

Film thickness and surface roughness are related by Stribeck [4] using the specific film thickness:

$$\lambda = \frac{h}{\sigma} \quad (2.5)$$

where h is the lubricant film thickness and σ is the roughness height of the asperities on the contact surfaces. Figure 2.8 presents the various lubrication regimes and their associated coefficient of friction. For rougher surfaces, mixed-EHL occurs where contact of surface asperities occurs, increasing friction. The coefficient of friction then reduces as the film increases or asperity height reduces, until the hydrodynamic regime is reached, and the thicker films increase viscous friction.

2.5 Artifical Neural Networks

The most common machine learning (ML) algorithm used in tribological applications are ANNs, first utilised in the 1990s [73]. Ezugwu *et al.* [74] achieved an 80% success rate in predicting wear and failure rate of machine tools. Subsequent studies improved ANN accuracy for wear rate prediction in coatings [75] and mechanical systems [76], with Jones *et al.* optimising their ANN structure using the coefficient of determination

(R^2) to achieve 90% wear rate prediction accuracy. Similar studies were then conducted in the domain of friction and wear rate of composite materials under dry conditions [77] [78] [79], as well as tools steels [80].

ANNs have also been used in lubricated friction modelling. Bhaumik *et al.* [81] utilised ANNs to develop a new lubricant with multiple friction modifiers, with the target output being coefficient of friction. Fast and accurate predictions of traction coefficients under various thermal-elastohydrodynamic operating conditions have also been achieved [82], with errors lower than 3% in most cases. Relative viscosity predictions [83] [84] have also achieved deviation margins substantially lower than empirical correlations.

In the area of manufacturing processes, the input data array can be reduced drastically to contain only process-specific parameters such as load, speed, and vibration. This approach was taken to investigate flank wear in drilling [85] and surface roughness of machined parts [86]. Reducing the number of input parameters, reduces the amount of training data required to achieve good predictions. This reduction method is notable for the film thickness estimations.

The above studies all utilised experimental data to train the ANNs. Whilst experimental data benefits from the lack of assumptions in numerical models, there is often high cost and time associated with obtaining it. Consequently, the training datasets for the ANN were limited to approximately one hundred points [77] [79], or fewer [74] [75], with the largest being 216 points [80]. Since the training process optimises the ability of the ANN to interpolate between data points for varying input conditions, a greater number of training points is advantageous. This was noted by Ezugwu *et al.* [74] and Zhang *et al.* [77], and is a common observation shared across several studies and scientific applications [87].

An alternative method of achieving large data sets without the costs of experimentation is to use numerical modelling. Wang and Tsai [88] identified the need for larger training sets in the field of tribology, utilising Reynolds equation to predict maximum Hertzian pressure in thermohydrodynamic slider bearings. The training algorithm and data sample size was shown to significantly affect the prediction quality. Senatore and Ciortan [89] used training data obtained from numerical hydrodynamic lubrication simulations to achieve excellent prediction quality when optimizing frictional performance in a piston-cylinder. Gorasso and Wang [90] also utilised a numerical solution of Reynolds equation in conjunction with computational fluid dynamics (CFD) simulations to train an ANN for journal bearing optimization. Numerical data crucially allows for larger data sets to be generated that can cover a much larger range of input data; a requirement for generic implementation within dynamic models.

Physics-Informed Neural Networks (PINNs) have been applied to solve the Reynolds boundary value problem [91], demonstrating good agreement with analytical solutions. However, efficiency improvements are needed for real-time applications. Since the ANN in this research is to be implicitly embedded within a dynamic simulation, efficiency is critical. Data driven solutions are therefore preferable. Although ANNs lack the physical understanding provided by numerical solutions, they offer nearly real-time performance comparable to analytical solutions while benefiting from the accuracy of numerical methods [82].

Marian *et al.* [92] recently demonstrated for the first time the generation of EHL film thickness data, using a Finite Element Method (FEM) to train an ANN. The ANNs could predict locally-resolved film thickness across the contact domain 25-times faster than FE-based EHL simulations. However, even though contacts in common machine elements were the focus of the study, some combinations of the input data ranges deviate from the EHL regime. This influences the required number of training points for an accurate model. Moreover, the authors note the potential for this approach to be utilised within an FMBD environment for tribological modelling, something that is not currently reported on.

2.6 Closure



A review of the open literature shows that considerable advancements have been and continue to be made in the field of dynamic bearing modelling and tribology. Relevant modelling methods have been reviewed for the purpose of addressing the research aims of this work. However, there remains a notable gap in integrating these fields in the context of electrified automotive powertrains. Of critical interest is the influence of the EHL film formation on bearing and system dynamics under the high speed (up to 25 000 *rpm*) and moderate, time-varying load operating conditions within these powertrains. The EHL film has been shown to act as an interference element between the roller and race, affecting contact stiffness at high entrainment velocities. Conventional dynamic bearing analyses have focused on moderate speeds and higher loads, where dry bearing modelling is common due to the influence of the EHL film being less critical. Developments to model the EHL film both explicitly and implicitly within static and dynamic models have since emerged. However, none of the existing lubricated models are embedded within a system level model comprising flexible bodies at high-speed. Consequently, the impact of the EHL film-induced variations on contact stiffness remain unaddressed at the system level. With the trend towards high-speed motors in future automotive powertrains, the impact of this film growth must be explored.

The literature also demonstrates that ANNs can be successfully used to model tribological phenomena. However, these investigations are often limited by the range of input data available. Recent studies utilising numerical methods to obtain training data do not sufficiently constrain the data to the realistic operating conditions of the EHL contacts within bearings, leading to an inefficient training process. These methodologies could be further refined to improve their applicability. Furthermore, tribology-focused ANN research widely acknowledges the potential for integrating ANNs within FMBD models. This circumvents the requirement for a computationally intensive numerical solution to the EHL film thickness problem, whilst also improving on the accuracy of the commonly deployed regressed equations. Thus far, this approach has not been assessed for high-speed bearing modelling in FMBD environments.

Chapter 3

Investigating the Effect of Lubrication on the Tribodynamic Behaviour of High-Speed Roller Bearings

3.1 Introduction

A review of the literature revealed that a comprehensive understanding of bearing performance in modern electrified powertrains requires a multi-physics approach comprising dynamics and tribology at high speeds. The working conditions for the tribological contacts between rollers and races are affected by the dynamic behaviour of the bearing. The dynamic behaviour itself is affected by the tribological phenomena at the lubricated conjunctions via its influence on the contact stiffness [34] [27]. Therefore, a coupled tri-dynamic methodology must be established for more accurately capturing the system's behaviour.

To determine the contact conditions within bearings, the relative motion between the bearing races must first be established. Traditionally, this motion is derived from dynamic models by solving the equations of motion. However, these can be computationally intensive and often lack required physics such as system flexibility.

This chapter presents a high-speed experimental test rig which has been instrumented to experimentally measure the kinematic motion of a bearing at rotational speeds and loads up to 15 000 rpm and 750 N respectively. This motion was used as the boundary conditions for tribological modelling. Roller-race contact load and film thickness are obtained using a lubricated contact model, whereby the EHL film is considered implicitly at the roller-race conjunction. EHL pressure and film thickness distributions are then

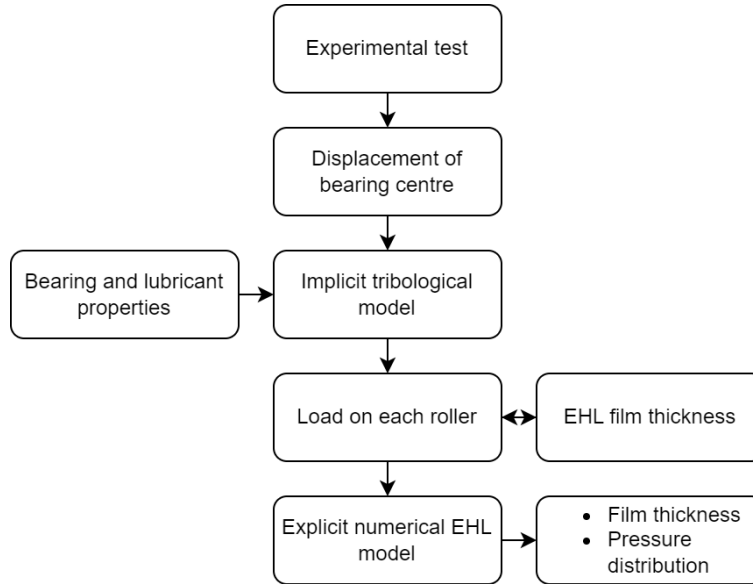


Figure 3.1 Experimental tribodynamics methodology overview.

obtained using an explicit 1D numerical EHL model. Fundamental equations used in the subsequent chapters are also introduced.

This initial work was performed to ascertain which models must be developed in the tribology domain without the requirement for a complex flexible dynamic model. The necessity of implicit inclusion of the EHL film when considering roller bearing dynamics at high-speed, and the shortcoming of conventional dry analyses at these speeds and loading conditions is established.

3.2 Workflow

An experimental test rig is used to measure the relative displacement between the inner and outer races of a cylindrical roller bearing (CRB). At each instantaneous position of a roller's orbit, the Hertzian load-deflection relationship in conjunction with the EHL central film thickness is used to determine the roller-race contact load. Experiments are performed across a speed range from 0 – 15 000 *rpm*. To implicitly consider the EHL film, an analytical tribological model is iterated to account for tribodynamic coupling between film thickness, contact deflection and load. After the experimentally informed tribological model is solved, load and speed values at specific rotational velocities are used within an explicit numerical EHL model to calculate film thickness and pressure distribution across the contact. The flow diagram in Figure 3.1 illustrates the methodology used. Interactions between each stage are explained in subsequent sections.

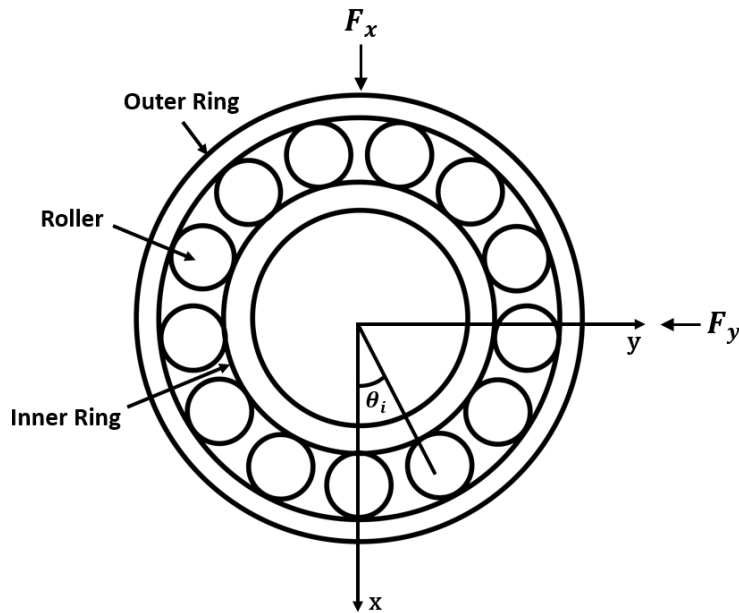


Figure 3.2 Cylindrical roller bearing in equilibrium position.

3.2.1 Operating Principles

The rollers within a bearing carry an instantaneous share of the overall applied load [93]. Deviation of the supported shaft from its nominal geometric centre results in a loaded region of the bearing. Due to the non-conformal nature of the contact between the bearing roller and race, these loads generate high pressures, leading to local surface deformation and increased lubricant viscosity. In conjunction with relative motion at the contact, this results in EHL film formation [94] [46]. In the unloaded region of the bearing, emerging clearances result in a shift to the hydrodynamic regime of lubrication, which can result in sliding and roller-cage collisions [30]. Hence, the contact may go through different regimes of lubrication throughout operation[95].

Figure 3.2 shows a cylindrical roller bearing (CRB) in equilibrium position with zero preload or design clearance. In the absence of an applied radial load, F_0 , the initial deformation, δ_o , and radial clearance, C_0 , between rollers and races are both zero. On application of external force, the resulting instantaneous radial load, F_i , will displace the inner bearing race from its equilibrium state (Δx and Δy). By analysing an individual roller at its instantaneous angular position, θ_i , the resultant displacement of the bearing centre can be used to determine the deflection at the roller-race contact, δ_i . These contact deformations will result in contact forces, W_i , which maintain the roller and races in dynamic equilibrium. The above interpretation is valid considering rigid inner and outer races.

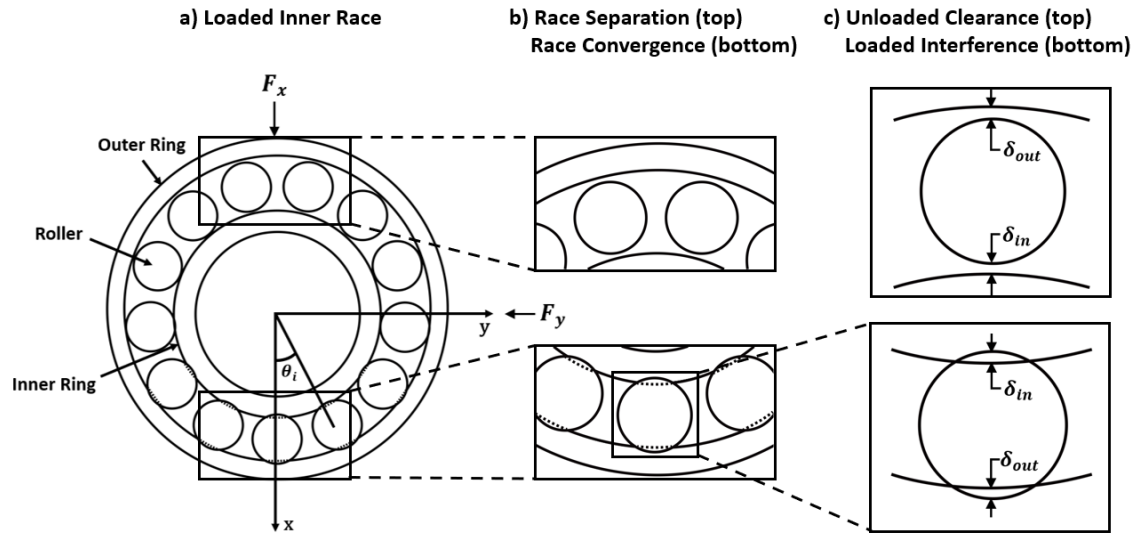


Figure 3.3 Mutual separation and convergence of inner and outer races.

Figure 3.3 presents the case whereby an instantaneous load is applied to the inner race. This causes deflection of the rollers in the loaded region and generates clearance around the rollers in the unloaded region. The deflections at the inner and outer race correspond to the normal component of the bearing centre's displacement at the instantaneous position of that roller. In the current study, this displacement was experimentally measured from the test rig and used quasi-statically as the boundary condition for the tribological model. It should be noted that this study considers in-plane, 2-DOF motion. This is a valid assumption under dominant vertical radial loading with secondary horizontal motion from the full system dynamics.

3.2.2 Lubricated Contact Mechanics

To calculate contact force based on deflection between the roller and race, the Hertzian load-deflection relationship is used. For low-speed, highly loaded analysis, the EHL film is typically neglected and the contact is considered dry. However, at high entrainment velocities, the literature study revealed that the EHL film also influences this contact force. The lubricant imposes additional deformation at the contact points which, changes the calculated force. Figure 4.4 in Chapter 4 demonstrates this graphically.

In this study, the central film thickness at the roller-race conjunction is calculated using an extrapolated central film thickness formula. The impact of the film on deflection, and consequently contact force, is evaluated using an iterative approach due to the interdependence between contact load and film thickness. In this part of the workflow,

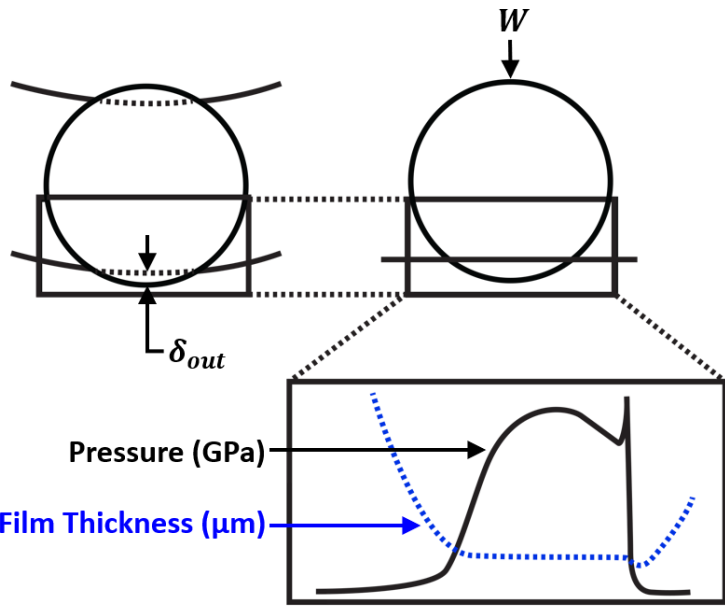


Figure 3.4 EHL film thickness and pressure distribution at contact.

the stiffness and damping of the EHL film is neglected due to its rigid-like stiffness, which is several orders of magnitude higher than the Hertzian contact [96] [97] [98].

For detailed tribological investigations, the numerical solution of the fluid film is essential. This provides the pressure, film thickness and shear distributions at the contact. This allows for further evaluation of the durability and frictional efficiency of the system. In the current study, the load on the roller and contact kinematics obtained from the implicit bearing model is used explicitly in a 1D elastohydrodynamic model to obtain film thickness and pressure distribution for specific loading periods through the speed sweep, as is shown in Figure 3.4. Since misalignment along the length of the rollers is not considered due to the high stiffness of the shaft and bracket, the 1D EHL analysis is sufficient [21]. This explicit approach significantly improves the computational efficiency of the model by negating the requirement for an implicit numerical EHL calculation at each sampling point.

3.2.3 Experimental Test Rig

The displacement of the bearing centre governs the conditions at the contact and was found experimentally using a high-speed bearing test rig. A 5 kW AC synchronous motor, capable of speeds up to 32 000 rpm was coupled to a steel shaft that is supported by two bearing brackets. Radial force was transferred to the inner bearing race via the shaft using a hinge/arm mechanism and a point load application device on the shaft.

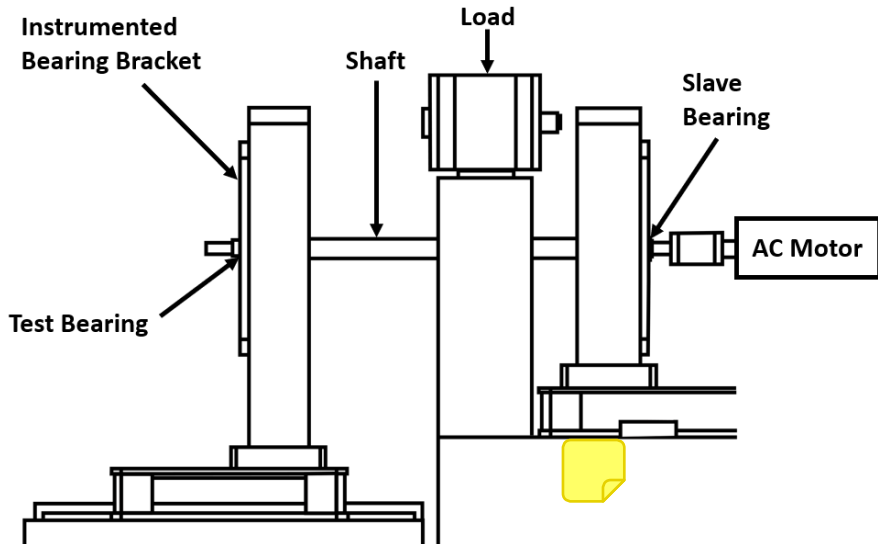


Figure 3.5 Experimental rig schematic.

Displacement data were obtained from an instrumented bearing bracket. Figure 3.5 shows a schematic of the rig.

The motor control unit was connected to a voltage input, transmitted via an NI cDAQ-9178 USB chassis for optimum resolution of the input voltage. A MATLAB script controlled the voltage ramp over a specified time-period and thus the spindle acceleration. In this study, a transient speed sweep was performed from 0 – 15 000 rpm over a 4 s period, with 750 N of static radial load applied to the shaft. The bearing under test was a single row cylindrical roller bearing, NU 205 ECP, located in an aluminium test bracket that has an extruded bore for instrumentation.

3.2.4 Instrumentation

The outer surface of the bearing bore was instrumented with two Type 4383 single-axis piezo-electric charge accelerometers, with a frequency range of 0.1 – 8.5 kHz and sensitivity of 3.16 pC/ms². These measured acceleration of the bracket's bore, corresponding to the outer race of the bearing (Figure 3.6). Two single beam laser vibrometers measured the displacement of the shaft at the edge of the bearing which corresponds to the displacement of the inner race of the bearing (Figure 3.7). A dual-beam vibrometer was used to measure the rotational speed of the shaft. All laser vibrometers had a frequency range of 0 – 10 kHz and maximum speed of 20 000 rpm.

A program in MATLAB controlled the speed of the shaft through a ramped voltage input. Data was simultaneously acquired from the accelerometers and laser vibrometers through synchronised input channels at a sampling rate of 100 kHz. Simultaneous

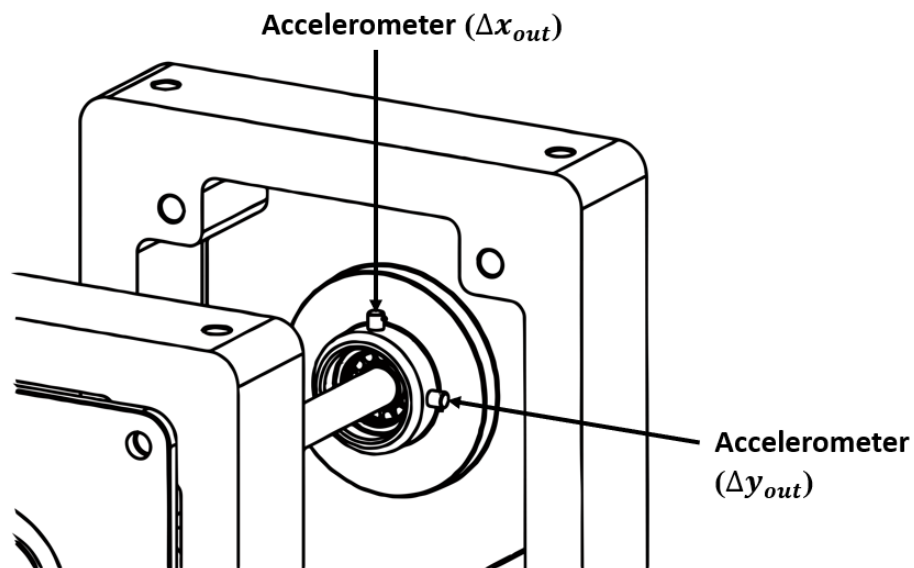


Figure 3.6 Accelerometer locations on test bracket.

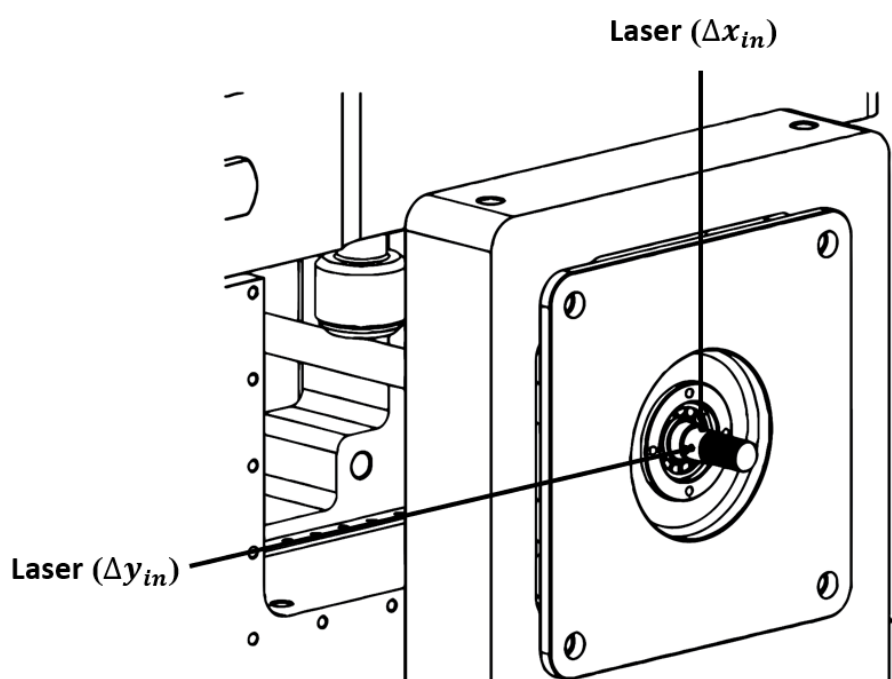


Figure 3.7 Laser vibrometer locations on shaft.

control and data acquisition ensure accurate results between different instrumentation locations.

3.2.5 Signal Processing

The bearing race displacements were obtained from the instrumented bearing using time-domain data from the accelerometers and laser vibrometers. The laser vibrometer directly provided displacement data, whereas the accelerometer data required post-processing of acceleration data. To ascertain the displacement of the bearing bore and thus outer bearing race, the accelerometer results were integrated twice:

$$v_{out}(t) = v_{0,out} + \int_0^t a_{out} dt \quad (3.1)$$

$$x_{out}(t) = x_{0,out} + \int_0^t v_{out} dt \quad (3.2)$$

As this double integration amplifies non-linearities in the original signal, it requires pre-processing [99]. Low frequency drift is removed from the unfiltered time-domain data by applying a linear fit to the data and then removing the trend from it.

To extract the frequency content of the speed ramp, waterfall plots were generated using the accelerometer and laser vibrometer data. Short-time fast-Fourier transform (STFFT) was used, with data windows of six shaft rotations at each 100 rpm increment. The resulting signal was then filtered using a Butterworth bandpass filter for a frequency range of 70 - 10 000 Hz to remove the high amplitude low frequency noise that was inherent to the equipment setup. The filter used 3 dB of passband ripple and 7 dB attenuation in the stopbands, which were set at 35 - 12 500 Hz. The relative displacement of the bearing centre could then be obtained from the relative displacement between the shaft (measured using the single beam laser vibrometer) and bearing bore:

$$\Delta x = \Delta x_{in} - \Delta x_{out} \quad (3.3)$$

$$\Delta y = \Delta y_{in} - \Delta y_{out} \quad (3.4)$$

where Δx_{in} and Δx_{out} correspond to the displacements of the shaft and bearing bore respectively.



3.2.6 Contact Mechanics at the Roller Race Conjunction

The contact between roller and race is modelled as an elastic deformation between an equivalent finite length elastic cylinder and rigid plate. This assumption is realistic under the conditions of an EHL line contact. The contact force on an individual roller at each instantaneous position, W_i , is obtained from the Hertzian load-deflection relationship:

$$W_i = k\delta_i^n \quad (3.5)$$

where k is the Hertzian contact stiffness non-linearity between a rolling element and the inner or outer raceway groove. For the case of rolling element bearings, the exponent of localised deflection, n , is equal to $10/9$ [8]. The contact deflection of a roller relative to the race, δ_i , is due to the normal dynamic motion (i.e. the local mutual convergence) of the inner and outer bearing races, contribution of lubricant film thickness and any additional clearance or interference fit [30]. This is expressed as:

$$\delta_i = 2(h_{c,i} - C) + x\cos(\theta_i) + y\sin(\theta_i) \quad (3.6)$$

where C is the local radial clearance, and x and y are the displacement components of the inner bearing race from its geometric centre. This normal approach between both races is the sum of the total deformation of the rollers and both races [100], hence:

$$\delta_i = \delta_{i,in} + \delta_{i,out} \quad (3.7)$$

The equilibrium of forces in a system of stiffnesses in series is therefore:

$$W_i = W_{i,out} = W_{i,in} \quad (3.8)$$

To find the individual deflection of each contact due to differences in contact stiffness, the following relationship is used:

$$\delta_{i,in}k_i = \delta_{i,out}k_{out} \quad (3.9)$$

The deflection value at each contact based on the total deflection and relationship between contact stiffness is then found from Equations 3.7 and 3.9 to give:

$$\delta_{i,out} = \frac{\delta_i}{\left(\frac{k_{out}}{k_{in}}\right)^{\frac{1}{n}} + 1} \quad (3.10)$$

The normal stiffness of the inner and outer races differs due to their geometry. To calculate the stiffness at each contact, the following equation is used:

$$\delta = \frac{F}{\pi E_r L} \left[\ln \left(\frac{4\pi E_r R_{zx} L}{F} \right) - 1 \right] \quad (3.11)$$

The deflection for a range of loads is calculated based on the geometry and material properties at the inner and outer race contacts. This non-linear relationship is numerically obtained and then curve fitted and represented by a power function in the form $F = a\delta^b$, with $b = 10/9$ and a representing the contact stiffness. Individual contact stiffness and deflection at the inner and outer race contacts is then found. The overall contact stiffness, $K_{i,\text{total}}$, is given by:

$$K_{i,\text{total}} = \frac{1}{\left(\frac{1}{K_{i,\text{in}}}\right) + \left(\frac{1}{K_{i,\text{out}}}\right)} \quad (3.12)$$

where $K_{i,\text{in}}$ and $K_{i,\text{out}}$ are the stiffnesses of the inner and outer race contacts respectively.

3.2.7 Implicit Tribological Model

A stepwise solution was performed on an individual roller at each orbital position. The roller bearing and bracket tolerances are such that the internal clearance is $0 \mu m$ between roller and race. In an unloaded state, there is no deflection of elements or raceway. Displacement in positive $x - y$ corresponds to the same total magnitude of deflection of roller and race contacts. For each time step, the bearing is first assumed to be in equilibrium position and film thickness is assumed to be $0 \mu m$. The deflection of the bearing is calculated under these conditions and is therefore a function of the relative displacement between inner and outer bearing races. With deflection at the time step calculated, the resultant lubricant regime and subsequent analytical solutions can be performed based on the following three conditions:

1. $\delta = 0$ indicates a film of $0 \mu m$ and no load.
2. $\delta < 0$ indicates complete separation of the roller and race. In this instance, the lubricant is assumed to fill the separation gap, with the film thickness value equalling the magnitude of the separation:

$$h_i = |\delta_i| \quad (3.13)$$

Under this condition, the lubrication is in the hydrodynamic regime. The hydrodynamic lubricant reaction load was derived by Rahnejat [101], and is given by:

$$W_i = \frac{2bu_i\eta_0R_{zx}}{h_i} \quad (3.14)$$

where b is the half length of the contact, u_i is the speed of lubricant entrainment into the contact, η_0 is the lubricant viscosity, R_{zx} is the reduced radius of the roller and race and h is lubricant film thickness.

3. $\delta > 0$ indicates deflection at the roller-race contact. This means that contact pressure is sufficiently high for the lubrication regime to be elastohydrodynamic. For the elastohydrodynamic regime, an iterative process is performed to solve the film thickness. This is due to the contribution of EHL film towards deformation and consequently the load in the contact.

The cylindrical roller and race contacts are modelled by an equivalent rigid roller against a semi-infinite elastic half space of equivalent elastic modulus, E_r . The extrapolated central film thickness for a line contact is therefore obtained [51] from:

$$h_c = R_{zx} \left[3.06G^{*0.56}U^{*0.69}W^{*-0.1} \right] \quad (3.15)$$

where the following dimensionless parameters are used:

$$G^* = \alpha E_r \quad (3.16)$$

$$U^* = \frac{u\eta_0}{R_{zx}E_r} \quad (3.17)$$

$$W^* = \frac{W}{LE_rR_{zx}} \quad (3.18)$$

where R is the reduced radius of the contact, L is the length of the roller and u is the speed of entraining motion into the contact and W is the contact load. Assuming pure rolling, the speed of entraining motion is given by:

$$u_i = \frac{1}{2}(\omega_{c,i} - \omega_{ri,i})r_{in} \quad (3.19)$$

An iterative process is used to calculate load on the roller based on total deflection including lubricant film (Equation 3.6). At each time step where an EHL film is

Table 3.1 Surface topography data

Parameter	Value	
	Roller	Inner race
Root-mean-square height	$0.197 \mu m$	$0.065 \mu m$
Density of peaks	$0.00116 \mu m^{-2}$	$0.00153 \mu m^{-2}$
Arithmetic mean peak curvature	$0.180 \mu m^{-1}$	$0.038 \mu m^{-1}$

present, the following convergence criteria must be met before the next time step is calculated:

$$\frac{h_i^n - h_i^{n-1}}{h_i^{n-1}} \leq 0.01 \quad (3.20)$$

3.2.8 Surface Topography Measurements

To assess the likelihood of asperity interaction, the roughness height of asperities, σ , must be measured for the roller and race. Surface topography measurements were performed using an Alicona InfiniteFocus Variation Microscope with a $\times 10$ objective. This had a vertical resolution of $30 nm$ and sampling point separation of $176.9 nm$ in the $y - z$ plane of the roller and $1 nm$ in x . An area of 530 by $588 \mu m$ was captured. Data was processed using Vision65 Map Premium software, where the profile radius of the roller and race was removed. The measured parameters for a roller and race are presented in Table 3.1. The resulting composite surface roughness of a roller-race contact is $0.207 \mu m$.

3.3 Numerical EHL Model

Whilst the analytical solution used in the implicit tribological model provides central film thickness, the film thickness and pressure distributions can only be obtained explicitly through the full solution of Reynolds equation in conjunction with rheological and elastic field models. In a line contact, where contact dimensions in the side-leakage direction, y_c , are much larger than the direction of entraining motion, x_c , pressure in y_c direction is assumed constant due to the negligible gradient and the contact can be analysed in one dimension. This assumption is valid in the contact apart from small regions near the edge. A simplified 1D version of Reynolds equation can therefore be used [21].

3.3.1 Reynolds Equation

Reynold's equation [41] is the governing equation of fluid film lubrication theory. For Newtonian fluids it can be derived from the full Navier-Stokes equations making the following assumptions, primarily the neglection of inertial forces and only retaining viscous forces on the lubricant [94]:

1. Body forces are negligible (mass of film is negligible)
2. Pressure is constant through the lubricant film (z -direction) due to the thin film (dimensions of the region of pressure are typically 100 times the central film thickness).
3. No slip at the boundaries
4. Lubricant flow is laminar (low Reynolds number)
5. Inertia and surface tension forces are negligible compared with viscous forces (working fluid has low mass and low acceleration)
6. Shear stress and velocity gradients are only significant across the lubricant film
7. The lubricant behaves as a Newtonian fluid
8. Lubricant viscosity is constant across the film
9. The lubricant boundary surfaces are parallel or at a small angle with respect to each other

Reynolds equation is a second order, non-linear partial differential equation. It is made up of the pressure induced terms (Poiseuille flow) and the boundary velocity-induced term (Couette flow).

The simplified 1D version of Reynolds equation is given by:

$$\frac{\partial}{\partial x} \left[\frac{\rho h^3}{6\eta} \left(\frac{\partial p}{\partial x} \right) - \rho h u \right] = 2 \frac{\partial(\rho h)}{\partial t} \quad (3.21)$$

To solve Reynolds equation numerically, it must first be discretized and then solved using the finite-difference method. The following procedure explains this discretization.

Due to the steady state nature of the investigations, with the absence of shock loading, the transient squeeze term can be removed:

$$\frac{\partial}{\partial x} \left[\frac{\rho h^3}{6\eta} \left(\frac{\partial p}{\partial x} \right) - \rho h u \right] = 0 \quad (3.22)$$

Due to the many orders of magnitude differences between lubricant film thickness (μm) and pressures (GPa), the numerical solution often becomes unstable. Dimensionless parameters are therefore defined to remove this instability. These are as follows:

$$\begin{aligned}
 U &= \frac{u}{u_{av}} & \partial x &= a \partial X \\
 X &= \frac{x}{a} & \partial \rho &= \rho_0 \partial \bar{\rho} \\
 \bar{\rho} &= \frac{\rho}{\rho_0} & \partial \eta &= \eta_0 \partial \bar{\eta} \\
 \bar{\eta} &= \frac{\eta}{\eta_0} & \partial h &= \frac{a^2}{R_{zx}} \partial H \\
 H &= \frac{h R_x}{a^2} & \partial p &= p_h \partial P \\
 P &= \frac{p}{p_h} \\
 W^* &= \frac{w}{E_r R_{zx} L}
 \end{aligned} \tag{3.23}$$

Terms in the simplified Reynolds equation are replaced with dimensionless parameters. Similar terms are then grouped and rearranged to give the final form:

$$\frac{\partial}{\partial X} \left[\frac{\bar{\rho} H^3}{6 \bar{\eta}} \left(\frac{\partial P}{\partial X} \right) \right] = \Psi \left[\frac{\partial}{\partial X} \bar{\rho} H U \right] \tag{3.24}$$

where

$$\Psi = \frac{12 u_{av} R_{zx}^2 \eta_0}{p_h} \tag{3.25}$$

Grouping terms for simplicity

$$M = \frac{\bar{\rho} H^3}{6 \bar{\eta}} \tag{3.26}$$

$$Q = \bar{\rho} H \tag{3.27}$$

Making substitutions

$$\frac{\partial}{\partial X} \left[M \left(\frac{\partial P}{\partial X} \right) \right] = \Psi \frac{\partial}{\partial X} [Q U] \tag{3.28}$$

$$\left[M \frac{\partial^2 P}{\partial X^2} + \left(\frac{\partial M}{\partial X} \right) \frac{\partial P}{\partial X} \right] = \Psi \left[U \frac{\partial Q}{\partial X} + Q \frac{\partial U}{\partial X} \right] \tag{3.29}$$

The final term is removed, as velocity, U , is independent of x when no stretching of the surfaces occurs. This is then differentiated to give:

$$\frac{\partial M}{\partial X} = \frac{\partial}{\partial X} \left[\frac{\bar{\rho}H^3}{6\bar{\eta}} \right] = \frac{H^2}{2\bar{\eta}} \left[\left(\frac{H}{3} \right) \frac{\partial P}{\partial X} + \bar{\rho} \frac{\partial H}{\partial X} - \left(\frac{\bar{\rho}H}{2\bar{\eta}} \right) \frac{\partial \bar{\eta}}{\partial X} \right] \quad (3.30)$$

and

$$\frac{\partial Q}{\partial X} = \frac{\partial}{\partial X} [\bar{\rho}H] = H \frac{\partial \bar{\rho}}{\partial X} + \bar{\rho} \frac{\partial H}{\partial X} \quad (3.31)$$

Substituting into Equation 3.29 gives the following:

$$\frac{\bar{\rho}H^3}{6\bar{\eta}} \frac{\partial^2 P}{\partial X^2} + \frac{H^2}{2\bar{\eta}} \left[\frac{H}{3} \frac{\partial \bar{\rho}}{\partial X} + \bar{\rho} \frac{\partial H}{\partial X} - \frac{\bar{\rho}H}{2\bar{\eta}} \frac{\partial \bar{\eta}}{\partial X} \right] \frac{\partial P}{\partial X} - \Psi U \left[H \frac{\partial \bar{\rho}}{\partial X} + \bar{\rho} \frac{\partial H}{\partial X} \right] = 0 \quad (3.32)$$

$$\frac{\partial^2 P}{\partial X^2} + \frac{3}{\bar{\rho}H} \left[\frac{H}{3} \frac{\partial \bar{\rho}}{\partial X} + \bar{\rho} \frac{\partial H}{\partial X} - \frac{\bar{\rho}H}{2\bar{\eta}} \frac{\partial \bar{\eta}}{\partial X} \right] \frac{\partial P}{\partial X} - \frac{6\bar{\eta}}{\bar{\rho}H^3} \Psi U \left[H \frac{\partial \bar{\rho}}{\partial X} + \bar{\rho} \frac{\partial H}{\partial X} \right] = 0 \quad (3.33)$$

The final form of the equation is therefore:

$$\frac{\partial^2 P}{\partial X^2} + \left[\frac{1}{\bar{\rho}} \frac{\partial \bar{\rho}}{\partial X} + \frac{3}{H} \frac{\partial H}{\partial X} - \frac{3}{2\bar{\eta}} \frac{\partial \bar{\eta}}{\partial X} \right] \frac{\partial P}{\partial X} - \frac{6\bar{\eta}}{H^2} \left[\frac{1}{\bar{\rho}} \frac{\partial \bar{\rho}}{\partial X} + \frac{1}{H} \frac{\partial H}{\partial X} \right] \Psi U = 0 \quad (3.34)$$

3.3.2 Finite Difference Formulation

To solve Reynolds equation computationally, a finite difference formulation required. The central difference formula based on Taylor series expansion [102] is used. The second derivative of pressure using second order central discretization for the spatial domain is therefore:

$$\frac{\partial^2 P}{\partial X^2} = \frac{P_{i-1} - 2P_i + P_{i+1}}{\Delta X^2} \quad (3.35)$$

and the first derivative is given by:

$$\frac{\partial P}{\partial X} = \frac{P_{i+1} - P_{i-1}}{2\Delta X} \quad (3.36)$$

Replacing terms in the final form of discretized Reynold equation:

$$\frac{P_{i-1} - 2P_i + P_{i+1}}{\Delta X^2} + \left[\frac{1}{\bar{\rho}} \frac{\partial \bar{\rho}}{\partial X} + \frac{3}{H} \frac{\partial H}{\partial X} - \frac{3}{2\bar{\eta}} \frac{\partial \bar{\eta}}{\partial X} \right] \frac{P_{i+1} - P_{i-1}}{2\Delta X} - \frac{6\bar{\eta}}{H^2} \left[\frac{1}{\bar{\rho}} \frac{\partial \bar{\rho}}{\partial X} + \frac{1}{H} \frac{\partial H}{\partial X} \right] \Psi_U = 0 \quad (3.37)$$

$$\frac{P_{i-1} + P_{i+1}}{\Delta X^2} + \left[\frac{1}{\bar{\rho}} \frac{\partial \bar{\rho}}{\partial X} + \frac{3}{H} \frac{\partial H}{\partial X} - \frac{3}{2\bar{\eta}} \frac{\partial \bar{\eta}}{\partial X} \right] \frac{P_{i+1} - P_{i-1}}{2\Delta X} - \frac{6\bar{\eta}}{H^2} \left[\frac{1}{\bar{\rho}} \frac{\partial \bar{\rho}}{\partial X} + \frac{1}{H} \frac{\partial H}{\partial X} \right] \Psi_U = \frac{2P_i}{\Delta X^2} \quad (3.38)$$

Pressure at each node point can then be represented by:

$$P_i = \frac{\frac{P_{i-1} + P_{i+1}}{\Delta X^2} + \left[\frac{1}{\bar{\rho}} \frac{\partial \bar{\rho}}{\partial X} + \frac{3}{H} \frac{\partial H}{\partial X} - \frac{3}{2\bar{\eta}} \frac{\partial \bar{\eta}}{\partial X} \right] \frac{P_{i+1} - P_{i-1}}{2\Delta X} - \frac{6\bar{\eta}}{H^2} \left[\frac{1}{\bar{\rho}} \frac{\partial \bar{\rho}}{\partial X} + \frac{1}{H} \frac{\partial H}{\partial X} \right] \Psi_U}{2 \left(\frac{1}{\Delta X^2} \right)} \quad (3.39)$$

Simplified to

$$P_i = \frac{P_{xx} + P_x - E}{2 \left(\frac{1}{\Delta X^2} \right)} \quad (3.40)$$

where

$$P_{xx} = \frac{P_{i-1} + P_{i+1}}{\Delta X^2} \quad (3.41)$$

$$P_x = \frac{P_{i+1} - P_{i-1}}{2\Delta X} \left[\frac{1}{\bar{\rho}} \frac{\partial \bar{\rho}}{\partial X} + \frac{3}{H} \frac{\partial H}{\partial X} - \frac{3}{2\bar{\eta}} \frac{\partial \bar{\eta}}{\partial X} \right] \quad (3.42)$$

$$E = \frac{6\bar{\eta}}{H^2} \left[\frac{1}{\bar{\rho}} \frac{\partial \bar{\rho}}{\partial X} + \frac{1}{H} \frac{\partial H}{\partial X} \right] \Psi_U \quad (3.43)$$

3.3.3 Effect of Pressure on Lubricant Viscosity

EHL temperatures are typically in the region of 0.5 - 4 GPa. The resultant behaviour of the viscosity at these pressures is instrumental in forming the EHL film and must be accounted for. The Barus law [103] determines viscosity increase with pressure assuming constant ambient temperature:

$$\eta = \eta_0 \exp(\alpha p) \quad (3.44)$$

where η is the lubricant viscosity at gauge pressure, p , η_0 is the viscosity at $p = 0$, and α is the pressure-viscosity coefficient (m^2/N) and is specific to the lubricant. This

relationship does not account for the change in α with temperature and pressure [35], becoming inaccurate above 0.5 GPa.

A more comprehensive relationship which simultaneously includes the effects of temperature and pressure was one proposed by Roelands [104] and developed by Houpert [105]. Roelands law is therefore accurate at higher contact pressures:

$$\eta = \eta_0 \exp(\alpha^* p) \quad (3.45)$$

The Roelands pressure-viscosity coefficient, α^* , is a function of both p and θ , with θ_0 being the reference or ambient temperature, for example at the inlet:

$$\alpha^* p = [\ln(\eta_0 + 9.67)] \left\{ \left(\frac{\theta - 138}{\theta_0 - 138} \right)^{-S_0} \left[\left(1 + \frac{p}{p_0} \right)^{Z_0} - 1 \right] \right\} \quad (3.46)$$

where

$$z_0 = \frac{\alpha}{5.1 \times 10^{-9} [\ln(\eta_0) + 9.67]} \quad (3.47)$$

and

$$S_0 = \frac{\beta (\theta_0 - 138)}{\ln(\eta_0) + 9.67} \quad (3.48)$$

The oil constants Z_0 and S_0 are independent of both pressure and temperature, and Z_0 can be typically taken as 0.68 for computational purposes.

3.3.4 Effect of Pressure on Lubricant Density

For accurate film EHL film shape calculations, the effect that pressure has on the lubricant density must be considered. The most common equation for this is the widely used Dowson and Higginson model [106]:

$$\rho = \rho_0 \left(1 + \frac{0.6 \times 10^{-9} p}{1 + 1.7 \times 10^{-9} p} \right) \quad (3.49)$$

where ρ_0 is the lubricant atmospheric pressure. Further modifications can be made to account for the effects of temperature:

$$\rho = \rho_0 \left(1 + \frac{0.6 \times 10^{-9} p}{1 + 1.7 \times 10^{-9} p} \right) [1 - 0.65 \times 10^{-3} (\theta - \theta_0)] \quad (3.50)$$

3.3.5 Effect of Temperature on Lubricant Viscosity



Most EHL work assumes constant temperature of the contact and that viscosity and density are dependent on pressure only. Standard experiments have been performed to assess effect of temperature on viscosity. Results have previously been curve fit by Crouch and Cameron [107], with the most simple fit due to Reynolds:

$$\eta = \eta_s \exp(-\beta \Delta \theta) \quad (3.51)$$

where η_s is the viscosity of the lubricant at temperature θ_s , η is the viscosity at representative temperature, θ , and $\Delta \theta$ represents the temperature difference between the two. β is the thermoviscous constant and is lubricant specific. This relationship is only valid for small temperature rises of the lubricant. A more accurate and widely used equation is the expression from Vogel:

$$\eta = K \exp\left(\frac{b}{\theta + c}\right) \quad (3.52)$$

with the three constants dependant on the lubricant, obtained from knowing three pairs of values for θ and η .

3.3.6 1D EHL Solution Methodology

The methodology for the 1D EHL solution used within this thesis is as follows.

Reynolds equation is used to calculate contact pressures. Assuming a thin film of Newtonian lubricant in a line contact, the following form is used and discretized as described in Section 3.3.2:

$$\frac{\partial}{\partial X} \left[\frac{\bar{\rho} H^3}{6\bar{\eta}} \left(\frac{\partial P}{\partial X} \right) \right] = \Psi \left[\frac{\partial}{\partial X} \bar{\rho} H U \right] \quad (3.53)$$



where X is the direction of entraining motion into the contact. Squeeze film motion is neglected for this analysis. The pressure-density relationship in the compressible model is modelled using Dowson-Higginson [106] (3.49). Roelands equation [104] (3.45) is used for the pressure-viscosity relationship.

Pressure distribution is obtained from the variations in film thickness at the contact, which is defined as below:

$$h = h_0 + \frac{x^2}{2R_{zx}} - \frac{2}{\pi E_r} \int_{x_{c, \text{in}}}^{x_{c, \text{out}}} p \ln(x - x')^2 dx' \quad (3.54)$$

where h_0 is the central film thickness, the second term represents an idealised film thickness parabola, with the final term representing the localised contact deflection. Central film thickness is first estimated using [51]:

$$h_0 = R_{zx}3.06G^{*0.56}U^{*0.69}W^{*-0.1} \quad (3.55)$$

$$G^* = \alpha E_r \quad (3.56)$$

$$U^* = \frac{u\eta_0}{R_{zx}E_r} \quad (3.57)$$

$$W^* = \frac{w}{LE_rR_{zx}} \quad (3.58)$$

Below, the method of solution for the numerical EHL model is provided:

1. Input the load value obtained from the implicit tribological model for an instantaneous position as well as contact kinematics from experimental conditions.
2. An initial estimation of lubricant film thickness, h_0 is made.
3. Inlet and outlet distances are set to $-4.5a$ to $1.5a$ based on the contact half width calculation. This sets up the computational domain, and assumes fully flooded inlet conditions [64].
4. Pressure distribution and film thickness are obtained through simultaneous solutions of equations 3.53 to 3.55 using the dimensionless parameters defined in 3.23. The Newton-Raphson iterative scheme is used for speed and robustness of convergence [57]. Pressure convergence criterion is required for the iterative solution:

$$\text{Err}_{\text{pressure}} = \frac{\sum_{i=1}^n |p_{\text{new}} - p_{\text{old}}|}{\sum_{i=1}^n p_{\text{old}}} \leq \epsilon_p \quad (3.59)$$

where $\epsilon_p = 1 \times 10^{-5}$.

Under-relaxation is applied between successive iterations where the criterion is not met:

$$p_{\text{new}} = (1 - \gamma)p_{\text{old}} + \gamma p_{\text{new}} \quad (3.60)$$

where the under-relaxation factor is typically $0.01 \leq \gamma \leq 0.8$

5. Hydrodynamic reaction load is calculated using the integration of pressure over the computational domain:

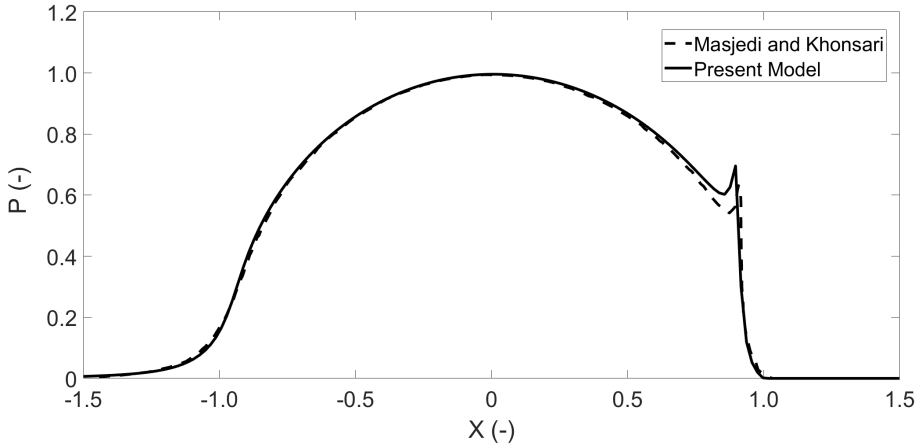


Figure 3.8 Validation of dimensionless pressure distribution, present model (solid), Masjedi and Khonsari (dashed).

$$W_h = L \int pdx \quad (3.61)$$

The total reaction from the hydrodynamic load should be equal to the total load share on the roller, W_i , obtained from the explicit tribological model. The following convergence criterion is applied:

$$\frac{|W_i - W_h|}{W_i} \leq \varepsilon_W \quad (3.62)$$

where $\varepsilon_W = 0.001$

3.3.7 Numerical EHL Model Validation

Conjunction level validation of the numerical method for solving the EHL film thickness and pressure distributions was performed using the work of Masjedi and Khonsari [108]. These were validated against their smooth surface plots with no asperity pressure contribution. The dimensionless input parameters were $W^* = 1 \times 10^{-4}$, $U^* = 1 \times 10^{-11}$ and $G^* = 4500$. The results shown in Figure 3.8 and Figure 3.9 show a good agreement between the model used in the study and the work of Masjedi and Khonsari for the dimensionless pressure, P , and dimensionless film thickness, H , respectively.

3.3.8 Experimental Result Verification

The experimental results obtained from the presented rig were verified against analytically calculated frequency contents. This was to ensure the correct post processing of

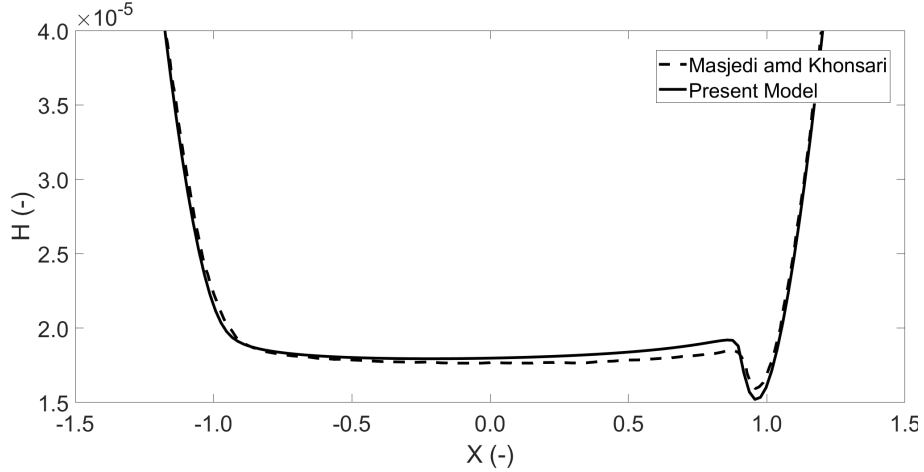


Figure 3.9 Validation of dimensionless film thickness distribution, present model (solid), Masjedi and Khonsari (dashed).

data for the input to tribological models. The bearing and lubricant data properties are given in Table 3.2 and Table 3.3 respectively.

Primary frequencies in the system due to the interaction of the rolling elements, races and the shaft could be verified. These frequencies were calculated analytically, with f_{bpi} and f_{bpo} representing the ball pass frequencies of the inner and outer race respectively and f_{shaft} being the rotational frequency of the shaft:

$$f_{bpi} = \frac{\omega_s N}{2\pi} \frac{1}{2} \left(1 - \frac{D_r}{D_p} \right) \quad (3.63)$$

$$f_{bpo} = \frac{\omega_s N}{2\pi} \frac{1}{2} \left(1 + \frac{D_r}{D_p} \right) \quad (3.64)$$

$$f_{shaft} = \frac{\omega_s}{2\pi} \quad (3.65)$$

At 14 000 rpm, the theoretical inner and outer race frequencies are calculated to be 1669 Hz and 1131 Hz respectively, with the experimental results being 1611 Hz and 1131 Hz. The first order shaft rotational frequency from the experiment was 232 Hz compared to theoretical calculation of 233 Hz. The above frequencies can be seen clearly in Figure 7, which shows the bearing bore displacement spectra, and Figure 8 which represents the shaft displacement spectra. The verification frequencies are identical in both, confirming that the bearing motion is accurately measured by the experimental methodology. It is observed that at certain speeds, the ball pass frequency of the outer race has a larger contribution than the inner race. This is particularly highlighted at 12 000 - 14 000 rpm. These regional effects are contributed by modal behaviour of the bracket and the bed. The critical speed of the unloaded shaft, where lateral bending

Table 3.2 Bearing specification

Parameter	Value
Inner race bore	25 mm
Inner race diameter	31.5 mm
Outer race diameter	46.5 mm
Roller diameter	7.5 mm
Roller length	9 mm
Number of rollers	12
External load	750 N
Radial interference	0 μm

Table 3.3 Lubricant and material properties

Parameter	Value
Pressure viscosity coefficient (α)	$2.1 \times 10^{-8} \text{ Pa}^{-1}$
Atmospheric lubricant dynamic viscosity	0.08 Pa.s
Lubricant inlet density (ρ_0)	833.8 $\text{kg} \cdot \text{m}^{-3}$
Eyring stress (τ_0)	2 MPa
Shear strength of asperities	0.3
Thermal conductivity of fluid	1600 $\text{W} \cdot \text{m}^{-1} \cdot \text{K}^{-1}$
Modulus of elasticity of contacting solids	210 GPa
Poisson's ratio of contacting solids	0.3
Density of contacting solids	7850 $\text{kg} \cdot \text{m}^{-3}$
Thermal conductivity of contacting solids	46 $\text{W} \cdot \text{m}^{-1} \cdot \text{K}^{-1}$
Specific heat capacity of contacting solids	470 $\text{J} \cdot \text{kg}^{-1} \cdot \text{K}^{-1}$

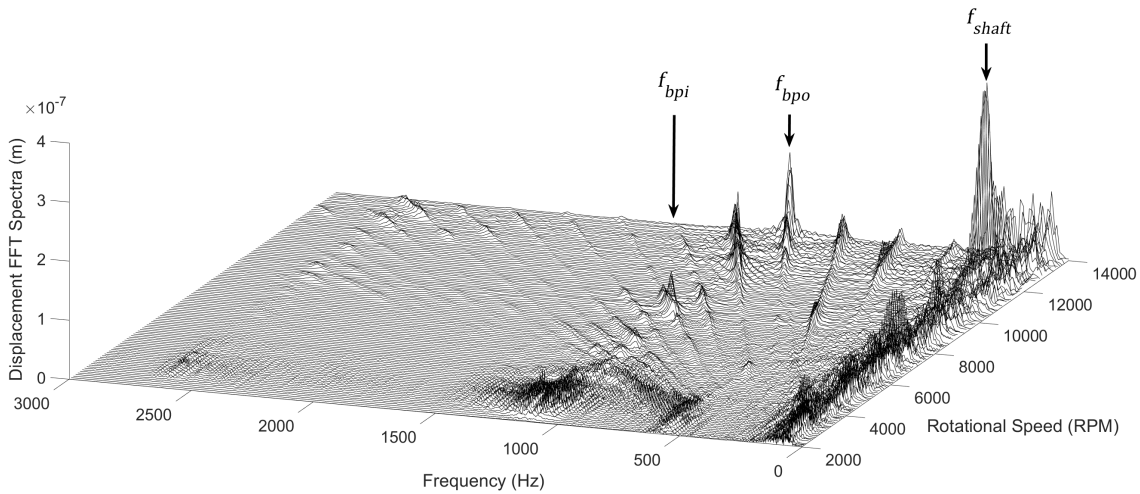


Figure 3.10 Bearing bore displacement frequency spectra.

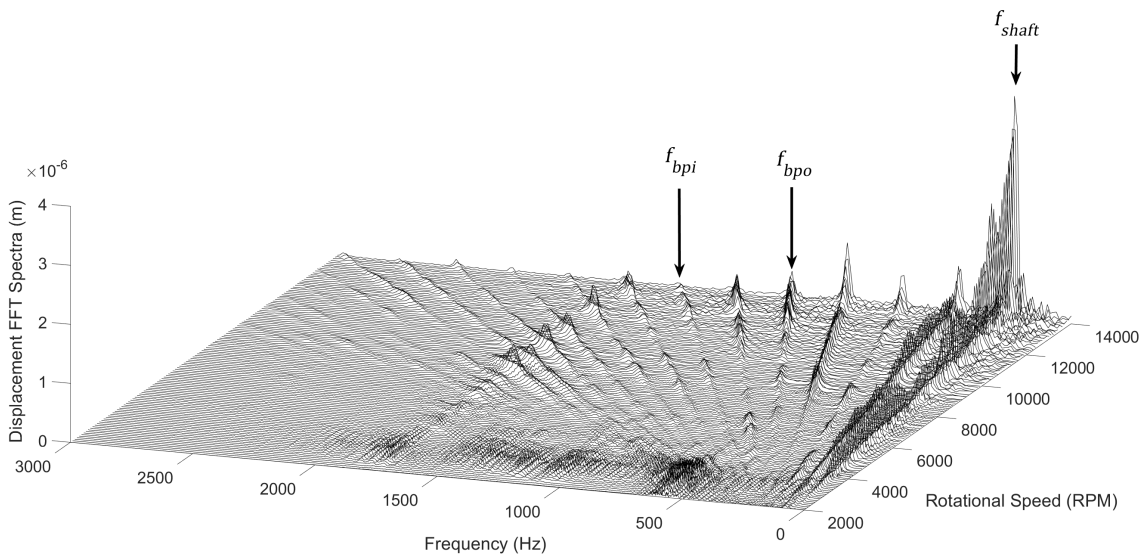


Figure 3.11 Shaft displacement frequency spectra.

frequency of the shaft is equal to the rotation frequency [109], occurs at 12 660 *rpm* and 211 *Hz*.

3.4 Results and Discussion

This section presents the results of the numerical tribological models. The kinematic data from the experimental test rig are used as the boundary conditions to the implicit and explicit models.

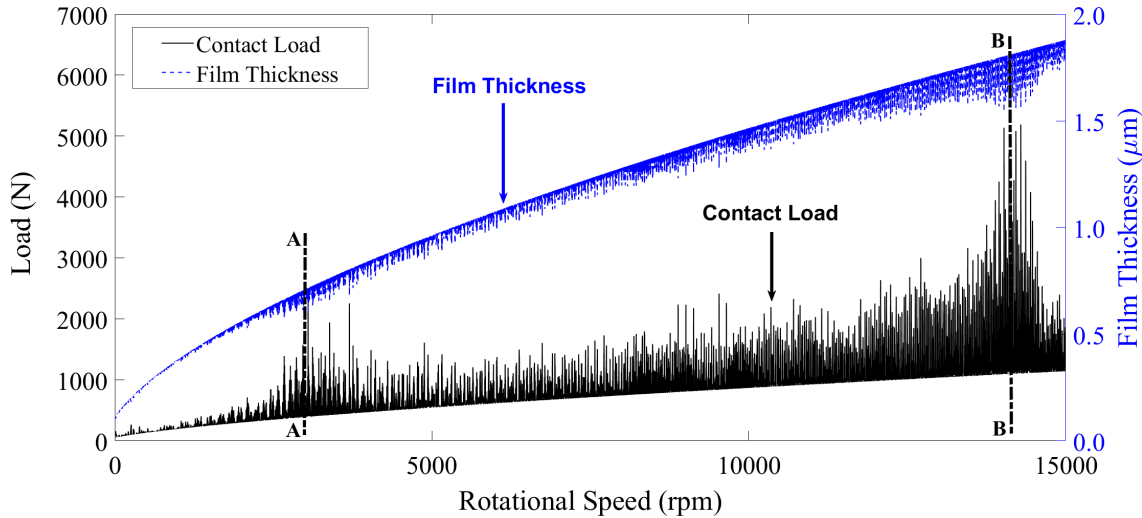


Figure 3.12 Contact load and film thickness - Outer race.

3.4.1 Film Thickness and Load Across Speed Sweep

The variation in EHL film thickness and roller contact load across the speed sweep from 0 - 15 000 *rpm* at the outer race contact are shown in Figure 3.12. Only the EHL regions are shown, where loads are significant enough to cause contact deformation. The upper limit of the film is where the roller and races diverge and approach the hydrodynamic regime where the film is hence governed by the entraining motion of lubricant into the contact. The lubricant film, as seen from the film thickness equation, is more affected by the speed of entraining motion rather than the load. This explains the increasing film thickness values in Figure 3.12, despite increasing load. The film thickness is increased from 0.1 to 1.9 μm across the speed sweep, revealing a significant increase that can affect the tribodynamic behaviour of the bearing, as explained in following sections. Full system and rotor dynamics also contribute to the total load on the roller, with periods of resonance at 3 000 *rpm* and 14 000 *rpm*, marked as A and B respectively in Figure 3.12.

Figure 3.13 presents an interval of the speed sweep where the effect of the EHL load on reducing the film thickness under oscillating conditions can be observed and the hydrodynamic film growth as the roller is unloaded. It is possible to see the effect of the resonant frequency at 1765 *Hz* superimposed on the lower fundamental train frequency within the loaded region as the inner and outer rings converge and diverge. The results in Figure 3.13 confirm the significant effect of dynamic behaviour as well as the multi-regime nature of the lubrication due to dynamic effects.

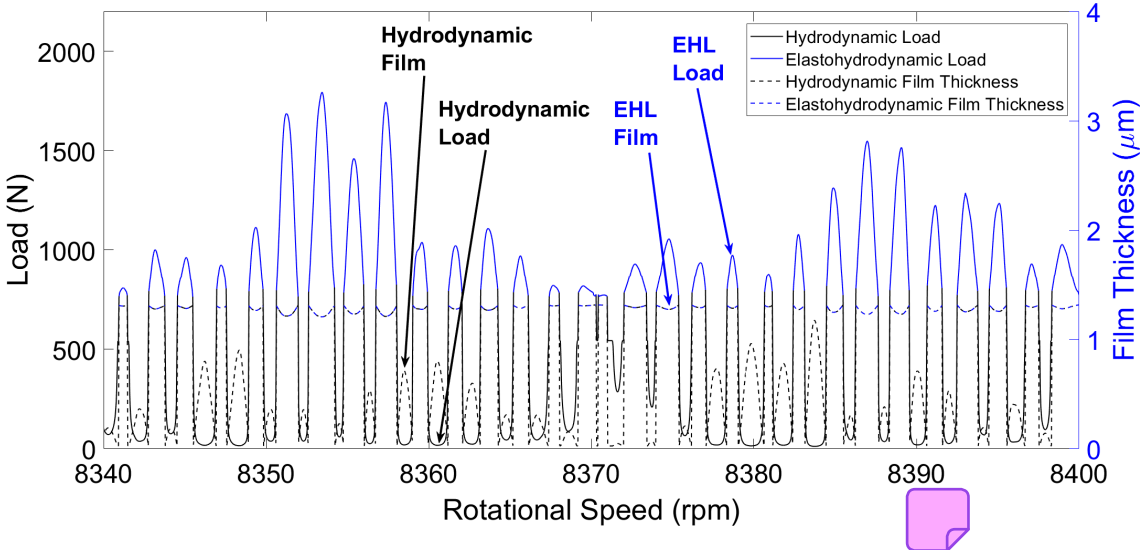


Figure 3.13 Film and load - EHL to hydrodynamic regime.

3.4.2 EHL Regimes

As has been demonstrated in the results analysis, the contact conditions deviate from the elastohydrodynamic regime of lubrication into the hydrodynamic regime throughout the roller orbital motion. These conditions can be verified by presenting the results on the Greenwood chart for fluid regimes of lubrication. The charts display the physical effects instrumental to EHL formation under isothermal conditions: viscosity rise due to pressure and elastic deformation of the surface. These two effects are quantified by two dimensionless parameters, G_e and G_v , as defined below [94]:

$$G_e = \frac{W^*}{U^{*1/2}} \quad (3.66)$$

$$G_v = \frac{W^{*3/2} G^*}{U^{*1/2}} \quad (3.67)$$

Four regions exist and the boundaries of these regions are defined by the geometry of contacting bodies, material, and lubricant properties. As is shown in Figure 3.14, the outer roller-race contact conditions move between the viscous elastic (VE) and iso-viscous rigid (IR) regimes. The VE regime signifies the EHL regime of lubrication where contact pressures are such that the elastic deformation of the surfaces and viscosity rise due to pressure increase is significant. The IR regime occurs when the magnitude of elastic deformation is insignificant, and the contact pressures are low enough that viscosity rise is negligible, i.e. hydrodynamic lubrication [110]. The boundary between the two also corresponds well with the distinction being made between hydrodynamic and EHL in this methodology, presented by the black and blue regions of the plot.

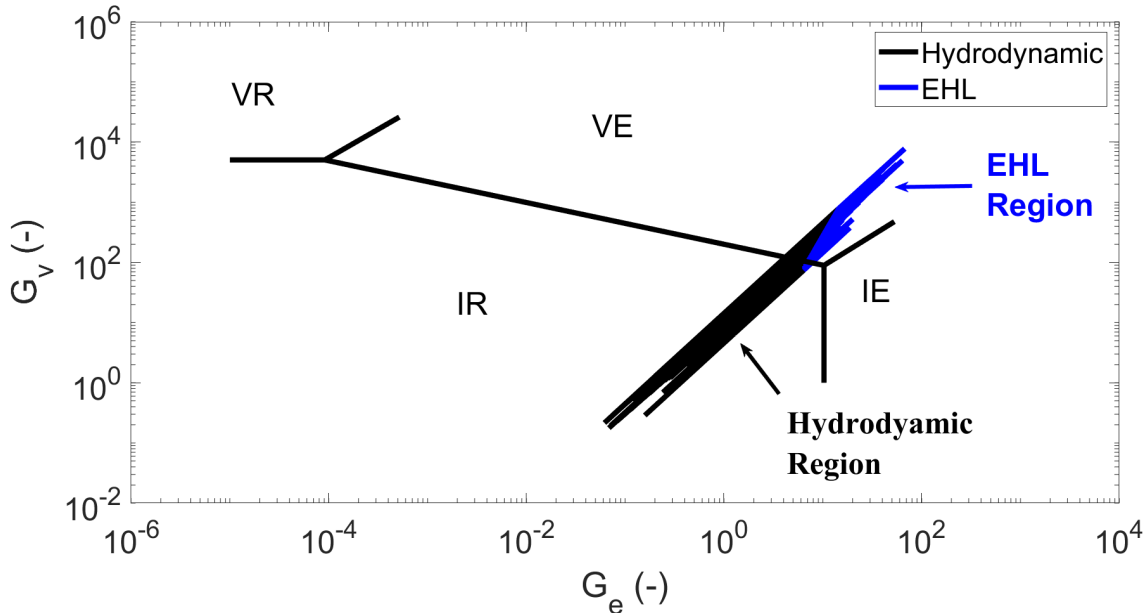


Figure 3.14 EHL and hydrodynamic conditions during roller operation. Key: IR = Iso-viscous Rigid, VR = Viscous Rigid, VE = Viscous Elastic, IE = Iso-viscous Elastic.

3.4.3 Dry vs Lubricated Tribodynamic Model

Previously presented results confirmed the significance of considering tribodynamic coupling on the tribological predictions. The aim of this section is to assess the significance of this coupling on dynamics via affecting contact load and stiffness values. The surface deformation at the EHL contact is further exacerbated by the presence of the lubricant film. Since the contact load and contact stiffness are governed by this deformation, neglecting the film leads to an underestimation of the total load at the roller-race contact. At higher speeds, such as those present in modern electrified powertrains, the growth of the lubricant film due to the increased entraining motion into the conjunction cannot be neglected – as is shown in Figure 3.12 with a film growth from 0.1 to 1.9 μm . The implicit tribological model was run for two cases, including and negating lubricant film thickness in the deformation obtained from Equation 3.6. The difference in magnitude at each time step is computed, and the increase in load magnitude between a dry and lubricated model is calculated. For EHL loads, the magnitude of the load difference through the speed sweep is plotted in Figure 3.15.

There is an increasing contact load difference across the speed sweep, with fluctuations arising from the dynamics of the system. To fully understand the requirement for a lubricated bearing model, the percentage difference between both cases is presented at three different rotational speed snapshots of 3 050 rpm, 14 135 rpm, and 14 855 rpm in Figure 3.16. At low speeds and relatively low dynamic load, the addition of the film

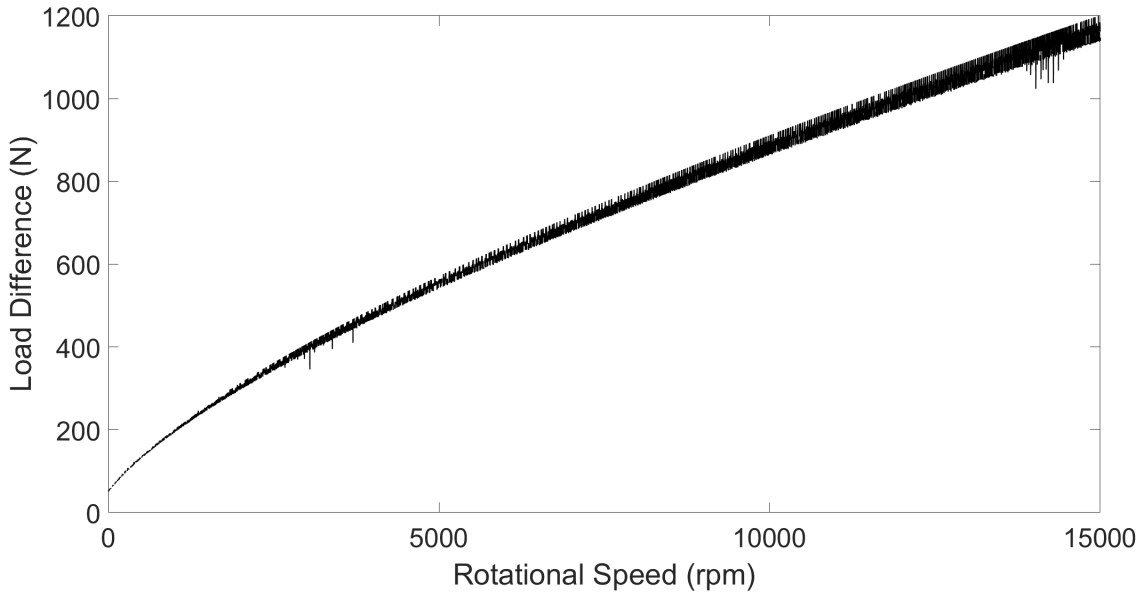


Figure 3.15 Contact load difference between dry and lubricated model.

contributes to a 14.8% greater load prediction than a dry model, showing that the film inclusion has a significant contribution even at low rotational speeds. At shaft speeds of 14 135 rpm, the first order resonance in the system, as shown in the frequency plots, creates high dynamic loading. At peak load, the growth of the film is still present, however, the high contact deformation is close to the magnitude of the film growth, hence the difference between dry and lubricated model reaches 25.1%. As the system passes through this resonant region and the overall dynamic load is reduced, the percentage load difference reaches values as high as 149% as the effect of the film growth at high speeds exceeds that of the surface deformation.

At high speeds in periods of resonance, the magnitude of the bearing load dominates, and the effect of the increasing film thickness with speed diminishes in regions of resonance. The percentage difference between the dry and lubricated model is lower as the external force and corresponding surface deformation prevails the effect of the film. However, at high speeds outside of this period of resonance, the film thickness is of the same order as the deformation and the percentage difference between the two models is much greater.

3.4.4 Numerical EHL Results

Full numerical simulation is required to obtain detailed pressure and film thickness distributions. These distributions reveal the realistic pressure and film values at the contact for in-depth durability, efficiency and thermal analysis. At 8 350 rpm, focussing on one roller orbit, the selected points for EHL numerical analysis are shown in Figure

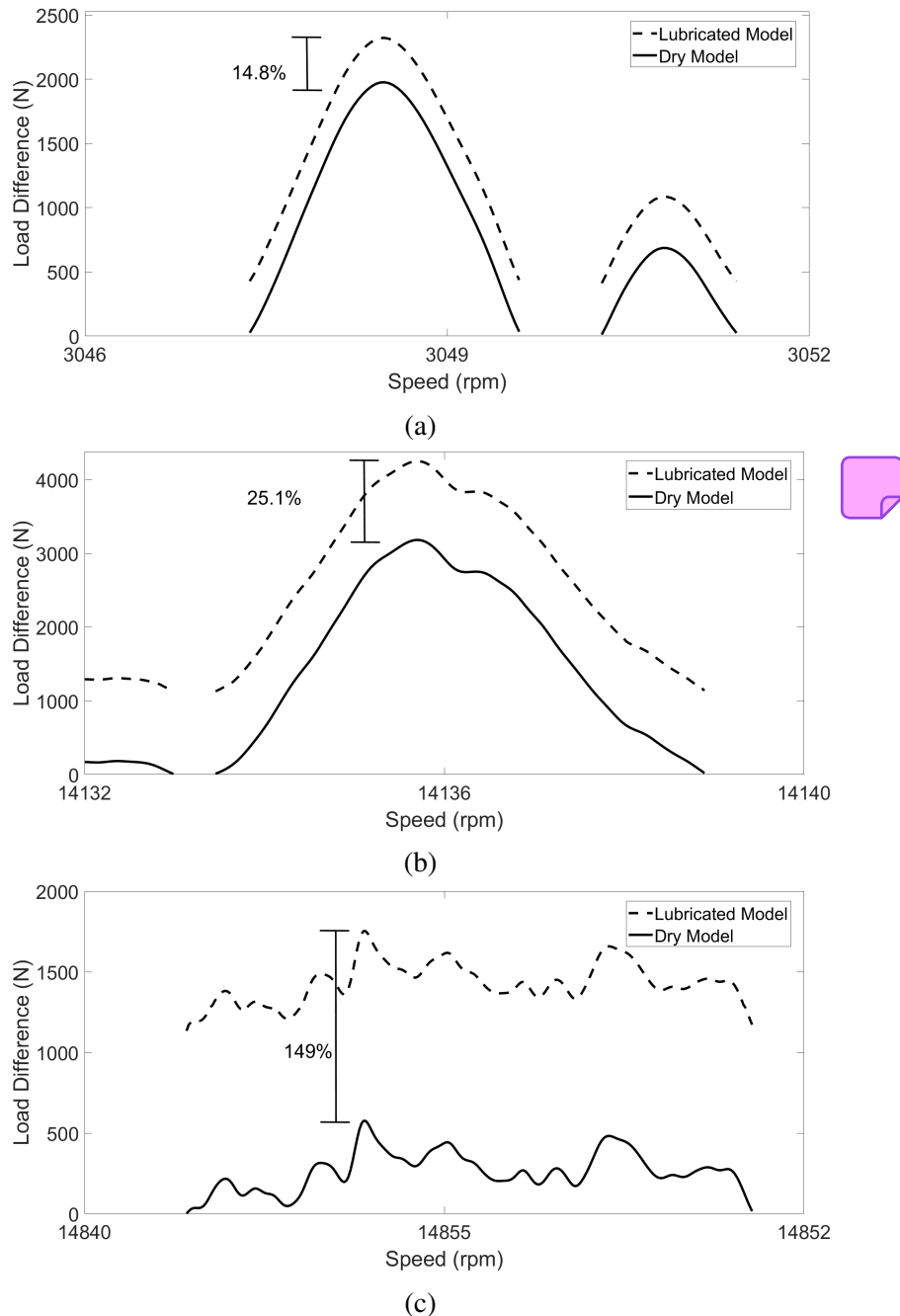


Figure 3.16 Dry and lubricated model load difference: a) 3 050 rpm, b) 14 135 rpm, c) 14 855 rpm.

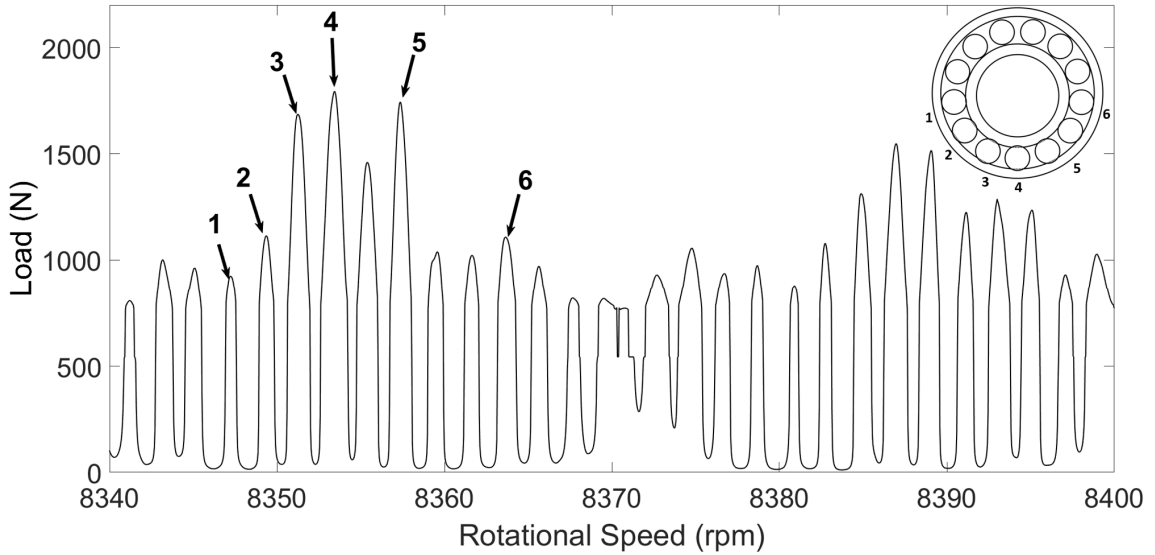


Figure 3.17 Selected points for the numerical EHL model.

3.17. These load values are found from the implicit tribological model when the roller enters the loaded region of the bearing. The corresponding points on the bearing circumference are also shown.

The load values are passed explicitly to the numerical EHL model along with entrainment velocity, lubricant and solid properties. From the nodes presented, the pressure distribution and film thickness across the contact are obtained. These are presented in Figure 18.

In each of these plots, it is possible again to see the central film thickness drop as the roller enters, then exits the loaded region. These central film values are represented by circles in Figure 18. Agreement between the extrapolated film formulae and the numerical model for calculating central film values are presented in Table 3.4. The extrapolated formula over-predicts the central film thickness by an average of 7.7%, with a peak of 11.3%. It is also shown that the central nodes which correspond to the higher loads in the loaded region have the lowest percentage difference in comparison to the lightly loaded nodes at the outer edges.

3.5 Conclusions

A novel methodology comprising experiments and numerical modelling was developed to allow component and conjunction level tribodynamic analysis of a roller bearing under speeds and loading conditions previously not reported. The experimental data contain the physics of the dynamics and tribology within the bearing, negating the need for a simplified and computationally intensive dynamic bearing model. The

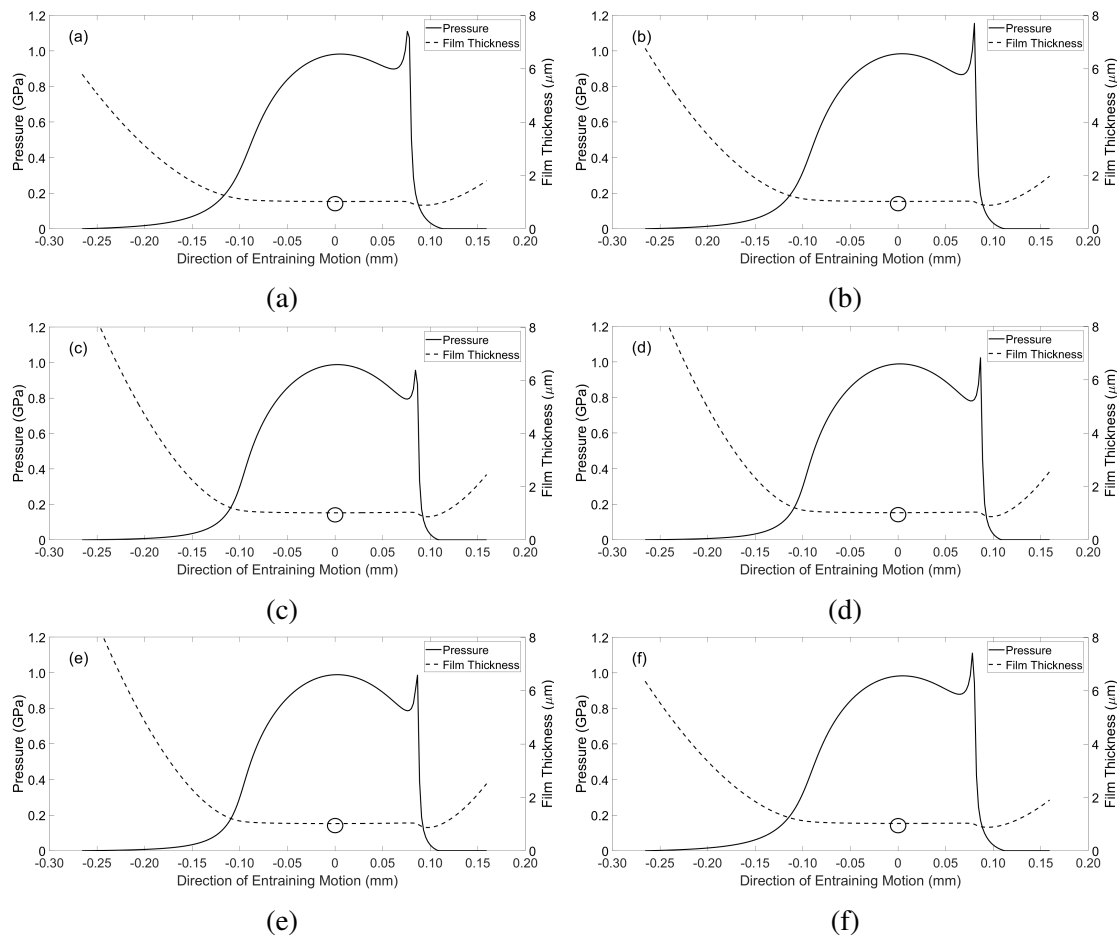


Figure 3.18 EHL pressure and film thickness distributions: a) Node 1, b) Node 2, c) Node 3, d) Node 4, e) Node 5, f) Node 6.

Table 3.4 Extrapolated film formulae and numerical model central film thickness comparison

Node	Extrapolated Formulae Central Film Thickness (μm)	Numerical Model Central Film Thickness (μm)	Percentage Difference (%)
1	1.142	1.026	11.3
2	1.122	1.025	9.46
3	1.075	1.019	5.49
4	1.068	1.016	5.11
5	1.072	1.018	5.30
6	1.122	1.025	9.46

tribological conditions at the contact between an individual roller and raceways are numerically analysed. All lubrication regimes, including mixed-EHL and hydrodynamic, are considered as the roller passes through loaded and unloaded regions. The following conclusions can be made based on presented results:

1. The contact experiences an order of magnitude increase in film thickness (0.1 - 1.9 μm) across the speed sweep from 0 - 15 000 rpm. This leads to a 1 200 N higher contact load for the analysis considering the EHL film implicitly when compared to the conventional dry modelling approach. This contact force difference is due to the EHL film acting as an interference element at the roller-race conjunction, leading to greater contact deformation.
2. Further comparison between the dry and lubricated contact model reveals a percentage increase in load between both models of up to 149% at 14 855 rpm. At lower speeds, and moderate loads, this increase is significantly lower, at just 14.8%. During a period of system resonance at 14 135 rpm, where the dry contact deformation dominates over the film growth, this increase is only 25.1% despite the high speed. These findings show that the most significant difference between modelling methods occurs at high entrainment velocities with low loads.
3. The load values obtained from the lubricated tribological model have been used explicitly within a 1D EHL model to calculate the pressure distribution and film thickness across the contact. Employing the numerical EHL calculation explicitly negates the need for a computationally inefficient coupling of the numerical model at each sample point. At 8 350 rpm, the extrapolated formula over-predicts the central film thickness by an average of 7.7%.

This chapter introduced the importance of implicitly including the lubricant film in high-speed dynamic bearing models. At high speeds and low contact loads, the effect of the EHL film is shown to considerably affect the resulting contact forces. These operating conditions align with those of an input bearing in an electrified powertrain transmission, where input torque and hence bearing load decreases as rotational speeds increase.

Additionally, this chapter introduced the fundamental tribological contact models and governing numerical methods used within this thesis. The contact methodology is further enhanced in the next chapter, and the 1D numerical model presented here will also be used for further analysis in the subsequent chapters. The next stage of these studies is to examine how this increase in contact load affects bearing and system

dynamics under realistic electrified powertrain operating conditions. Due to the non-linear force-deflection relationship at the contact, the contact stiffness will also change. To answer the aims of this research, the effect of this stiffness must be analysed within a flexible system-level model.,

Chapter 4

Modelling Lubricated Bearings in a Flexible Multi-Body Dynamic Environment

4.1 Introduction

The previous chapter highlights the necessity of modelling the EHL film for high-speed, low load roller bearing operation. A workflow was established to implicitly account for the lubricant film at the roller-race conjunction. However, bearing motion was obtained experimentally, which limits the investigations to component level analysis. Since this work aims to investigate the effect of the EHL film at system level, and dynamic model must be developed.

This chapter presents a new flexible dynamic model for drive systems comprising lubricated bearings operating under conditions representative of electrified vehicle powertrains. This is achieved by embedding a non-linear lubricated bearing model within an FMBD model. The time-varying system operating conditions reflect that of an electrified powertrain. The kinematic behaviour of a flexible shaft at each time step of a dynamic simulation is passed to the bearing model. A contact slicing method [11] is employed to calculate the reaction forces of the individual rolling elements based on the roller–race contact deflection [111]. The total deflection is influenced by the thickness of the EHL film within the contact, which is implicitly included within the analysis through an iterative procedure. The resulting race forces are returned to the system level model and the equations of motion are solved at each time step. Comparisons are made between modelling the bearings as dry and lubricated. The dynamic results including

acceleration, force magnitudes and stiffness variations have been obtained for realistic loading conditions of a 54 kW electric hub motor up to speeds of 21 000 *rpm*.

The elastohydrodynamic (EHL) film is shown to increase contact deflection, leading to increased contact forces and total bearing stiffness as rotational speeds increase. Results show that at 21 000 *rpm*, the input bearing EHL film reaches a thickness of 4.15 μm . The lubricant entrainment increases the roller–race contact deflection, causing the contact stiffness to increase non-linearly with speed. The contribution of the lubricant film leads to a 16.6% greater bearing stiffness at 21 000 *rpm* when compared to conventional dry bearing modelling methods used in current FMBD software.

4.2 Methodology

A co-simulation methodology combines a system-level model of a flexible shaft and rigid housing, developed in AVL EXCITETM, with component level models of the lubricated bearings, developed in MATLAB® and Simulink®. Operating conditions such as rotational speed and external forces are defined in the system-level model. Time step, iteration accuracy and simulation length are also defined. Material, geometric and rheological properties of the bearings are defined in the component-level model. The kinematic conditions from the system-level model (i.e., displacements and velocities in all active degrees of freedom) are passed to the component-level model at each time step. For each individual rolling element, the non-linear force–deflection relationship is employed in conjunction with the EHL film calculations to compute the contact reaction force between the roller and race. The resultant force on the inner bearing race due to the contact forces and orbital positions of all elements is then returned to the system level model. The equations of motion are then solved, and the time step is advanced once numerical convergence is achieved. A flowchart of these models representing each time step of the simulation is shown in Figure 4.1.

4.3 System Level Flexible Model

The system level model consists of a flexible shaft, supported by two cylindrical roller bearings in a rigid housing (see Figure 4.2). The shaft is 472.5 mm between bearing centres, with a 50 mm main diameter and 25 mm diameter bearing seats. The cylindrical roller bearings act as interference elements between the shaft and housing. The shaft can exhibit lateral motion in both vertical (*z*) and horizontal (*y*) directions and rotation about the *x*-axis (see Figure 4.2). External load is applied at the shaft centre as a time-varying

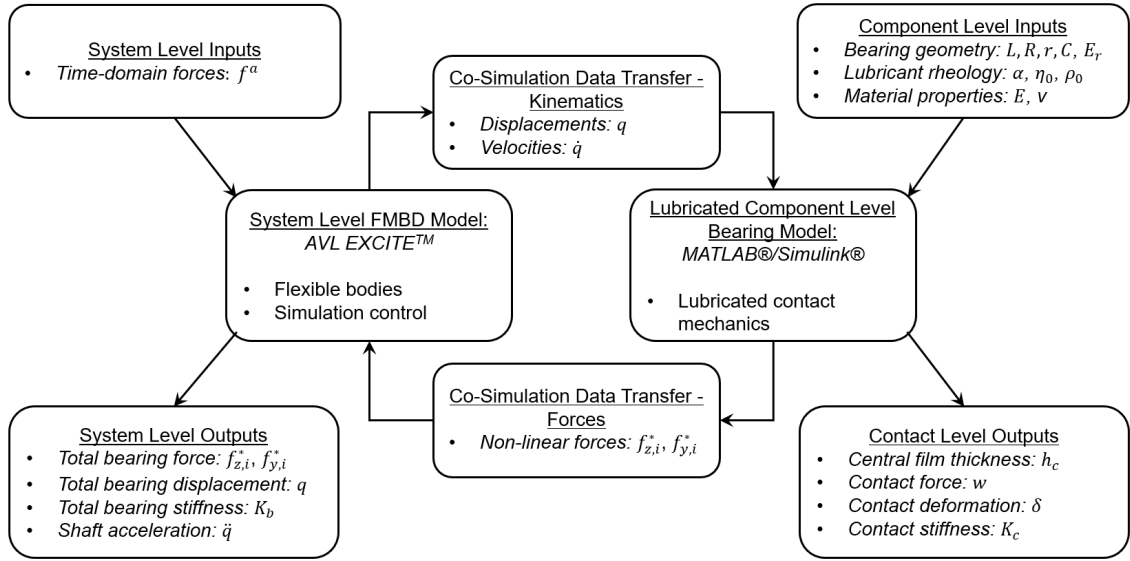


Figure 4.1 Flowchart of models.

input force, to simulate the gear mesh excitation, or as a static load. The rotational speed is input as a boundary condition.

In typical configurations containing flexible structures, it is possible for both the inner and outer races of a rolling element bearing to move when subject to load. For this analysis, however, it is sufficient to fix the outer race in space and consider only the displacement of the inner bearing race [13]. The housing in this study is treated as a rigid body of infinite stiffness; therefore, the race dynamics of the bearing are influenced only by the motion of the flexible shaft in the model. The loading on the inner race is reacted by the rolling elements on the inner raceway; this must therefore be solved to achieve a dynamic equilibrium.

Within the model, the shaft is treated as a body having linear elastic behaviour and the housing is treated as rigid. The bearings are modelled via non-linear contact forces acting between the shaft and housing.

The shaft is represented by a condensed finite element model and is discretised into partial masses [112]. The total elastic deformation of the shaft is represented by translational and rotational displacement components of these individual partial masses. The mathematical modelling used in the FMBD solver is based on Newton's equations of motion and Euler's equation of angular momentum, respectively:

$$m_i \frac{\partial^2 x_i^{Abs}}{\partial t^2} = f_{F,i}^{Abs} \quad (4.1)$$

$$\frac{\partial}{\partial t} \left(I_{C,i}^{Abs} \omega_i^{Abs} \right) = f_{M,i}^{Abs} \quad (4.2)$$

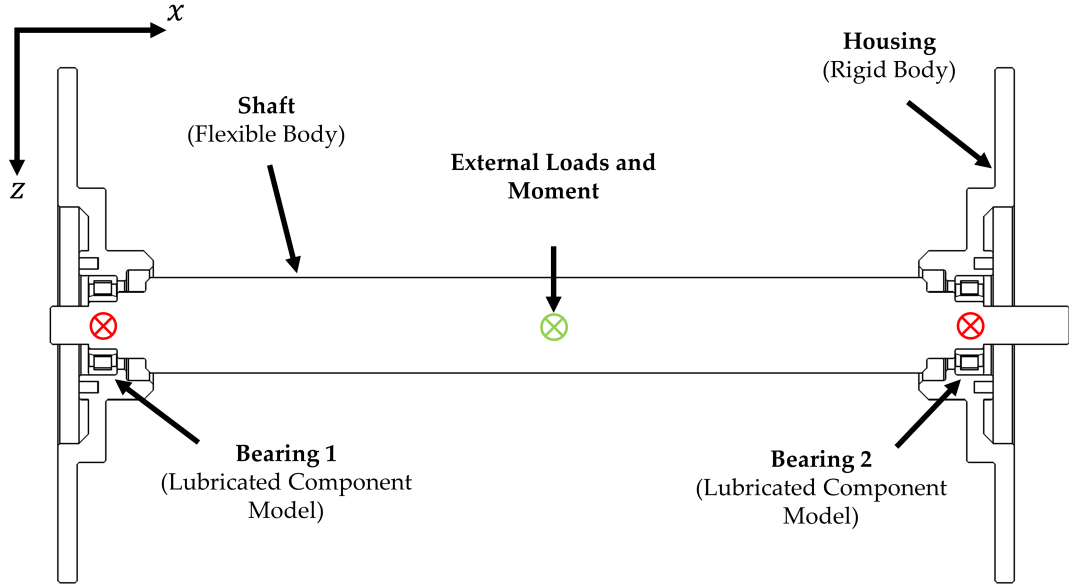


Figure 4.2 System level model schematic.

where m_i and $I_{C,i}^{Abs}$ represent the mass and inertia tensors of the partial masses, i . The vectors of displacement and angular velocity are represented by x_i^{Abs} and ω_i^{Abs} respectively and are related to the centre of gravity of each partial mass. The force and moment vectors, $f_{F,i}^{Abs}$ and $f_{M,i}^{Abs}$, must be fulfilled for all partial masses in the shaft.

The combination of displacement and rotations of the shaft takes the form:

$$M\ddot{q} = f \quad (4.3)$$

where M represents the block-diagonal mass matrix of the shaft, consisting of the sub-matrices $M_i, i \in \{1, \dots, n\}$ that make up each partial mass of the full shaft. Acceleration, \ddot{q} , represents the second derivative of the displacement vector of all partial masses, $q = (q_1, q_2, \dots, q_n)^t$. Each element of this vector has 6 elements associated with it that represent the 6 degrees of freedom - 3 rotational and 3 translational ($q_i = (u_{t1}, u_{t2}, u_{t3}, \theta_1, \theta_2, \theta_3)^t$)

The forces and moments acting on each partial mass are contained in sub-vectors of force, $f = (f_1, f_2, \dots, f_n)^t$. These are split into a sum of internal force terms, f_i^{int} , external force terms, f_i^{ext} , and non-linear inertia terms, p^* . As with the partial mass terms, these are made up of six elements, each representing a degree of freedom:

$$f_i^{int} = \begin{pmatrix} f_{i,1}^{int} \\ f_{i,2}^{int} \\ f_{i,3}^{int} \\ f_{i,4}^{int} \\ f_{i,5}^{int} \\ f_{i,6}^{int} \end{pmatrix} \quad (4.4)$$

where each component of force, $f_{i,k}^{int}, k = 1, \dots, 6$ is evaluated using the linear-elastic approach

$$f_{i,k}^{int} = \sum_{j=1}^{6,n} f_{i,j,k}^{int} \quad (4.5)$$

$$f_{i,j,k}^{int} = - (d_{i,j,k} \dot{q}_k + k_{i,j,k} q_k) \quad (4.6)$$

where d and k represent the material damping and stiffness coefficients, respectively.

Grouping the damping and stiffness coefficients into one matrix gives the equation of motion after rearrangement. This equation represents the behaviour of the total system of rigid partial masses that make up the shaft, and considers both general global motion and small body motion (vibrations) [113]:

$$M \cdot \ddot{q} + D \cdot \dot{q} + K \cdot q = f^{ext} + p^* \quad (4.7)$$

The vector of external forces and moments, f^{ext} , is the sum of excitation forces, f^* , and external loads, f^a . External loads and moments applied to the shaft, f^a , are determined functions given in time and are input as both time-varying and static loads on the system. The non-linear excitation force term, f^* , represents the reaction forces from the lubricated component level bearing model.

$$f^{ext} = f^* + f^a \quad (4.8)$$

Partial mass displacements (q_i) and velocities (\dot{q}_i) at the bearing locations are output from the dynamic model and used as boundary conditions within the lubricated component level bearing model at each time step of the simulation. This model returns resultant forces and torques on the inner race of each bearing (f_i^*) which are then used to solve the equation of motion (Equation 4.7) within the dynamic model (see Figure 4.1).

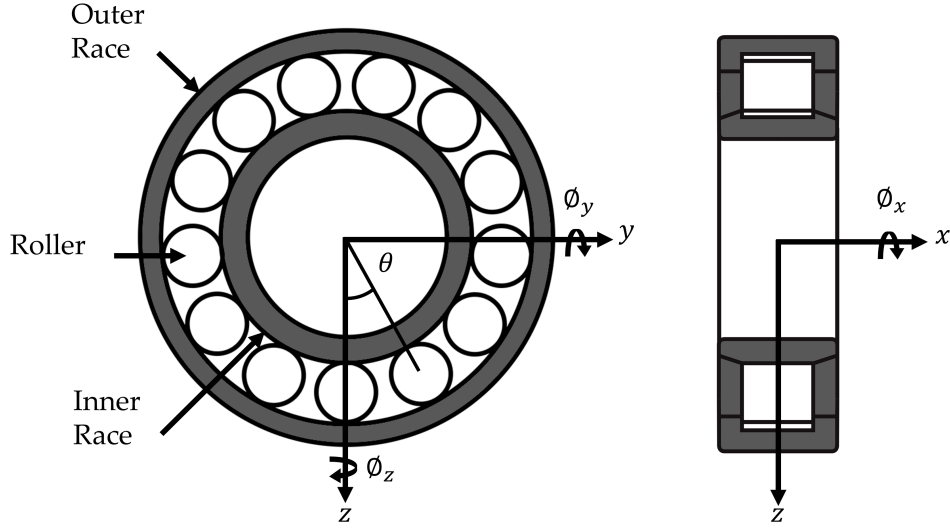


Figure 4.3 Bearing schematic.

4.3.1 Lubricated Component Level Model

The displacement and velocity vectors from each node connecting the shaft to the bearings (q_i and \dot{q}_i respectively) comprise six-DOF. For this lateral DOF model, translations in z and y are considered, as well as angular displacement around the rotational axis, x . A schematic of the bearing is shown in Figure 4.3.

Between the roller and raceways, under sufficient load, the pressures in the non-conformal contact are high enough to cause elastic deformation of the surfaces and a significant increase in lubricant viscosity. This, combined with relative motion between contacting bodies, leads to the generation of an EHL contact. The stiffness of the EHL film is typically 1-2 orders greater than the stiffness of the contacting bodies [26]. In this analysis, the film stiffness was calculated using:

$$K_{EHL} = \frac{dw}{dh_c} \quad (4.9)$$

The lowest average film stiffness was 5.1×10^9 N/m, which is over one order greater than the contacting material stiffness. The material therefore dominates the stiffness of the contact, and the stiffness of the EHL film can be neglected. The film is modelled as a rigid element that is present between the roller and race [96] [97] [98].

The contact deformation (δ) is therefore a function of the displacement of the inner bearing race, angular displacement of the roller about the rotational axis (θ), central

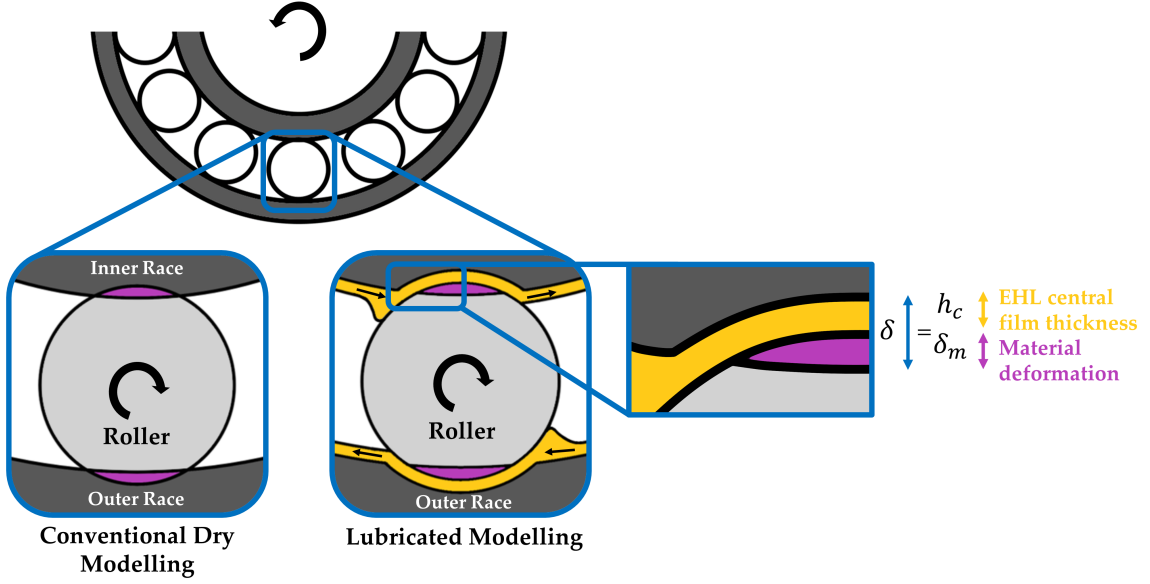


Figure 4.4 Dry vs lubricated roller-race contact.

EHL film thickness (h_c) and any clearance or radial preload ($\pm C$) within the bearing [28] [30]:

$$2\delta = 2(h_c - C) + z \cos(\theta) + y \sin(\theta) \quad (4.10)$$

Figure 4.4 demonstrates this more clearly. The total contact deformation is the summation of (h_c) and the material deformation, (δ_m) predicted from the dry-Hertzian contact assumption. Conventional dry analysis only accounts for the dry material deformation at the contact.

The extrapolated central film thickness for a line contact, assuming a fully flooded contact inlet, is therefore obtained from [51]:

$$h_c = R_r \left[3.06 G^{*0.56} U^{*0.69} W^{*-0.1} \right] \quad (4.11)$$

where the following dimensionless parameters are used:

$$W^* = \frac{W}{E_r R_r l_a}, U^* = \frac{\eta_0 U}{E_r R_r}, G^* = E_r \alpha \quad (4.12)$$

Comprehensive analytical models [114] [115] account for the tilting and skew of the rolling elements. Skew has the effect of varying the entrainment speed along the length of the roller, and tilt will affect the contact gap. Due to the stiff housing and shaft used in this analysis, the tilt and skew angles are very small. The entraining motion and

contact gap along the contact length can be considered consistent, and a 1D analysis for EHL film thickness is therefore appropriate [21].

The bearings are modelled with light preload due to mounting interference. In practical applications, preload is applied to prevent skidding and chaotic behaviour due to the emergence of zero stiffness regions [116]. In contrast, excessive preload can lead to frictional power loss and wear. Assuming pure rolling, the speed of entraining motion is given by [117] [118]:

$$u = \frac{R\omega}{r} \left(\frac{(R+2r)}{(R+r)} \right) \quad (4.13)$$

Due to the dependency of load on film thickness, an iterative approach is performed to calculate the contact force. Convergence criteria for the EHL film must be met at each time step of the simulation before the bearing forces are returned to the system level model and the equations of motion are solved:

$$\frac{h_c^m - h_c^{m-1}}{h_c^{m-1}} \leq 0.001 \quad (4.14)$$

where m represents the iteration number.

Individual roller-race contact forces are calculated based on the contact deformation. In the case of a rolling element, a cylindrical body of finite length, the contact problem is non-Hertzian. The surfaces cannot be modelled as locally quadratic due to the presence of crowned (rounded) edges [119]. The most widely used technique to calculate the force-deflection relationship is the contact slicing technique. Whilst this does not reflect edge stress concentrations, these stresses are only distributed over a small area and hence can be neglected for the purpose of force equilibrium [120]. In general, this technique is favoured for its simplicity, speed, and sufficient accuracy. The contact slicing technique employed in this study was developed by Andreason [11] for modelling these non-Hertzian line contacts.

Modelling the roller-race contacts as a line contact between a cylindrical roller and a flat surface, Lundberg's [111] expression between contact force per unit length (w) and deformation (δ) was used.

$$\frac{\delta}{l_a} = \frac{2w}{\pi E_r l_a} \ln \frac{\pi E_r l_a}{w} \quad (4.15)$$

where E_r is the equivalent elastic modulus of the two materials and l_a is the active length of the roller. This assumes that the pressure distribution is uniform along the length of the contact, and elliptical across it. This neglects side leakage along the contact

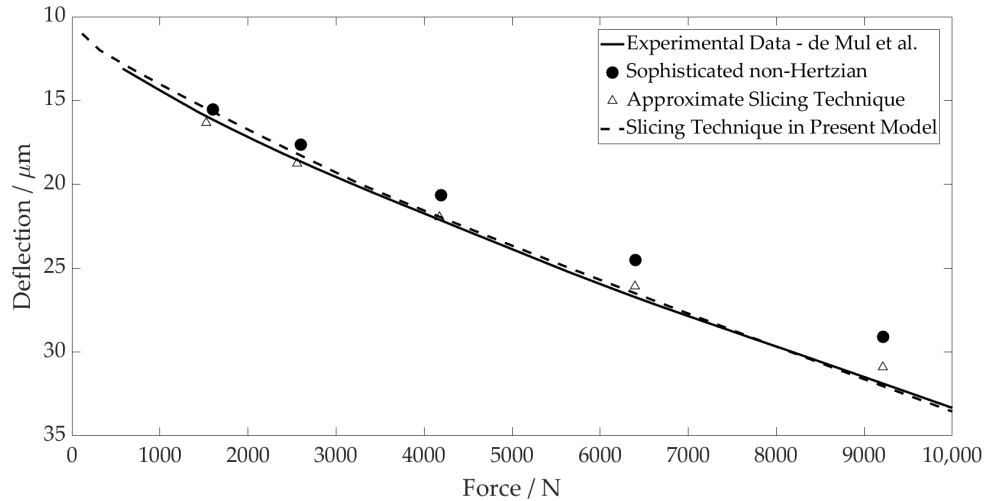


Figure 4.5 Contact level validation.

(x_c) due to the contact dimensions in this direction being much larger than dimensions across it (y_c) . This is valid apart from the small regions at the edges of the contact.

From Equation 4.15, contact forces per unit length of an individual slice along the roller-race contact can be calculated. This is valid if there is no separation of the bodies, i.e., the contact deformation does not become negative ($\delta_k > 0$).

$$w_s = \pi E_r l_s \left(\frac{0.5\delta_s}{7.358l_s} \right)^{1.11} \quad (4.16)$$

where s represents the slice number, and l represents the slice length.

The application of the slicing technique was validated against open literature [13]. The study compared results obtained from an experimental rig with numerical results calculated using both the approximate slicing technique and the sophisticated non-Hertzian technique [121]. By replicating the geometry of the test bearing used in their analysis, the application of Andreason's slicing technique used for this analysis was validated with good agreement (see Figure 4.5). This method is a much faster way of calculating contact load and moment than more sophisticated methods by [13], yet still maintains high accuracy.

The total contact load W and moment T are obtained by summing the contributions from all loaded slices:

$$W = \sum_s w_s l_s \quad (4.17)$$

$$T = \sum_s w_s l_s x_{c,s} \quad (4.18)$$

with $x_{c,s}$ being the distance to the centre of each slice in the conjunction coordinate system. It is assumed that total contact deflection is shared equally between the inner and outer races despite slight differences in contact geometry. The entrainment velocity is equal at each contact, which is the governing parameter for the lubricated contact force differences.

Experimental measurements show that the damping of a rolling element bearing arises from multiple sources [26], including:

1. Lubricant film damping at the contacts.
2. Material damping due to Hertzian deformations.
3. Interface damping between assembled components

These measurements show that damping decreases with rotational speed, tending towards a constant value. Sopanen and Mikkola [16] summarize the findings of Mitsuya et al. [122] and Aini et al. [29], concluding that the film damping is moderate. The linearized viscous damping method adopted in their study is therefore also adopted here. The damping force for each roller is obtained as a factor of the contact stiffness and contact penetration velocity [123]. This is defined as:

$$|F_d| = -f_{\text{damp}} K_c \dot{q} \quad (4.19)$$

where K_c is the contact stiffness, and the damping factor, f_{damp} , is in the range of $(0.25 - 2.5) \times 10^{-5}$ as reported by [123].

At each time step of the analysis, these calculations are performed for each individual roller in the complement. The total bearing force acting on the inner race is solved by separating the total contact force on each roller into its components and summing their contributions.

$$f_{z,i}^* = \sum_N W \cos(\theta) - \sum_N F_d \cos(\theta) \quad (4.20)$$

$$f_{y,i}^* = \sum_N W \sin(\theta) - \sum_N F_d \sin(\theta) \quad (4.21)$$

Due to the bearing preload, contact is maintained throughout the rollers' orbit; hence no emerging clearances are modelled in the lubricated analysis. The contact separation is also unaffected by rolling element centrifugal forces, which are negligible when compared to the contribution of the dynamic load and the EHL film in this study. These have therefore been neglected.

Table 4.1 Cylindrical roller bearing specification

Parameter	Value
Inner race bore diameter	25 mm
Pitch diameter	60 mm
Roller diameter	8.8 mm
Roller length	15 mm
Number of rollers	17
Operating clearance	-2 μ m

Table 4.2 Bearing material and rheological properties

Parameter	Value
Pressure viscosity coefficient (α)	$2.1 \times 10^{-8} \text{ Pa}^{-1}$
Atmospheric lubricant dynamic viscosity	0.08 Pa.s
Lubricant inlet density (ρ_0)	833.8 $\text{kg} \cdot \text{m}^{-3}$
Modulus of elasticity of contacting solids	210 GPa
Poisson's ratio of contacting solids	0.3

Surface measurements of the rollers used in this analysis were taken using an Alicona InfiniteFocus Variation Microscope (see Section 3.2.8). The composite surface roughness value of a roller and inner race was calculated to be 0.207 μ m. This gives a lambda value of 2.59 for the thinnest EHL film at 1000 rpm. Asperity interaction is not considered as the EHL film fully supports the load. Due to the pure rolling and zero sliding assumption, friction at the contacts is therefore neglected and the analysis is performed under isothermal conditions.

The bearing geometry is detailed in Table 4.1. Rheological and material properties are detailed in Table 4.2, representing ambient operating conditions in an individual hub-motor transmission.

4.3.2 Representative Excitation Methodology

The system level model is decomposed, with excitation forces calculated externally before application within the model. A separate electrified transmission model is used

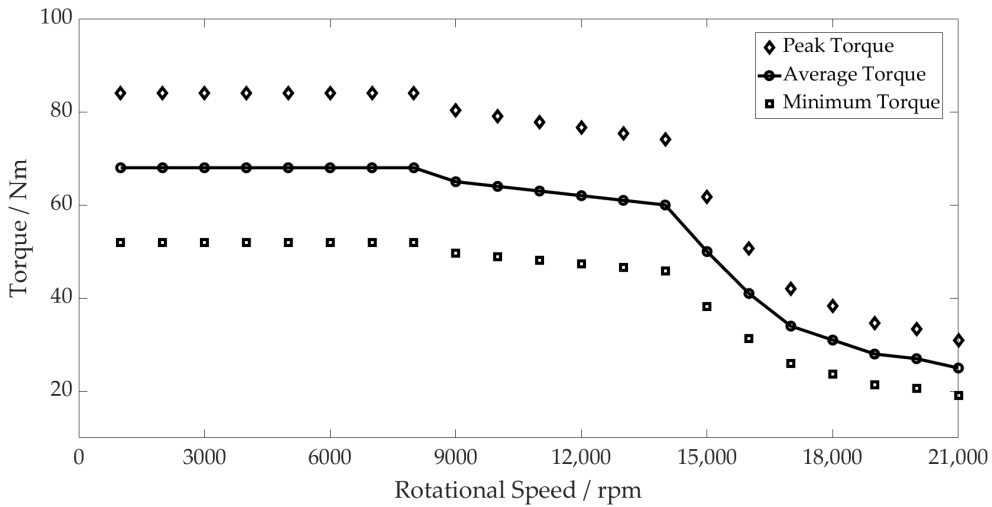


Figure 4.6 PMSM torque profile and maximum and minimum torque fluctuation.

to generate realistic excitation forces and torques from a spur gear pair and a permanent magnetic synchronous motor (PMSM). This system represents the first stage of an electric hub motor used in automotive applications.

Radial and tangential gear pair forces at the pinion centre, as well as torque fluctuations of the electric motor are extracted to be used as inputs to the system level model. These are applied as external forces to the shaft, f^a , from Equation 4.8. All bodies in this separate system were modelled as rigid, so that structural excitation forces did not contribute to the resultant forces at the pinion.

The motor has a peak torque of 68 Nm, and a maximum operating speed of 21 000 rpm. The torque transfer through the gear pair reduces as the speed increases due to the torque profile of the PMSM, as shown in Figure 4.6. Stator tooth forces from the PMSM are neglected in the model due to their minimal contribution to lateral forces once resolved. For input to the model, the radial and normal forces are simplified by adopting sinusoidal inputs of the same magnitude and frequency of the gear pair at different speeds. The torque ripple from the motor is simplified using the same method.

4.3.3 Co-Simulation of Coupled Models

A coupled simulation approach is employed to implement the lubricated components level bearing model within the flexible multi-body dynamic (FMBD) environment. AVL EXCITE™ Power Unit R2022.1 contains integrated “Link to MATLAB” functionality, whereby joints within the model can be replaced with a user function created in MATLAB Simulink® R2022b.



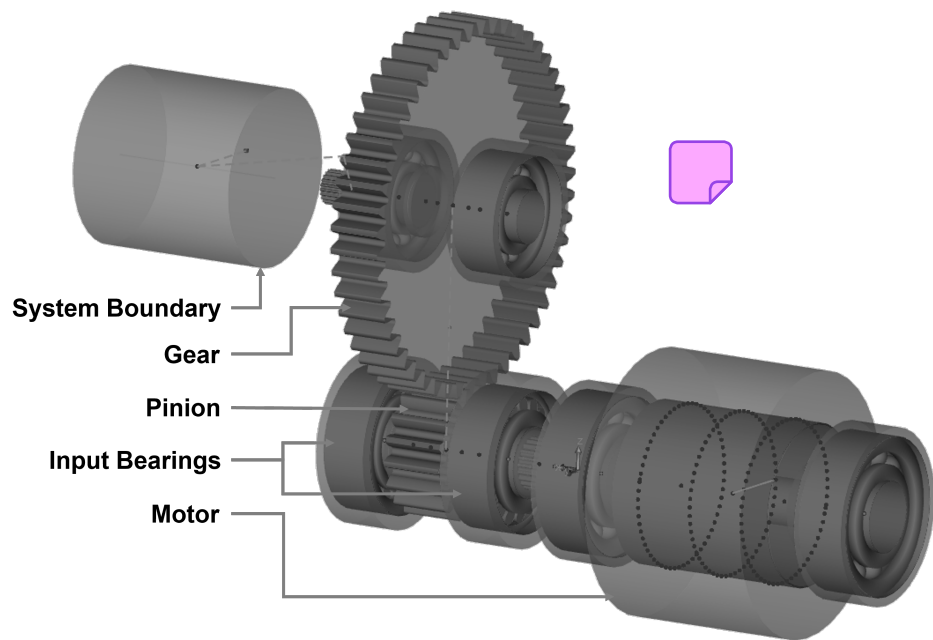


Figure 4.7 Hub motor excitation model.

Table 4.3 Pinion geometry

Parameter	Value
Number of teeth	17
Normal module	0.004 <i>m</i>
Normal pressure angle	20 °
Helix angle at pitch circle	0 °
Active tip diameter	0.076 <i>m</i>
Active root diameter	0.065 <i>m</i>
Width	0.035 <i>m</i>

Table 4.4 Gear geometry

Parameter	Value
Number of teeth	51
Normal module	0.004 m
Normal pressure angle	20 °
Helix angle at pitch circle	0 °
Active tip diameter	0.212 m
Active root diameter	0.202 m
Width	0.030 m

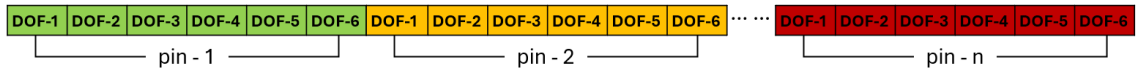


Figure 4.8 Communication vector and degrees of freedom.

Connected Degrees of Freedom Connections are created between bodies in the FMBD software using pins. Pins are assigned to specific nodes on the shaft and housing. The pins transmit a 6-element vector that describe the 6 DOF of the connection point. The first 3 elements represent translational DOFs, whilst the latter represent rotational DOFs. This are concatenated into a single communication vector that is then transferred to MATLAB®.

Two vectors are transferred from EXCITE to MATLAB®: one containing displacement information in all 6 DOF and the other containing velocity information. Force vectors of equal size are then computed within the component level model in MATLAB® and returned to EXCITE™ Power Unit.

The connection to MATLAB® is facilitated via an S-function. Therefore, a Simulink® model is required. A generic block developed by AVL, the EXCITE™ Power Unit Simulink® block, is used for this purpose:

Output Port Output data from the FMBD model is organised in vector format, of size $6n$ where n is the total number of connections being passed from MATLAB® to EXCITE™ Power Unit. To access data for each connection, and then split this into specific DOFs, two levels of Demux elements are needed.

1. The first level of Demux splits the output vector into n pins, of size 6 to represent the DOFs at each pin.

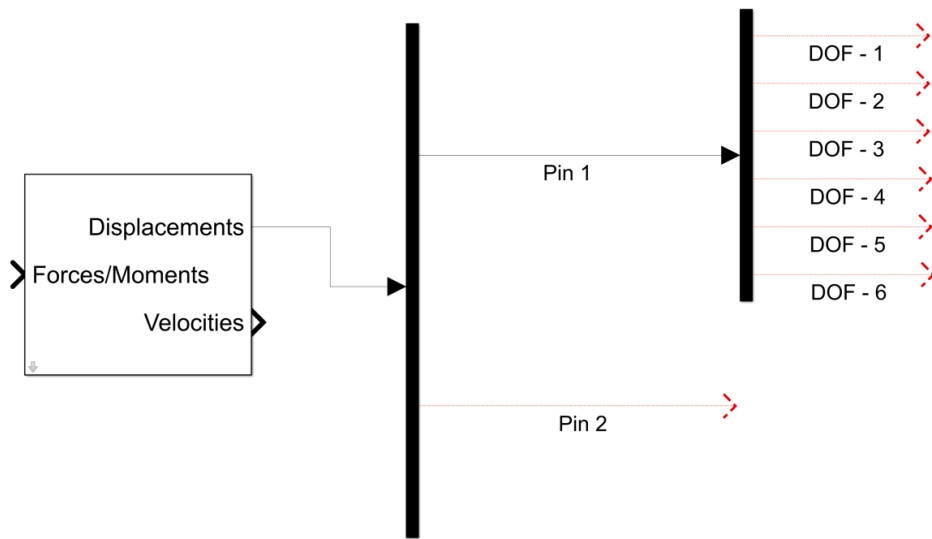


Figure 4.9 Output port Demux blocks and degrees of freedom.

2. The second level of Demux blocks splits the 6-element vector for each pin into the 6 scalar values that represent the data for each DOF. These can then be used as inputs to the MATLAB® function block within the Simulink® model.

Input Port At the input port to the EXCITE™ Power Unit Simulink block, a vector of $6n$ elements must be passed. This requires two Mux blocks: the first to combine the DOFs of each pin, and the second to combine all of these connection vectors into a single vector that is passed to EXCITE™ Power Unit.

Simulink Model To integrate the lubricated bearing model into the Simulink® model, the MATLAB® Function block is used. The input variable sizes are defined at the beginning of the function, and the appropriate DOFs are connected to the block in the order of which they appear in the function. The function blocks and hence lubricated bearing models are highlighted in 4.11, as well as the ports and the demux blocks that split the DOFs.

The coupled simulation supported by EXCITE™ Power Unit is explicit in nature. There is no iteration at each time step between the dynamic solver and the bearing model. Error accumulation can therefore lead to numerical divergence. Investigations were performed from $0.1 - 1 \times 10^{-5}$ s in steps of 0.1×10^{-5} s. It was found that a simulation time step of 1×10^{-6} s was fine enough to ensure numerical convergence at all operating conditions, while also remaining computationally efficient.

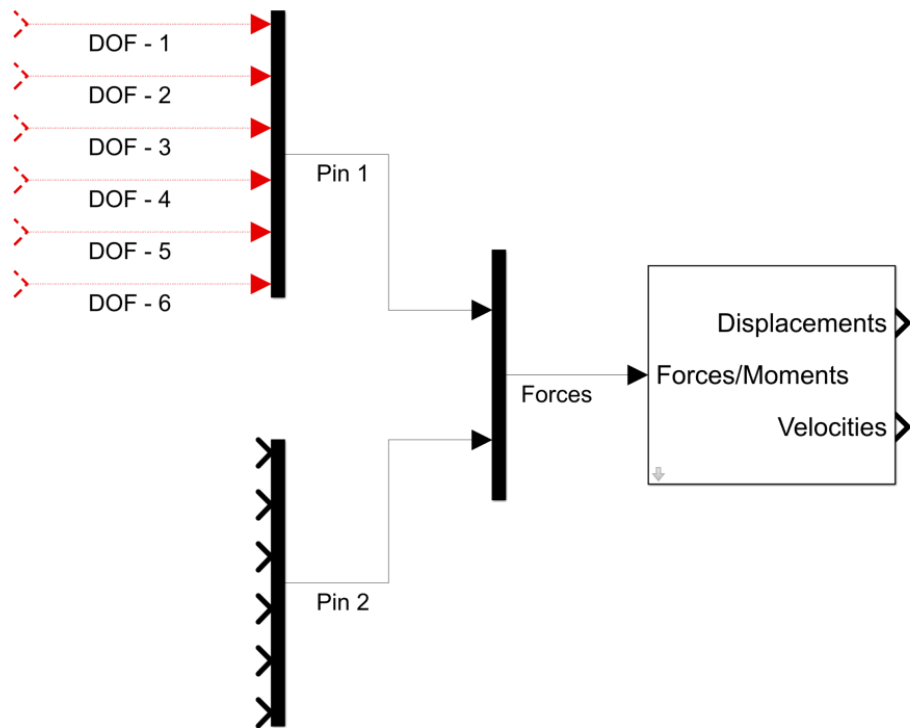


Figure 4.10 Input port Mux blocks and degrees of freedom.

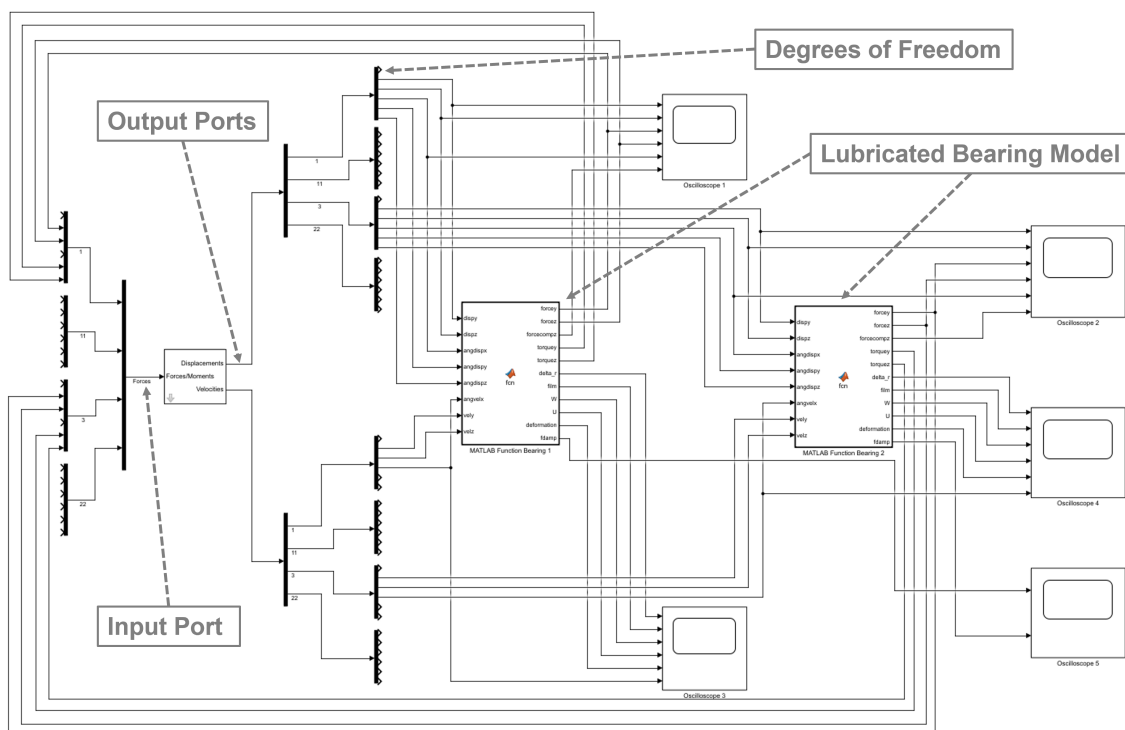


Figure 4.11 Simulink® model schematic.

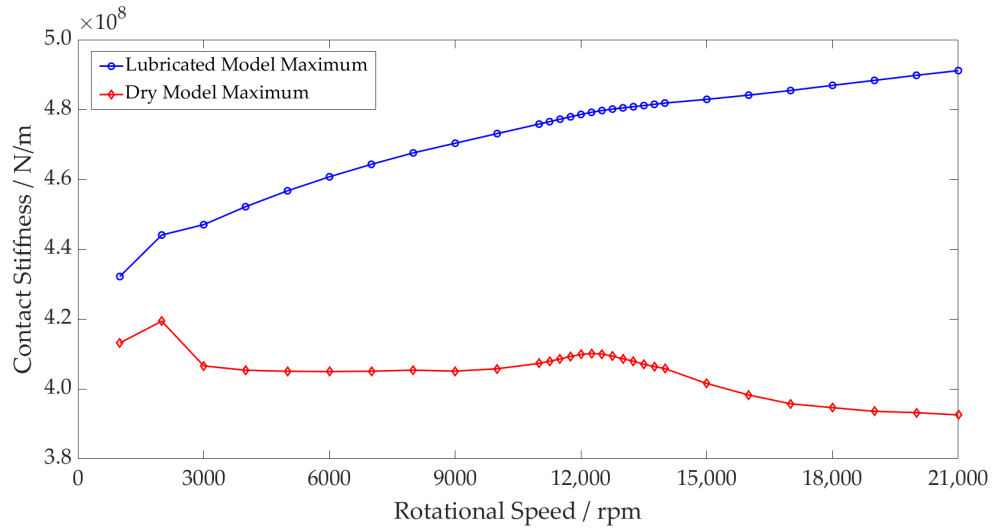


Figure 4.12 Rolling element contact stiffness - Dry vs lubricated maximum values.

4.4 Results and Discussion

A quasi-dynamic speed sweep has been performed from 1 000 to 21 000 *rpm*. The simulations are performed every 1000 *rpm*, refined to 250 *rpm* intervals throughout a period of system resonance between 12 000 *rpm* and 14 000 *rpm*. The operating envelopes are generated by plotting the maximum and minimum values from the steady-state signals at each speed interval. The conjunction level results are obtained from an individual roller and its contact with the inner raceway. The component and system level results are taken from the geometric centre of the inner bearing race, corresponding to the bearing seat on the shaft. The following figures represent results in the *y*-direction, the largest component of excitation due to the tangential force from the gear meshing.

The contact level results (Figure 4.12) show a difference in the contact stiffness between the dry and lubricated models. The dry model follows the torque profile of the motor, with stiffness decreasing as the contact forces reduce. The period of resonance leads to the larger amplitude excitation of the shaft, resulting in an increase in the contact stiffness due to the force-deflection non-linearity. The lubricated model, however, shows an increase in the contact stiffness throughout the speed sweep. This is due to the higher levels of deformation at the contact as the lubricant is entrained, which increases with the shaft rotational velocity. This behaviour was experimentally observed by Dietl, concluding that the oil-wedge between the rolling elements and raceways reduces the internal clearance of the bearing and increases its stiffness [26]. The contact stiffness in the lubricated bearing model under the same operating conditions is therefore 24.9% greater at 21 000 *rpm*.

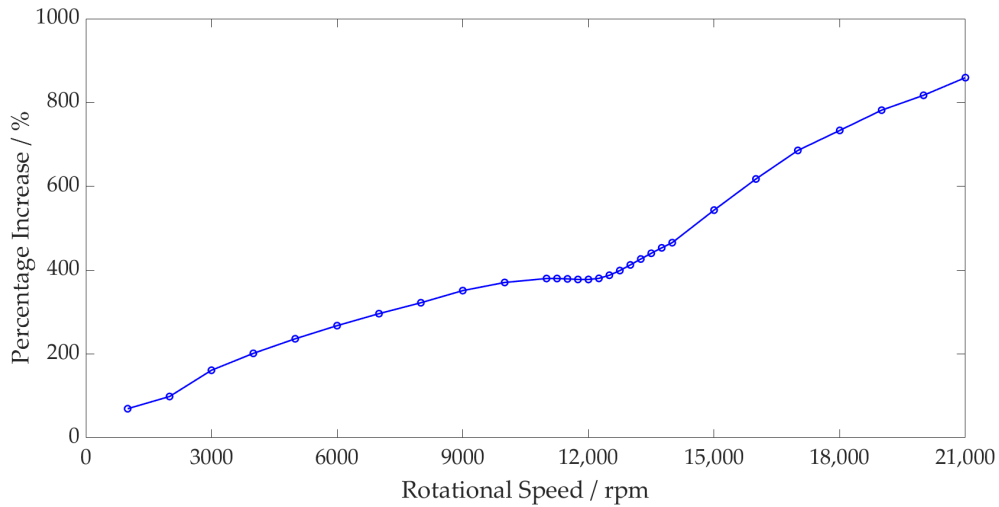


Figure 4.13 Rolling element contact force - Dry vs lubricated percentage increase.

The peak contact force has been compared between both models. The percentage increase between the dry and lubricated models is shown in Figure 4.13. This more clearly shows the disparity between both models at the contact, with the largest difference being 9.6 times at maximum speed. During resonance, the inner race force reaches a peak of 1 514 N, resulting in surface deformation magnitudes of $0.92 \mu\text{m}$ and $3.81 \mu\text{m}$ at the dry and lubricated conjunctions, respectively. As noted in the Chapter 3, higher loads lead to a greater surface deformation to the film thickness ratio, causing the percentage difference between the dry and lubricated models to reduce. Once the loads reduce as the speed increases, the percentage increase continues to rise.

The total bearing stiffness is a combination of all contact stiffnesses between the elements and raceways. These contact stiffnesses vary non-linearly with force, resulting in the total bearing stiffness varying accordingly. For the dry model, this is clearly demonstrated, with the greater total bearing stiffness at the peak of the resonance due to the greater bearing forces (see Figure 4.14). This does not, however, capture the change of the total bearing stiffness with speed; the average bearing stiffness does not change. The lubricated bearing is not only stiffer than the dry bearing, but this stiffness also increases with speed. This is shown in Figure 4.14 by the non-linear increase in the average lubricated bearing stiffness values compared to the constant values for the dry model. The combination of these two factors leads to the lubricated model having a 16.6% greater maximum total bearing stiffness at 21 000 rpm than the dry model.

Due to the greater total stiffness of the bearing, the shaft displacement of the lubricated model is lower both on average and peak to peak for the same applied force in comparison to the dry model (see Figure 4.15). Through the period of resonance, the

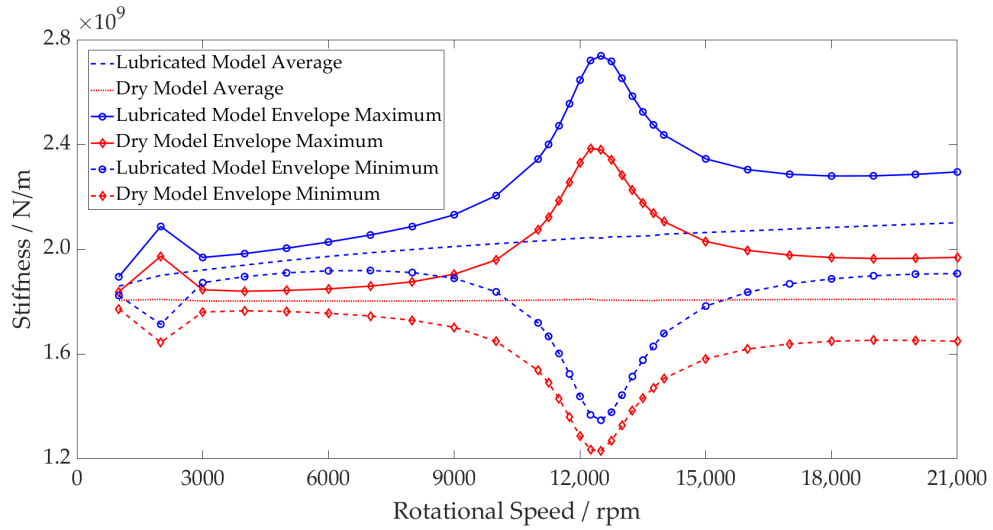


Figure 4.14 Inner race stiffness - Dry vs lubricated operating envelope.

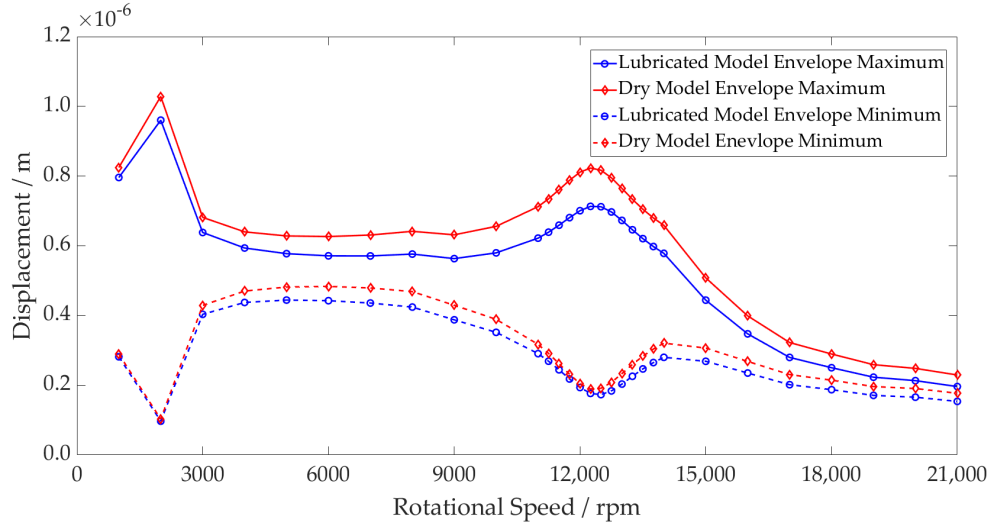


Figure 4.15 Inner race displacement - Dry vs lubricated operating envelope.

large inner race forces result in the roller–race separation of the unloaded rollers within the dry model. This leads to greater shaft displacement as the inner race moves into this region of zero stiffness until roller–race contact is made, and a reaction force is established.

Figure 4.16 shows that the acceleration peak of the system resonance occurs at 12 500 rpm (3 5420Hz) for the lubricated model as opposed to 12 250 rpm (3 470 Hz) for the dry model. This shift in natural frequency indicates a stiffer overall system. The magnitude difference between the dry and lubricated models can also be attributed to the unloaded regions of the dry bearing. The contact deformation arising from the loading of the inner race is sufficient to cause the rollers geometrically opposite to become

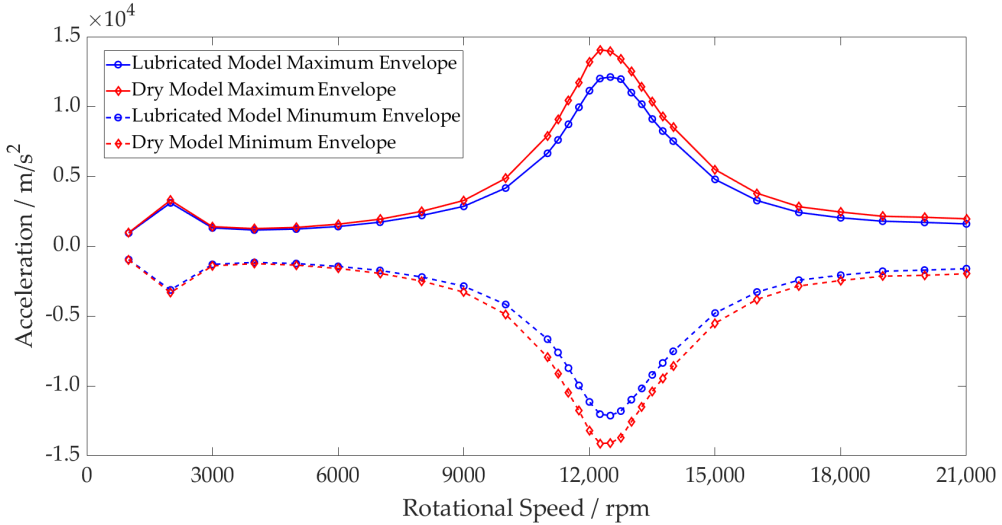


Figure 4.16 Inner race acceleration - Dry vs lubricated operating envelope.

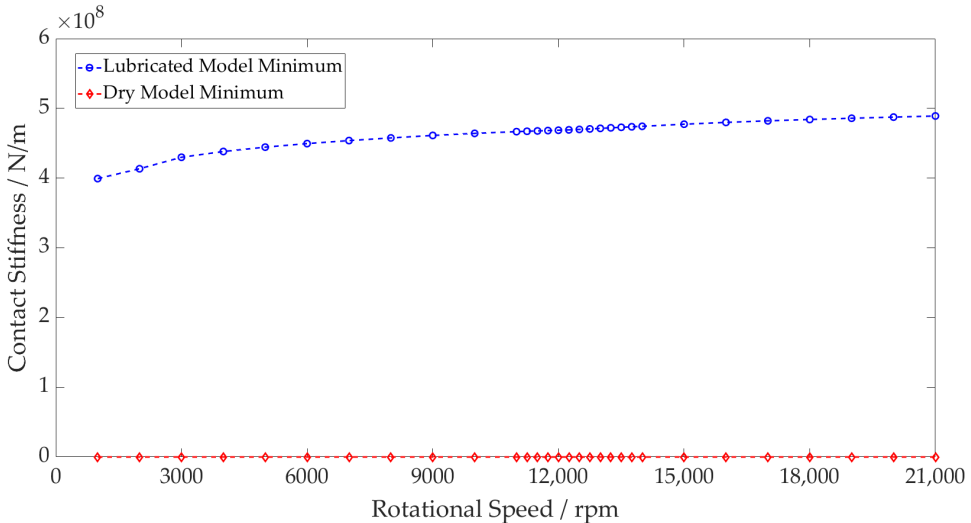


Figure 4.17 Rolling element contact stiffness - Dry vs lubricated minimum values.

separated from their contacts. Contact is lost between the roller and raceway, leading to zero contact stiffness. The inner race moves into this region until it is reacted by a contact force once again. These regions of zero stiffness are shown in Figure 4.17, where the minimum stiffness of an individual rolling element and raceway contact in the dry model drops to zero due to separation. For the lubricated model, contact is maintained throughout.

Analysing the conjunction level results from the lubricated model, the contact force due to the gear mesh frequency is shown superimposed on the ball pass frequency as an individual element passes through the loaded region of the bearings (Figures 4.18 and 4.19). The higher contact forces result in a reduction in the central film thickness, also

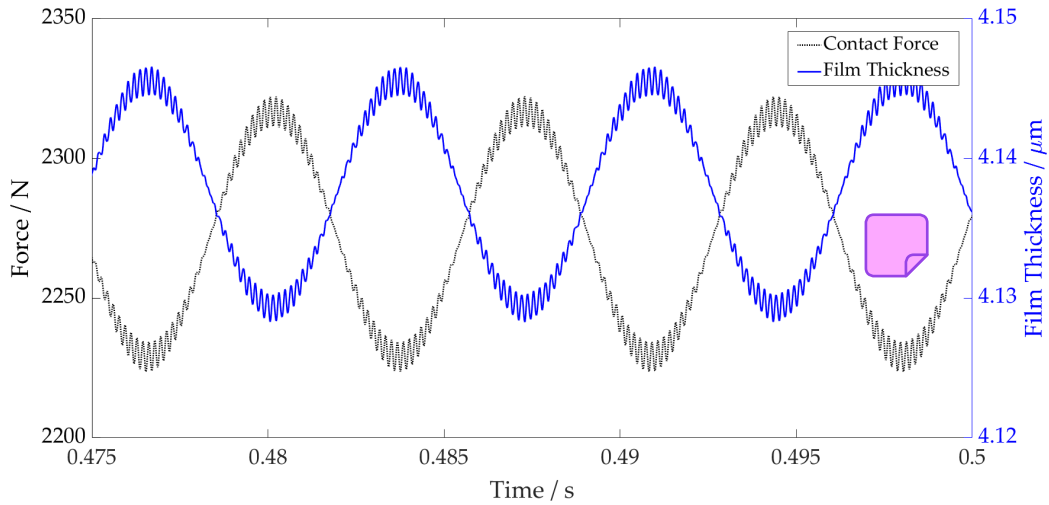


Figure 4.18 Film thickness vs contact force 21 000 rpm.

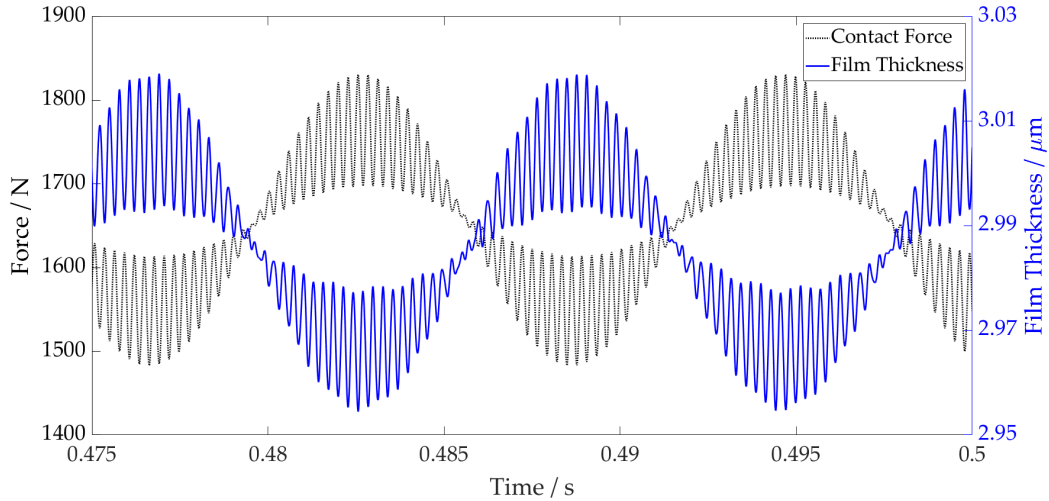


Figure 4.19 Film thickness vs contact force 12 500 rpm.

shown when observing the variation in film thickness for both plots. At 12 500 rpm, the force and film thickness fluctuations are much larger due to the high excitation levels of the shaft during resonance. At 21 000 rpm, even with a much lower torque transfer through the gear pair, the contact forces are greater than at 12 500 rpm. This is due to the contribution of the film enhancing the total contact deflection and hence increasing the contact force.

4.4.1 Conclusions

A coupled co-simulation approach has been presented to consider implicitly the EHL film in roller bearings within a high-speed system-level FMBD model. The model

replicates the operating conditions of a 54 kW permanent magnet synchronous motor (PMSM) coupled to a first stage gear pair, operating at speeds up to 21 000 rpm. This was the first time in open literature that an implicitly lubricated multi-physics bearing model has been considered in the context of electrified powertrain dynamics. The conjunction level and system level results have been analysed to compare the lubricated and conventional dry-bearing modelling techniques, and the following conclusions have been drawn:

1. Results show that the film thickness reaches 4.15 μm at 21 000 rpm. This leads to 9.6 times greater contact forces and hence 24.9% greater contact stiffness between the dry and lubricated models due to the lubricant entrainment and non-linear Hertzian force–deflection relationship.
2. The contribution of all the rolling elements leads to the lubricated model having a 16.6% greater maximum total bearing stiffness at 21 000 rpm than the dry model. Moreover, this stiffness is shown to increase with speed due to the film thickness increasing with the entrainment velocity; this is something that dry models do not account for. It behaves as a non-linear speed-dependant preload.
3. This increase in the total bearing stiffness leads to an increase in the stiffness of the total system. By modelling the shaft as a flexible body, the influence on the natural frequency of the system is seen. The natural frequency increases from 3470 Hz to 3542 Hz, corresponding to a 250 rpm increase from the dry estimation at 12 500 rpm. This increase with speed coincides with the higher frequency excitation from the gear meshing.
4. Implicit inclusion of the film in the analysis was therefore shown to affect the predicted NVH response of the system. The increased bearing stiffness also reduced the total radial displacement of the shaft across the entire speed range.

Understanding the influence of the roller bearings on the transmission stiffness is of particular importance in automotive applications, and this change shows the effect of the lubricant film on the already complex contact phenomena. Neglecting the effect of the lubricant film can lead to an underestimation of the bearing stiffness, impacting the accuracy of dynamic analyses such as noise, vibration and harshness (NVH) prediction. As transmissions operate at higher speeds with more complex interconnected structures and noise paths, it is important that these behaviours are modelled accurately. Furthermore, underestimation of the contact forces will also lead to a miscalculation of contact pressures, impacting future sub-surface stress and wear analyses for the life predictions of these crucial critical machine elements.

The central film thickness is the governing contributor to these stiffness disparities. It was, however, noted in Chapter 3, Section 3.4.4 that the regressed equation overestimates the central film thickness when compared to the numerical solution by up to 11.3% at 8 350 rpm. To further investigate this behaviour, explicit numerical analysis was performed at each speed point in the bearing presented within this chapter. The results of this are shown in Chapter 5, Figure 5.1. The analysis revealed that the calculated film values diverge with increasing rotational speed and hence entrainment velocity.

The literature review highlighted the potential of ANNs to predict central film thickness. They have demonstrated accuracy comparable to numerical EHL solutions whilst significantly reducing computational cost. Embedding an ANN within the implicit lubricated bearing model is one way to overcome the above stated discrepancy whilst maintaining computationally efficiency. This efficiency is vital for FMBD solvers, due to the fine resolution of time steps required for the systems of equations and the iterative nature of the tribological contact solution. Since an ANN can be trained using a wide range of input data, the effects of other tribological phenomena such as starvation and thermal effects can also be considered, expanding the potential for further analysis.

Chapter 5

Artificial Neural Networks for EHL Film Thickness Predictions

5.1 Introduction

Tribodynamic modelling generally employs analytical equations for the prediction of film thickness in elastohydrodynamic contacts; chosen due to their timely solution. Whilst computationally efficient, these do not achieve the accuracy of the full numerical solution outside the bounds of the data used to generate the analytical equations. In the context of dynamic simulation, a full numerical solution at each time step of a system level model would, however, yield excessive computation time. This has led to the emerging use of data driven solutions, such as machine learning, in the field of tribology. These can achieve accuracy much closer to the numerical solution, whilst significantly improving computational time.

This chapter details the development of an Artificial Neural Network (ANN) for prediction of central film thickness at the roller-race conjunction. ANNs are trained using data generated by the numerical EHL solution, with the data set constrained to realistic operating conditions using the Greenwood regimes of lubrication. Multiple ANNs are compared to find the optimum structure, accounting for training time and accuracy¹. The ANN is then deployed explicitly, using the boundary conditions of a simple bearing model to test the film thickness accuracy and speed of solution. The trained ANN is then deployed implicitly in the system level FMBD introduced in Chapter 4, replacing the analytical film equations in the model.

The aim of this chapter is to improve the accuracy of the central film thickness estimation, whilst maintaining a timely solution in the context of a full dynamic solution.

¹I would like to thank Dr Jack Walker for his collaboration in training, processing and validating the large quantities of data required for this study.

This workflow employed is not only relevant to roller bearings; it can be applied to a wide range of contacts and different sources of training data depending on the modelling requirements.

5.2 Numerical vs Analytical Film Thickness Values at High Entrainment Velocities

Two main approaches exist for determination of the complex non-linear problem of film thickness in lubricated contacts. The first approach involves employing numerical methods [48], where systems of partial differential equations are formulated to describe the state of the contact and then solved iteratively [124]. Whilst this method yields accurate results and is applicable to a wide range of operating conditions, it is computationally intensive due to its iterative nature. The second approach involves developing regressed analytical equations from experimental or numerical studies which can be used for specific lubrication regimes. These equations offer quick estimates of key parameters, such as central [51] and minimum film thickness [125]. However, whilst more computationally efficient than the full numerical solution, this approach has limitations.

The applicability of regressed equations is often limited to the range of data used for their development. There is also a requirement for extensive effort in collecting experimental or numerical data to develop them. The entrainment velocities considered in this work (up to $32 \text{ m} \cdot \text{s}^{-1}$) exceed the typical range over which the regressed equations are experimentally derived. Whilst it is possible to exceed the range of input data, it must be done with caution [94].

Figure 5.1 shows a comparison between the central film thickness calculated using the numerical method (see Section 3.3) and the analytical equation (Equation 3.15) across a speed range of 1 000 - 21 000 *rpm* with a constant contact force of 3000 *N*. The bearing used for this comparison is the same as in Section 4.3. Geometry is detailed in Table 4.1, with rheological and material properties detailed in Table 4.2.

It is shown that as rotational speed and hence entrainment velocity increase, the film thickness prediction of the numerical and analytical calculations diverge. At 21 000 *rpm*, entrainment velocities of $30.7 \text{ m} \cdot \text{s}^{-1}$ leads to a 20.3% difference between the methods, with the analytical equation overestimating the film thickness.

The implementation of ANNs within tribology is one way to overcome the computational expense of the full numerical solution and this limited validity of the analytical approach. Overcoming the above stated discrepancy is not the only advantage of a

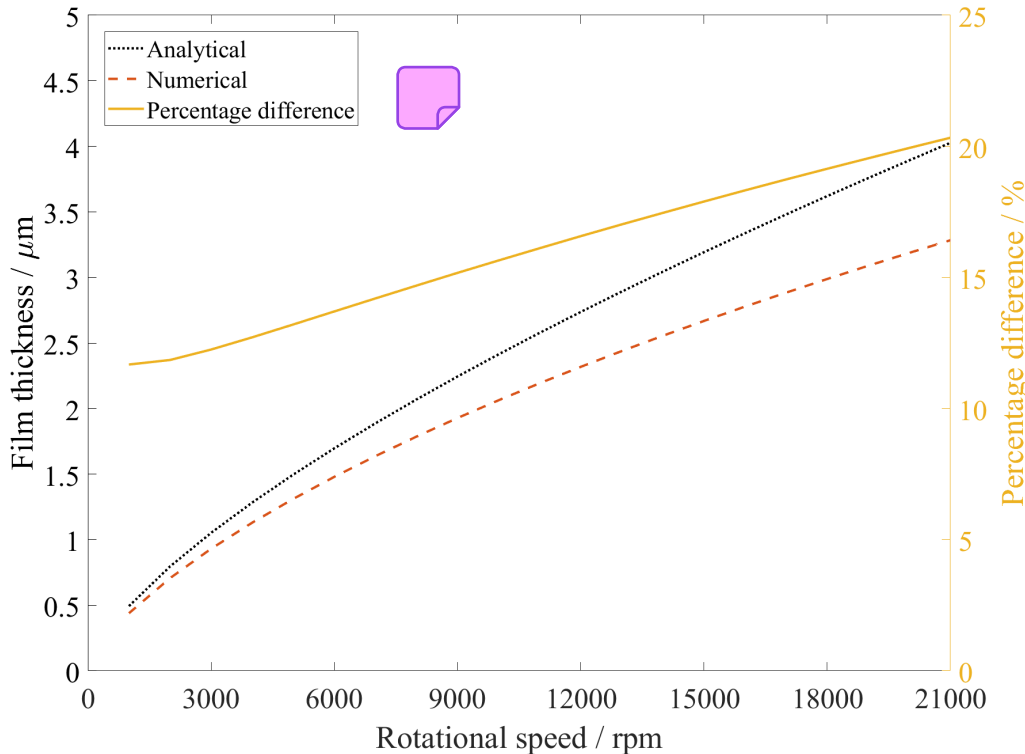


Figure 5.1 Central film thickness - EHL vs analytical.

numerical EHL informed ANN. Since an ANN can be trained using a wide range of input data, the effects of other tribological phenomena such as starvation and thermal effects can also be considered. Furthermore, the training of such ANNs is not bound to only numerical inputs; the results of experimental testing could be used to generate an experimentally validated ANN.

5.3 ANN Fundamentals

An Artificial Neural Network (ANN) is a computational model that is inspired by the biological neural networks present in the natural brain [126]. ANNs are a subset of machine learning (ML) that can be trained using supervised, unsupervised, or reinforcement learning techniques. In supervised learning, ANNs are particularly useful for regression tasks, where they can model complex non-linear relationships between inputs and outputs. ANNs compare their outputs with target values during training and, due to their structure, can adapt for a wide range of applications. The goal of this training is to minimise the error, and to improve the ability of the network to generalise and make accurate predictions for new, unseen data.

ANNS consist of a set of interconnected processing elements known as neurons. These are represented computationally as nodes, and the terms are often used inter-

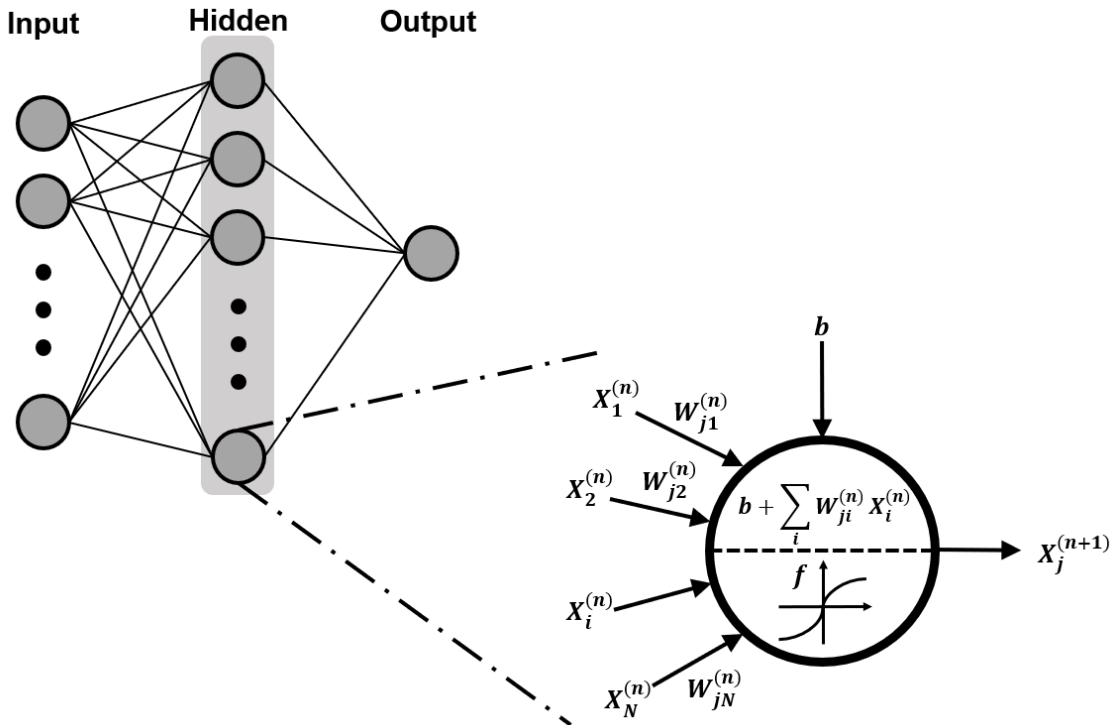


Figure 5.2 ANN schematic.

changeably. These elements have the ability to adapt to input data for the purpose of solving complex non-linear functions. The neurons are organised into three main layers, shown in Figure 5.2: Input layer; Hidden layer(s) and Output layer. The adaptation is performed using weighted connections that link each neuron layer. These weightings are adjusted during the learning process, and determine the strength of the connections between neurons.

The following section provides descriptions of the common terms that will be referenced throughout this chapter.

5.3.1 Network Architecture

- **Input layer:** Input data is assigned to input nodes in the first layer of the network. In the case of the film thickness estimation, **nine input variables** and hence nine nodes are required.
- **Hidden layer(s):** These layers are located between the input and output layer. There can be multiple hidden layers, each consisting of multiple nodes. Multi-layer networks enable the resolution of non-linear problems, whereas single layer networks (no hidden layers) are limited to linear problems [127].

- **Output layer:** The output layer represents the final computed results. For the film thickness estimation, the output consists of a single node corresponding to the predicted central film thickness.

The type of ANN used in this study is called a multi-layer feedforward backpropagation neural network. Forward propagation through the network is used to make predictions based on the input data. Backpropagation is then performed to calculate prediction error and modify the network to minimise this. This process is repeated until the desired prediction accuracy is achieved.

5.3.2 Forward Propagation

Input data propagates through the neural network in the following manner:

1. **Weights:** The input data to the nodes is multiplied by corresponding weights, and a bias term is added (see Figure 5.2). The general equation for ANNs is:

$$z = f(b + \sum_i W_{ji}^{(n)} X_i^{(n)}) \quad (5.1)$$

where z represents the activated output of the neuron. W_{ji} is the weight connecting the i -th neuron of the previous layer to the j -th neuron of the current layer in the n -th layer. $X_i^{(n)}$ is the input value to the neuron from the i -th neuron in the previous layer. The bias is represented by b , and f represents the activation function applied to the weighted sum.

2. **Activation function:** The weighted sum plus bias ($x_w = b + \sum_i W_{ji}^{(n)} X_i^{(n)}$) is passed through an activation function, f , which introduces non-linearity to the system to enable the learning of complex patterns.
3. **Bias:** The bias term, b , is able to shift the activation function's output. It ensures that a neuron can still activate even in the case where all input values are zero.
4. **Output generation:** Data is propagated through the system until it reaches the final prediction at the output layer.

5.3.3 Backpropagation

The learning process of an ANN is achieved by adjusting the weights in the network. This is done using a process called backpropagation [128]:

1. **Loss function:** During training, the target output of the ANN is known. The predicted output of the ANN is therefore measured against this using a loss function. In the case of ANNs used for regression, mean squared error (MSE) is used.
2. **Backpropagation:** This error is backpropagated through the system to determine the contribution of each weight to that error.
3. **Optimization:** Optimization algorithms, such as Levenberg-Marquardt [129] [130] [131], are used to update the weights and biases to reduce the loss.
4. **Epochs:** The above process repeats over multiple cycles, known as epochs. This is performed until the desired MSE is achieved.
5. **Overfitting:** This is the phenomenon whereby an ANN becomes too specialised at learning the training data, and as a result performs poorly with new, unseen data. This occurs when the network extensively adjusts its internal parameters to fit noise or outliers in the training set [132]. It is therefore necessary to limit the number of epochs once sufficient performance is achieved.

5.4 Methodology

This section details the following methodology:

1. Generating training data for the ANN using the numerical EHL method (Section 3.3), and constraining this input data to a range valid for machine element contacts.
2. Evaluating the best ANN structure for the central film thickness estimation.
3. Testing the ANN using by calculating bearing film thickness explicitly based on kinematic condition obtained from a dynamic bearing model.
4. Embedding the ANN within a FMBD model to calculate and implicitly consider the film thickness within the bearing at each time step of the simulation.

The workflow describing the EHL data generation, variable constraints, training methodology and structure evaluation is presented in Figure 5.3. This workflow resulted in a structurally optimised trained ANN that could be used for the explicit and implicit modelling tests.

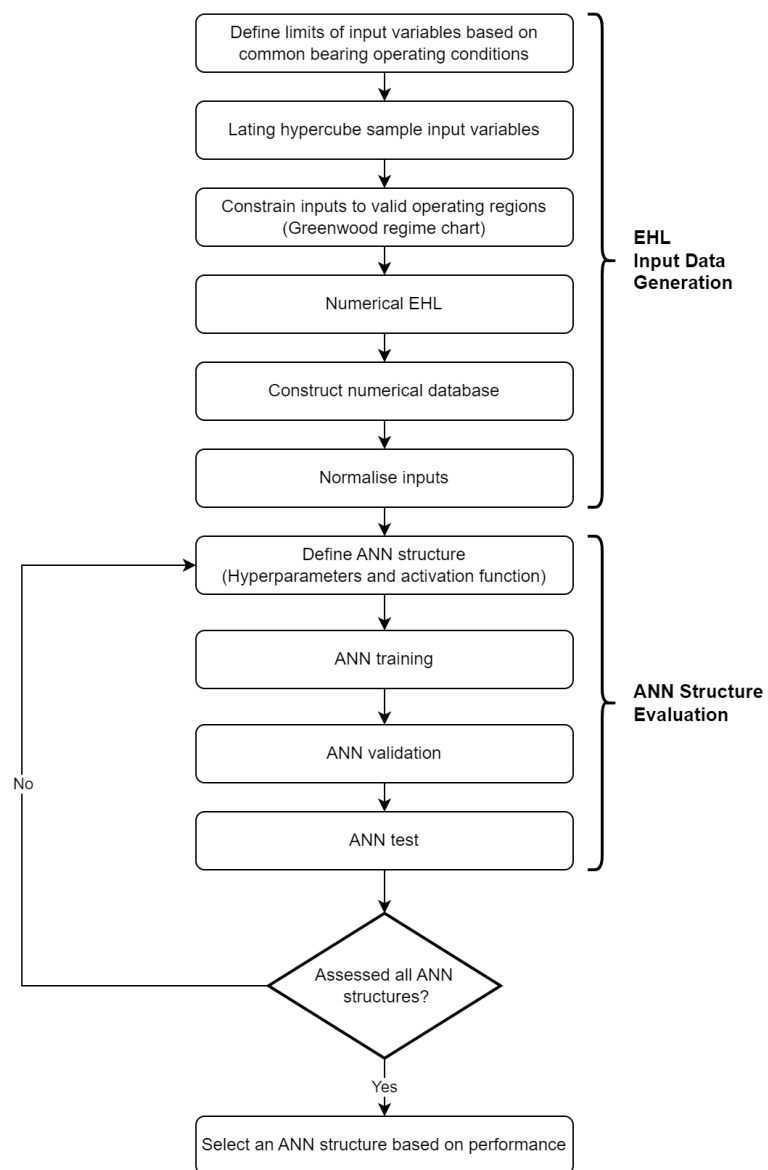


Figure 5.3 ANN data flow, models and training flowchart.

5.4.1 EHL Input Data Generation

Training an ANN requires a comprehensive data set. For this study, the training data was generated using the numerical EHL model presented in Section 3.3. This approach was selected due to the large size of the dataset required for training, and the relatively low resource-intensive nature to generate this. It is important to note that the training data could also be obtained from experimental work, which would further enhance the applicability of this approach for future studies.

Sampling Input Variables

Due to the large design space covered by the high number and range of input parameters, a robust sampling technique must be chosen to create the training data set. In traditional random sampling, each of the parameters is randomly sampled within its defined range. This may lead to insufficient coverage of the parameter space and simple bias, as it lacks a systematic approach to ensure even distribution [133].

The Latin Hypercube Sampling (LHS) method was utilised by Marian et al. [92], and was also selected for this study. It is a statistical method used to efficiently sample a high-dimensional parameter space, such as that required for the central film thickness calculation. LHS is derived from Latin Hypercube Design (LHD), where each parameter's range is divided into equal intervals along each dimension. Each interval is then randomly assigned to a unique position within its corresponding dimension. The process results in a matrix, where each row represents a combination of parameter values. Contrary to the random sampling method, LHS ensures that each interval is sampled exactly once per dimension, preventing clustering and improving representation across the space [133]. This ensures lower computational effort required for ANN training, despite the high number of input variables and value ranges required for the EHL solution.

The LHD is a $n_s \times n_f$ matrix, where n_s and n_f represent the number of simulations the number of factors respectively. LHS enhances LHD by introducing a randomization component. The randomly selected samples within each interval undergo permutation, ensuring that samples are not biased by the order of selection.

LHS elements are generated by subtracting a random number between zero and one $Z_r \in [0, 1]$ from each LHD element $x_{ij,LHD}$. This is then divided by the number of test points [134]:

$$x_{ij,LHS} = \frac{x_{ij,LHD} - Z_r}{n_s} \quad (5.2)$$

This equation rescales the LHD values to a range between 0 and 1. By subtracting a random number between 0 and 1 and dividing by the total number of sample points, the

resulting Latin hypercube samples are spread evenly across the interval (0,1) for each parameter. This is important, because it allows the Latin hypercube samples to be easily transformed to any desired range or distribution. This transformation to the design space is done using the limits of the tribological parameters in Table 5.2.

The quality of the test field (freedom of correlation and uniform distribution) can be assessed based on the distances between data points [135]. The MaxiMin criterion in the MATLAB® Statistics and Machine Learning toolbox was used to optimise the LHS. This maximises the the minimum distance between individual test points such that the LHS test field is uniformly distributed:

$$\text{MaxiMin} = \left[\sum_{1 \leq i < j \leq n_1} d(x_i, x_j)^{-\xi} \right]^{-\frac{1}{\xi}} \quad (5.3)$$

where d represents all distances in the test field, and subscripts i and j are indexes for the parameter and sample point respectively. ξ represents the application dependant factor which determines the degree of importance assigned to the distances [134].

Constraining the Input Data Bounds

The performance of ANNs is heavily reliant upon the quality of the data set provided for training. To construct a training database, [92] utilised a Finite Element Method (FEM) solver for film thickness calculations. The database covered a very large range of lubricant and material properties for relatively low entrainment speed conditions ($< 0.4 \text{ m} \cdot \text{s}^{-1}$ for the 2D line contact studies). Contact conditions for some combinations of these input parameters exceeded realistic conditions within common machine elements, including bearings. To further improve upon this methodology, the input data range required constraining.

The Greenwood Regime chart [136] was used for this purpose. The regions of the chart, as shown in Figure 5.4, are:

- Isoviscous Rigid (IR)
- Isoviscous Elastic (IE)
- Piezoviscous Rigid (PR)
- Piezoviscous Elastic (PE)

The bounds indicate the transition between the lubrication regimes, which are classified based on material, rheological and geometric properties. To find which

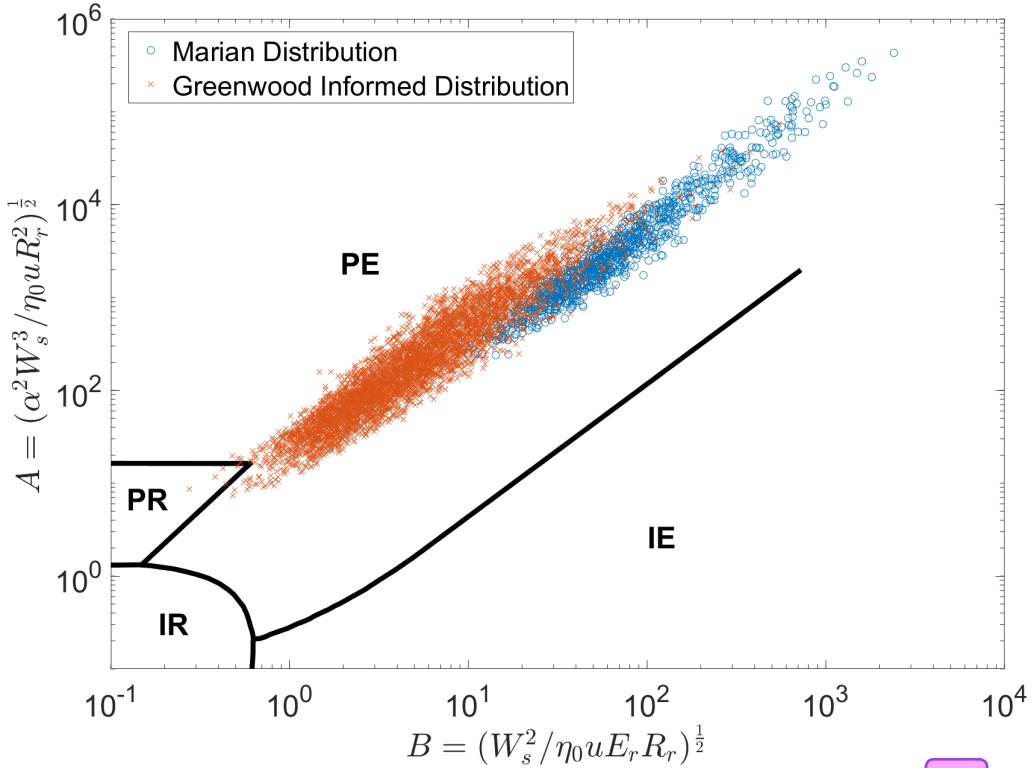


Figure 5.4 Greenwood informed training data vs Marian et al. [92]

regime a contact is operating within, the dimensionless elasticity (G_e) and viscosity (G_v) parameters can be calculated:

$$G_e = \left(\frac{\alpha^2 W_i^3}{\eta_0 u R_r^2} \right)^{\frac{1}{2}} \quad (5.4)$$

$$G_v = \left(\frac{W_i^2}{\eta_0 u E_r R_r} \right)^{\frac{1}{2}} \quad (5.5)$$

The PE region signifies an EHL contact, where pressures are high enough to elastically deform the material and increase the viscosity of the lubricant. The IR region relates to the hydrodynamic regime of lubrication, where the contact load does not deform the surface and viscosity remains constant. Since these investigations are focussed on improving the EHL film thickness estimation, the training data set was required to fall within the PE region of the Greenwood plot.

The initial range of each parameter is shown in Table 5.1. A training data set was then generated using these limits. The input data was then constrained further to ensure Hertzian pressures, P , were between 300 MPa and 3.5 GPa, as well as redistributing any points that fell outside of the PE and PR regions. A flowchart to explain the process of constraining the input variables is shown in Figure 5.5.

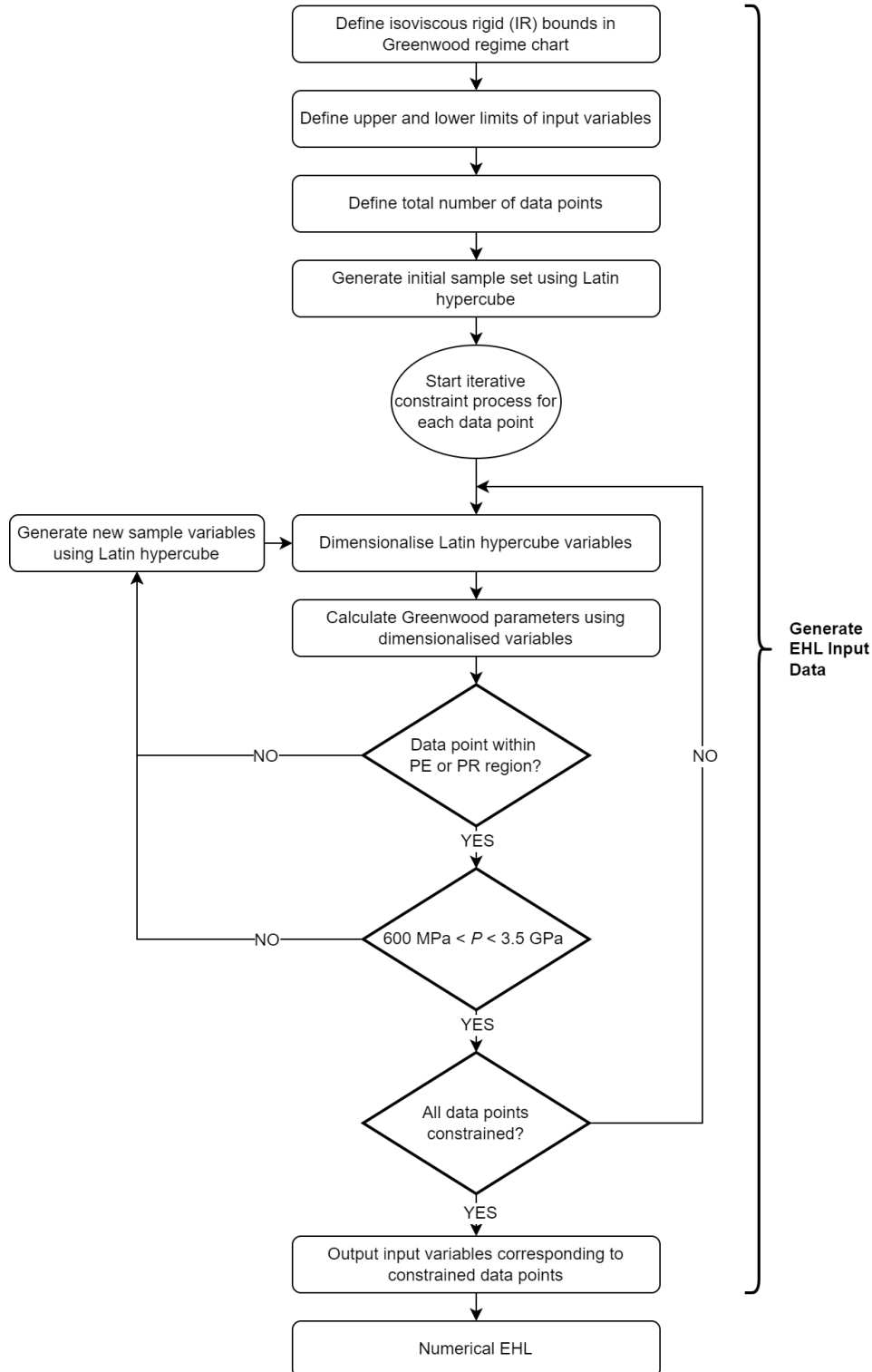


Figure 5.5 Workflow to constrain training input data using Greenwood regimes.

Table 5.1 Range of ANN film thickness calculation parameters

Parameter	Unit	Minimum	Maximum
Load	N	150	5000
Entrainment velocity	$m \cdot s^{-1}$	0.6	30
Reduced radius	m	0.0001	0.02
Reduced elastic modulus	GPa	200	250
Pressure-viscosity coefficient	GPa ⁻¹	10	30
Lubricant viscosity	Pa · s	0.0005	0.1
Lubricant density	kg/m ³	7750	8050
Poisson's ratio	—	0.3	0.35
Contact length	m	0.001	0.050

A comparison of an the unconstrained and constrained input variables used for the training data is shown in Figure 5.6. It is shown that for the same number of data points (5 000), the constrained data cloud is concentrated over a smaller region of the chart. This improved the point density in regions of interest, increasing the likelihood that the training data more closely matches the test data.

Constructing the Numerical Database

The 1D EHL model presented in Section 3.3 was used to generate the numerical database for training the ANN. The variables corresponding to each constrained data point in Figure 5.6 were used as inputs to the calculation. The target output of central film thickness was calculated.

5.4.2 ANN Structure Evaluation

The general structure of the ANN is described in the following format, as per [77]:

$$N_{in} - [N_{h1} - N_{h2} - N_{h3}]_t - N_{out} \quad (5.6)$$

The number of neurons in each layer is denoted by N , with the input and output layers indicated by the subscripts *in* and *out*, respectively. Subscripts $h1$, $h2$, and $h3$ denote the hidden layers, with t being the total number of hidden layers. A graphic

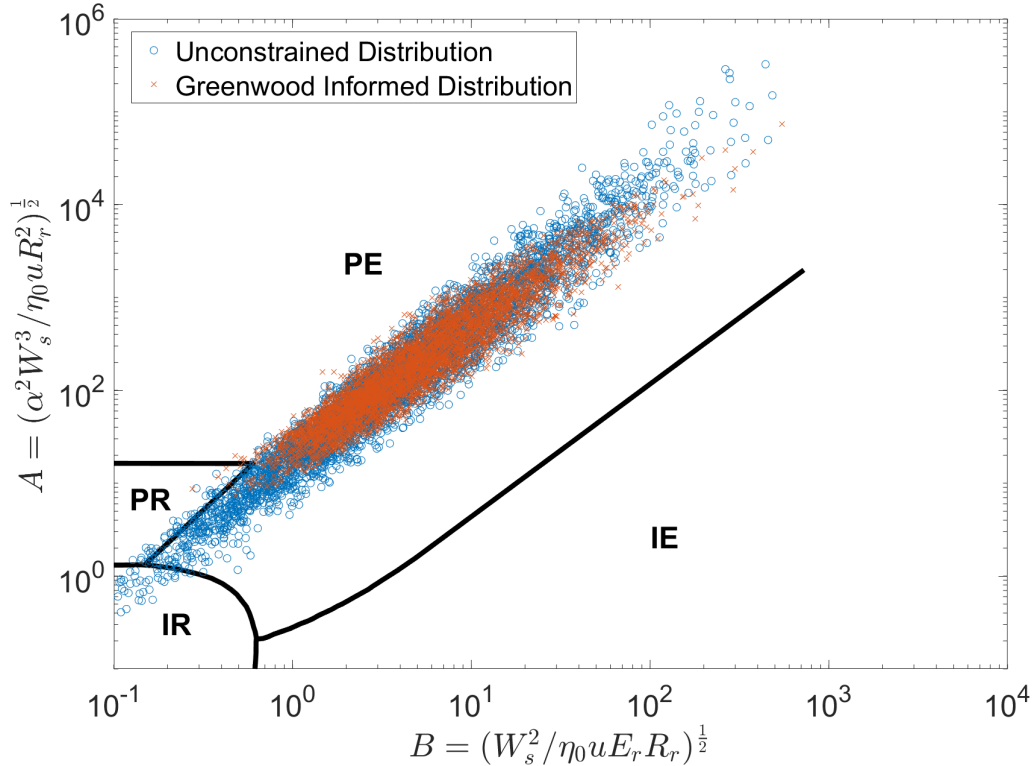


Figure 5.6 Greenwood informed training data vs unconstrained data.

representation of the structure used for the film thickness estimations is show in Figure 5.7. As the structural complexity of ANNs increases, the training time increases due to the greater number of neurons and layers. Implementations of ANN in the field of tribology, specifically film thickness predictions, are typically limited to between one and three hidden layers [137].

The structure of an ANN affects both its training time and prediction accuracy. To evaluate the performance of different ANN structures, and hence select an appropriate structure for this application, a sensitivity study was performed. The study comprised of over 500 different ANN structures. The input data range remained constant across all structures, whilst the variables listed in Table 5.2 were adjusted. This involved varying the hyperparameters: the number of hidden layers varied from one to four, and the number of neurons from 10 to 20. Three activation functions: Hyperbolic tangent, Logistic sigmoid and Rectilinear were evaluated. The wall time for each training data point generation was recorded, as well as the total training time of each ANN structure.

Selection of the final structure to be used for film thickness estimation in the bearing models was based on total training time, coefficient of determination (R^2), and the potential for the ANN to overfit. R^2 (Equation 5.12) was evaluated for the test data sets, since this gives an accurate indication of the networks ability to predict film thickness with unseen input variables.

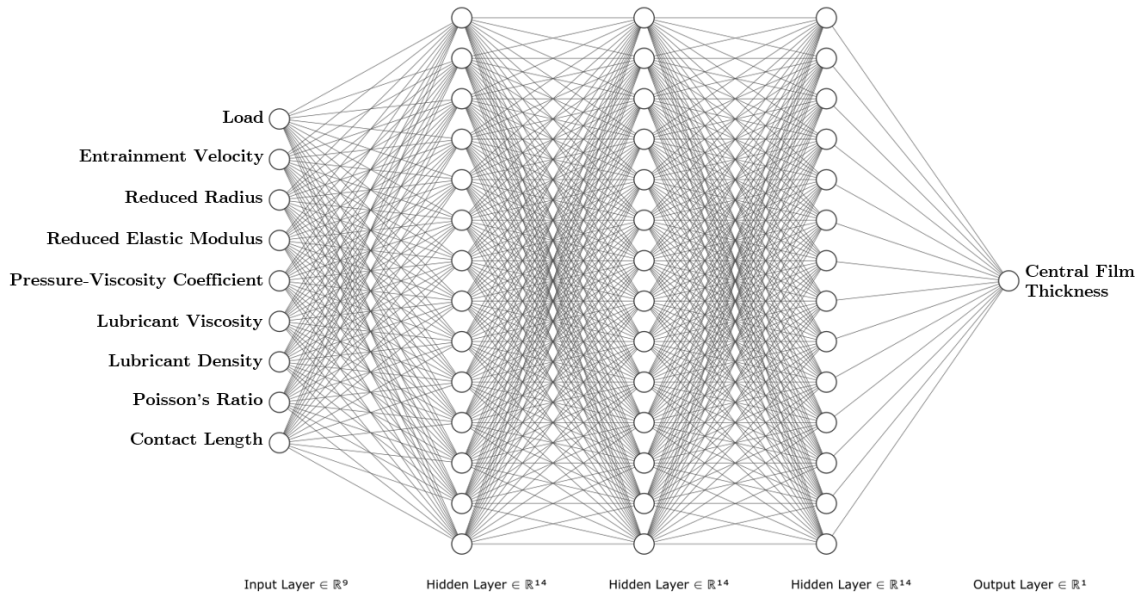


Figure 5.7 ANN structure to predict EHL central film thickness (9 – [14 – 14 – 14]3 – 1).

Table 5.2 Sensitivity study of ANN structure

Variable	Value
Number of training data points	600 - 1500
Number of hidden layers, t	1 - 4
Number of neurons, N	10 - 20
Activation function type	Hyperbolic tangent (Tanh), Logistic sigmoid (LogSig), Rectilinear (ReLU)

The following sections describe the evaluation process of each network structure:

Training, Validation and Test Datasets

The dataset was first divided into three sets: the training set, the validation set, and the test set, each containing 70 %, 15 % and 15 % of the training data respectively:

1. **Training Set:** The training set is the portion of the dataset used to train the ANN, containing the input data and the corresponding output data. As aforementioned, the ANN adjusts the internal parameters based on this data to learn the underlying patterns.
2. **Validation Set:** The validation set is used to tune the performance of the ANN during the training process. It is an independent dataset that the network has not seen before, allowing for the evaluation of its generalization capabilities. The network's performance on the validation set is monitored during training to make decisions on adjusting hyperparameters (number of hidden layers, neurons per hidden layer, activation functions), or stopping the training process to prevent overfitting.
3. **Test Set:** The test set is a completely independent dataset that is not used during training or validation. It is used to assess the final performance and generalization ability of the trained ANN. By evaluating the network on unseen data, the test set provides an unbiased estimate of the model's performance in actual use.

To evaluate the optimum ANN structure, the size of the training data set was varied (600, 1000, 2000 and 5000) to observe the its effect on the quality of the predictions. A limit of 1000 epochs was also implemented, restricting the ANN to 1000 full iterations through the entire training set. This achieved low MSE whilst preventing overfitting (see Section 5.4.2).

Data Normalisation

The input and target parameters were normalised using the min-max normalisation function:

$$\tilde{x} = \frac{x - x_{\min}}{x_{\max} - x_{\min}}(u_n - l_n) + u_n \quad (5.7)$$

where u_n , and l_n represent the upper and lower normalised unit values of 1 and -1 respectively. The dimensional target input value is denoted by x , and the final normalised

input or output parameter of the ANN is denoted by \tilde{x} . x_{\max} and x_{\min} are retained to dimensionalise the output variable after the prediction.

Activation Functions

As suggested in [92], four suitable activation functions for the hidden layers were selected for testing. These are mathematical functions that are applied to the output of each neuron in a layer of the neural network. They introduce non-linearity which allows the network to learn complex input-output relationships. Activation functions help determine the output of a neuron based on the weighted sum of its inputs. A description of each function is provided below:

- **Sigmoid (logistic):** This function transforms the input values into a range between 0 and 1. It has continuously differentiable smooth S-shaped curve and is given by the following formula [138]:

$$\text{log sig}(x_w) = \frac{1}{1 + e^{-x_w}} \quad (5.8)$$

Sigmoid functions may suffer from the "vanishing gradient" problem where the partial derivative reaches zero [139], leading to slower convergence during training.

- **ReLU (Rectified Linear Unit):** This function outputs the input value directly if it is positive, and zero otherwise. The mathematical definition is:

$$\text{ReLU} = \begin{cases} x_w, & x_w \geq 0 \\ 0, & x_w \leq 0 \end{cases} \quad (5.9)$$

The gradient is 1 when the neuron is activated, and zero when it is deactivated. This function is computationally efficient and addresses the vanishing gradient problem to an extent [139].

- **Tanh (Hyperbolic Tangent):** The hyperbolic tangent or tanh function is defined as:

$$\tanh(x_w) = \frac{2}{1 + e^{-2x_w}} - 1 \quad (5.10)$$

The formulation and behaviour is very similar to sigmoid. It produces values which range from -1 to 1, having a centred mean around zero.

- **Linear:** A simple linear activation was used on the output.

Evaluating the Network Performance

During backpropagation of the ANN, the Mean Squared Error (MSE) was used to evaluate the network's performance:

$$MSE = \frac{1}{N_p} \sum_{i=1}^{N_p} (t_i - y_i)^2 \quad (5.11)$$

where t_i and y_i are the target and predicted value respectively. The total number of training points being trained, validated or tested is denoted by N_p .

To assess the goodness of fit of the ANN, the statistical metric R^2 , known as the coefficient of determination, was used. This measures the proportion of variance in the dependant variable (film thickness) that is predictable from the input variables (Table 5.1) in the model. This value ranges from 0 to 1, with a higher value indicating the best fit of the model to the data. This was post-processed after training and is calculated as follows:

$$R^2 = 1 - \frac{\sum_{i=1}^{N_p} (t_i - y_i)^2}{\sum_{i=1}^{N_p} (y_i - \bar{y})^2} \quad (5.12)$$

where \bar{y} is the mean of the target sample. The numerator of the fraction, $\sum_{i=1}^{N_p} (t_i - y_i)^2$, represents the sum of squared residuals, which quantifies the variation in the target variable that is not explained by the model. The denominator, $\sum_{i=1}^{N_p} (y_i - \bar{y})^2$, is the total sum of squares, which captures the total variation in the target variable [92].

Preventing Overfitting

Early stopping and regularisation was used to prevent statistical overfitting during training [140]. Early stopping halts the training process before the model reaches the maximum number of epochs. This is done by monitoring the MSE performance (Equation 5.11) of the network against the validation set during training. Once the performance reaches a plateau, or begins to degrade, the training is stopped early. Regularisation adds additional constraints to the learning process. It modifies the performance criteria by accounting for the change in mean square of the network weights and biases (Mean Squared Weight (MSW)). This is calculated in Equation 5.13:

$$MSW = \frac{1}{N} \sum_{j=1}^N W_j^2 \quad (5.13)$$

where W_j is the individual weight value associated with the j -th neuron or connection in the network.

By applying an adjustment factor, denoted as γ' , the weights and biases can be reduced during propagation (Eq. 5.14), thus mitigating the risk of overfitting and improving the network's generalization capability.

$$MSE_{reg} = \gamma' * MSW + (1 - \gamma') * MSE \quad (5.14)$$

5.4.3 Explicit Bearing Film Thickness Predictions

After identifying a suitable training data size and structure, an ANN was trained to estimate the EHL central film thickness. These results could then be compared to the analytical (Equation 4.11) and numerical (Section 3.3) methods for calculating the film thickness under realistic bearing operating conditions.

The FMBD model used in Chapter 4 was used for this study. The shaft was modelled as a rigid body, and loading in the radial direction was purely static to remove the influence of additional dynamic effects. The shaft was constrained to one rotational and two lateral degrees of freedom. Bearing specification, material and rheological properties are shown in Tables 4.1 and 4.2.

The bearing was modelled as dry, without the influence of the EHL film at the roller-race contacts. The kinematic and dynamic results necessary for the film thickness estimation were extracted from an individual roller at each time step of the simulation. These results include roller load, contact entrainment velocity, and reduced radius of the contact between the roller and inner-race.

The loading pattern is cyclic in nature as the roller enters and exits the most highly loaded region of the bearing, corresponding to the radial force vector applied to the inner race. The contact reduced radius (3.03 mm) and entrainment speed ($20\text{ m}\cdot\text{s}^{-1}$) do not change throughout the orbit as they are a function of bearing geometry and constant operating speed. The normal contact load fluctuation is shown in Figure 5.8.

The operating conditions of the bearing were within the range of validity of the training data set. This is demonstrated in Figure 5.9 whereby the Greenwood parameters for the bearing operating points are calculated and overlayed on the training data cloud.

The structure chosen for this study was based on the conclusions drawn in Section 5.5.1. A structure of 3 hidden layers with 14 neurons per layer was selected ($9 - [14 - 14 - 14]_3 - 1$). Logistic sigmoid was selected as the activation function for the hidden layers. This structure is represented graphically in Figure 5.7.

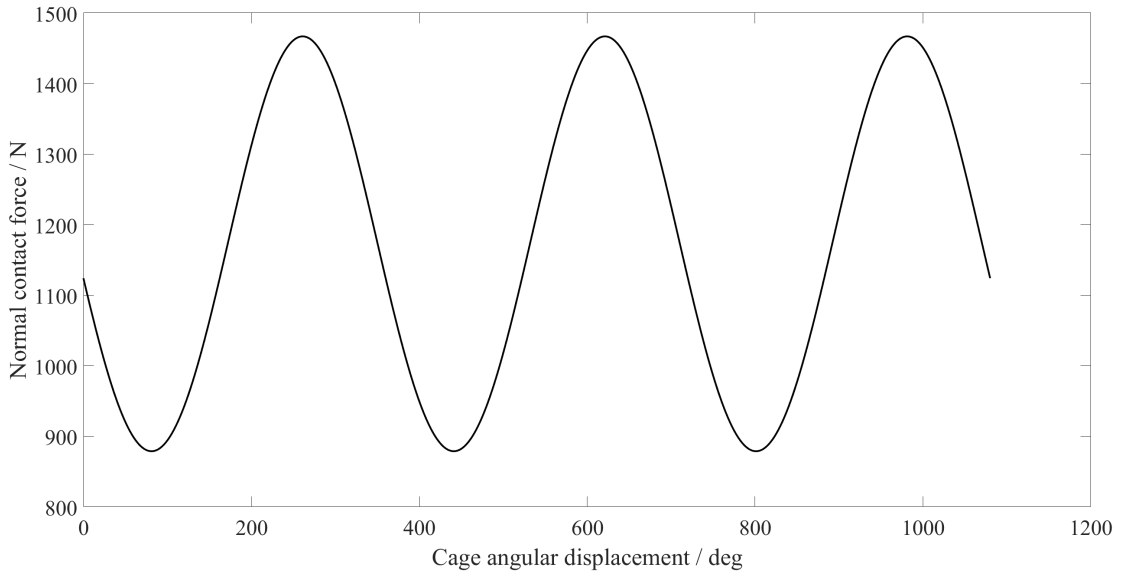


Figure 5.8 Normal contact load vs cage angular displacement.

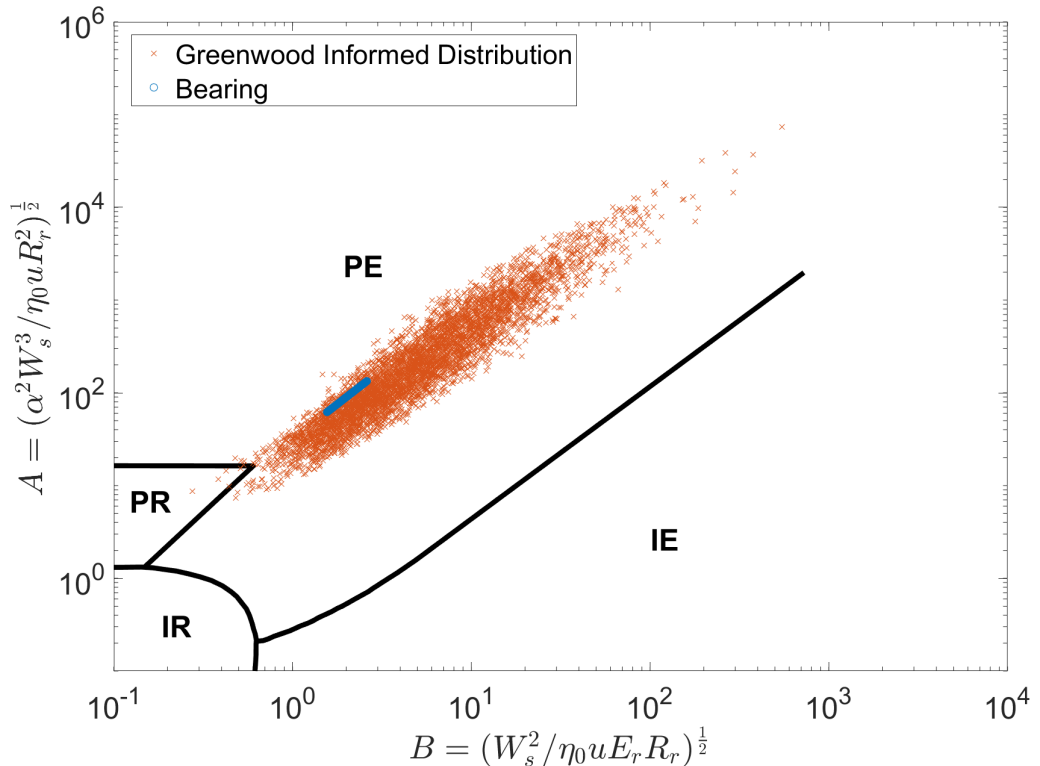


Figure 5.9 Bearing operating conditions vs Greenwood informed training data.

5.4.4 Implicit Bearing Film Thickness Predictions

To assess the viability of using ANNs as an alternative to the regressed film thickness equations in FMBD modelling, the trained ANN was embedded within the system level model introduced in Section 4.3. The extrapolated film equation (4.11) used within the lubricated bearing model in Section 4.3.1 was replaced with the trained neural network function.

The operating points investigated were at speeds of 5 000 - 20 000 *rpm* in increments of 5 000 *rpm*. The time-varying forces associated with the gear meshing events were present at each speed increment. The models were run for a total input shaft angular displacement of 50 *rad*. The first 10 *rad* of shaft rotation covered the period of system convergence. During this period, and for a further period of 20 *rad*, the analytical formula was used. The trained ANN was then deployed for the final 20 *rad* of steady state operation.

Simulations were performed at a fixed time step of 1×10^{-6} s to ensure convergence of the explicitly coupled models. The CPU time per time step was measured. Since the solver utilised an angle based simulation interval, the number of calculation steps varied from 95 493 to 23 874 for 5 000 *rpm* and 20 000 *rpm* respectively. Computational timings per point were recorded to assess the viability of this solution.

5.5 Results and Discussion

The following data was obtained using consumer grade hardware with the following specifications: Intel® Core™ i7-9750H CPU 6 cores @ 2.60GHz, 32GB RAM; GPU: NVIDIA GeForce GTX 1650. Identical hardware was used for both the full numerical and the ANN solutions to provide performance comparisons and assess the suitability of ANNs for film thickness calculations in FMBD solvers.

5.5.1 ANN Structure Evaluation

The 1D EHL model presented in Section 3.3 was used to generate the numerical database for training the ANN. Each numerical solution and hence training point took an average of 5.88 s to compute. The construction of the entire database on a single core therefore has a wall time of between 58.8 *min* and 489 *min* for 600 and 5000 points respectively. This wall time is noted for baseline comparisons, and can be significantly improved if parallelisation across multiple cores is utilised.

Tables 5.3 - 5.5 present the R^2 values obtained from 600 training data points, considering different activation functions described in Section 5.4.2. The number of layers

and neurons was varied for each activation function. Among the activation functions tested, the rectilinear (ReLU) function consistently underperformed when compared to the logistic sigmoid (LogSig) and hyperbolic tangent (Tanh) functions across all network structures. Similar to the work of Marian et al. [137], the optimum layer number was found to be between two and three, however the activation function was shown to be the dominating determinate of R^2 performance.

The LogSig activation function demonstrated the best R^2 performance, even for lower complexity structures. This was therefore selected for each hidden layer to assess the influence of training data quantity R^2 performance. Tables 5.6 - 5.9 present the training times for networks with varying numbers of training points and structural configurations. The results indicate that training time increases with the number of layers and neurons in the network. However, training time exhibits a much stronger positive correlation with the number of data points rather than with the complexity of the network structure.

Figure 5.10 illustrates the influence of the number of training points on the R^2 value when using the LogSig activation function. The results indicate that 600 data points are sufficient to train an ANN to the accuracy required for the central film thickness prediction ($R^2 = 0.99791$). Increasing the dataset to 5 000 data points resulted in an R^2 value of 1, however this came with significant time cost for structures with higher complexity; reaching 600 s for 4 layers of 20 neurons and a total of 1000 epochs. Combined with a data generation time of 489 min, this represents a computationally inefficient trade-off between accuracy and training cost. It is therefore concluded that 1000 - 2000 training data points are sufficient to achieve accurately trained neural networks for predicting the central film thickness whilst maintaining computational efficiency.

The results of this study guided the decision for the network structure to be used for the bearing models. A structure of 3 hidden layers with 14 neurons per layer was selected ($9 - [14 - 14 - 14]_3 - 1$). Logistic sigmoid was selected as the activation function for the hidden layers. This was trained using 2000 data points.

Table 5.3 R^2 performance of ANN structures using 600 data points and a LogSig activation function

Activation Function: LogSig													Key $R^2 [-]$	
R^2		Number of Neurons												
Number of Layers	1	10	11	12	13	14	15	16	17	18	19	20		
	2	0.997	0.995	0.998	0.998	0.999	0.999	0.999	0.998	0.998	0.995	0.999		
	3	0.999	0.999	0.999	0.997	1.000	0.996	0.998	0.998	0.997	0.997	0.995		
	4	1.000	0.998	0.998	0.999	0.997	0.997	0.997	0.998	0.993	0.995	0.996		

Table 5.4 R^2 performance of ANN structures using 600 data points and a Tanh activation function

Activation Function: Tanh												
R^2		Number of Neurons										
		10	11	12	13	14	15	16	17	18	19	20
Number of Layers	1	0.998	0.999	0.995	0.998	0.998	0.994	0.998	0.999	0.998	0.998	0.998
	2	0.999	0.998	0.998	0.999	0.996	0.998	0.996	0.996	0.996	0.993	0.994
	3	0.999	0.992	0.996	0.995	0.992	0.989	0.989	0.985	0.994	0.970	0.984
	4	0.997	0.997	0.992	0.994	0.991	0.983	0.982	0.978	0.990	0.989	0.983

Key
$R^2 [-]$
0.990
0.993
0.997
1.000

Table 5.5 R^2 performance of ANN structures using 600 data points and a Tanh activation function

Activation Function: ReLU												
R^2		Number of Neurons										
		10	11	12	13	14	15	16	17	18	19	20
Number of Layers	1	0.985	0.991	0.994	0.993	0.993	0.994	0.992	0.994	0.995	0.987	0.990
	2	0.993	0.996	0.995	0.993	0.992	0.984	0.989	0.993	0.992	0.993	0.992
	3	0.986	0.983	0.996	0.988	0.984	0.980	0.992	0.992	0.988	0.986	0.988
	4	0.981	0.990	0.975	0.928	0.951	0.986	0.985	0.986	0.986	0.982	0.985

Key
$R^2 [-]$
0.990
0.993
0.997
1.000

Table 5.6 Training time of ANN structures with LogSig activation function and 600 data points

600 Data Points, Activation Function: LogSig												
Training Time [s]		Number of Neurons										
		10	11	12	13	14	15	16	17	18	19	20
Number of Layers	1	0.76	0.96	1.16	1.01	1.49	1.30	1.41	1.72	1.12	0.90	1.13
	2	1.01	2.93	1.94	1.43	1.88	1.80	1.56	1.80	1.33	2.51	1.77
	3	2.81	1.29	2.58	2.22	2.27	1.52	1.67	2.26	2.06	1.94	3.57
	4	1.64	5.97	2.21	2.79	6.70	2.66	4.36	2.51	2.76	2.61	2.90

Key
Time [s]
0.00
10.00
100.00
600.00

Table 5.7 Training time of ANN structures with LogSig activation function and 1000 data points

1000 Data Points, Activation Function: LogSig												
Training Time [s]		Number of Neurons										
		10	11	12	13	14	15	16	17	18	19	20
Number of Layers	1	1.00	1.10	1.36	1.11	1.89	2.20	2.09	1.01	1.58	2.83	1.10
	2	3.25	1.66	2.33	2.72	4.00	3.07	2.35	2.81	5.35	1.97	3.77
	3	2.74	6.35	4.76	5.58	4.17	2.36	4.88	7.56	7.18	6.55	5.18
	4	2.59	2.29	8.12	6.47	7.17	3.81	7.70	11.46	19.01	12.14	8.92

Key

Table 5.8 Training time of ANN structures with LogSig activation function and 2000 data points

2000 Data Points, Activation Function: LogSig												
Training Time [s]		Number of Neurons										
		10	11	12	13	14	15	16	17	18	19	20
Number of Layers	1	0.90	2.47	1.70	1.74	4.38	2.61	2.49	1.81	4.54	2.58	2.67
	2	6.06	7.19	10.66	13.38	6.20	6.54	6.76	14.61	16.32	7.86	20.32
	3	18.72	13.45	4.55	5.19	21.54	23.88	26.00	25.44	27.50	11.66	19.71
	4	11.49	18.79	16.06	6.69	41.55	30.72	28.04	67.86	14.78	62.17	57.13

Key

Table 5.9 Training time of ANN structures with LogSig activation function and 5000 data points

5000 Data Points, Activation Function: LogSig												Key Time [s]	
Training Time [s]		Number of Neurons										Key Time [s]	
		10	11	12	13	14	15	16	17	18	19	20	
Number of Layers	1	1.74	4.06	3.12	3.24	3.82	3.78	2.11	11.73	3.45	14.25	12.07	0.00
	2	10.86	22.86	37.50	30.99	20.02	19.95	38.09	11.02	48.89	134.95	37.88	10.00
	3	14.53	33.38	34.62	116.81	61.86	57.12	140.49	124.75	228.28	71.22	85.55	100.00
	4	94.66	36.71	139.61	70.20	13.33	229.45	88.24	155.37	217.48	500.54	600.01	600.00

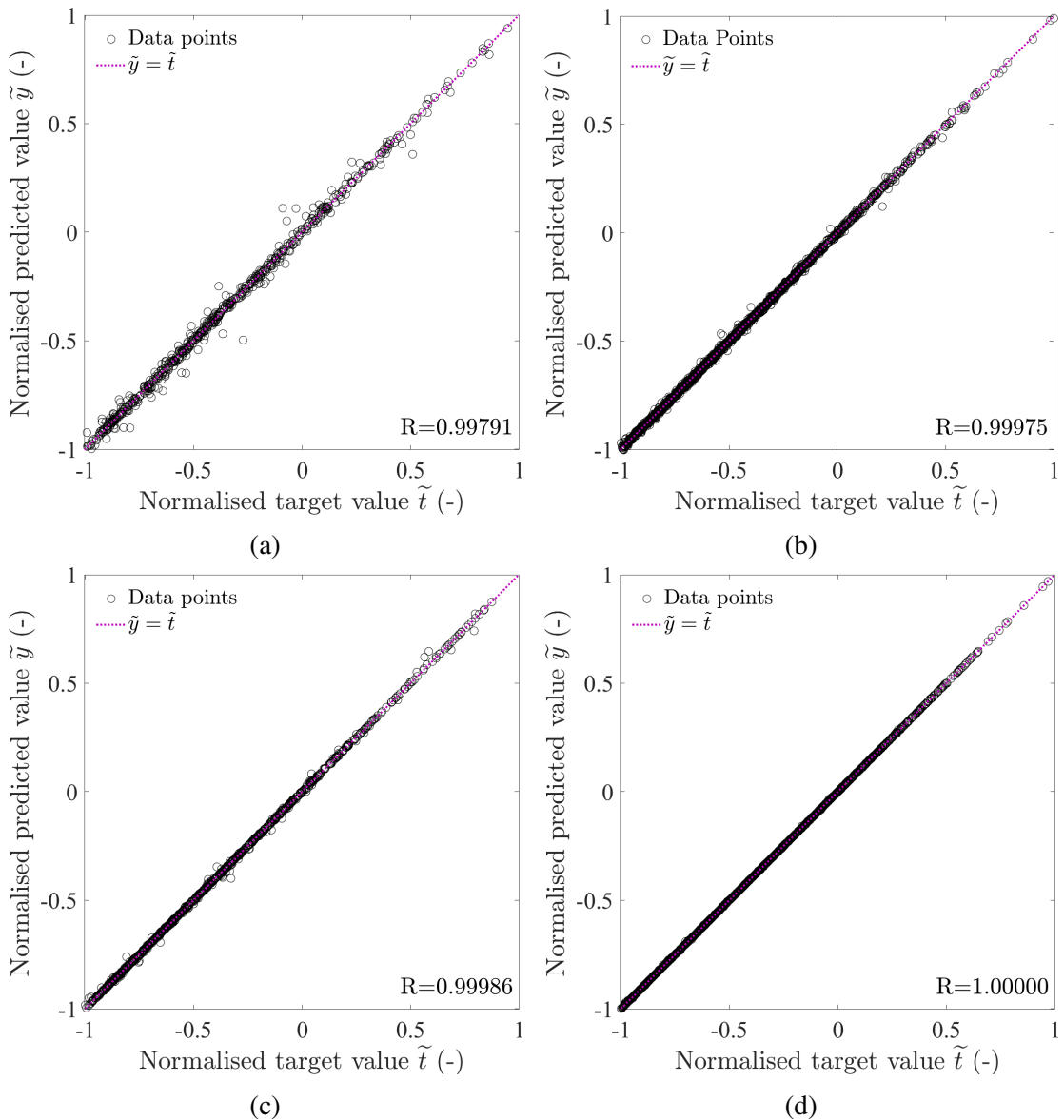


Figure 5.10 R^2 performance of ANN structure ($N=14$, $t=3$) using a Logistic Sigmoid activation function at each hidden layer: a) 600 points, b) 1000 points, c) 2000 points, d) 5000 points.

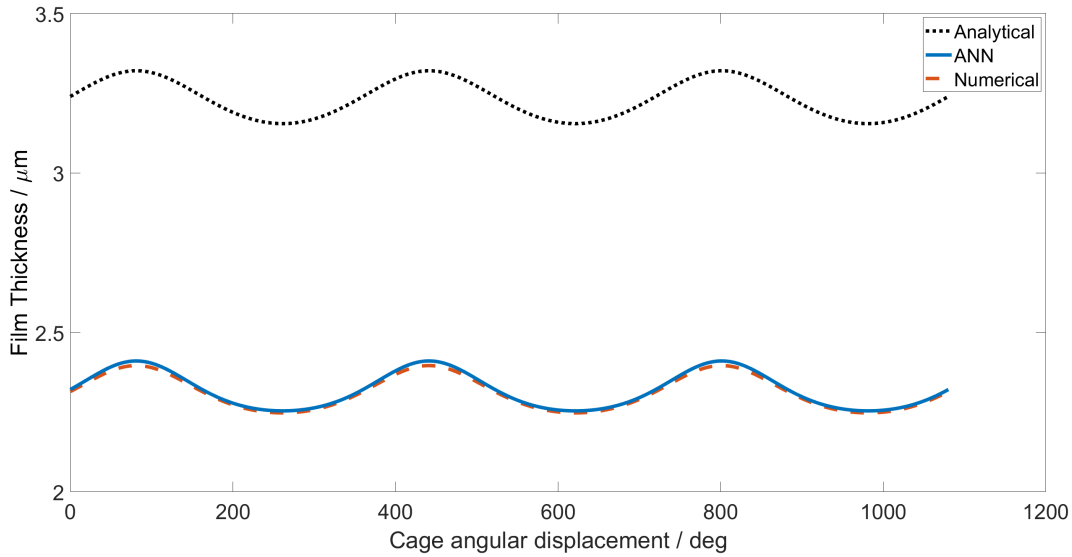


Figure 5.11 ANN, numerical and analytical central film thickness comparisons.

5.5.2 Explicit Bearing Film Thickness Predictions

The performance of the selected ANN was compared to the computed numerical and analytical results during several operating cycles of the bearing model presented in Section 5.4.3.

Figure 5.11 demonstrates that the ANN prediction of film thickness matches very closely with the numerical calculation. The periodic fluctuations arise due to the varying contact load as the roller enters and exits the loaded region. At minimum contact load, the maximum central film thickness is $2.410 \mu\text{m}$ and $2.396 \mu\text{m}$ for the ANN and numerical model respectively. By comparison, the analytical equation overestimates the peak central film thickness to be $3.321 \mu\text{m}$.

Table 5.10 demonstrates the relative performance of the ANN for both computation time and MSE for the analysis in Figure 5.11. The ANN demonstrates a ~ 1570 factor computation time reduction in comparison with the ANN, whilst maintaining excellent accuracy as shown by the MSE. The analytical solution is a factor of ~ 70 faster than the ANN, but is significantly less accurate. This achieved an MSE across the operating cycle of $8.47 \times 10^{-1} \mu\text{m}^2$, compared to the ANN performance of $7.65 \times 10^{-5} \mu\text{m}^2$. As discussed in Section 5.2, the analytical error will increase further with entrainment velocity.

Figure 5.12 demonstrates the accuracy of the ANN prediction across the speed range from 1 000 - 21 000 rpm. Unlike the divergence of the analytical film from the numerical result as entrainment velocities increase, the ANN demonstrates excellent agreement. The MSE across the speed range is $3.18 \times 10^{-4} \mu\text{m}^2$. This proves the effectiveness of this solution across a broad range of operating conditions.

Table 5.10 Film thickness computation methodology performance relative to the numerical solution

Method	Time per point [s]	MSE [μm^2]
Numerical	4.87	-
Analytical	4.43×10^{-5}	8.47×10^{-1}
ANN	3.10×10^{-3}	7.65×10^{-5}

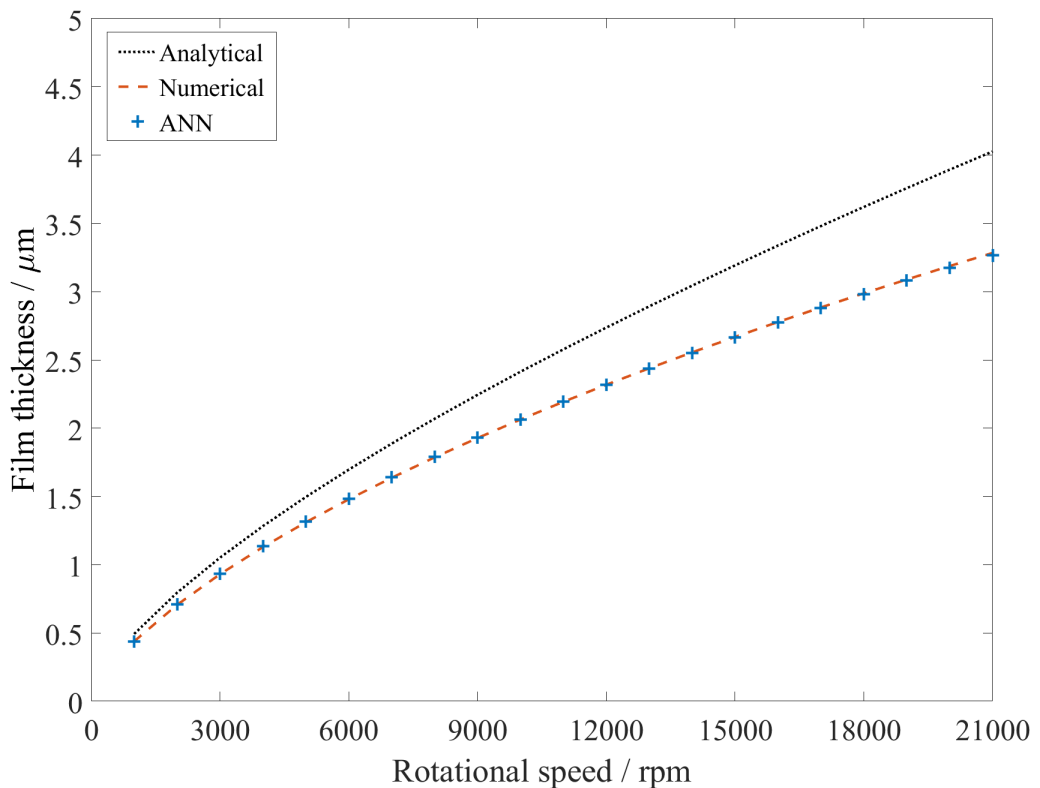


Figure 5.12 Central film thickness - EHL vs ANN vs analytical at increasing shaft rotational speed.

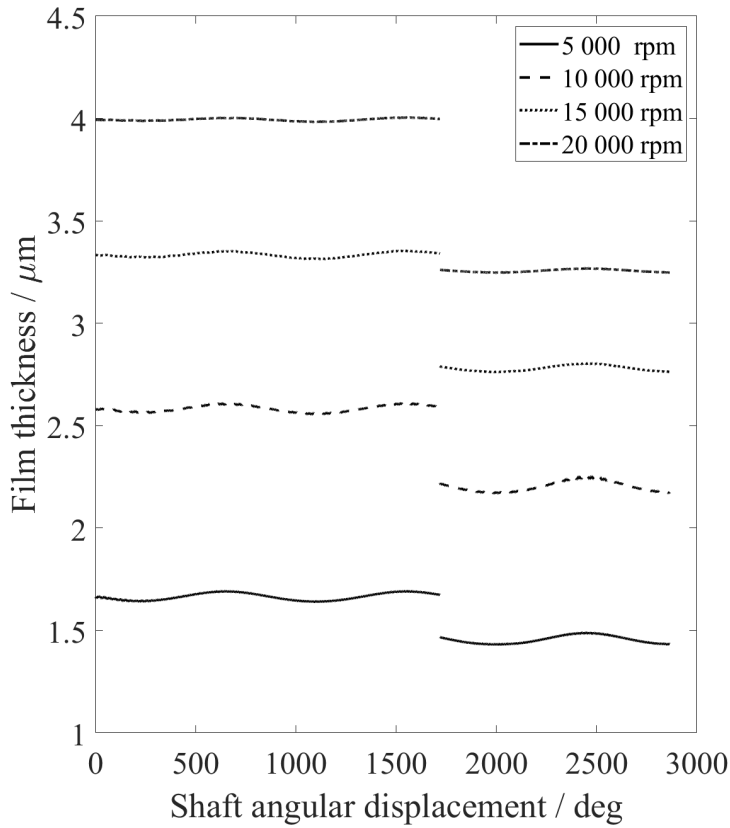


Figure 5.13 ANN vs analytical film thickness at speed intervals from 5 000 - 20 000 *rpm*.

5.5.3 Implicit Bearing Film Thickness Predictions

The central film thickness values at a roller-race contact are shown in Figure 5.13 for each incremental speed condition. The dominating fluctuation frequency corresponds to the rollers entering and exiting the loaded zone of the bearing. The first period, up to a shaft angular displacement of 1 718 *deg*, shows the results obtained from the implicit analytical solution. At this angular position, the method of film prediction is changed to the ANN. The corresponding decrease in central film thickness associated with the change in numerical method is evident. At higher entrainment velocities, the magnitude of the film thickness difference is larger. These are quantified in Table 5.11, and the percentage differences correlate with those presented in Figure 5.12. At 20 000 *rpm*, the ANN film prediction is 0.74 μm lower than the regressed equation.

The computation time for each film thickness methodology is shown graphically in Figure 5.14. Each simulation was run on one CPU, and the CPU time per time step of the simulation was measured. At 1 718 *deg*, the changing gradient of each operating point corresponds to the change of calculation method. The CPU time per angle is higher at lower rotational speeds due to the time-based simulation method, hence the larger gradient for both the analytical and ANN calculation. Table 5.12 presents

Table 5.11 Implicit central film thickness comparison: ANN vs analytical

Speed [rpm]	Central film thickness [μm]		Percentage difference
	ANN	Analytical	
5 000	1.47	1.67	13.2
10 000	2.21	2.59	15.7
15 000	2.79	3.34	18.0
20 000	3.26	4.00	20.3

Table 5.12 Implicit CPU time comparison: ANN vs analytical

Speed [rpm]	CPU time per time step [s]		Relative difference	Factor difference	Mean iterations per time step
	ANN	Analytical			
5 000	0.384	6.28×10^{-3}	1.64×10^{-2}	61.1	2.72
10 000	0.399	6.24×10^{-3}	1.56×10^{-2}	64.0	2.97
15 000	0.367	7.60×10^{-3}	2.06×10^{-2}	48.5	3.56
20 000	0.359	7.40×10^{-3}	2.06×10^{-2}	48.6	3.08

the average CPU time per time step for each method at each speed increment. The largest difference between computation time occurred at 10 000 rpm , and the lowest at 15 000 rpm , corresponding to the ANN being 64.0 and 48.5 times slower than the analytical respectively. The CPU time per time step did not directly correlate with the mean number of iterations per time step. The number iterations for film convergence within the lubricated bearing model accounted for this variability. At 5 000 rpm , the analytical solution took 246.5 s for 20 rad of shaft angular displacement. The ANN took 13 990 s for the same period of rotation. Due the large computation time of the numerical solution (4.87 s per film thickness iteration), it was not computationally viable to embed this within the FMBD model.

5.6 Conclusions

A tribological ANN has been trained and employed to calculate the central EHL film thickness at a roller-race conjunction. Different ANN structures were evaluated to find the optimum structure for the film thickness estimation. Numerically generated training data was sampled using Latin Hypercube Sampling (LHS), and constrained to realistic contact conditions using the Greenwood regime. This ensured a high quality dataset;

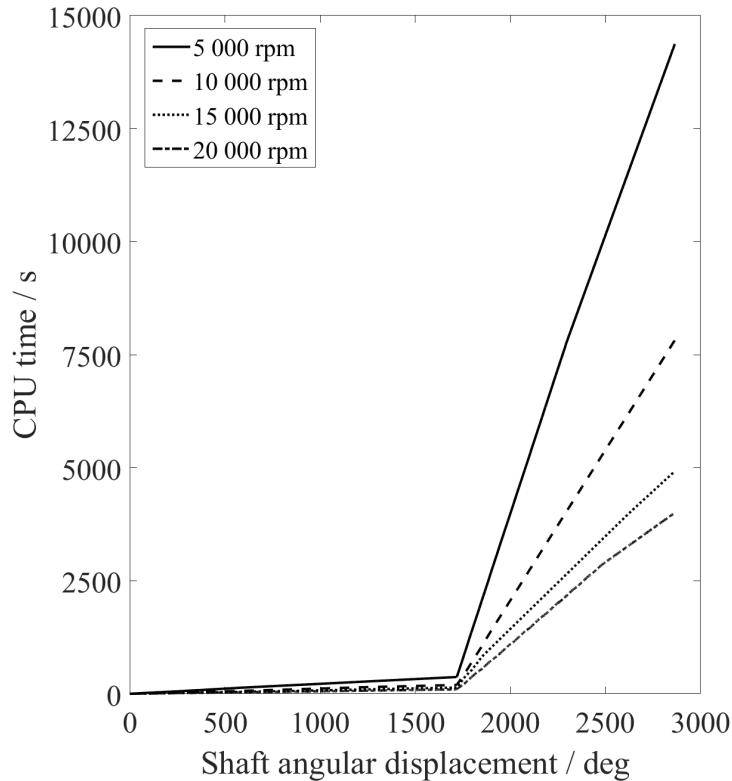


Figure 5.14 ANN vs analytical CPU time per simulation.

essential for high prediction accuracy. The trained ANN was then used to calculate film thickness in a roller bearing explicitly using a simple bearing model under constant load. The ANN was then employed in an FMBD model, where the film thickness was estimated implicitly at each time step of a dynamic simulation and considered in the prevailing contact mechanics. The following conclusions are drawn from this work:

1. Each numerical solution to generate a training data point took 5.88 s. The single core wall time for 600 and 5 000 training points was 58.8 min and 489 min respectively. The numerical solution database could benefit from explicit parallelisation i.e.. use of multiple computational cores of the CPU.
2. 600 training points achieved sufficient coefficient of determination performance ($R^2 = 0.99791$) to accurately predict central film thickness. Whilst 5000 points resulted in an R^2 value of 1, training of the network and effort to generate this quantity of training data rendered it computationally inefficient.
3. An ANN structure with three hidden layers, each containing 14 neurons and using a logistic sigmoid activation function, was found to be optimal for the operating bounds investigated in this study when trained on 2,000 data points.

4. The analytical equations increasingly deviate from the numerical calculation at high entrainment velocities; up to 20.3 % at 21 000 rpm for the bearing examined in this study. At the same speed, the ANN had an error of 1.58 %. Across a speed range from 0 - 21 000 rpm, the MSE of the ANN was $3.18 \times 10^{-4} \mu\text{m}^2$.
5. For the explicit bearing case study, the mean squared error (MSE) of the ANN film thickness prediction was $7.65 \times 10^{-5} \mu\text{m}^2$ when benchmarked against the numerical solution for a fluctuating contact load. This is a significant improvement over the MSE of the analytical model which was $8.47 \times 10^{-1} \mu\text{m}^2$.
6. For the explicit bearing case study, the ANN was shown to be ~ 1570 times faster than the numerical solution with a very small margin of error. The ANN is a factor of ~ 75 times slower than the analytical equation, but a factor of 11×10^4 more accurate when comparing MSE performance against the numerical method.
7. For the implicit study where the ANN was embedded within the FMBD model, the ANN achieved an average of 0.377 s per time step compared to the analytical value of $6.88 \times 10^{-2} \text{ s}$ across the incremental speed range from 5 - 20 000 rpm. The ANN is 54.8 times slower per time step than the analytical solution. However, the accuracy was close to that of the numerical solution, with the analytical equation over predicting the film thickness by 20.3% at 20 000 rpm.
8. The methodology of changing numerical method from analytical to ANN once the FMBD model reached steady-state operating conditions is one that could be employed within future system-level models. It preserves fast computation in the initial system stabilisation, and offers numerical accuracy in the period of results analysis.

This investigation has demonstrated that ANNs provide an accurate and computationally efficient method for predicting EHL central film thickness, despite lacking an inherent physical understanding of the system. Their accuracy and efficiency make them well suited for integration into tribological models within FMBD solvers. Whilst the solution time remains considerably slower than the regressed equations, advancements in this field of research are expected to improve this constraint.

However, a key consideration is the ability of the ANN to extrapolate beyond the bounds of the training data set. Excessive extrapolation may introduce instability to the dynamic solution due to abrupt changes in the contact stiffness. This risk can be mitigated by selecting a sufficient design space and robust sampling method such as LHS to ensure a comprehensive training data set.

Roller bearings are just one application of this trained ANN. Its use cases extend far beyond roller bearings to key components in automotive, machining and other industrial applications where interactions between contiguous surfaces can be approximated as line contacts. Such applications include gears and cams. Many of these machine elements operate within the parameter range that this ANN was trained to, making it a readily deployable solution.

Chapter 6

Conclusions and Future Work

6.1 Overall Conclusions

This thesis has presented investigations into the influence of considering the elastohydrodynamic (EHL) film implicitly at the roller-race conjunction in high-speed rolling element bearing modelling. Experimental studies using a novel test rig have highlighted the influence of the EHL film on contact forces, with measured bearing motion serving as boundary conditions for tribological analyses. A coupled simulation approach was developed, integrating an implicit lubricated bearing model within a system level, flexible multi-body dynamic (FMBD) model. Results at the contact and system levels have been evaluated under high-speed electrified vehicle (EV) operating conditions to compare lubricated and non-lubricated analyses. An artificial neural network (ANN) was trained to predict EHL film thickness across a wide range of bearing geometries, tribological parameters and operating conditions. The ANN was then employed within the coupled simulation as a more accurate alternative to the regressed film thickness equations, with its performance evaluated against numerical and analytical approaches in terms of predictive accuracy and computational efficiency. The following conclusions have been drawn from the results and analyses contained in this research:

1. Experimental and tribological tests were conducted at speeds of up to 15 000 *rpm*, with a radial load of 750 N applied to a shaft-bearing system. The results showed that dry modelling of a roller bearing underestimates the contact load by 149% at 15 000 *rpm*. This discrepancy is attributed to the additional deformation incurred as a result of lubricant entrainment into the EHL contact. The central film thickness increased from 0.1 - 1.9 μm for a quasi-dynamic speed sweep from 0 - 15 000 rpm, leading to an increasing difference in contact load between dry and lubricated modelling with speed. However, at higher bearing loads, such as

during system resonance, the contact load difference reduces to 21% due to the contact deformation predicted by the dry Hertzian assumption closely matching the magnitude of the film ($1.58 \mu\text{m}$ at $14\,134 \text{ rpm}$). This therefore concludes that the most significant difference between these modelling techniques occurs at higher rotational speeds and low load. This matches the operating characteristics and magnitudes of electrified transmissions, and hence the consideration of the film at the roller-race conjunction cannot be neglected in their modelling.

2. To assess the impact of this contact load calculation disparity on bearing dynamics, a coupled simulation approach was developed to integrate a lubricated bearing model within a system-level FMBD model. The approach implicitly considers the influence of the EHL film on the bearing contact mechanics at each time step of the dynamic analysis. Quasi-dynamic simulations were performed up to $21\,000 \text{ rpm}$ using loading conditions from a first stage gear pair coupled to a 54 kW permanent magnet synchronous motor (PMSM) with a peak torque of 68 Nm . Results show that the lubricant film increases contact stiffness by up to 24.9 % at $21\,000 \text{ rpm}$ when compared to conventional dry analyses. This is due to the non-linear force-deflection relationship at the contact. The contribution of the lubricated contact stiffnesses increases the total bearing stiffness by 16.6 %. This total stiffness consequently increases the natural frequency of the system from 3470 Hz to 3542 Hz , corresponding to a 250 rpm increase from the dry estimation at $12\,500 \text{ rpm}$. Implicit inclusion of the film in the analysis was therefore shown to affect the predicted NVH response of the system. The increased bearing stiffness also reduced the total radial displacement of the shaft across the entire speed range.
3. It was demonstrated that the analytical central film thickness equation increasingly deviates from the numerical solution as entrainment velocities increase. At $30.7 \text{ m} \cdot \text{s}^{-1}$, corresponding to $21\,000 \text{ rpm}$ in the bearings under investigation, it was shown to overestimate the film thickness by 20.3%.
4. An ANN was trained using a broad value range of tribological input data to predict EHL central film thickness. The training input data was constrained using the Greenwood regimes of lubrication, improving data cloud point density and achieving a coefficient of determination (R^2) of 0.99791 and 0.99986 with just 600 and 2 000 data points respectively.
5. In a static bearing model, the central film thickness for entrainment velocities of $1.53 - 30.7 \text{ m} \cdot \text{s}^{-1}$ were predicted by the trained ANN. Unlike the 20.3%

over-prediction of the central film using the analytical equations, the ANN under predicted the film by just 1.58% at 21 000 *rpm*, having a mean squared error (MSE) of just $3.18 \times 10^{-4} \mu\text{m}^2$ across the speed range. Static operating points with time-varying contact loads were also investigated at 10 000 *rpm*. Across the loading cycle, the mean squared error (MSE) of the ANN film thickness prediction was $7.65 \times 10^{-5} \mu\text{m}^2$ when benchmarked against the numerical solution for a fluctuating contact load. This is a significant improvement over the MSE of the analytical model which was $8.47 \times 10^{-1} \mu\text{m}^2$.

6. In the static bearing model, the ANN was shown to be ~ 1 570 times faster than the numerical solution with a very small margin of error when tested across 750 data points spanning a large value range of film thickness input variables. The ANN is a factor of ~ 75 times slower than the analytical equation, but a factor of 11×10^4 more accurate when comparing MSE performance of both against the numerical method.
7. The ANN was embedded within the aforementioned FMBD system model to calculate EHL film thickness and consider it implicitly in the evaluation of the bearing dynamics. The ANN achieved an average of 0.377 s per time step compared to the analytical value of $6.88 \times 10^{-2} \text{ s}$ across the incremental speed range from 5 - 20 000 *rpm*. The ANN is 54.8 times slower per time step than the analytical solution. However, the accuracy matched that of the static bearing test models, with the analytical equation over predicting the film thickness by 20.3% at 20 000 *rpm*. This investigation proved the effectiveness of ANNs for film thickness estimations, and established a workflow that will further enhance contact modelling in FMBD simulations.

6.2 Contributions to Knowledge

The main novelties and contributions to knowledge from this thesis are summarised below:

1. A novel experimental test rig was designed and constructed to measure the kinematic motion of a bearing at rotational speeds and loads up to 750 *N* and 15 000 *rpm* respectively. The bearing orbital motion was measured and used for conjunction and component level tribological analysis. The methodology of coupling experimental test with numerical tribological models has not been previously reported in this manner at these speeds. The outcome of this demonstrated the requirement of implicitly modelling the EHL film in future high-speed

applications, since it contributed to a 149% contact load increase at 15 000 *rpm* when compared to conventional dry analyses.

2. A coupled co-simulation approach was established to implicitly consider the EHL film in roller bearings within a high-speed system-level FMBD model. The model, consisting of a flexible shaft and rigid housing, replicates the operating conditions of a 54 kW permanent magnet synchronous motor (PMSM) coupled to a first stage gear pair, operating at speeds up to 21 000 *rpm*. This was the first time in open literature that an implicitly lubricated multi-physics bearing model has been considered in the context of electrified powertrain dynamics. The outcome of this demonstrated that the increased contact deflection, due to the lubricant film inclusion, increases total bearing stiffness by 24.9 % at 21 000 rpm. This effectively behaves as a non-linear, speed dependant radial preload on the bearing. The contribution of this stiffness increased the natural frequency of the system, and hence affected NVH response. This proves the requirement to consider the EHL film implicitly for rolling element bearing modelling under the high speed, low load operating conditions of electrified powertrains.
3. An ANN was trained to predict EHL central film thickness with input data calculated using a 1D numerical EHL model. A wide value range of input variables necessary for the EHL calculation were used to train the model. The value range was consistent with common machine element contacts, with its applicability also extending to gear pairs and cam contacts. The novel methodology of constraining the training data using the Greenwood regime ensured high data quality whilst only requiring 2 000 training data points. The ANN achieved an MSE of $7.65 \times 10^{-5} \mu\text{m}^2$ when benchmarked against the numerical solution, whilst reducing calculation time by a factor of 1 570. This methodology will further contribute to the computational efficiency and accuracy of tribological ANNs.
4. The ANN was embedded within an FMBD system-level model to calculate EHL film thickness and consider it implicitly in the evaluation of the bearing and system dynamics. The film thickness evaluation achieves the accuracy of the numerical model without the associated computational limitations. This modelling method of combining a component level tribological ANN within an FMBD system-level model has not been previously reported.

6.3 Addressing the Research Questions

The primary objective of this work was to investigate the interaction between tribology and dynamics in rolling element bearings, with particular focus on the significance of this multi-physics interaction in high-speed automotive applications. On reviewing the conclusions drawn from this thesis, it can be demonstrated that the research questions presented in Section 1.1 have been addressed.

The findings of this thesis are to be implemented into the commercial software AVL EXCITE™ M and AVL EXCITE™ Power Unit to support future rolling element bearing development. The influence of the lubricant film in dynamic analysis is of particular interest. The workflow of coupling contact level artificial neural networks into system level FMBD models is also of significance. This approach has applications beyond rolling element bearings, as a generic contact approach could also improve non-conformal contact modelling for gears and cams.

6.4 Future Work

The novel approaches presented in this thesis open up further opportunities to advance this area of research. These include:

- For wider adoption of the ANN solution, the ability to extrapolate beyond the bounds of the training data must be addressed. Extrapolation errors in the film thickness estimation could yield unrealistic film thickness values, introducing potential impulses to the dynamic system. This could affect the stability of an FMBD model and lead to divergence.
- Develop a computationally efficient methodology for integrating ANNs into FMBD software. A suggested approach is to train the model using known input variables and kinematic conditions in a first stage static analysis. This trained model could then be called at each time step of the dynamic simulation. Alternatively, a library of trained models could be established using the Greenwood regime constraints outlined in this work.
- Expand the training data set for the ANN to include experimental measurements from high-speed mini traction machines. This would provide experimentally validated training data to further improve the accuracy of predictive FMBD tools.

References

- [1] European Parliament and of the Council of 19 April 2023, “Regulation (eu) 2023/851,” pp. 1–19, 4 2023.
- [2] W. Cai, X. Wu, M. Zhou, Y. Liang, and Y. Wang, “Review and development of electric motor systems and electric powertrains for new energy vehicles,” *Automotive Innovation*, vol. 4, pp. 3–22, 2021. [Online]. Available: <https://doi.org/10.1007/s42154-021-00139-z>
- [3] T. A. Harris and M. N. Kotzalas, *Essential Concepts of Bearing Technology*, 5th ed. Taylor and Francis Group, 2007.
- [4] R. Stribeck, “Ball bearings for various loads,” *Trans. ASME*, vol. 29, pp. 420–463, 1907.
- [5] G. Lundberg and A. Palmgren, “Dynamic capacity of roller bearings,” *Acta Polytechnica; Mechanical Engineering Series, Royal Swedish Academy of Engineering Sciences*, vol. 2, pp. 96–127, 1952.
- [6] A. Palmgren, *Ball and Roller Bearing Engineering*, 3rd ed. SKF Industries, 1959.
- [7] A. B. Jones, “A general theory for elastically constrained ball and radial roller bearings under arbitrary load and speed conditions,” *Journal of Fluids Engineering, Transactions of the ASME*, vol. 82, pp. 309–320, 1960.
- [8] T. Harris, *Roller Bearing Analysis*, 5th ed. CRC Press, 11 2006.
- [9] H. Sjovall, “The load distribution within ball and roller bearings under given external radial and axial load,” *Teknisk Tidskrift, Mek.*, vol. 9, 1933.
- [10] J. Rumbarger, “Thurst bearings with eccentric loads,” *Mach des.*, pp. 172–179, 1962.

- [11] S. Andréason, “Load distribution in a taper roller bearing arrangement considering misalignment,” *Tribology*, vol. 6, pp. 84–92, 6 1973. [Online]. Available: <https://linkinghub.elsevier.com/retrieve/pii/0041267873902418>
- [12] J. Y. Liu, “Analysis of tapered roller bearings considering high speed and combined loading.” *American Society of Mechanical Engineers*, pp. 564–572, 1976.
- [13] J. M. de Mul, J. M. Vree, and D. A. Maas, “Equilibrium and associated load distribution in ball and roller bearings loaded in five degrees of freedom while neglecting friction—part ii: Application to roller bearings and experimental verification,” *Journal of Tribology*, vol. 111, pp. 149–155, 1 1989. [Online]. Available: <https://asmedigitalcollection.asme.org/tribology/article/111/1/149/432349/Equilibrium-and-Associated-Load-Distribution-in>
- [14] B. R. Jorgensen and Y. C. Shin, “Dynamics of machine tool spindle/bearing systems under thermal growth,” *Journal of Tribology*, vol. 119, pp. 875–882, 1997.
- [15] J. M. de Mul, J. M. Vree, and D. A. Maas, “Equilibrium and associated load distribution in ball and roller bearings loaded in five degrees of freedom while neglecting friction—part i: General theory and application to ball bearings,” *Journal of Tribology*, vol. 111, pp. 142–148, 1 1989. [Online]. Available: <https://asmedigitalcollection.asme.org/tribology/article/111/1/142/432329/Equilibrium-and-Associated-Load-Distribution-in>
- [16] J. Sopanen and A. Mikkola, “Dynamic model of a deep-groove ball bearing including localized and distributed defects. part 1: Theory,” *Proceedings of the Institution of Mechanical Engineers, Part K: Journal of Multi-body Dynamics*, vol. 217, pp. 201–211, 9 2003. [Online]. Available: <http://journals.sagepub.com/doi/10.1243/14644190360713551>
- [17] C. T. Walters, “The dynamics of ball bearings,” *Journal of Tribology*, vol. 93, pp. 1–10, 1971.
- [18] L. D. Meyer, F. F. Ahlgren, and B. Weichbrodt, “An analytic model for ball bearing vibrations to predict vibration response to distributed defects,” *Journal of Mechanical Design*, vol. 102, pp. 205–210, 4 1980. [Online]. Available: <https://asmedigitalcollection.asme.org/mechanicaldesign/article/102/2/205/430940/An-Analytic-Model-for-Ball-Bearing-Vibrations-to>

- [19] C. S. Sunnersjö, “Varying compliance vibrations of rolling bearings,” *Journal of Sound and Vibration*, vol. 58, pp. 363–373, 1978.
- [20] M. Matsubara, H. Rahnejat, and R. Gohar, “Computational modelling of precision spindles supported by ball bearings,” *International Journal of Machine Tools and Manufacture*, vol. 28, pp. 429–442, 1988. [Online]. Available: [http://dx.doi.org/10.1016/0890-6955\(88\)90056-9](http://dx.doi.org/10.1016/0890-6955(88)90056-9)
- [21] P. K. Gupta, “Dynamics of rolling-element bearings—part i: Cylindrical roller bearing analysis,” *Journal of Lubrication Technology*, vol. 101, pp. 293–302, 7 1979. [Online]. Available: <https://asmedigitalcollection.asme.org/tribology/article/101/3/305/410221/Dynamics-of-RollingElement-BearingsPart-IIhttps://asmedigitalcollection.asme.org/tribology/article/101/3/293/410262/Dynamics-of-RollingElement-BearingsPart-I>
- [22] R. Aini, H. Rahnejat, and R. Gohar, “A five degrees of freedom analysis of vibrations in precision spindles,” *International Journal of Machine Tools and Manufacture*, vol. 30, pp. 1–18, 1990.
- [23] H. Rahnejat and S. Rothberg, *Mulit-body dynamics: Monitoring and simulation techniques III*, 1st ed. Wiley, 2004.
- [24] H. Questa, M. Mohammadpour, S. Theodossiades, C. Garner, S. Bewsher, and G. Offner, “Tribo-dynamic analysis of high-speed roller bearings for electrified vehicle powertrains,” *Tribology International*, vol. 154, p. 106675, 2 2021. [Online]. Available: <https://linkinghub.elsevier.com/retrieve/pii/S0301679X20305004>
- [25] B. J. Stone, “The state of the art in the measurement of the stiffness and damping of rolling element bearings,” *CIRP Annals - Manufacturing Technology*, vol. 31, pp. 529–538, 1982.
- [26] P. Dietl, “Damping and stiffness characteristics of rolling element bearings-theory and experiment,” Ph.D. dissertation, 1997.
- [27] L. Bizarre, F. Nonato, and K. Cavalca, “Formulation of five degrees of freedom ball bearing model accounting for the nonlinear stiffness and damping of elastohydrodynamic point contacts,” *Mechanism and Machine Theory*, vol. 124, pp. 179–196, 6 2018. [Online]. Available: <https://linkinghub.elsevier.com/retrieve/pii/S0094114X1830106X>

- [28] H. Rahnejat and R. Gohar, “The vibrations of radial ball bearings,” *Proceedings of the Institution of Mechanical Engineers, Part C: Journal of Mechanical Engineering Science*, vol. 199, pp. 181–193, 1985.
- [29] R. Aini, H. Rahnejat, and R. Gohar, “Vibration modeling of rotating spindles supported by lubricated bearings,” *Journal of Tribology*, vol. 124, pp. 158–165, 2002.
- [30] M. Mohammadpour, P. Johns-Rahnejat, and H. Rahnejat, “Roller bearing dynamics under transient thermal-mixed non-newtonian elastohydrodynamic regime of lubrication,” *Proceedings of the Institution of Mechanical Engineers, Part K: Journal of Multi-body Dynamics*, vol. 229, pp. 407–423, 12 2015. [Online]. Available: <https://doi.org/10.1177/1464419315569621http://journals.sagepub.com/doi/10.1177/1464419315569621>
- [31] J. Sopanen and A. Mikkola, “Dynamic model of a deep-groove ball bearing including localized and distributed defects. part 2: Implementation and results,” *Proceedings of the Institution of Mechanical Engineers, Part K: Journal of Multi-body Dynamics*, vol. 217, pp. 213–223, 9 2003. [Online]. Available: <http://journals.sagepub.com/doi/10.1243/14644190360713560>
- [32] N. Sawalhi and R. B. Randall, “Simulating gear and bearing interactions in the presence of faults. part i. the combined gear bearing dynamic model and the simulation of localised bearing faults,” *Mechanical Systems and Signal Processing*, vol. 22, pp. 1924–1951, 2008.
- [33] J. Liu and Y. Shao, “Vibration modelling of nonuniform surface waviness in a lubricated roller bearing,” *JVC/Journal of Vibration and Control*, vol. 23, pp. 1115–1132, 2017.
- [34] F. Nonato and K. L. Cavalca, “An approach for including the stiffness and damping of elastohydrodynamic point contacts in deep groove ball bearing equilibrium models,” *Journal of Sound and Vibration*, vol. 333, pp. 6960–6978, 2014. [Online]. Available: <http://dx.doi.org/10.1016/j.jsv.2014.08.011>
- [35] R. Gohar and H. Rahnejat, *Fundamentals of Tribology*, 3rd ed. World Scientific Publishing Europe Ltd., 2019.
- [36] K. L. Johnson, *Contact Mechanics*. Cambridge University Press, 1985.

- [37] E. V. Zaretsky, “Rolling bearing life prediction, theory, and application,” *NASA/TP—2013-215305/REV1*, 2016. [Online]. Available: <https://ntrs.nasa.gov/api/citations/20160013905/downloads/20160013905.pdf>
- [38] H. Hertz, “On the contact of elastic solids,” *J. Reine Angew. Math.*, vol. 92, pp. 156–171, 1881.
- [39] S. Kabus, M. R. Hansen, and O. Mouritzen, “A new quasi-static cylindrical roller bearing model to accurately consider non-hertzian contact pressure in time domain simulations,” *Journal of Tribology*, vol. 134, pp. 1–10, 2012.
- [40] R. Teutsch and B. Sauer, “An alternative slicing technique to consider pressure concentrations in non-Hertzian line contacts,” *Journal of Tribology*, vol. 126, pp. 436–442, 2004.
- [41] O. Reynolds, “On the theory of lubrication and its application to Mr. Lowe’s experiments,” *Philosophical Transactions of the Royal Society of London*, vol. 177, pp. 157–234, 1886. [Online]. Available: https://scholar.google.com/scholar?q=related:zTMHxIMaYncJ:scholar.google.com/&hl=en&as_sdt=0,39&as_ylo=1886&as_yhi=1886#0
- [42] H. M. Martin, “Lubrication of gear teeth,” *Engineering (London)*, vol. 102, pp. 119–121, 1916.
- [43] W. Peppler, “Untersuchung über die druckübertragung bei belasteten und geschmierten umlaufenden achsparallelen zylindern,” *Maschinenelemente-Tagung*, vol. 42, 1936.
- [44] A. Meldahl, “Contribution to theory of lubrication of gears and of stressing of lubricated flanks of gear teeth,” *Brown Boveri Review*, vol. 28, pp. 374–382, 1941.
- [45] E. K. Gatcombe, “Lubrication characteristics of involute spur gears—a theoretical investigation,” *Trans. ASME*, vol. 67, pp. 177–185, 1945.
- [46] A. N. Grubin, *Fundamentals of the Hydrodynamic Theory of Lubrication of Heavily Loaded Cylindrical Surfaces*, 3rd ed. Central Scientific Research Institute for Technology and Mechanical Engineering, 1949.
- [47] A. I. Petrusovich, “Fundamental conclusion from the contact-hydrodynamic theory of lubrication,” *Izv. Akad. Nauk. SSSR (OTN)*, vol. 2, p. 209, 1951.

- [48] D. Dowson and G. R. Higginson, “A numerical solution to the elastohydrodynamic problem,” *Journal of Mechanical Engineering Science*, vol. 1, pp. 6–15, 1959.
- [49] D. Dowson and G. Higginson, “New roller bearing lubrication formula,” *Engineering*, pp. 158–159, 1961.
- [50] D. Dowson and G. R. Higginson, *Elastohydrodynamic Lubrication*. Pergamon, 1966.
- [51] D. Dowson and S. Toyoda, “A central film thickness formula for elastohydrodynamic line contacts,” *Proceedings of the Fifth Leeds-Lyon Symposium on Tribology, Mechanical Engineering Publications*, pp. 60–65, 1978.
- [52] A. M. Ertel, “Hydrodynamic lubrication based on new principles,” *Akad. Nauk SSSR Prikadnaya Mathematica i Mekhanika*, vol. 3, pp. 41–52, 1939.
- [53] H. P. Evans and R. W. Snidle, “Elastohydrodynamic lubrication of point contacts at heavy loads.” *Proceedings of The Royal Society of London, Series A: Mathematical and Physical Sciences*, vol. 382, pp. 183–199, 1982.
- [54] B. J. Hamrock and B. O. Jacobson, “Elastohydrodynamic lubrication of line contacts,” *ASLE Transactions*, vol. 27, pp. 275–287, 1984.
- [55] B. J. Hamrock and D. Dowson, “Isothermal elastohydrodynamic lubrication of point contacts - 1. Theoretical formulation.” *J Lubr Technol Trans ASME*, vol. 98 Ser F, pp. 223–229, 1976.
- [56] R. J. Chittenden, D. Dowson, J. F. Dunn, and C. M. Taylor, “Theoretical analysis of the isothermal elastohydrodynamic lubrication of concentrated contacts. i. Direction of lubricant entrainment coincident with the major axis of the hertzian contact ellipse.” *Proceedings of The Royal Society of London, Series A: Mathematical and Physical Sciences*, vol. 397, pp. 245–269, 1985.
- [57] H. Okamura, *A contribution to the numerical analysis of isothermal elastohydrodynamic lubrication*. Elsevier, 1983, pp. 313–320.
- [58] L. G. Houptert and B. J. Hamrock, “Fast approach for calculating film thicknesses and pressures in elastohydrodynamically lubricated contacts at high loads.” *Journal of Tribology*, vol. 108, pp. 411–419, 1986.

- [59] A. A. Lubrecht, W. E. T. Napel, and R. Bosma, “Multigrid, an alternative method for calculating film thickness and pressure profiles in elastohydrodynamically lubricated line contacts,” *Journal of Tribology*, vol. 108, pp. 551–556, 1986.
- [60] C. H. Venner, W. E. ten Napel, and R. Bosma, “Advanced multilevel solution of the EHL line contact problem,” *Journal of Tribology*, vol. 112, pp. 426–431, 7 1990. [Online]. Available: <https://asmedigitalcollection.asme.org/tribology/article/112/3/426/435217/Advanced-Multilevel-Solution-of-the-EHL-Line>
- [61] F. Chevalier, A. A. Lubrecht, P. M. E. Cann, F. Colin, and G. Dalmaz, “Starvation phenomena in EHL point contacts: Influence of inlet flow distribution,” *Proceedings of 22nd Leeds-Lyon Symposium on Tribology, Elseviers Tribology Series*, vol. 31, pp. 213–233, 1995.
- [62] P. M. Lutz and G. E. Morales-Espejel, “A review of elasto-hydrodynamic lubrication theory,” *Tribology Transactions*, vol. 54, pp. 470–496, 3 2011. [Online]. Available: <http://www.tandfonline.com/doi/abs/10.1080/10402004.2010.551804>
- [63] P. E. Wolveridge, K. P. Baglin, and J. F. Archard, “The starved lubrication of cylinders in line contact,” *Proceedings of the Institution of Mechanical Engineers*, vol. 185, pp. 1159–1169, 6 1970. [Online]. Available: http://journals.sagepub.com/doi/10.1243/PIME_PROC_1970_185_126_02
- [64] B. J. Hamrock and D. Dowson, “Isothermal elastohydrodynamic lubrication of point contacts - 4. Starvation results.” *American Society of Mechanical Engineers (Paper)*, pp. 223–228, 1976.
- [65] P. Yang, S. Qu, Q. Chang, and F. Guo, “On the theory of thermal elastohydrodynamic lubrication at high slide-roll ratios - line contact solution,” *Journal of Tribology*, vol. 123, pp. 36–41, 2001.
- [66] K. H. Kim and F. Sadeghi, “Three-dimensional temperature distribution in EHD lubrication: Part i - Circular contact,” *Journal of Tribology*, vol. 114, pp. 32–41, 1 1992. [Online]. Available: <https://asmedigitalcollection.asme.org/tribology/article/114/1/32/435058/ThreeDimensional-Temperature-Distribution-in-EHD>
- [67] K. H. Kim and F. Sadeghi, “Three-dimensional temperature distribution in EHD lubrication: Part ii - Point contact and numerical formulation,”

- Journal of Tribology*, vol. 115, pp. 36–45, 1 1993. [Online]. Available: <https://asmedigitalcollection.asme.org/tribology/article/115/1/36/435348/ThreeDimensional-Temperature-Distribution-in-EHD>
- [68] X. Liu and P. Yang, “Analysis of the thermal elastohydrodynamic lubrication of a finite line contact,” *Tribology International*, 2002.
- [69] D. Zhu and S. zhu Wen, “A full numerical solution for the thermoelastohydrodynamic problem in elliptical contacts,” *Journal of Tribology*, vol. 106, pp. 246–254, 4 1984. [Online]. Available: <https://asmedigitalcollection.asme.org/tribology/article/106/2/246/435892/A-Full-Numerical-Solution-for-the>
- [70] W. Habchi, D. Eyheramendy, S. Bair, P. Vergne, and G. Morales-Espejel, “Thermal elastohydrodynamic lubrication of point contacts using a newtonian,” *Tribology Letters*, pp. 41–52.
- [71] R. Larsson, *EHL Film Thickness Behavior*. Springer US, 2013, pp. 817–827. [Online]. Available: http://link.springer.com/10.1007/978-0-387-92897-5_639
- [72] Y. H. Ali, R. A. Rahman, and R. I. R. Hamzah, “Artificial neural network model for monitoring oil film regime in spur gear based on acoustic emission data,” *Shock and Vibration*, vol. 2015, 2015.
- [73] I. Argatov, “Artificial neural networks (ANNs) as a novel modeling technique in tribology,” *Frontiers in Mechanical Engineering*, vol. 5, pp. 1–9, 2019.
- [74] E. O. Ezugwu, S. J. Arthur, and E. L. Hines, “Tool-wear prediction using artificial neural networks,” *Journal of Materials Processing Tech.*, vol. 49, pp. 255–264, 1995.
- [75] K. L. Rutherford, P. W. Hatto, C. Davies, and I. M. Hutchings, “Abrasive wear resistance of tin/nbn multi-layers: Measurement and neural network modelling,” *Surface and Coatings Technology*, vol. 86-87, pp. 472–479, 1996.
- [76] S. P. Jones, R. Jansen, and R. L. Fusaro, “Preliminary investigation of neural network techniques to predict tribological properties,” *Tribology Transactions*, vol. 40, pp. 312–320, 1997.
- [77] Z. Zhang, K. Friedrich, and K. Velten, “Prediction on tribological properties of short fibre composites using artificial neural networks,” *Wear*, vol. 252, pp. 668–675, 2002.

- [78] K. Genel, S. C. Kurnaz, and M. Durman, “Modeling of tribological properties of alumina fiber reinforced zinc-aluminum composites using artificial neural network,” *Materials Science and Engineering A*, vol. 363, pp. 203–210, 2003.
- [79] M. Hayajneh, A. M. Hassan, A. Alrashdan, and A. T. Mayyas, “Prediction of tribological behavior of aluminum-copper based composite using artificial neural network,” *Journal of Alloys and Compounds*, vol. 470, pp. 584–588, 2009.
- [80] L. Cavaleri, P. G. Asteris, P. P. Psyllaki, M. G. Douvika, A. D. Skentou, and N. M. Vaxevanidis, “Prediction of surface treatment effects on the tribological performance of tool steels using artificial neural networks,” *Applied Sciences (Switzerland)*, vol. 9, 2019.
- [81] S. Bhaumik, S. D. Pathak, S. Dey, and S. Datta, “Artificial intelligence based design of multiple friction modifiers dispersed castor oil and evaluating its tribological properties,” *Tribology International*, vol. 140, p. 105813, 2019.
- [82] J. E. Otero, E. de la Guerra Ochoa, E. C. Tanarro, P. L. Morgado, A. D. Lantada, J. M. Munoz-Guijosa, and J. L. M. Sanz, “Artificial neural network approach to predict the lubricated friction coefficient,” *Lubrication Science*, vol. 26, pp. 141–162, 4 2014. [Online]. Available: <https://onlinelibrary.wiley.com/doi/10.1002/ls.1238>
- [83] M. Afrand, K. N. Najafabadi, N. Sina, M. R. Safaei, A. Kherbeet, S. Wongwises, and M. Dahari, “Prediction of dynamic viscosity of a hybrid nano-lubricant by an optimal artificial neural network,” *International Communications in Heat and Mass Transfer*, vol. 76, pp. 209–214, 8 2016. [Online]. Available: <https://linkinghub.elsevier.com/retrieve/pii/S0735193316301610>
- [84] M. H. Esfe, H. Rostamian, S. Esfandeh, and M. Afrand, “Modeling and prediction of rheological behavior of al₂o₃-mwcnt/5w50 hybrid nano-lubricant by artificial neural network using experimental data,” *Physica A: Statistical Mechanics and its Applications*, vol. 510, pp. 625–634, 2018.
- [85] S. Panda, D. Chakraborty, and S. Pal, “Flank wear prediction in drilling using back propagation neural network and radial basis function network,” *Applied Soft Computing*, vol. 8, pp. 858–871, 3 2008. [Online]. Available: <https://linkinghub.elsevier.com/retrieve/pii/S1568494607000762>

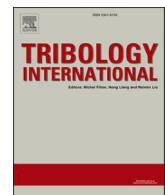
- [86] I. Asiltürk and M. Çunkaş, “Modeling and prediction of surface roughness in turning operations using artificial neural network and multiple regression method,” *Expert Systems with Applications*, vol. 38, pp. 5826–5832, 2011.
- [87] J. G. A. Barbedo, “Impact of dataset size and variety on the effectiveness of deep learning and transfer learning for plant disease classification,” *Computers and Electronics in Agriculture*, vol. 153, pp. 46–53, 10 2018. [Online]. Available: <https://linkinghub.elsevier.com/retrieve/pii/S0168169918304617>
- [88] N. Wang and C. M. Tsai, “Assessment of artificial neural network for thermohydrodynamic lubrication analysis,” *Industrial Lubrication and Tribology*, vol. 72, pp. 1233–1238, 2020.
- [89] A. Senatore and S. Ciortan, “An application of artificial neural networks to piston ring friction losses prediction,” *Mechanical Testing and Diagnosis*, vol. 1, pp. 7–14, 2011.
- [90] L. Gorasso and L. Wang, “Journal bearing optimization using nonsorted genetic algorithm and artificial bee colony algorithm,” *Advances in Mechanical Engineering*, vol. 6, p. 213548, 1 2014. [Online]. Available: <http://journals.sagepub.com/doi/10.1155/2014/213548>
- [91] A. Almqvist, “Fundamentals of physics-informed neural networks applied to solve the reynolds boundary value problem,” *Lubricants*, vol. 9, p. 82, 8 2021. [Online]. Available: <https://www.mdpi.com/2075-4442/9/8/82>
- [92] M. Marian, J. Mursak, M. Bartz, F. J. Profito, A. Rosenkranz, and S. Wartzack, “Predicting EHL film thickness parameters by machine learning approaches,” *Friction*, 6 2022. [Online]. Available: <https://link.springer.com/10.1007/s40544-022-0641-6>
- [93] Y. Guo and J. Keller, “Validation of combined analytical methods to predict slip in cylindrical roller bearings,” *Tribology International*, vol. 148, p. 106347, 2020. [Online]. Available: <https://doi.org/10.1016/j.triboint.2020.106347>
- [94] R. Gohar, *Elastohydrodynamics*. Imperial College Press, 1988.
- [95] M. Denni, N. Biboulet, V. Abousleiman, and A. A. Lubrecht, “Dynamic study of a roller bearing in a planetary application considering the hydrodynamic lubrication of the roller/cage contact,” *Tribology International*, vol. 149, p. 105696, 2019. [Online]. Available: <https://doi.org/10.1016/j.triboint.2019.03.054>

- [96] T. L. H. Walford and B. J. Stone, “The sources of damping in rolling element bearings under oscillating conditions,” *Proceedings of the Institution of Mechanical Engineers, Part C: Journal of Mechanical Engineering Science*, vol. 197, pp. 225–232, 10 1983. [Online]. Available: http://journals.sagepub.com/doi/10.1243/PIME_PROC_1983_197_102_02
- [97] D. W. Dareing and K. L. Johnson, “Fluid film damping of rolling contact vibrations,” *Journal of Mechanical Engineering Science*, vol. 17, pp. 214–218, 8 1975. [Online]. Available: http://journals.sagepub.com/doi/10.1243/JMES_JOUR_1975_017_031_02
- [98] H. Mehdigoli, H. Rahnejat, and R. Gohar, “Vibration response of wavy surfaced disc in elastohydrodynamic rolling contact,” *Wear*, vol. 139, pp. 1–15, 1990.
- [99] R. Takeda, G. Lisco, T. Fujisawa, L. Gastaldi, H. Tohyama, and S. Tadano, “Drift removal for improving the accuracy of gait parameters using wearable sensor systems,” *Sensors*, vol. 14, pp. 23 230–23 247, 12 2014. [Online]. Available: <http://www.mdpi.com/1424-8220/14/12/23230>
- [100] B. J. Hamrock and D. Dowson, *Ball Bearing Lubrication: The Elastohydrodynamics of Elliptical Contacts*. John Wiley and Sons, 1981.
- [101] H. Rahnejat, “Influence of vibration on the oil film in concentrated contacts,” Ph.D. dissertation, 1984.
- [102] K. A. Hoffmann and S. T. Chiang, *Computational Fluid Dynamics*, 4th ed. Engineering Education System, 2000.
- [103] C. Barus, “Isothermals isopietics and isometrics in relationship to viscosity,” *American Journal of Science 3rd Series*, vol. 45, pp. 87–96, 1893.
- [104] C. Roelands, “Correlational aspects of the viscosity-temperature-pressure relationship of lubricating oils,” Ph.D. dissertation, 1966.
- [105] L. Houpert, “New results of traction force calculations in elastohydrodynamic contacts.” vol. 107, pp. 241–245, 1984.
- [106] D. Dowson and G. Higginson, *Elasto-hydrodynamic lubrication*. Pergamon Press, 1977.
- [107] R. F. Crouch and A. Cameron, “Viscosity-temperature equations for lubricants,” *J. Inst. Petroleum*, vol. 47, pp. 307–313, 1961.

- [108] M. Masjedi and M. M. Khonsari, “Film thickness and asperity load formulas for line-contact elastohydrodynamic lubrication with provision for surface roughness,” *Journal of Tribology*, vol. 134, 1 2012. [Online]. Available: <https://asmedigitalcollection.asme.org/tribology/article/doi/10.1115/1.4005514/439343/Film-Thickness-and-Asperity-Load-Formulas-for>
- [109] R. G. Budynas and J. K. Nisbett, *Shigley’s Mechanical Engineering Design*, 9th ed. McGraw-Hill, 2011.
- [110] B. J. Hamrock, “Film thickness for different regimes of fluid-film lubrication,” pp. 1–14, 1980.
- [111] G. Lundberg and E. Yhland, *Cylinder compressed between two plane bodies*. SKF, 1949.
- [112] T. Parikyan, T. Resch, and H. H. Priebisch, “Structured model of crankshaft in the simulation of engine dynamics with AVL/EXCITE,” in *Volume 3: Engine Systems: Lubrication, Components, Exhaust and Boosting, System Design and Simulation*, vol. 67. American Society of Mechanical Engineers, 9 2001, pp. 105–114. [Online]. Available: <https://asmedigitalcollection.asme.org/ICEF/proceedings/ICEF2001/80159/105/1081821>
- [113] G. Offner, “Modelling of condensed flexible bodies considering non-linear inertia effects resulting from gross motions,” *Proceedings of the Institution of Mechanical Engineers, Part K: Journal of Multi-body Dynamics*, vol. 225, pp. 204–219, 2011.
- [114] D. Nelias, I. Bercea, and V. Paleu, “Prediction of roller skewing in tapered roller bearings,” *Tribology Transactions*, vol. 51, pp. 128–139, 2008.
- [115] F. Majdoub, L. Saunier, C. Sidoroff-coicaud, and B. Mevel, “Tribology international experimental and numerical roller skew in tapered roller bearings,” *Tribology International*, vol. 145, p. 106142, 2020. [Online]. Available: <https://doi.org/10.1016/j.triboint.2019.106142>
- [116] B. Mevel and J. L. Guyader, “Routes to chaos in ball bearings,” pp. 471–487, 1993.
- [117] H. Spikes, “Basics of EHL for practical application,” *Lubrication Science*, vol. 27, pp. 45–67, 2015.
- [118] X. Shi and L. Wang, “TEHL analysis of high-speed and heavy-load roller bearing with quasi-dynamic characteristics,” *Chinese Journal of Aeronautics*, vol. 28, pp.

- 1296–1304, 8 2015. [Online]. Available: <http://dx.doi.org/10.1016/j.cja.2015.06.013>
<https://linkinghub.elsevier.com/retrieve/pii/S1000936115001181>
- [119] K. P. Singh and B. Paul, “Numerical solution of non-hertzian elastic contact problems,” *Journal of Applied Mechanics*, vol. 41, pp. 484–490, 6 1974. [Online]. Available: <https://asmedigitalcollection.asme.org/appliedmechanics/article/41/2/484/422784/Numerical-Solution-of-NonHertzian-Elastic-Contact>
- [120] T. A. Harris and M. N. Kotzales, *Advanced Concepts of Bearing Technology*, 5th ed. Taylor and Francis Group, 2007.
- [121] J. M. de Mul, J. J. Kalker, and B. Fredriksson, “The contact between arbitrarily curved bodies of finite dimensions,” *Journal of Tribology*, vol. 108, pp. 140–148, 1 1986. [Online]. Available: <https://asmedigitalcollection.asme.org/tribology/article/108/1/140/418690/The-Contact-Between-Arbitrarily-Curved-Bodies-of>
- [122] Y. Mitsuya, H. Sawai, M. Shimizu, and Y. Aono, “Damping in vibration transfer through deep-groove ball bearings,” *Transactions of the Japan Society of Mechanical Engineers Series C*, vol. 58, pp. 3714–3721, 1992.
- [123] E. Krämer, *Dynamics of Rotors and Foundations*. Springer Berlin Heidelberg, 1993. [Online]. Available: <http://link.springer.com/10.1007/978-3-662-02798-1>
- [124] R. Gohar and H. Rahnejat, *Fundamentals of Tribology*. World Scientific (Europe), 9 2018. [Online]. Available: <https://www.worldscientific.com/worldscibooks/10.1142/q0152>
- [125] D. Dowson, “Paper 10: Elastohydrodynamics,” *Proceedings of the Institution of Mechanical Engineers, Conference Proceedings*, 1967.
- [126] D. Sarkar, R. Bali, and T. Sharma, *Practical Machine Learning with Python: A Problem-Solver’s Guide to Building Real-World Intelligent Systems*. Apress L.P., 12 2017.
- [127] J. Bell, *Machine Learning: Hands-On for Developers and Technical Professionals*, 1st ed. Wiley, 11 2014.
- [128] C. M. Bishop, *Pattern Recognition and Machine Learning*. Springer, 2006, pp. 21–24.
- [129] K. Levenberg, “A method for the solution of certain non-linear problems in least squares,” *Quarterly of Applied Mathematics*, vol. 2, pp. 164–168, 1944. [Online]. Available: <https://about.jstor.org/terms>

- [130] D. W. Marquardt, “An algorithm for least-squares estimation of nonlinear parameters,” *Journal of the Society for Industrial and Applied Mathematics*, vol. 11, pp. 431–441, 1963.
- [131] B. M. Wilamowski and H. Yu, “Improved computation for levenberg–marquardt training,” *IEEE Transactions on Neural Networks*, vol. 21, pp. 930–937, 6 2010. [Online]. Available: <http://ieeexplore.ieee.org/document/5451114/>
- [132] X. Ying, “An overview of overfitting and its solutions,” *Journal of Physics: Conference Series*, vol. 1168, p. 022022, 2 2019. [Online]. Available: <https://iopscience.iop.org/article/10.1088/1742-6596/1168/2/022022>
- [133] R. Preece and J. V. Milanovic, “Efficient estimation of the probability of small-disturbance instability of large uncertain power systems,” *IEEE Transactions on Power Systems*, vol. 31, pp. 1063–1072, 3 2016. [Online]. Available: <http://ieeexplore.ieee.org/document/7084698/>
- [134] K. Siebertz, D. van Bebber, and T. Hochkirchen, *Statistische Versuchsplanung*. Springer Berlin Heidelberg, 6 2017. [Online]. Available: <http://link.springer.com/10.1007/978-3-662-55743-3>
- [135] M. E. Johnson, L. M. Moore, and D. Ylvisaker, “Minimax and maximin distance designs,” Tech. Rep., 1990.
- [136] K. L. Johnson, “Regimes of elastohydrodynamic lubrication,” *Journal of Mechanical Engineering Science*, vol. 12, pp. 9–16, 2 1970. [Online]. Available: http://journals.sagepub.com/doi/10.1243/JMES_JOUR_1970_012_004_02
- [137] M. Marian and S. Tremmel, “Current trends and applications of machine learning in tribology—a review,” *Lubricants*, vol. 9, p. 86, 9 2021. [Online]. Available: <https://www.mdpi.com/2075-4442/9/9/86>
- [138] J. Han and C. Moraga, *The influence of the sigmoid function parameters on the speed of backpropagation learning*, 1995, pp. 195–201. [Online]. Available: http://link.springer.com/10.1007/3-540-59497-3_175
- [139] S. Sharma, S. Sharma, and A. Athaiya, “Activation functions in neural networks,” *International Journal of Engineering Applied Sciences and Technology*, vol. 4, pp. 310–316, 2020. [Online]. Available: <http://www.ijeast.com>
- [140] T. M. Inc., “Improve shallow neural network generalization and avoid overfitting,” 2022. [Online]. Available: <https://uk.mathworks.com/help/deeplearning/ug/improve-neural-network-generalization-and-avoid-overfitting.html>



Tribo-dynamic analysis of high-speed roller bearings for electrified vehicle powertrains

H. Questa^{a,*}, M. Mohammadpour^a, S. Theodossiades^a, C.P. Garner^a, S.R. Bewsher^b, G. Offner^b

^a *Wolfson School of Mechanical, Electrical and Manufacturing Engineering, Loughborough University, Loughborough, LE11 3TU, United Kingdom*

^b *AVL List GmbH, Graz, Austria*

ARTICLE INFO

Keywords:
Electrified powertrain
Roller bearings
EHL
Dynamics
Efficiency

ABSTRACT

Roller bearings are critical components in electrified powertrains. At high speeds, the critical role of the elastohydrodynamic lubrication (EHL) cannot be ignored, necessitating a tribo-dynamic analysis. This paper investigates the behaviour of roller bearings under operating conditions present in high-speed electrified powertrains. The bearing motion is obtained experimentally using a novel experimental rig. The bearing centre's orbital motion is acquired from the experiment and used as the boundary condition for tribological analysis. Results reveal that the EHL film thickness increases from 0.2 to 1.9 μm across a speed range of 0–15 000 rpm. A comparison with conventional dry contact analysis shows that roller load can be underestimated if the lubricant film is neglected in the roller-race contact deformation.

1. Introduction

Due to shifts in emissions regulations, technology and customer attitudes, electric and hybrid electric vehicles are estimated to have a global market share of 48% by 2030 [1]. The electric motors used in these powertrains are often lightweight to meet packaging and mass constraints and operate at high rotational speeds to achieve power requirements. This style of powertrain architecture involves high-speed bearing operation in both the motor and transmission. The associated performance characteristics of these bearings such as friction and wear [2], thermal stability and generated vibration and noise must be modelled accurately at the development stage to ensure system level success [3].

To fully understand bearing performance under the conditions present in modern electrified vehicles, a multi-physics approach comprising dynamics and tribology of the system at high speeds is required. Since load is transmitted through the bearing, for example via a gear tooth load during a meshing cycle, the rolling elements undergo complex oscillatory motion that results in impact at lubricated contacts between the rollers and races. This dynamic behaviour of the bearing prevails the force transmission from the excitation source to the housing and the structure. Hence, noise, vibration and harshness (NVH) refinement is affected. It also dictates the working conditions for the tribological contacts. The dynamic behaviour itself is affected by the tribological

phenomena at the lubricated conjunctions via introduced frictional dissipation and potential stiffness [4,5] and damping effects of the lubricant film. Therefore, a coupled tribo-dynamic methodology needs to be established to more accurately capture the system's behaviour.

Accounting for lubricant film thickness distribution at the roller-race conjunction at each step of a dynamic analysis is a time-consuming simulation. Previous studies have de-coupled the analysis into two stages. Bearing centre displacement is obtained through solving equations of motion, utilizing dry-Hertzian contact mechanics to calculate the roller-raceway load-deflection relationship. Extrapolated film formulae are then employed to calculate the film thickness at the contact based on the reaction force [6]. This does not consider implicitly the effect of the lubricant film on the prevailing bearing motion and load which is hence underestimated. Rahnejat and Gohar [7] overcame this by using extrapolated central film formulae to account for film thickness as well as deflection at the contact. More realistic bearing vibration amplitudes were reported; however the extrapolated film formulae are somewhat limited to the range of operating parameters used in original simulations. Film shape and pressure profile at the contact, as well as thermal and sub-surface stress analysis could not be performed without full numerical EHL analysis. To determine tribological contact conditions, Mohammadpour et al. [8] utilised a full numerical elastohydrodynamic analysis explicitly. The abovementioned models were limited to low operating speeds and did not account for the flexibility of the system, which is crucial for high-speed conditions.

* Corresponding author.

E-mail address: h.questa@lboro.ac.uk (H. Questa).

Nomenclature	
A_a	Asperity apparent contact area (m^2)
A	Apparent contact area (m^2)
a	Acceleration (m.s^{-2})
b	Half-length of the contact (mm)
C	Radial clearance (μm)
c'	Solid specific heat capacity ($\text{J.kg}^{-1}.\text{K}^{-1}$)
D_r	Diameter of roller (mm)
D_p	Pitch diameter (mm)
E_r	Equivalent (reduced) elastic modulus (Pa)
F_x	Radial load in x-direction (N)
F_y	Radial load in y-direction (N)
f	Total friction (N)
f_b	Boundary friction (N)
f_v	Viscous friction (N)
f_{bpi}	Ball pass frequency of inner race (Hz)
f_{bpo}	Ball pass frequency of outer race (Hz)
f_{shaft}	Shaft rotational frequency (Hz)
G^*	Dimensionless equivalent geometry (-)
h_c	Central film thickness (m)
k	Stiffness (Nm^{-1})
K	Lubricant thermal conductivity ($\text{W.m}^{-1}.\text{K}^{-1}$)
L	Roller length (mm)
n	Exponent of localized deflection (-)
N	Number of rolling elements (-)
p	Contact pressure (Pa)
\bar{p}	Average pressure at the apparent contact (Pa)
r_{in}	Radius of inner race (mm)
R_{zx}	Equivalent radius of contact (mm)
u	Speed of entraining motion (m.s^{-1})
U^*	Dimensionless speed parameter (-)
v	Velocity (m.s^{-1})
W	Contact load (N)
W^*	Dimensionless load parameter (-)
W_a	Asperity load (N)
x	Displacement in x-direction (m)
x_c	Conjunction x-coordinate (-)
y	Displacement in y-direction (m)
y_c	Conjunction y-coordinate (-)
<i>Greek Symbols</i>	
θ	Angular position (rad)
α	Pressure viscosity coefficient ($\text{m}^2.\text{N}^{-1}$)
δ	Contact deflection (m)
κ	Average asperity tip radius of curvature (m)
λ	Striebeck parameter (-)
η_0	Atmospheric lubricant dynamic viscosity (Pa.s)
η	Lubricant dynamic viscosity (Pa.s)
ρ	Lubricant density (kg.m^{-3})
ρ_0	Atmospheric lubricant density (kg.m^{-3})
ρ'	Solid density (kg.m^{-3})
σ	Composite surface roughness (m)
ς	Boundary shear strength of asperities (-)
τ_0	Eyring stress (Pa)
ω_c	Angular velocity of cage (rad.s^{-1})
ω_{ri}	Angular velocity of inner race (rad.s^{-1})
ω_s	Angular velocity of shaft (rad.s^{-1})
γ	Relaxation factor (-)
ζ	Asperity density (m^{-2})

The work presented in this study investigates the tribo-dynamic behaviour of rolling element bearings under high-speed conditions which are representative of modern electrified vehicle applications. Considering the necessity of conducting a multi-physics study, the methodology follows the approach conducted by Mohammadpour et al. [8]; however, the motion of the bearing is obtained experimentally rather than numerically. This allows the consideration of detailed and realistic dynamic behaviour. In this method, the bearing centre's orbital motion is obtained from the component level experiment as the boundary condition for the tribological analysis. The contact load, film thickness, viscous and boundary friction as well as the EHL pressure and film thickness distributions are then obtained using an implicit tribological model and an explicit 1-dimensional numerical EHL model. This approach addresses the need for a dynamic model of the bearing whilst removing the associated numerical uncertainty. More importantly, it allows for the tribological behaviour of the lubricated conjunctions within the bearing to be captured and understood under modern electrified powertrain operating conditions. To simulate these conditions, a novel experimental rig was developed that was able to provide static and dynamic radial loads to a shaft-bearing system up to rotational speeds of 32 000 rpm, far in excess of similar component level rigs previously reported [9–11]. Such an approach, combining the experimental measurement of the bearing motion and the numerical simulation of tribological contacts under high-speed conditions has not been previously reported in literature, to the authors' knowledge.

The significance of this conducted research is that it investigates a new range of bearing working conditions at high speeds from a tribological perspective. It improves the understanding of the governing regimes of lubrication, range of tribological quantities such as film thickness and pressure as well as interaction of tribological behaviour with dynamics of the system. The deeper understanding of these matters

will support more objective development of these modern powertrains in future to enhance their efficiency, durability and NVH refinement. The acquired knowledge will also guide future developments of predictive numerical methodologies by understanding the interaction of tribology and dynamics and the significance of considering or neglecting this link.

2. Methodology

2.1. Overall workflow

To obtain the film thickness at the roller-race contact, the load on each roller must be calculated implicitly based on the contact deflection. This is obtained conventionally from a dynamic model by solving the equations of motion, but these are currently lacking the required in-depth physics such as system flexibility, flexibility of races and thermal effects [12–15]. To circumvent the need for a complex flexible dynamic model and to capture real behaviour of a bearing under test, displacement of the bearing centre and hence contact deflection is captured from experimental test results.

An experimental test rig is used to obtain the relative displacement between the inner and outer bearing races. Then, using the Hertzian load-deflection relationship and accounting for the lubricant film thickness, load on an individual roller is found at each instantaneous position around the bearing centre through a speed sweep of 0–15 000 rpm. An implicit analytical tribological model is used which calculates the film thickness at the contact. This loop is iterated to account for the tribo-dynamic coupling. After the experimentally informed implicit tribo-dynamic model is solved, load and speed values at specific rotational velocities are used within an explicit numerical EHL model to calculate film thickness and pressure distribution across the contact. The

flow diagram in Fig. 1 illustrates the methodology used. Interactions between each stage will be explained in subsequent sections.

The rollers within a bearing carry an instantaneous share of the overall load applied to the bearing [16]. Deviation of the supported shaft centre from its nominal geometric centre results in a loaded region of the bearing. In the conjunction between the bearing roller and race, the non-conformal nature of contact generates very high pressures when under load. This causes local surface deformation and an increase in lubricant viscosity, resulting in EHL film formation [17,18]. Emerging clearances in unloaded regions of the bearing occur, which can cause the roller-to-race contact to deviate from the EHL regime towards the hydrodynamic regime, resulting in sliding and roller-cage collisions [8]. Hence, the contact may go through different regimes of lubrication throughout its rotation [19].

Fig. 2 shows the cylindrical roller bearing (CRB) in equilibrium position with zero preload or design clearance. Under zero applied radial load, F_0 , the initial deformation, δ_0 , and radial clearance, C_0 , between rollers and races are both zero. Due to external force application and system dynamics, an instantaneous radial load, F_i , will displace the inner bearing race from its equilibrium state (Δx and Δy). By analysing an individual roller at its instantaneous angular position, θ_i , the resultant displacement of the bearing centre can be used to find deflection at the roller-race contact, δ_i . These contact deformations will result in contact forces, W_i , which act to keep the rollers and races in dynamic equilibrium. The above interpretation is valid considering rigid inner and outer races.

Fig. 3 presents the case whereby an instantaneous force is applied to the inner race. This causes deflection of the rollers in the loaded region and clearance, or less deflection, around the rollers in the unloaded region. The value of the total deflection, δ_i , at the inner and outer race contacts corresponds to the component of displacement of the bearing centre at the instantaneous position of that particular roller. In the current study, this value was experimentally measured from the test rig and is used quasi-statically as the boundary condition for the tribological model. It should be noted that in-plane two degrees of freedom motion are analysed in this study which is a valid assumption under dominant radial loading with secondary horizontal motion from the full system dynamics. Misalignment along the length of the rollers is not considered

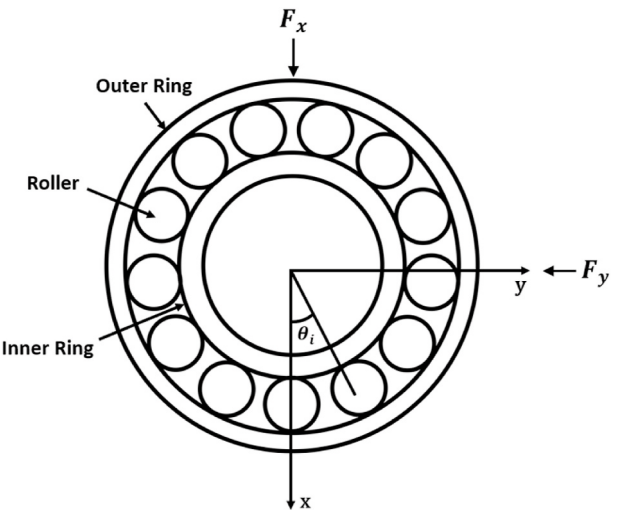


Fig. 2. CRB in equilibrium position.

due to the high stiffness of the shaft and bracket, hence a 1-dimensional analysis for EHL is sufficient [20].

In the loaded region, the Hertzian load-deflection relationship is used to obtain the resulting instantaneous load on the roller. This value is then used implicitly within an analytical tribological model to calculate contact film thickness for an individual roller as it passes through different angular positions during a speed sweep. An extrapolated film thickness formula is used for this purpose. The calculated film thickness imposes additional deformation at the contact points which itself changes the calculated load (as shown in equation (5)). Hence, an iterative approach is required between the force calculation and implicit tribological model. In this part of the workflow, the stiffness and damping of the EHL film is neglected due to its rigid-like stiffness, which is several orders of magnitude higher than the Hertzian contact [21,22].

For in-depth tribological investigations, the numerical solution of the fluid film is essential. This provides the pressure, film thickness and shear distributions in the contact to study the durability and frictional efficiency of the system. In the current study, the load on the roller and contact kinematics obtained from the implicit bearing model is used explicitly in a 1-dimensional elastohydrodynamic model to acquire film thickness and pressure distribution at the contact for specific loading periods through the speed sweep, as is shown in Fig. 4. This explicit approach significantly improves the computational efficiency of the model and in principle, maintains the accuracy since only the central value of the film is required in the load calculation.

2.2. Experimental test rig

The displacement of the bearing centre governs the conditions at the contact and was found experimentally using a high-speed bearing test rig, originally reported by Walker et al. [23]. A 5 kW AC synchronous motor, capable of reaching up to 32 000 rpm, was coupled to a steel shaft that is supported by two bearing brackets. Radial force was transferred to the inner bearing race via the shaft using a hinge/arm mechanism and load application device on the shaft. Displacement data were obtained from an instrumented bearing bracket. Fig. 5 shows a schematic of the rig.

The motor control unit was connected to a voltage input, transmitted via an NI cDAQ-9178 USB chassis for optimum resolution of the input voltage. A MATLAB script controlled the voltage ramp over a specified time-period and thus the motor acceleration. In this study, a transient speed sweep was performed from 0 to 15 000 rpm in a 4 s period, with 750 N of static radial load applied to the shaft. The bearing under test was a single row cylindrical roller bearing, NU 205 ECP, located in an

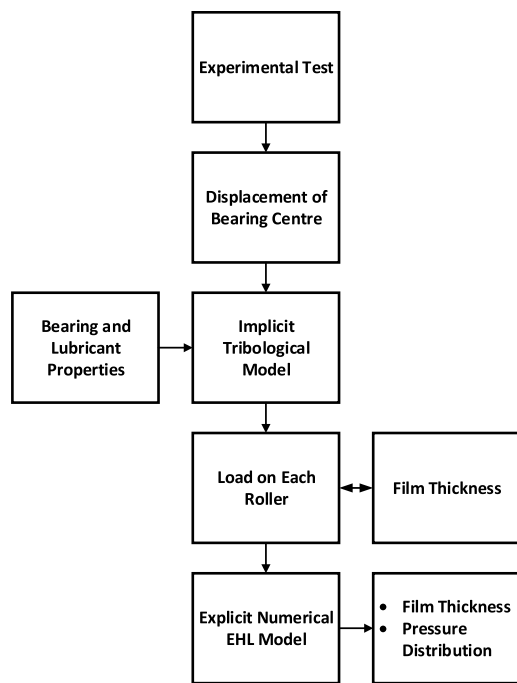


Fig. 1. Methodology overview.

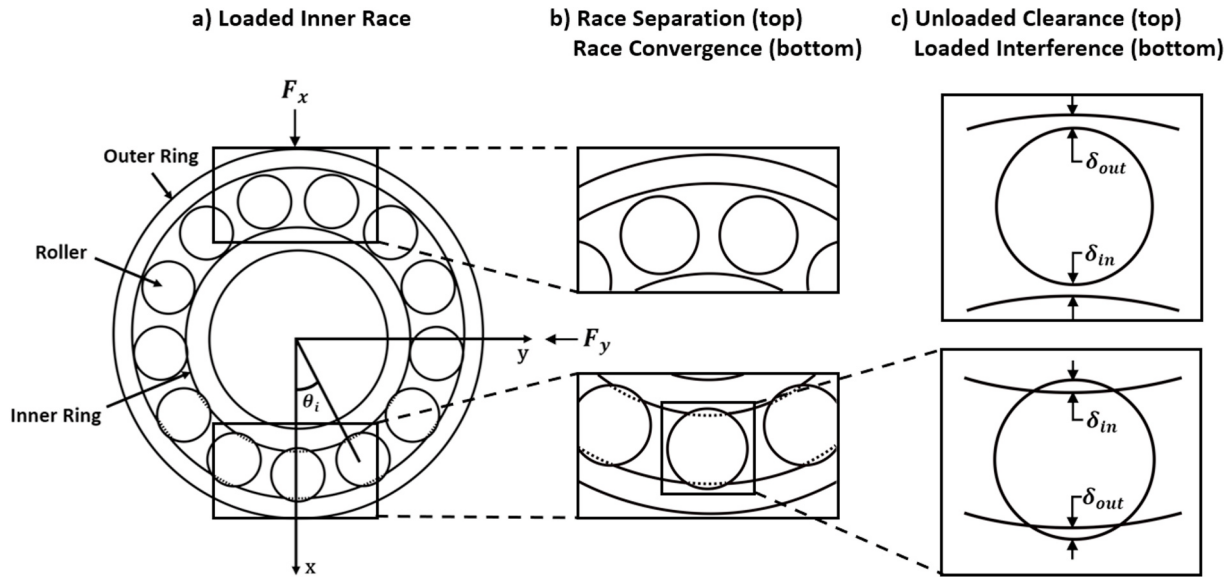


Fig. 3. Mutual separation and convergence of inner and outer races: a) Loaded inner race, b) Race separation and convergence, c) Resultant interference and clearance.

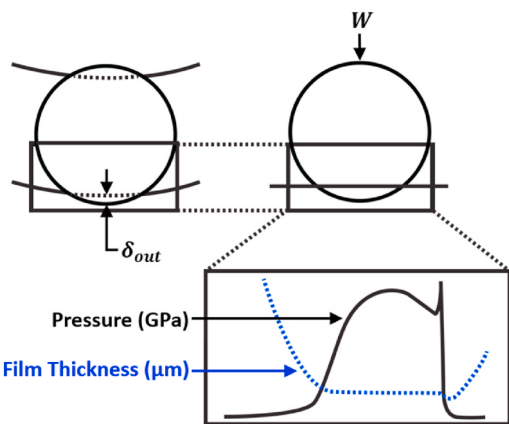


Fig. 4. EHL film thickness and pressure distribution at contact.

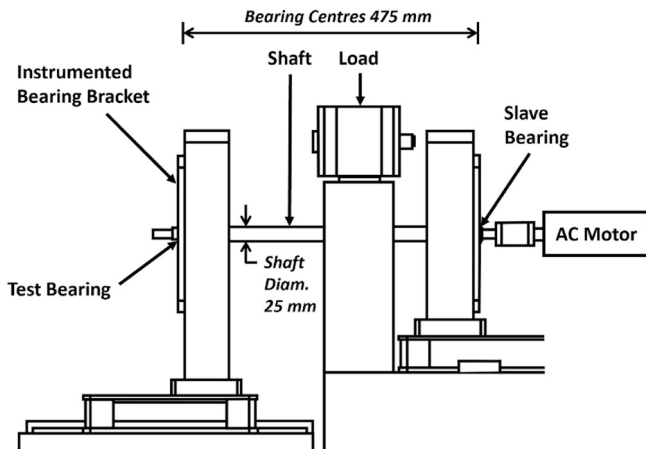


Fig. 5. Experimental rig schematic.

aluminium test bracket that had an extruded bore for instrumentation.

2.3. Instrumentation

The outer surface of the bearing bore was instrumented with two Type 4383 single axis piezo-electric charge accelerometers, with a frequency range of 0.1–8.5 kHz and sensitivity of 3.16 pC/ms². These measured acceleration of the bracket's bore, corresponding to the outer race of the bearing (Fig. 6(a)). Two single beam laser vibrometers measured the displacement of the shaft at the edge of the bearing which corresponds to the displacement of the inner race of the bearing (Fig. 6(b)). A dual-beam laser vibrometer was used to measure the rotational speed of the shaft. All laser vibrometers had a frequency range of 0–10 kHz and maximum speed of 20 000 rpm.

A program in MATLAB controlled the speed of the shaft through a ramped voltage input. Data was simultaneously acquired from the accelerometers and laser vibrometers through synchronised input channels at a sampling rate of 100 kHz. Simultaneous control and data acquisition ensured accurate results between different instrumentation locations.

2.4. Signal processing

The bearing race displacements were obtained from the instru-

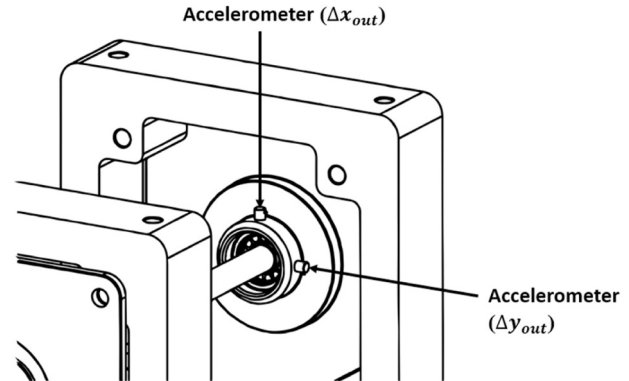


Fig. 6a. Accelerometer locations on the test bracket.

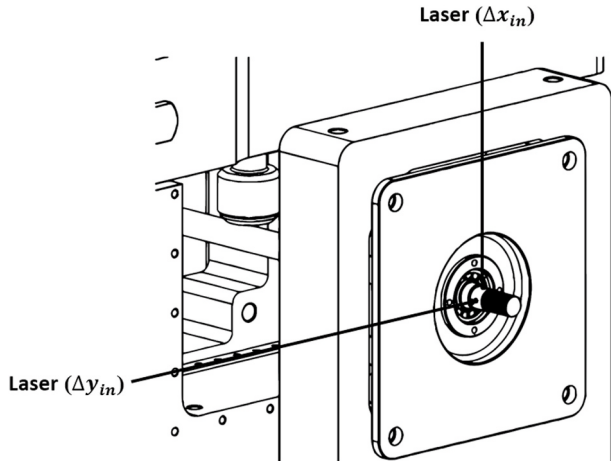


Fig. 6b. Laser vibrometer locations on the shaft.

mented bearing using time-domain data from the accelerometers and laser vibrometers. The laser vibrometer directly provided displacement data, whereas the accelerometer data required post-processing of acceleration data. To ascertain the displacement of the bearing bore and thus outer bearing race, the accelerometer results were integrated twice:

$$v_{out}(t) = v_{0,out} + \int_0^t a_{out} dt \quad (1)$$

$$x_{out}(t) = x_{0,out} + \int_0^t v_{out} dt \quad (2)$$

As this double integration amplifies non-linearities in the original signal, it requires pre-processing [24]. Low frequency drift is removed from the unfiltered time-domain data by applying a linear fit to the data and then removing the trend from it.

To extract the frequency content of the speed ramp, waterfall plots were generated using the accelerometer and laser vibrometer data. Short-time fast-Fourier transform (STFFT) was used, with data windows of six shaft rotations at each 100 rpm increment. The resulting signal was then filtered using a Butterworth bandpass filter for a frequency range of 70–10 000 Hz to remove the high amplitude low frequency noise that was inherent to the equipment setup. The filter used 3 dB of passband ripple and 7 dB attenuation in the stopbands, which were set at 35–12 500 Hz.

The relative displacement of the bearing centre could then be obtained from the relative displacement between the shaft (measured using the single beam laser vibrometer) and bearing bore:

$$\begin{aligned} \Delta x &= \Delta x_{in} - \Delta x_{out} \\ \Delta y &= \Delta y_{in} - \Delta y_{out} \end{aligned} \quad (3)$$

where Δx_{in} and Δx_{out} correspond to the displacements of the shaft and bearing bore respectively.

2.5. Contact mechanics of the roller-race conjunction

The contact between roller and race is modelled as an elastic deformation between an equivalent finite length elastic cylinder and rigid plate. This assumption is realistic under the conditions of an EHL contact. The contact force on an individual roller at each instantaneous position, W_i , is obtained from the Hertzian load-deflection relationship:

$$W_i = k\delta_i^n \quad (4)$$

where k is the Hertzian contact stiffness non-linearity between a rolling element and the inner or outer raceway groove. For the case of rolling

element bearings, the exponent of localised deflection, n , is equal to 10/9 [25]. The contact deflection of a roller relative to the race, δ_i , is due to the normal dynamic motion (i.e. the local mutual convergence) of the inner and outer bearing races, contribution of lubricant film thickness and any additional clearance or interference fit [8]. This is expressed as:

$$\delta_i = 2(h_{c,i} - C) + x\cos(\theta_i) + y\sin(\theta_i) \quad (5)$$

where C is the local radial clearance, and x and y are the displacement components of the inner bearing race from its geometric centre. This normal approach between both races is the sum of the total deformation of the rollers and both races [26], hence:

$$\delta_i = \delta_{i,in} + \delta_{i,out} \quad (6)$$

The equilibrium of forces in a system of stiffnesses in series is therefore:

$$W_i = W_{i,out} = W_{i,in} \quad (7)$$

To find the individual deflection of each contact due to differences in contact stiffness, the following relationship is used:

$$\delta_{i,in}^n k_{in} = \delta_{i,out}^n k_{out} \quad (8)$$

The deflection value at each contact based on the total deflection and relationship between contact stiffness is then found from Equations (6) and (8) to give:

$$\delta_{i,out} = \frac{\delta_i}{\left(\frac{k_{out}}{k_{in}}\right)^{\frac{1}{n}} + 1} \quad (9)$$

The normal stiffness of the inner and outer races differs due to their geometry. To calculate the stiffness at each contact, the following equation is used to find the contact deflection for a given load based on the geometry and material properties at each contact:

$$\delta = \frac{F}{\pi E_r L} \left[\ln\left(\frac{4\pi E_r R_{zx} L}{F}\right) - 1 \right] \quad (10)$$

The deflection for a range of loads is then calculated, and the non-linear relationship between load and deflection is numerically obtained for the specific bearing. This is then curve fitted and represented by a power function in the form $F = a\delta^b$, with $b = 10/9$ and a representing the contact stiffness. Individual contact stiffness and deflection at the inner and outer race contacts is then found. The overall contact stiffness, $k_{i,total}$, is given by:

$$k_{i,total} = \frac{1}{\left(\frac{1}{k_{i,in}}\right) + \left(\frac{1}{k_{i,out}}\right)} \quad (11)$$

where $k_{i,in}$ and $k_{i,out}$ are the stiffnesses of the inner and outer race contacts respectively.

2.6. Implicit tribological model

A stepwise solution is performed on an individual roller as it passes through each angular position. The roller bearing and bracket tolerances are such that the internal clearance is 0 µm between roller and race. This means that in an unloaded state, there is no deflection of elements or raceway. It also means that displacement in positive x-y corresponds to the same total magnitude of deflection of the roller and race contact. For each time step, the bearing is first assumed to be in equilibrium position, and film thickness is assumed to be 0 µm. The deflection of the bearing is calculated under these conditions and is therefore a function of the relative displacement between inner and outer bearing races. With deflection at the time step calculated, the resultant lubricant regime and subsequent analytical solutions can be performed based on the following three conditions:

- a) $\delta = 0$ indicates a film of 0 μm and no load.
b) $\delta < 0$ indicates complete separation of the roller and race. In this instance, the lubricant is assumed to fill the separation gap, with the film thickness value equalling the magnitude of the separation:

$$h_i = |\delta_i| \quad (12)$$

Under this condition, the lubrication is in the hydrodynamic regime. The hydrodynamic lubricant reaction load was derived by Rahnejat [27], and is given by:

$$W_i = \frac{2bu_i\eta_0 R_{zx}}{h_i} \quad (13)$$

where b is the half length of the contact, u is the speed of lubricant entrainment into the contact, η_0 is the lubricant viscosity, R_{zx} is the reduced radius of the roller and race and h is lubricant film thickness.

- c) $\delta > 0$ indicates deflection at the roller-race contact. This means that contact pressure is sufficiently high for the lubrication regime to be elastohydrodynamic. For the elastohydrodynamic regime, an iterative process is performed to solve film thickness. This is due to the contribution of EHL film towards deformation and consequently the load in the contact.

The cylindrical roller and race contacts are modelled by an equivalent rigid roller against a semi-infinite elastic half space of equivalent elastic modulus, E_r . The extrapolated central film thickness for a line contact [28] is therefore obtained from:

$$h_c = R_{zx} [3.06G^{*0.56} U^{*0.69} W^{*-0.1}] \quad (14)$$

where the following dimensionless parameters are used:

$$W^* = \frac{W_i}{E_r R_{zx} L}, \quad U^* = \frac{\eta_0 u}{E_r R_{zx}}, \quad G^* = E_r \alpha \quad (15)$$

where R_{zx} is the reduced radius of the contact, L is the length of the roller, u is the speed of entraining motion into the contact and W is the contact load. Assuming pure rolling, the speed of entraining motion is given by:

$$u_i = \frac{1}{2} (\omega_{c,i} - \omega_{ri,i}) r_{in} \quad (16)$$

An iterative process is used to calculate load on the roller based on total deflection including lubricant film (back to Eq. (5)). At each time step where an EHL film is present, the following convergence criteria must be met before the next time step is calculated:

$$\frac{h_i^n - h_i^{n-1}}{h_i^{n-1}} \leq 0.01 \quad (17)$$

2.7. Friction calculations

Frictional power is a crucial factor for characterising bearing performance. Under modern high-speed conditions, it is important to also understand the frictional behaviour of the system. Roller bearings often operate within the mixed elastohydrodynamic regime of lubrication. Friction is generated by a combination of viscous shear of the lubricant and asperity interactions. Total friction at the mixed-EHL contact is a combination of the boundary friction, f_b , and hydrodynamic or viscous friction, f_v :

$$f = f_v + f_b \quad (18)$$

Boundary friction is a function of asperity contact pressure, calculated using the Greenwood and Tripp model in this paper [29]:

$$f_b = \tau_0 A_a + \varsigma W_a \quad (19)$$

where τ_0 is the Eyring shear stress of lubricant and ς is the pressure coefficient for shear strength of asperities, obtained from asperity level friction measurement. Asperity load, W_a , and area occupied by asperities within the apparent contact A_a are obtained as below, assuming a Gaussian distribution of asperity peak counts:

$$W_a = \frac{16\sqrt{2}}{15} \pi (\zeta \kappa \sigma)^2 \sqrt{\frac{\sigma}{\kappa}} E_r A_a F_{5/2}(\lambda) \quad (20)$$

and

$$A_a = \pi^2 (\zeta \kappa \sigma)^2 A F_2(\lambda) \quad (21)$$

where $\lambda = \frac{h}{\sigma}$ is the Stribeck parameter and $F_{5/2}(\lambda)$ and $F_2(\lambda)$ are statistical functions obtained from numerical integration of the Gaussian distribution of asperities.

Viscous friction due to shearing of the lubricant film in the EHL contact is found using the below experimentally validated formulae [30]:

$$f_v = \mu W \quad (22)$$

where

$$\mu = 0.87\alpha\tau_0 + 1.74 \frac{\tau_0}{\bar{p}} \ln \left[\frac{1.2}{\tau_0 h} \left(\frac{2K\eta_0}{1 + 9.6\xi} \right)^{\frac{1}{2}} \right] \quad (23)$$

where \bar{p} is the average pressure at the apparent contact, K is the lubricant thermal conductivity and ξ is given by:

$$\xi = \frac{4}{\pi} \frac{K}{h/R_{zx}} \left(\frac{\bar{p}}{E_r R_{zx} K \rho' c' u} \right)^{\frac{1}{2}} \quad (24)$$

where K' , ρ' , and c' are respectively the thermal conductivity, density, and specific heat capacity of the contacting solid.

To inform the boundary friction model, surface topography data are required. An Alicona InfiniteFocus Variation Microscope with a $x10$ objective was used for topography measurements to calculate the roughness parameter, $n\sigma\beta$. This had a vertical resolution of 30 nm and sampling point separation of 176.9 nm in the y - z plane of the roller and 1 nm in x . An area of 530 by 588 μm was captured. Data was processed using Vision65 Map Premium, where the profile of the radius of the roller was removed. The measured parameters are presented in Table 1.

2.8. Explicit numerical EHL model

Whilst the analytical solution used in the implicit tribological model provides central film thickness, the film thickness and pressure distributions can only be obtained explicitly through the full solution of Reynolds equation in conjunction with rheological and elastic field models. In a line contact, where contact dimensions in the side-leakage direction (y_c) are much larger than the direction of entraining motion (x_c), pressure in y_c direction is assumed constant due to the negligible gradient and the contact can be analysed in one dimension. This assumption is valid in the contact apart from small regions near the edge. Reynolds equation is used to calculate contact pressures. Assuming a thin film of Newtonian lubricant in a line contact, the following form is used in this paper:

$$\frac{\partial}{\partial x_c} \left[\frac{\rho h^3}{\eta} \frac{\partial p}{\partial x_c} \right] - 6u \frac{\partial(\rho h)}{\partial x_c} = 0 \quad (25)$$

Table 1
Surface topography data.

Root-mean-square height	0.197 μm
Density of peaks	0.00116 1/ $(\mu\text{m})^2$
Arithmetic mean peak curvature	0.180 1/ μm

where x_c is the direction of entraining motion into the contact. For the pressure-density relationship in the compressible model, the Dowson-Higginson model [31] is used

$$\rho = \rho_0 \left(1 + \frac{0.6 \times 10^{-9} p}{1 + 1.7 \times 10^{-9} p} \right) \quad (26)$$

The increase in lubricant viscosity with pressure is modelled using Roelands equation [32] due to its known accuracy at higher contact EHL pressures;

$$\eta = \eta_0 \exp \{ (\ln(\eta_0) + 9.67) \times [-1 + (1 + 5.1 \times 10^{-9} p)^{z_0}] \} \quad (27)$$

where,

$$z_0 = \frac{\alpha}{5.1 \times 10^{-9} (\ln(\eta_0) + 9.67)} \quad (28)$$

It should be noted that equations (27) and (28) can reasonably model common lubricants for the application investigated in this work. For special lubricants with bespoke additive packages and non-conventional behaviour, alternative models can be utilised. The pressure distribution is obtained from the variations in film thickness at the contact, which is defined as below:

$$h = h_0 + \frac{x_c^2}{2R_{zx}} - \frac{2}{\pi E_r} \int_{x_{c,in}}^{x_{c,out}} p \ln(x - x')^2 dx' \quad (29)$$

where h_0 is the central film thickness, the second term represents an idealised film thickness parabola, and the ultimate term represents the localised contact deflection. Below, the method of solution for the numerical EHL model is provided:

Step 1. Input the load value obtained from the implicit tribological model for an instantaneous position as well as contact kinematics from experimental conditions.

Step 2. An initial estimation of lubricant film thickness, h_0 , is made.

Step 3. Inlet and outlet distances are set from $-4.5a$ to $1.5a$ based on the contact half width calculation. This sets up the computational domain.

Step 4. Pressure distribution and film thickness are obtained through simultaneous solutions of equations 25–29. Newton-Raphson iterative scheme is used for speed and robustness of convergence [33]. Pressure convergence criterion is required for the iterative solution:

$$Err_{pressure} = \frac{\sum_{i=1}^n |p_{new} - p_{old}|}{\sum_{i=1}^n p_{old}} \leq \varepsilon_p \quad (30)$$

where $\varepsilon_p = 1 \times 10^{-5}$.

Under-relaxation is applied between successive iterations where the criterion is not met:

$$p_{new} = (1 - \gamma)p_{old} + \gamma p_{new} \quad (31)$$

where the under-relaxation factor is typically $0.01 \leq \gamma \leq 0.8$.

Step 5. Hydrodynamic reaction load is calculated using the integration of pressure over the computational domain

$$W_h = L \int pdx \quad (32)$$

The total reaction from the hydrodynamic load should be equal to the total load share on the roller, W_i , obtained from the explicit tribological model. The following convergence criterion is applied:

$$\frac{|W_i - W_h|}{W_i} \leq \varepsilon_w \quad (33)$$

where $\varepsilon_w = 0.001$.

3. Validation and verification of results

3.1. Experimental result verification

The experimental results obtained from the presented rig were verified against analytically calculated frequency contents. This was to ensure the correct post processing of data for the input to numerical models. The bearing and lubricant data properties are given in Tables 2 and 3 respectively which were also used in simulations.

Primary frequencies in the system due to the interaction of the rolling elements, races and the shaft could then be verified. These frequencies were calculated analytically, with f_{bpi} and f_{bpo} representing the ball pass frequencies of the inner and outer race respectively and f_{shaft} being the rotational frequency of the shaft:

$$f_{bpi} = \frac{\omega_s N}{2\pi} \frac{1}{2} \left(1 - \frac{D_r}{D_p} \right) \quad (34)$$

$$f_{bpo} = \frac{\omega_s N}{2\pi} \frac{1}{2} \left(1 + \frac{D_r}{D_p} \right) \quad (35)$$

$$f_{shaft} = \frac{\omega_s}{2\pi} \quad (36)$$

At 14 000 rpm, the theoretical inner and outer race frequencies are calculated to be 1669 Hz and 1131 Hz respectively, with the experimental results being 1611 Hz and 1131 Hz. The first order shaft rotational frequency from the experiment was 232 Hz compared to theoretical calculation of 233 Hz. The above frequencies can be seen clearly in Fig. 7, which shows the bearing bore displacement spectra, and Fig. 8 which represents the shaft displacement spectra. The verification frequencies are identical in both, confirming that the bearing motion is accurately measured by the experimental methodology. It is observed that at certain speeds, ball pass frequency of the outer race has a larger contribution than the inner race. This is particularly highlighted at 12 000–14 000 rpm. These regional effects are contributed by modal behaviour of the bracket and the mounting bed. The critical speed of the unloaded shaft, where lateral bending frequency of the shaft is equal to the rotation frequency [34], occurs at 12 660 rpm and 211 Hz.

3.2. Numerical EHL validation

Conjunction level validation of the numerical method for solving the EHL film thickness and pressure distributions was performed using the work of Masjedi and Khonsari [35]. These were validated against their smooth surface plots with no asperity pressure contribution. The dimensionless input parameters were $W^* = 1 \times 10^{-4}$, $U^* = 1 \times 10^{-11}$ and $G^* = 4500$. The results shown in Fig. 9 and Fig. 10 show a good agreement between the model used in the study and the work of Masjedi and Khonsari for the dimensionless pressure, P , and dimensionless film thickness, H .

4. Results and discussion

This section presents the results of the numerical tribological models. The dynamic measurements presented in Section 3 are used as the

Table 2
Bearing specification.

Inner race bore	25 mm
Inner race diameter	31.5 mm
Outer race diameter	46.5 mm
Roller diameter	7.5 mm
Roller length	9 mm
Number of rollers	12
External load	740 N
Radial interference	0 μm

Table 3
Lubricant and material properties.

Pressure viscosity coefficient (α)	$2.1 \times 10^{-8} \text{ Pa}^{-1}$
Atmospheric lubricant dynamic viscosity (η_0)	0.08 Pa.s
Lubricant inlet density (ρ_0)	833.8 kg m^{-3}
Eyring stress (τ_0)	2 MPa
Shear strength of asperities (ζ)	0.3
Thermal conductivity of fluid	$1600 \text{ W m}^{-1} \text{ K}^{-1}$
Modulus of elasticity of contacting solids	210 GPa
Poisson's ratio of contacting solids	0.3
Density of contacting solids	7850 kg m^{-3}
Thermal conductivity of contacting solids	$46 \text{ W m}^{-1} \text{ K}^{-1}$
Specific heat capacity of contacting solids	$470 \text{ J kg}^{-1} \text{ K}^{-1}$

boundary conditions to the implicit and explicit models.

4.1. Film thickness and load across speed sweep

The variation in EHL film thickness and roller contact load across the speed sweep from 0 to 15 000 rpm at the outer race contact are shown in Fig. 11. Only the EHL regions are shown, where loads are significant enough to cause contact deformation. The upper limit of the film is where the roller and races diverge and approach the hydrodynamic regime where the film is hence governed by the entraining motion of

lubricant into the contact. The lubricant film, as seen from the film thickness equation, is more affected by the speed of entraining motion rather than the load. This explains the increasing film thickness values in Fig. 11 despite increasing load. The film thickness is increased from 0.1 to 1.9 μm across the speed sweep, revealing a significant increase that can affect the tribo-dynamic behaviour of the bearing, as explained in following sections. From the tribological model, it is possible to observe the transition between mixed-EHL to the purely hydrodynamic regime as the roller passes in and out of the loaded region of the bearing. Full system and rotor dynamics also contribute to the total load on the roller, with periods of resonance at 3 000 rpm and 14 000 rpm marked as A and B respectively in Fig. 11.

Fig. 12 presents an interval of the speed sweep where the effect of the EHL load on reducing the film thickness under oscillating conditions can be observed as well as the hydrodynamic film growth as the roller is unloaded. It is possible to see the effect of the resonant frequency at 1765 Hz superimposed on the lower fundamental train frequency within the loaded region as the inner and outer rings converge and diverge. The results in Fig. 12 confirm the significant effect of dynamic behaviour as well as multi-regime nature of the lubrication due to dynamic effects.

4.2. Friction

Focussing on data from the EHL regime, boundary and viscous

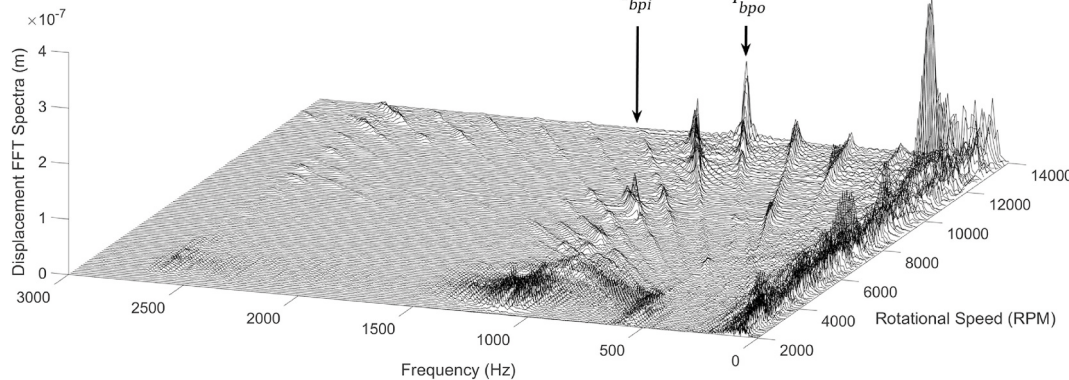


Fig. 7. Bearing bore displacement frequency spectra.

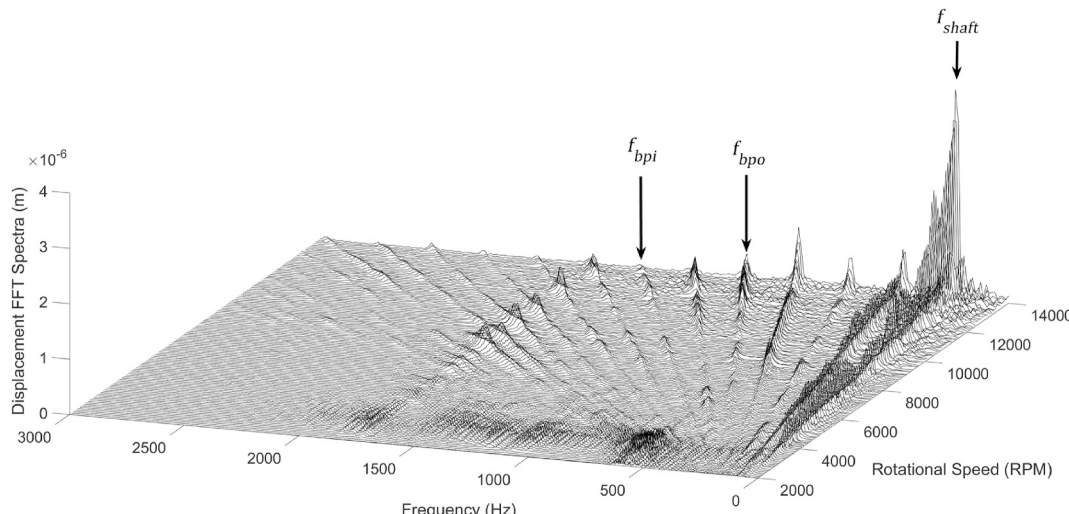


Fig. 8. Shaft displacement frequency spectra.

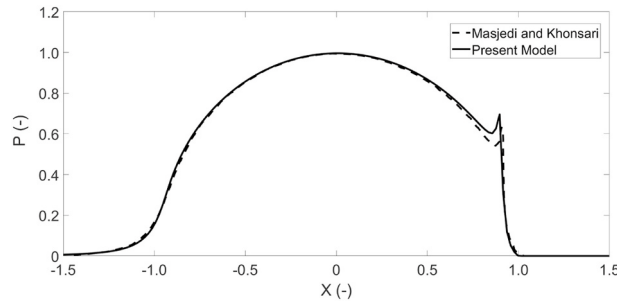


Fig. 9. Validation of dimensionless pressure distribution, present model (solid), Masjedi and Khonsari (dashed).

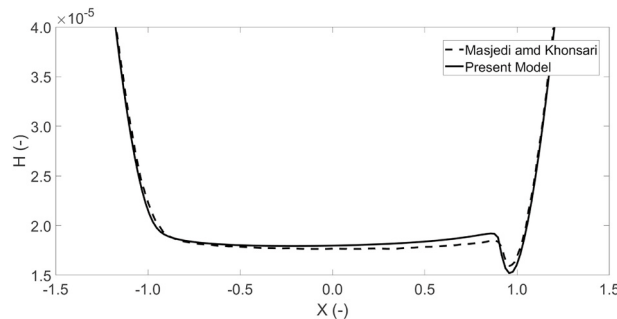


Fig. 10. Validation of dimensionless film thickness distribution, present model (solid), Masjedi and Khonsari (dashed).

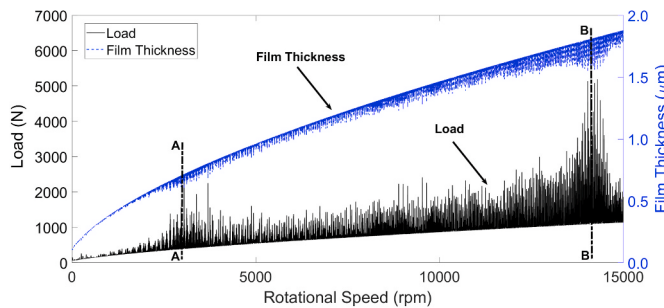


Fig. 11. Contact load and film thickness - outer race.

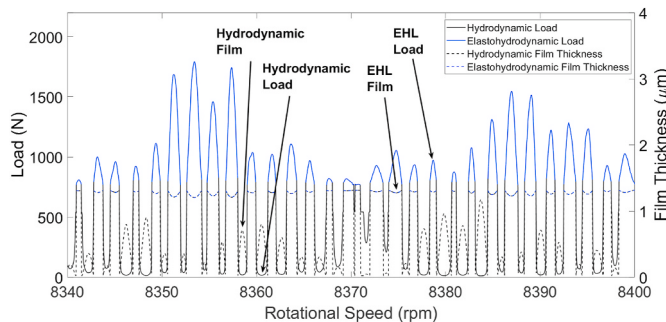


Fig. 12. Film and load - EHL to hydrodynamic regime.

friction through the speed sweep can be analysed. Fig. 13 shows the boundary and viscous frictions across the speed sweep. As the film thickness increases with speed, the separation of the contacting surfaces increases, reducing the boundary interaction of asperities. The resonant period at 14 000 rpm reduces the film height, increasing the likelihood of asperity interaction in that region and hence boundary friction and

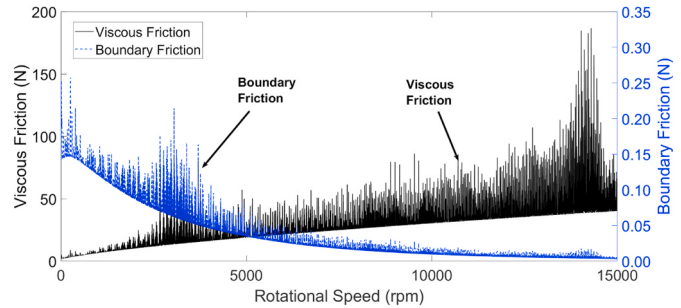


Fig. 13. Viscous and boundary Friction at outer race contact.

potential for wear. In general, the boundary friction reduces towards higher rotational and entrainment velocities. This does not, however, account for lubricant inlet starvation at high speeds or roller sliding. Viscous friction increases with higher speed and hence the shear as expected. Although the film thickness also increases at higher speeds which may reduce the amount of shear, the effect of increasing speed is more dominant. The peak values occur again at a resonance speed of 14 000 rpm, where the highest loads and smallest film occurs.

4.3. EHL regimes

As has been demonstrated in the results analysis, the contact conditions deviate from the elastohydrodynamic regime of lubrication into the hydrodynamic regime throughout the roller orbital motion. These conditions can be verified by presenting the results on the Greenwood chart for fluid regimes of lubrication. The charts display the physical effects instrumental to EHL formation under isothermal conditions: viscosity rise due to pressure and elastic deformation of the surface. These two effects are quantified by two dimensionless parameters, G_e and G_v , as defined below [17]:

$$G_e = \frac{W^*}{U^{*1/2}} \quad (37)$$

$$G_v = \frac{W^{*3/2} G^*}{U^{*1/2}} \quad (38)$$

Four regions exist and the boundaries of these regions are defined by the geometry of contacting bodies, material, and lubricant properties. As is shown in Fig. 14, the outer roller-race contact conditions move between the viscous elastic and iso-viscous rigid regimes, representing EHL and hydrodynamic respectively. The viscous elastic regime signifies the EHL regime of lubrication where contact pressures are such that elastic deformation of the surfaces and viscosity rise due to pressure increase are significant. The iso-viscous rigid regime occurs when the magnitude

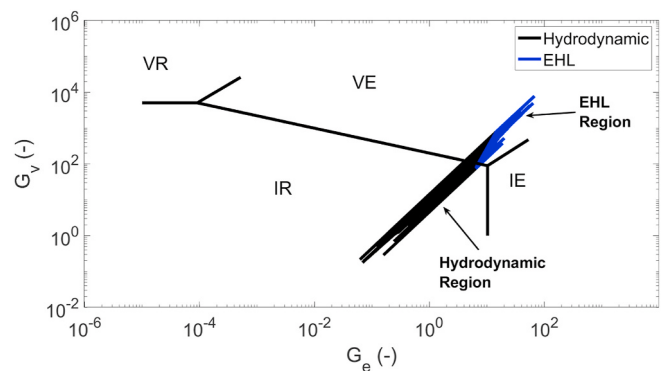


Fig. 14. EHL and hydrodynamic conditions during roller operation. Key: IR = Iso-viscous Rigid, VR = Viscous Rigid, VE = Viscous Elastic, IE = Iso-viscous Elastic.

of elastic deformation is insignificant, and the contact pressures are low enough that viscosity rise is negligible, i.e. hydrodynamic lubrication [36]. The boundary between the two also corresponds well with the distinction being made between hydrodynamic and EHL in this methodology, presented by the black and blue regions of the plot.

4.4. Dry vs lubricated tribo-dynamic model

Previously presented results confirmed the significance of considering tribo-dynamic coupling on the tribological predictions. The aim of this section is to assess the significance of this coupling on dynamics via affecting contact load and stiffness values. The surface deformation at the EHL contact is further exacerbated by the presence of the lubricant film. Since the contact load and contact stiffness are governed by this deformation, neglecting the film leads to an underestimation of the total load at the roller-race contact. At higher speeds, such as those present in modern electrified powertrains, the growth of the lubricant film due to the increased entraining motion into the conjunction cannot be neglected – as is shown in Fig. 11 with a film growth from 0.1 to 1.9 μm . The implicit tribological model was run for two cases, including and negating lubricant film thickness in the deformation obtained from equation (5). The difference in magnitude at each time step is computed, and the increase in load magnitude between a dry and lubricated model is calculated. For EHL loads, the magnitude of the load difference through the speed sweep is plotted in Fig. 15.

There is an increasing load difference across the speed sweep, with fluctuations arising from the dynamics of the system. It is clear that neglecting lubricant film thickness leads to significant underestimation of the contact load, hence inaccurate dynamics as well as tribological calculations. This effect gains more significance at higher speeds which highlights the necessity of considering tribo-dynamic coupling for high-speed conditions in electrified powertrains. To fully understand the requirement for a lubricated bearing model, the percentage difference between both cases is presented at three different rotational speed snapshots of 3 050 rpm, 14 135 rpm, and 14 855 rpm in Fig. 16. At low speeds and relatively low dynamic load, the addition of the film contributes to a 14.8% greater load prediction than a dry model, showing that the film inclusion has a significant contribution even at low rotational speeds. At shaft speeds of 14 135 rpm, the first order resonance in the system, as shown in the frequency plots, creates high dynamic loading. At peak load, the growth of the film is still present, however, the high contact deformation is close to the magnitude of the film growth, hence the difference between dry and lubricated model reaches 25.1%. As the system passes through this resonant region and the overall dynamic load is reduced, the percentage load difference reaches values as high as 149% as the effect of the film growth at high speeds exceeds that of the surface deformation.

At high speeds in periods of resonance, the magnitude of the bearing load dominates, and the effect of the increasing film thickness with speed diminishes in regions of resonance. The percentage difference

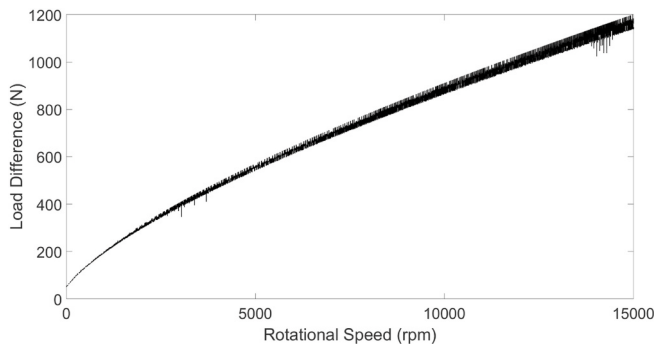


Fig. 15. Contact load difference between dry and lubricated model.

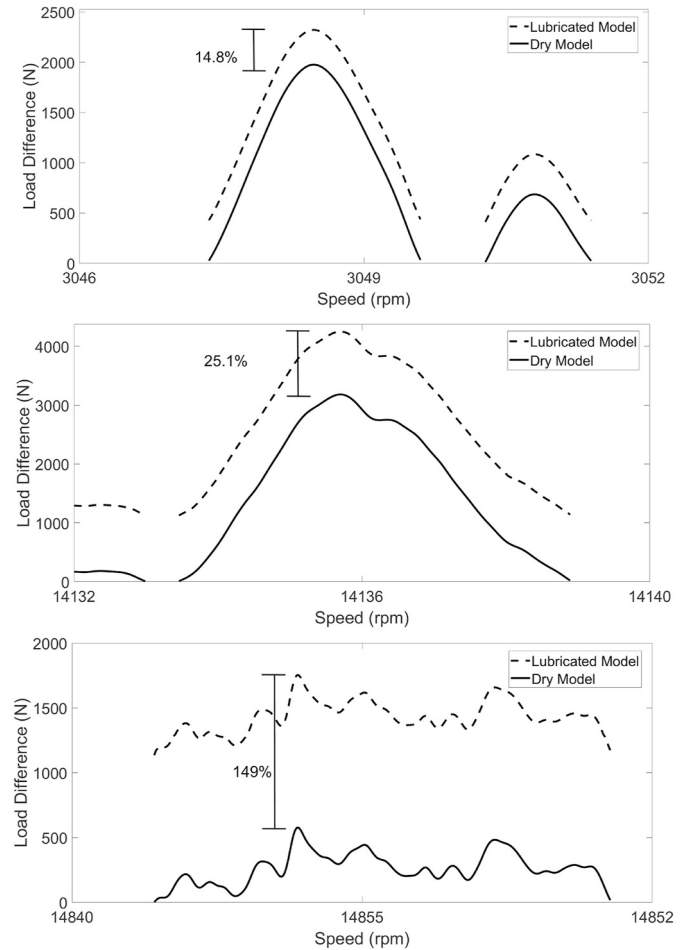


Fig. 16. Dry and lubricated model load difference: a) 3 050 rpm, b) 14 135 rpm, c) 14 855 rpm.

between the dry and lubricated model is lower as the external force and corresponding surface deformation prevails the effect of the film. However, at high speeds outside of this period of resonance, the film thickness is of the same order as the deformation and the percentage difference between the two models is much greater.

4.5. Numerical EHL results

Full numerical simulation is required to obtain detailed pressure and film thickness distributions. These distributions reveal the realistic pressure and film values at the contact for in depth durability, efficiency and thermal analysis. At 8 350 rpm, focussing on one roller orbit, the selected points for EHL numerical analysis are shown in Fig. 17. These load values are found from the implicit tribological model when the roller enters the loaded region of the bearing. The corresponding points on the bearing circumference are also shown.

The load values are passed explicitly to the numerical EHL model along with entrainment velocity, lubricant and solid properties. From the nodes presented, the pressure distribution and film thickness across the contact are obtained. These are presented in Fig. 18.

In each of these plots, it is possible again to see the central film thickness drop as the roller enters, then exits the loaded region. These central film values are represented by circles in Fig. 18. Agreement between the extrapolated film formulae and the numerical model for calculating central film values are presented in Table 4. This confirms the validity of using the extrapolated film thickness equation in the implicit tribological model. It is shown that the central nodes which correspond to the higher loads in the loaded region have the lowest

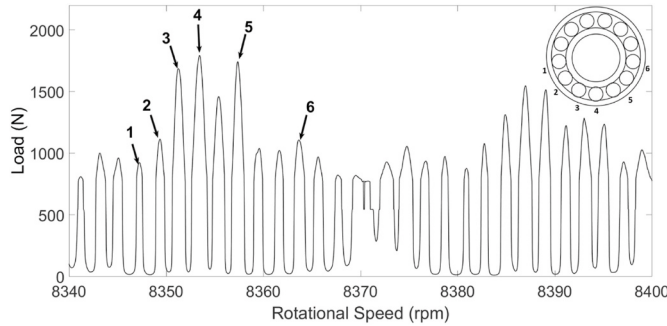


Fig. 17. Selected points for numerical EHL model.

percentage difference in comparison to the lightly loaded nodes at the outer edges.

5. Conclusions

A new methodology comprising experiments and numerical modelling has been developed to allow component and conjunction level tribodynamic analysis of a roller bearing under speeds and loading conditions previously not reported. The experimental data contain the physics of the dynamics and tribology within the bearing, negating the need for a simplified and computationally intensive dynamic bearing model. The tribological conditions at the contact between an individual roller and raceways are numerically analysed. All possible lubrication regimes, including mixed-EHL and hydrodynamic, are considered as the roller passes through loaded and unloaded regions.

The presented research investigates a new range of working conditions under high speeds, representative of modern electrified powertrains. This study helps to understand the prevailing regimes of lubrication as well as range of tribological quantities. Additionally, the interaction of tribological behaviour with dynamics of the system is investigated. The deeper and comprehensive understanding of these matters will support objective development of electrified powertrains in the future towards higher efficiency, durability and NVH refinement. The acquired knowledge and understanding will also support future developments of predictive tools by understanding the interaction of tribology and dynamics and the significance of considering this multi-physics interaction. The following conclusions can be made based on presented results:

- The contact experiences an order of magnitude increase in film thickness across the speed sweep. This highlights the necessity of implicitly including the lubricant film in any predictive tribodynamic model; an approach that is not reported on in open literature for high-speed dynamic roller bearing analysis.
- A comparison between the dry and lubricated contact model further reinforces the need to include the lubricant film in high-speed roller bearing analysis, with percentage differences in load between both models up to 149% at 14 855 rpm. Neglecting this film by using the common dry Hertzian approach would lead to an underestimation of the total load at the roller-race contact.
- At higher speeds, such as those present in modern electric powertrains, it is shown that the growth of the lubricant film must be included implicitly within the dynamic bearing analysis.
- The load values obtained from the lubricated tribological model have been used explicitly within a 1-dimensional EHL model to calculate the pressure distribution and film thickness across the contact. The workflow of using an explicit EHL model based on the analytical tribological contact mechanics is valid, with good agreement between central film thickness values for both.
- The explicit EHL approach significantly improves the computational efficiency of the model whilst maintaining accuracy, since only the

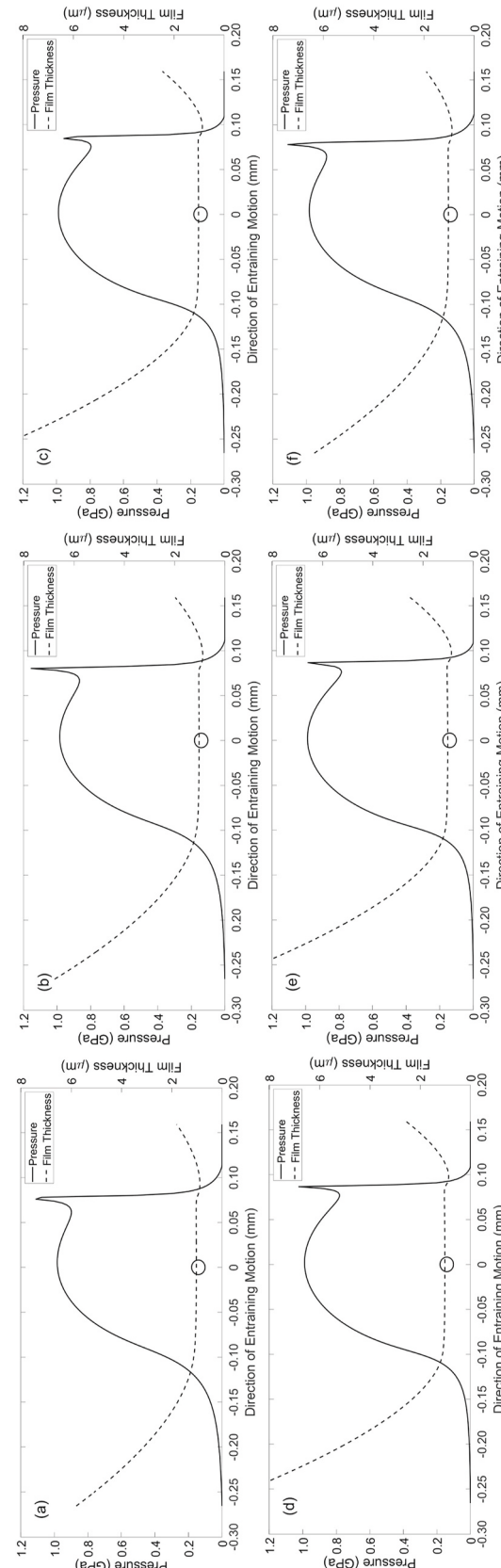


Fig. 18. EHL Pressure and Film Thickness Distributions: a) Node 1, b) Node 2, c) Node 3, d) Node 4, e) Node 5, f) Node 6.

Table 4

Extrapolated film formulae and numerical model central film thickness comparison.

Node	Extrapolated formulae central film thickness (μm)	Numerical model central film thickness (μm)	Percentage difference (%)
1	1.142	1.026	11.3
2	1.122	1.025	9.46
3	1.075	1.019	5.49
4	1.068	1.016	5.11
5	1.072	1.018	5.30
6	1.122	1.025	9.46

central value of the film is required in the load calculation. This can be implicitly coupled to broaden the scope of the analysis that is being performed.

CRediT authorship contribution statement

H. Questa: Methodology, Software, Validation, Writing - original draft. **M. Mohammadpour:** Conceptualization, Software, Writing - review & editing. **S. Theodosiades:** Supervision, Writing - review & editing. **C.P. Garner:** Supervision, Writing - review & editing. **S.R. Bewsher:** Supervision, Software, Writing - review & editing. **G. Offner:** Supervision, Writing - review & editing.

Declaration of competing interest

The authors declare that they have no known competing financial interests or personal relationships that could have appeared to influence the work reported in this paper.

Acknowledgement

The authors wish to acknowledge the support of the Loughborough University Wolfson School of Mechanical, Electrical and Manufacturing Engineering PhD Studentship Scheme and the support of AVL List GmbH.

References

- [1] Mosquet X, Zablit H, Dinger A, Xu G, Andersen M, Tominaga K. The electric car tipping point. 2018.
- [2] Farfan-Cabrera LI. Tribology of electric vehicles: a review of critical components, current state and future improvement trends. *Tribol Int* 2019;138:473–86. June.
- [3] Wensing JA. The dynamics of ball bearings. *Wear* Mar. 1972;19(3):360.
- [4] Hao X, Zhai J, Liang J, Chen Y, Han Q. Time-varying stiffness characteristics of roller bearing influenced by thermal behavior due to surface frictions and different lubricant oil temperatures. *Tribol Int* 2020;144:106125. December 2019.
- [5] Akemi N, Tsuha H, Cavalca KL. Finite line contact stiffness under elastohydrodynamic lubrication considering linear and nonlinear force models. *Tribol Int* 2020;106219.
- [6] Aini R, Rahnejat H, Gohar R. A five degrees of freedom analysis of vibrations in precision spindles. *Int J Mach Tool Manufact* 1990;30(1):1–18.
- [7] Rahnejat H, Gohar R. The Vibrations of Radial ball bearings. *Proc Inst Mech Eng Part C J Mech Eng Sci* 1985;199(3):181–93.
- [8] Mohammadpour M, Johns-Rahnejat P, Rahnejat H. Roller bearing dynamics under transient thermal-mixed non-Newtonian elastohydrodynamic regime of lubrication. *Proc Inst Mech Eng Part K J Multi-body Dyn Dec.* 2015;229(4):407–23.
- [9] Rajab MD. Modeling of the transmissibility through rolling-element bearings under radial and moment loads. 1982.
- [10] Lim TC, Singh R. Vibration transmission through rolling element bearings. Part II: geared rotor system studies. *J Sound Vib* 1991;151(1):31–54.
- [11] Flack RD, Kostrzewsky GJ, Taylor DV. A hydrodynamic journal bearing test rig with dynamic measurement capabilities. *Tribol Trans Jan.* 1993;36(4):497–512.
- [12] Meyer LD, Ahlgren FF, Weichbrodt B. An analytic model for ball bearing vibrations to predict vibration response to distributed defects. *J Mech Des Apr.* 1980;102(2):205–10.
- [13] Matsubara M, Rahnejat H, Gohar R. Computational modelling of precision spindles supported by ball bearings. *Int J Mach Tool Manufact* 1988;28(4):429–42.
- [14] Wang F, Jing M, Yi J, Dong G, Liu H, Ji B. Dynamic modelling for vibration analysis of a cylindrical roller bearing due to localized defects on raceways. *Proc Inst Mech Eng Part K J Multi-body Dyn* 2015;229(1):39–64.
- [15] Liu J, Shi Z, Shao Y. An analytical model to predict vibrations of a cylindrical roller bearing with a localized surface defect. *Nonlinear Dynam* 2017;89(3):2085–102.
- [16] Guo Y, Keller J. Validation of combined analytical methods to predict slip in cylindrical roller bearings. *Tribol Int* 2020;148:106347. April.
- [17] Gohar R. *Elastohydrodynamics*. London: Imperial College Press; 1988.
- [18] Grubin AN. *Fundamentals of the hydrodynamic Theory of Lubrication of heavily loaded cylindrical surfaces*, book No. 3. Moscow (DSIR translation). Central Scientific Research Institute for Technology and Mechanical Engineering; 1949.
- [19] Demni M, Biboulet N, Abousleiman V, Lubrecht AA. Dynamic study of a roller bearing in a planetary application considering the hydrodynamic lubrication of the roller/cage contact. *Tribol Int* 2019;149:105696. March 2019.
- [20] Gupta PK. ‘Dynamics of rolling-element bearings—Part I: cylindrical roller bearing analysis’. *J. Lubr. Technol. Jul.* 1979;101(3):293–302.
- [21] Dareing DW, Johnson KL. Fluid film damping of rolling contact vibrations. *J Mech Eng Sci Aug.* 1975;17(4):214–8.
- [22] Mehdigoli H, Rahnejat H, Gohar R. Vibration response of wavy surfaced disc in elastohydrodynamic rolling contact. *Wear* 1990;139(1):1–15.
- [23] Walker J, Questa H, Bewsher SR, Schweiger C, Sopouch M. Experimental design for characterization of force transmissibility through bearings in electric machines and transmissions. In: 10th international styrian noise, vibration & harshness congress: the European automotive noise conference; 2018. p. 1–6.
- [24] Takeda R, Lisco G, Fujisawa T, Gastaldi L, Tohyama H, Tadano S. Drift removal for improving the accuracy of gait parameters using wearable sensor systems. *Sensors Dec.* 2014;14(12):23230–47.
- [25] Harris TA. *Roller bearing analysis*. third ed. New York: John Wiley and Sons; 1984.
- [26] Hamrock BJ, Dowson D. *Ball bearing lubrication: the elastohydrodynamics of elliptical contacts*. New York: John Wiley & Sons; 1981.
- [27] Rahnejat H. *Influence of vibration on the oil film in concentrated contacts*. University of London; 1984.
- [28] Dowson D, Toyoda S. A central film thickness formula for elastohydrodynamic line. In: Proc. Fifth leeds-lyon symp. *Tribol. Mech. Eng. Publ.*; 1979. p. 60–5.
- [29] Greenwood JA, Tripp JH. The contact of two nominally flat rough surfaces. *Proc Inst Mech Eng* 1970;185(1):625–33.
- [30] Evans CR, Johnson KL. Regimes of traction in elastohydrodynamic lubrication. *Proc Inst Mech Eng Part C J Mech Eng Sci* 1986;200(5):313–24.
- [31] Dowson D, Higginson GR. *Elasto-hydrodynamic lubrication*, SI. Oxford: Pergamon Press; 1977.
- [32] Roelands CJA. Correlational aspects of the viscosity-temperature-pressure relationship of lubricating oils. Delft: Delft University; 1966.
- [33] Okamura H. A contribution to the numerical analysis of isothermal elastohydrodynamic lubrication. In: *Tribology of reciprocating engines*. Elsevier; 1993. p. 313–20.
- [34] Budynas RG, Nisbett JK. *Shigley's mechanical engineering design*. ninth ed. New York: McGraw-Hill; 2011.
- [35] Masjedi M, Khonsari MM. Film thickness and asperity load formulas for line-contact elastohydrodynamic lubrication with provision for surface roughness. *J Tribol Jan.* 2012;134(1).
- [36] Hamrock BJ. Film thickness for different regimes of fluid-film lubrication. Cleveland: NASA Technical Memorandum TM-81550; 1980. p. 1–14.

Article

Tribodynamic Modelling of High-Speed Rolling Element Bearings in Flexible Multi-Body Environments

Harry Questa ^{1,*}, Mahdi Mohammadpour ¹, Stephanos Theodossiades ¹, Colin P. Garner ¹, Stephen R. Bewsher ² and Günter Offner ²

¹ Wolfson School of Mechanical, Electrical and Manufacturing Engineering, Loughborough University, Loughborough LE11 3TU, UK

² AVL List GmbH, 8020 Graz, Austria

* Correspondence: h.questa@lboro.ac.uk

Abstract: This study presents a new flexible dynamic model for drive systems comprising lubricated bearings operating under conditions representative of electrified vehicle powertrains. The multi-physics approach importantly accounts for the tribological phenomena at the roller–race conjunction and models their effect on shaft-bearing system dynamics. This is achieved by embedding a non-linear lubricated bearing model within a flexible system level model; this is something which has not, to the authors' knowledge, been reported on hitherto. The elastohydrodynamic (EHL) film is shown to increase contact deflection, leading to increased contact forces and total bearing stiffness as rotational speeds increase. Results show that for a 68 Nm hub motor operating up to 21,000 rpm, the input bearing EHL film reaches a thickness of 4.15 μm . The lubricant entrainment increases the roller–race contact deflection, causing the contact stiffness to increase non-linearly with speed. The contribution of the lubricant film leads to a 16.6% greater bearing stiffness at 21,000 rpm when compared to conventional dry-bearing modelling methods used in current multi-body dynamic software. This new methodology leads to more accurate dynamic response of high-speed systems necessary for the next generation of electrified vehicles.



Citation: Questa, H.; Mohammadpour, M.; Theodossiades, S.; Garner, C.P.; Bewsher, S.R.; Offner, G. Tribodynamic Modelling of High-Speed Rolling Element Bearings in Flexible Multi-Body Environments. *Machines* **2023**, *11*, 93. <https://doi.org/10.3390/machines11010093>

Academic Editor: Vincenzo Niola

Received: 22 November 2022

Revised: 29 December 2022

Accepted: 6 January 2023

Published: 11 January 2023



Copyright: © 2023 by the authors. Licensee MDPI, Basel, Switzerland. This article is an open access article distributed under the terms and conditions of the Creative Commons Attribution (CC BY) license (<https://creativecommons.org/licenses/by/4.0/>).

1. Introduction

Simulating electrified powertrains using flexible multi-body dynamic (FMBD) models can enable substantial cost and time savings for automotive manufacturers due to a reduced need for physical prototyping. With increasing complexity and operational speeds of these systems, the accuracy at the component level is of major importance. Bearings are crucial structural components and their dynamic response significantly affects the behaviour of the interconnected structures.

Modern electrified motors and transmissions operate at considerably higher speeds and lower loads than conventional powertrains [1]. This leads to much higher lubricant entrainment velocities at the roller–race conjunction of the bearings. Consequently, the elastohydrodynamic (EHL) film thickness can be of the same order of magnitude and often exceed that of the contact deformation predicted by dry Hertzian assumptions; hence, non-lubricated analyses are no longer valid.

The operating conditions of roller bearings in modern electric vehicle (EV) powertrains require dynamic modelling to capture system transients such as time-varying input forces, acceleration and eccentricity. Early quasi-static bearing models [2–5], are only applicable under steady-state operating conditions; however, the static equilibrium solutions [6–8] are of use to calculate load-deflection and individual element loading within dynamic models. Simplified 2-degree of freedom dynamic models [9] consider the purely in-plane motion of

the rolling elements in the radial and lateral directions of the bearings for the investigation of the frequency response to defects [10], the varying compliance effect [11] and the radial loading affects [12]. These models increase in complexity up to 5 degrees of freedom (DOF) to observe moment loading and centrifugal effects [13,14]. These analyses assumed a dry contact between the rolling elements and races, which was considered to be valid at lower speeds and high loads. This, however, neglects the effect of the lubricant film thickness in the contact mechanics and thus underestimates the contact deflection and hence the load.

Based on the experimental and numerical findings [15–17], the EHL film can be shown to increase the bearing stiffness, which continues to rise non-linearly with speed. It is therefore clear that the lubricant film in roller bearings operating at high speeds must be implicitly included in dynamic analyses.

As stated by Bizarre et al. [18], there are few studies in the open literature that combine the stiffness and damping of an EHL contact with classical bearing dynamics. Early lubricated bearing models use extrapolated formulae to provide a relationship between the load share and film thickness at each element's contact with the bearing raceways [19]. Aini et al. [20] implemented the extrapolated film approach from the work of Rahnejat and Gohar [19] into a five-DOF bearing equilibrium model. The work computes the deformation at each roller–race contact, combining the EHL film thickness with the elastic deformation of the contacting solids. The force–displacement relationship is shown to follow a non-linear trend. Mohammadpour et al. [21] employed a similar implicit tribodynamic analysis and then utilised a full numerical EHL analysis explicitly for further tribological studies. In their analysis, input shaft speeds of $209 \text{ rad}\cdot\text{s}^{-1}$ resulted in much slower entrainment velocities than are applicable for electrified powertrain analyses.

Sopanen and Mikkola [22] modelled the influence of various surface characteristics on bearing dynamics, including contributions from surface waviness, roughness, localised and distributed effects. Their six-DOF model accounts for the Hertzian contact deformation and the EHL film implicitly within the contact. This model was embedded in a multi-body dynamic (MBD) software to utilise its mathematical capabilities. This work does not, however, demonstrate the effect that the EHL film has on bearing stiffness, and the effect on system dynamics using flexible bodies is not analysed [23]. Sawalhi and Randall [24] used a constant preload approach to imitate the stiffening effect of the film. Whilst this effective preload captures the increased contact stiffness due to the presence of the EHL film, the film thickness does not vary based on the contact conditions.

More recently, Liu and Shao [25] investigated the effects of surface waviness, including the effect of the lubricant film using an equivalent stiffness model. Nonato and Cavalca [26] presented a methodology to model EHL contacts using a set of non-linear springs and viscous dampers. Bizarre et al. [18] applied this lubricated non-linear force contact to a five-DOF model of an angular contact ball bearing. This enabled a combined solution scheme for the bearing force equilibrium and the EHL contact. The formulated system of equations was solved, achieving force equilibrium for each rotation of a bearing under constant external load. The authors of this study noted the interest of combining such models within FMBD system level models.

None of the combined models above are embedded within a system level model comprising flexible bodies, and the effect of the change in the contact stiffness due to the lubricant film is not investigated at the system level. Furthermore, the high-speed operation and time-varying loads representative of electrified vehicle transmissions are not considered.

The authors here present, for the first time in the open literature, a coupled simulation approach to combine an implicit lubricated bearing model within a high-speed system level FMBD model. The time-varying system operating conditions reflect that of an electrified powertrain. The kinematic behaviour of a flexible shaft at each time step of a dynamic simulation is passed to the bearing model. A contact slicing method [6] is employed to calculate the reaction forces of the individual rolling elements based on the roller–race contact deflection [27]. The total deflection is influenced by the thickness of the

EHL film within the contact, which is implicitly included within the analysis through an iterative procedure. The resulting race forces are returned to the system level model and the equations of motion are solved at each time step. Comparisons are made between modelling the bearings as dry and lubricated. The dynamic results including acceleration, force magnitudes and stiffness variations have been obtained for realistic loading conditions of a 54 kW electric hub motor up to speeds of 21,000 rpm.

2. Methodology

A co-simulation methodology combines a system level model of a flexible shaft and rigid housing, developed in AVL EXCITE™, with component level models of the lubricated bearings, developed in MATLAB and Simulink. Operating conditions such as rotational speed and external forces are defined in the system level model. Time step, iteration accuracy and simulation length are also defined. Material, geometric and rheological properties of the bearings are defined in the component level model. The kinematic conditions from the system level model (i.e., displacements and velocities in all active degrees of freedom) are passed to the component level model at each time step. For each individual rolling element, the non-linear force–deflection relationship is employed in conjunction with the EHL film calculations to compute the contact reaction force between the roller and race. The resultant force on the inner bearing race due to the contact forces and orbital positions of all elements is then returned to the system level model. The equations of motion are then solved, and the time step is advanced once numerical convergence is achieved. A flowchart of these models representing each time step of the simulation is shown in Figure 1.

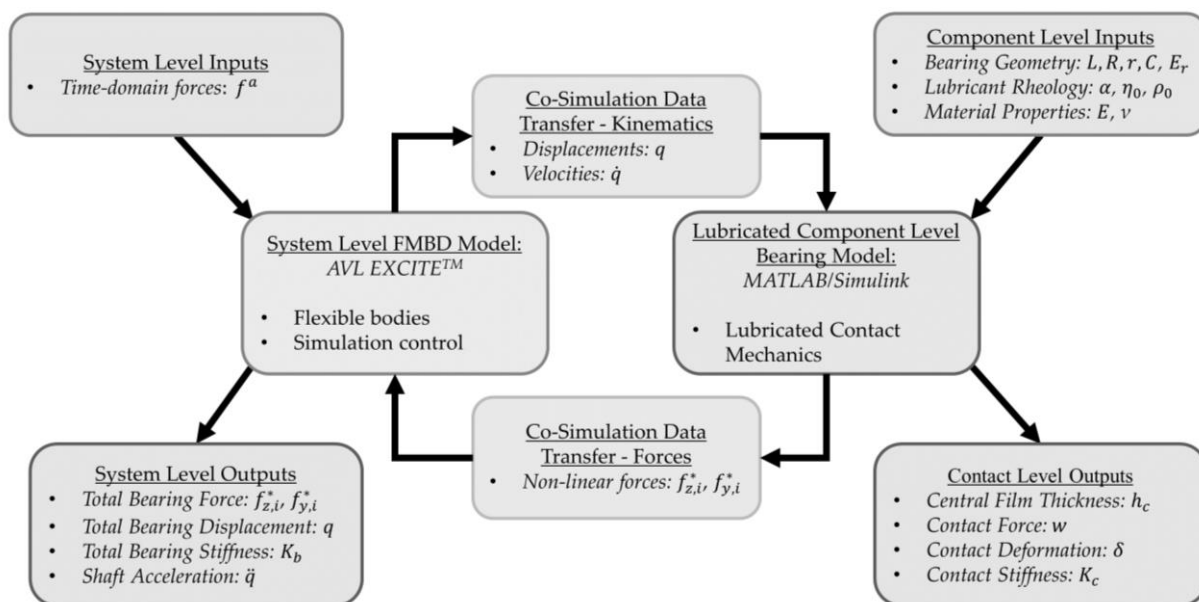


Figure 1. Flowchart of Models.

2.1. System Level Flexible Model

The system level model consists of a flexible shaft, supported by two cylindrical roller bearings in a rigid housing (see Figure 2). The shaft is 472.5 mm between bearing centres, with a 50 mm main diameter and 25 mm diameter bearing seats. The cylindrical roller bearings act as interference elements between the shaft and housing. The shaft can exhibit lateral motion in both vertical (z) and horizontal (y) directions and rotation about the x -axis (see Figure 2). External load is applied at the shaft centre as a time-varying input force, to simulate the gear mesh excitation, or as a static load. The rotational speed is input as a boundary condition.

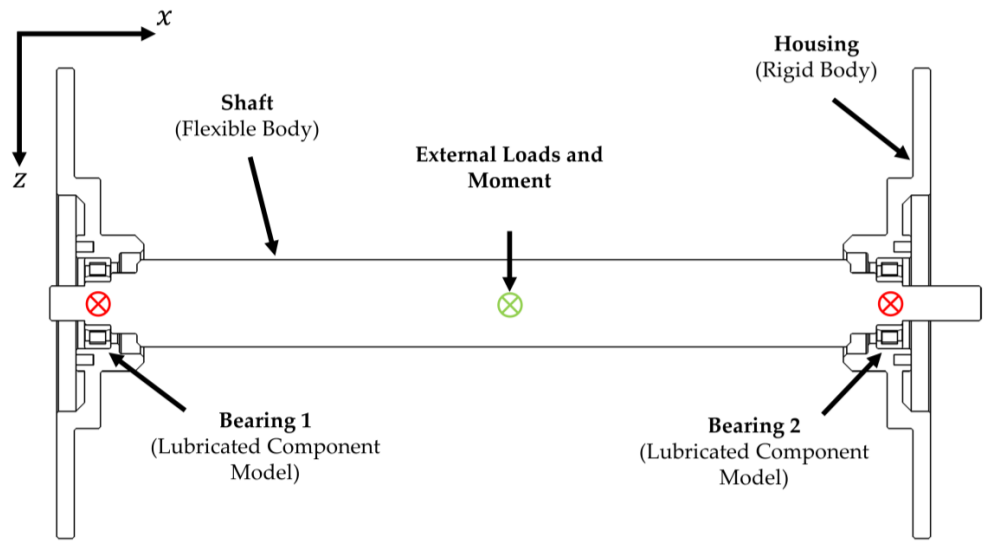


Figure 2. System Level Model Schematic.

In typical configurations containing flexible structures, it is possible for both the inner and outer races of a rolling element bearing to move when subject to load. For this analysis, however, it is sufficient to fix the outer race in space and consider only the displacement of the inner bearing race [28]. The housing in this study is treated as a rigid body of infinite stiffness; therefore, the race dynamics of the bearing are influenced only by the motion of the flexible shaft in the model. The loading on the inner race is reacted by the rolling elements on the inner raceway; this must therefore be solved to achieve a dynamic equilibrium.

Within the model, the shaft is treated as a body having linear elastic behaviour and the housing is treated as rigid. The bearings are modelled via non-linear contact forces acting between the shaft and housing.

The shaft is represented by a condensed finite element model and is discretised into a sufficiently high number of partial masses [29]. The total elastic deformation of the shaft is represented by translational and rotational displacement components of these individual partial masses. The mathematical modelling used in the FMBD solver is based on Newton's equations of motion and Euler's equation of angular momentum, respectively:

$$m_i \frac{\partial^2 x_i^{Abs}}{\partial t^2} = f_{F,i}^{Abs} \quad (1)$$

$$\frac{\partial}{\partial t} \left(I_{C,i}^{Abs} \omega_i^{Abs} \right) = f_{M,i}^{Abs} \quad (2)$$

where m_i and $I_{C,i}^{Abs}$ represent the mass and inertia tensors of the partial masses, i . The vectors of displacement and angular velocity are represented by x_i^{Abs} and ω_i^{Abs} , respectively, and are related to the centre of gravity of each partial mass. The force and moment vectors, $f_{F,i}^{Abs}$ and $f_{M,i}^{Abs}$, must be fulfilled for all partial masses in the shaft.

The combination of displacement and rotations of the shaft takes the form:

$$M\ddot{q} = f \quad (3)$$

where M represents the block-diagonal mass matrix of the shaft, consisting of the sub-matrices M_i , $i \in \{1, \dots, n\}$ that make up each partial mass of the full shaft. Acceleration, \ddot{q} , represents the second derivative of the displacement vector of all partial masses, $q = (q_1, q_2, \dots, q_n)^t$. Each element of this vector has six elements associated with it that represent the six degrees of freedom—three rotational and three translational ($q_i = (u_{t1}, u_{t2}, u_{t3}, \varnothing_1, \varnothing_2, \varnothing_3)^t$).

The forces and moments acting on each partial mass are contained in the sub-vectors of force, $f = (f_1, f_2, \dots, f_n)^t$. These are split into a sum of internal force terms, f_i^{int} , external force terms, f_i^{ext} and non-linear inertia terms, p^* . As with the partial mass terms, these are made up of six elements, each representing a degree of freedom:

$$f_i^{int} = \begin{pmatrix} f_{i,1}^{int} \\ f_{i,2}^{int} \\ f_{i,3}^{int} \\ f_{i,4}^{int} \\ f_{i,5}^{int} \\ f_{i,6}^{int} \end{pmatrix} \quad (4)$$

where each component of force, $f_{i,k}^{int}, k = 1, \dots, 6$ is evaluated using the linear-elastic approach.

$$f_{i,k}^{int} = \sum_{j=1}^{6,n} f_{i,j,k}^{int} \quad (5)$$

$$f_{i,j,k}^{int} = -\left(d_{i,j,k} \dot{q}_k + k_{i,j,k} q_k \right) \quad (6)$$

where d and k represent the material damping and stiffness coefficients, respectively.

Grouping the damping and stiffness coefficients into one matrix gives the equation of motion after rearrangement. This equation represents the behaviour of the total system of rigid partial masses that make up the shaft, and considers both general global motion and small body motion (vibrations) [30]:

$$M\ddot{q} + D\dot{q} + Kq = f^{ext} + p^* \quad (7)$$

The vector of external forces and moments, f^{ext} , is the sum of excitation forces, f^* , and external loads, f^a . The external loads and moments applied to the shaft, f^a , are determined functions given in time and are input as both time-varying and static loads on the system. The non-linear excitation force term, f^* , represents the reaction forces from the lubricated component level bearing model.

$$f^{ext} = f^* + f^a \quad (8)$$

Partial mass displacements (q_i) and velocities (\dot{q}_i) at the bearing locations are output from the dynamic model and used as boundary conditions within the lubricated component level bearing model at each time step of the simulation. This model returns resultant forces and torques on the inner race of each bearing (f_i^*) which are then used to solve the equation of motion (Equation (7)) within the dynamic model (see Figure 1).

2.2. Lubricated Component Level Model

The displacement and velocity vectors from each node connecting the shaft to the bearings (q_i and \dot{q}_i respectively) comprise six-DOF. For this lateral DOF model, translations in z and y are considered, as well as angular displacement around the rotational axis, x . A schematic of the bearing is shown in Figure 3.

Between the roller and raceways, under sufficient load, the pressures in the non-conformal contact are high enough to cause elastic deformation of the surfaces and a significant increase in lubricant viscosity. This, combined with relative motion between the contacting bodies, leads to the generation of an EHL contact. The stiffness of the EHL film is typically 1–2 orders greater than the stiffness of the contacting bodies [17]. In this analysis, the film stiffness was calculated using

$$K_{EHL} = \frac{dw}{dh_c} \quad (9)$$

The lowest average film stiffness was 5.1×10^9 N/m, which is over one order greater than the contacting material stiffness. The material therefore dominates the stiffness of the contact, and the stiffness of the EHL film can be neglected. The film is modelled as a rigid element that is present between the roller and race [31–33].

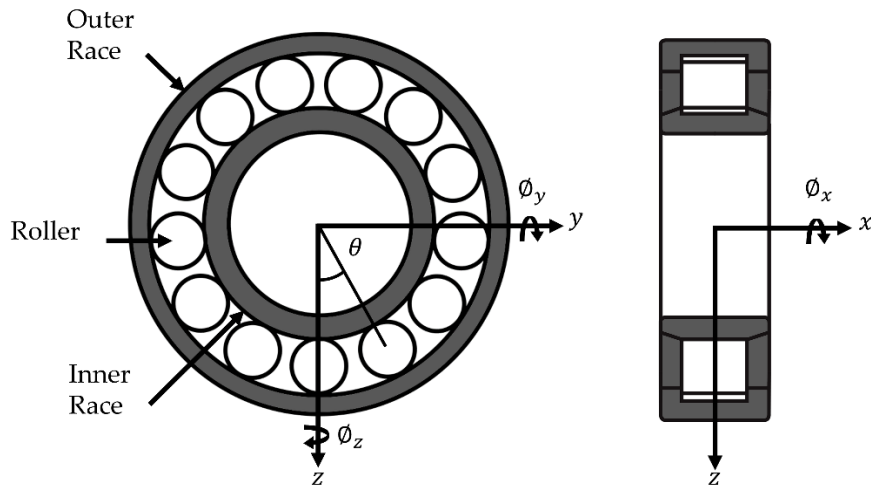


Figure 3. Bearing Schematic.

The contact deformation (δ) is therefore a function of the displacement of the inner bearing race, the angular displacement of the roller about the rotational axis (θ) thickness of the EHL film (h_c) and any clearance or radial preload ($\pm C$) within the bearing [19,21]:

$$2\delta = 2(h_c - C) + z\cos(\theta) + y\sin(\theta) \quad (10)$$

Figure 4 demonstrates this more clearly. The total contact deformation is the summation of the central film thickness (h_c) and the material deformation (δ_m) predicted from the dry-Hertzian contact assumption. Conventional dry analysis only accounts for the dry material deformation at the contact.

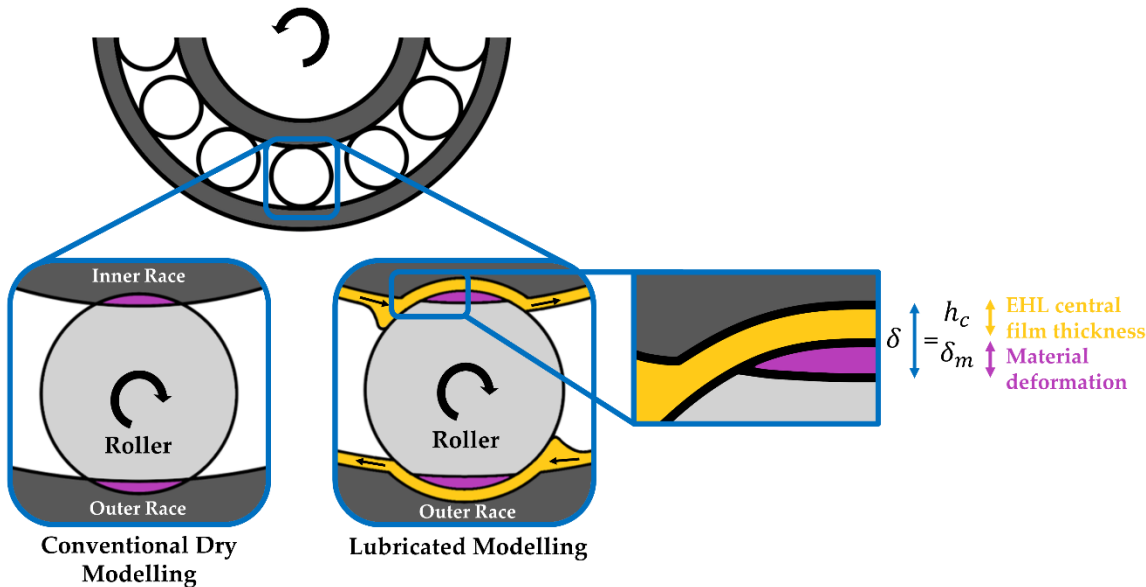


Figure 4. Dry vs. Lubricated Roller–Race Contact.

The extrapolated central film thickness for a line contact, assuming a fully flooded contact inlet, is therefore obtained from [34]:

$$h_c = R_r \left[3.06 G^{0.56} U^{0.69} W^{-0.1} \right] \quad (11)$$

where the following dimensionless parameters are used:

$$W^* = \frac{W}{E_r R_r l_a}, \quad U^* = \frac{\eta_0 U}{E_r R_r}, \quad G^* = E_r \alpha \quad (12)$$

Comprehensive analytical models [35,36] account for the tilting and skew of the rolling elements. Skew has the effect of varying the entrainment speed along the length of the roller, and tilt will affect the contact gap. Due to the stiff housing and shaft used in this analysis, the tilt and skew angles are very small. The entraining motion and contact gap along the contact length can be considered consistent, and a 1-dimensional analysis for the EHL film thickness is therefore appropriate [14].

The bearings are modelled with a light preload due to mounting interference. In practical applications, the preload is applied to prevent skidding and chaotic behaviour due to the emergence of zero stiffness regions [37]. In contrast, excessive preload can lead to frictional power loss and wear. Assuming pure rolling, the speed of the entraining motion is given by [38,39]:

$$u = \frac{R\omega}{r} \left(\frac{(R+2r)}{(R+r)} \right) \quad (13)$$

Due to the dependency of load on the film thickness, an iterative approach is performed to calculate the contact force. Convergence criteria for the EHL film must be met at each time step of the simulation before the bearing forces are returned to the system level model and the equations of motion are solved:

$$\frac{h_c^m - h_c^{m-1}}{h_c^{m-1}} \leq 0.001 \quad (14)$$

where m represents the iteration number.

The individual roller–race contact forces are calculated based on the contact deformation. In the case of a rolling element, a cylindrical body of finite length, the contact problem is non-Hertzian. The surfaces cannot be modelled as locally quadratic due to the presence of crowned (rounded) edges [40]. The most widely used technique to calculate the force–deflection relationship is the contact slicing technique. Whilst this does not reflect edge stress concentrations, these stresses are only distributed over a small area and hence can be neglected for the purpose of force equilibrium [41]. In general, this technique is favoured for its simplicity, speed and sufficient accuracy. The contact slicing technique employed in this study was developed by Andreason [6] for modelling these non-Hertzian line contacts.

Modelling the roller–race contacts as a line contact between a cylindrical roller and a flat surface, Lundberg’s [27] expression between contact force per unit length (w) and deformation (δ) was used.

$$\frac{\delta}{l_a} = \frac{2w}{\pi E_r l_a} \ln \frac{\pi E_r l_a}{w} \quad (15)$$

where E_r is the equivalent elastic modulus of the two materials and l_a is the active length of the roller. This assumes that the pressure distribution is uniform along the length of the contact, and elliptical across it. This neglects side leakage along the contact (x_c) due to the contact dimensions in this direction being much larger than the dimensions across it (y_c). This is valid apart from the small regions at the edges of the contact.

From Equation (15), the contact force per unit length of an individual slice along the roller–race contact can be calculated. This is valid if there is no separation of the bodies, i.e., the contact deformation does not become negative ($\delta_s > 0$).

$$w_s = \pi E_r l_s \left(\frac{0.5\delta_s}{7.358l_s} \right)^{1.11} \quad (16)$$

where s represents the slice number, and l represents the slice length.

The application of the slicing technique was validated against the open literature. de Mul et al. [28] compared results obtained from an experimental rig with the numerical results calculated using both the approximate slicing technique and the sophisticated non-Hertzian technique [42]. By replicating the geometry of the test bearing used in their analysis, the application of Andreason's slicing technique used for this analysis was validated with good agreement (see Figure 5). This method is a much faster way of calculating the contact load and moment than more sophisticated methods by de Mul, yet still maintains high accuracy.

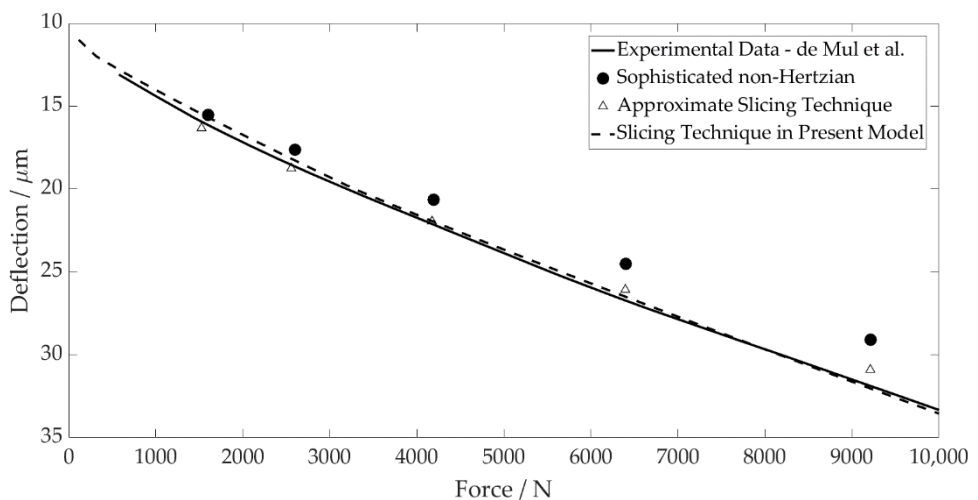


Figure 5. Contact Level Validation.

The total contact load W and moment T are obtained by summing the contributions from all loaded slices:

$$W = \sum_s w_s l_s \quad (17)$$

$$T = \sum_s w_s l_s x_{c,s} \quad (18)$$

with $x_{c,s}$ being the distance to the centre of each slice in the conjunction coordinate system. It is assumed that the total contact deflection is shared equally between the inner and outer races despite slight differences in the contact geometry. The entrainment velocity is equal at each contact, which is the governing parameter for the lubricated contact force differences.

Experimental measurements show that the damping of a rolling element bearing arises from multiple sources, including: (1) lubricant film damping at the contacts; (2) material damping due to Hertzian deformations and (3) interface damping between assembled components [17]. These measurements show that damping decreases with rotational speed, tending towards a constant value. Sopanen and Mikkola [22] summarised the findings of Mitsuya et al. [43] and Aini et al. [20], concluding that the film damping is moderate. The linearised viscous damping method adopted in their study is therefore also adopted here. The damping force for each roller is obtained as a factor of the contact stiffness and contact penetration velocity [44]. This is defined as:

$$|F_d| = -f_{damp} K_c \dot{q} \quad (19)$$

where K_c is the contact stiffness, and the damping factor, f_{damp} , is in the range of $(0.25 - 2.5) \times 10^{-5}$ as reported by Krämer [44].

At each time step of the analysis, these calculations are performed for each individual roller in the complement. The total bearing force acting on the inner race is solved by splitting the total contact force on each roller into its components and summing their contributions.

$$f_{z,i}^* = \sum_N W \cos(\theta) - \sum_N F_d \cos(\theta) \quad (20)$$

$$f_{y,i}^* = \sum_N W \sin(\theta) - \sum_N F_d \sin(\theta) \quad (21)$$

Due to the bearing preload, contact is maintained throughout the rollers' orbit; hence no emerging clearances are modelled in the lubricated analysis. The centrifugal forces on the rolling elements are negligible when compared to the contribution of the dynamic load and EHL film in this study. They are also not large enough to cause contact separation from the inner race, and have therefore been neglected.

Surface measurements of the rollers used in this analysis were taken using an Alicona InfiniteFocus Variation Microscope. The composite surface roughness value of a roller and inner race was calculated to be 91.3 nm. This gives a lambda value of 5.88 for the thinnest EHL film at 1000 rpm. The asperity interaction is not considered as the EHL film fully supports the load. Due to the pure rolling and zero sliding assumption, friction at the contacts is therefore neglected and the analysis is performed under isothermal conditions.

The bearing geometry is detailed in Table 1. The rheological and material properties are detailed in Table 2, representing ambient operating conditions in an individual hub-motor transmission.

Table 1. Bearing Specification.

Parameter	Value
Inner race bore diameter	25 mm
Pitch diameter	60 mm
Roller diameter	8.8 mm
Roller length	15 mm
Number of rollers	17
Radial interference	2 μ m

Table 2. Lubricant and Material Properties.

Parameter	Value
Pressure viscosity coefficient (α)	2.1×10^{-8} Pa $^{-1}$
Atmospheric lubricant dynamic viscosity (η_0)	0.08 Pa·s
Lubricant inlet density (ρ_0)	833.8 kg·m $^{-3}$
Modulus of elasticity of contacting solids (E)	210 GPa
Poisson's ratio of contacting solids (ν)	0.3

2.3. Representative Excitation Methodology

The system level model is decomposed, with the excitation forces calculated externally before the application within the model. A separate electrified transmission model is used to generate realistic excitation forces and torques from a spur gear pair and a permanent magnetic synchronous motor (PMSM). This system represents the first stage of an electric hub motor used in automotive applications.

Radial and tangential gear pair forces at the pinion centre, as well as torque fluctuations of the electric motor, are extracted to be used as inputs to the system level model. These are applied as external forces to the shaft, f^a , from Equation (8). All bodies in this separate system were modelled as rigid, so that structural excitation forces did not contribute to the resultant forces at the pinion.

The motor has a peak torque of 68 Nm, and a maximum operating speed of 21,000 rpm. The torque transfer through the gear pair reduces as the speed increases due to the torque profile of the PMSM, as shown in Figure 6. The stator tooth forces from the PMSM are neglected in the model due to their minimal contribution to the lateral forces once resolved. For input to the model, the radial and normal forces are simplified by adopting sinusoidal inputs of the same magnitude and frequency of the gear pair at different speeds. The torque ripple from the motor is simplified using the same method.

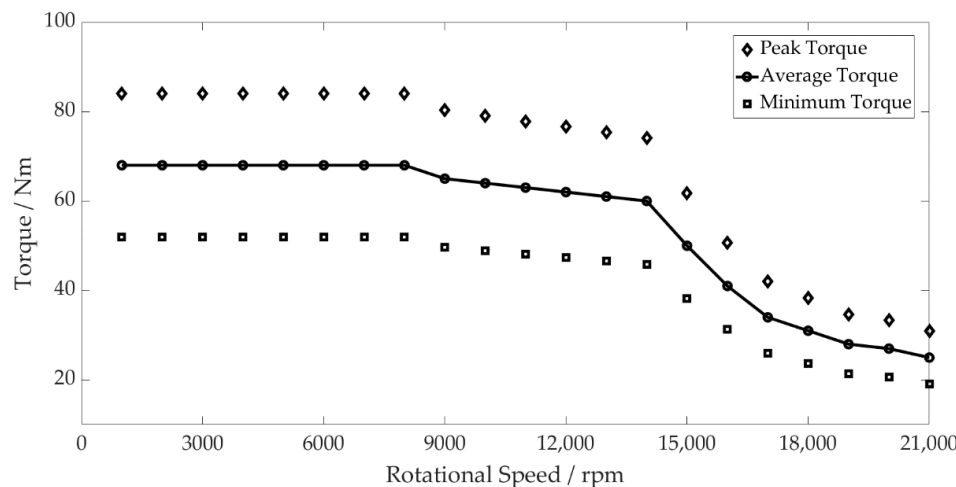


Figure 6. PMSM Torque Profile and Maximum and Minimum Torque Fluctuation.

The gear pair geometry is shown in Tables 3 and 4.

Table 3. Pinion Geometry.

Parameter	Value
Number of teeth	17
Normal module	0.004 m
Normal pressure angle	20°
Helix angle at pitch circle	0°
Active tip diameter	0.076 m
Active root diameter	0.065 m
Width	0.035 m

Table 4. Gear Geometry.

Parameter	Value
Number of teeth	51
Normal module	0.004 m
Normal pressure angle	20°
Helix angle at pitch circle	0°
Active tip diameter	0.212 m
Active root diameter	0.202 m
Width	0.030 m

3. Results and Discussion

A quasi-dynamic speed sweep has been performed from 1000 to 21,000 rpm. The simulations are performed every 1000 rpm, refined to 250 rpm intervals throughout a period of system resonance between 12,000 rpm and 14,000 rpm. The operating envelopes are generated by plotting the maximum and minimum values from the steady-state signals at each speed interval. The conjunction level results are obtained from an individual roller and its contact with the inner raceway. The component and system level results are taken

from the geometric centre of the inner bearing race, corresponding to the bearing seat on the shaft. The following figures represent results in the y -direction, the largest component of excitation due to the tangential force from the gear meshing.

The contact level results (Figure 7) show a difference in the contact stiffness between the dry and lubricated models. The dry model follows the torque profile of the motor, with stiffness decreasing as the contact forces reduce. The period of resonance leads to the larger amplitude excitation of the shaft, resulting in an increase in the contact stiffness due to the force–deflection non-linearity. The lubricated model, however, shows an increase in the contact stiffness throughout the speed sweep. This is due to the higher levels of deformation at the contact as the lubricant is entrained, which increases with the shaft rotational velocity. This behaviour was experimentally observed by Dietl, concluding that the oil-wedge between the rolling elements and raceways reduces the internal clearance of the bearing and increases its stiffness [17]. The contact stiffness in the lubricated bearing model under the same operating conditions is therefore 24.9% greater at 21,000 rpm.

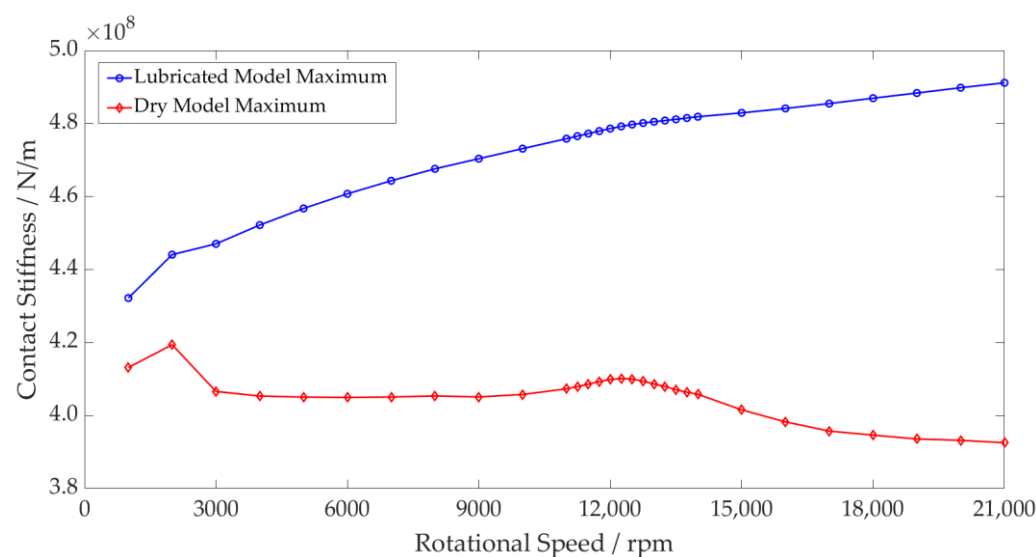


Figure 7. Rolling Element Contact Stiffness—Dry vs. Lubricated Maximum Values.

The peak contact force has been compared between both models. The percentage increase between the dry and lubricated models is shown in Figure 8. This more clearly shows the disparity between both models at the contact, with the largest difference being 9.6 times at maximum speed. During resonance, the inner race force reaches a peak of 1514 N, resulting in surface deformation magnitudes of 0.92 μm and 3.81 μm at the dry and lubricated conjunctions, respectively. As noted in previous works [15], higher loads lead to a greater surface deformation to the film thickness ratio, causing the percentage difference between the dry and lubricated models to reduce. Once the loads reduce as the speed increases, the percentage increase continues to rise.

The total bearing stiffness is a combination of all contact stiffnesses between the elements and raceways. These contact stiffnesses vary non-linearly with force, resulting in the total bearing stiffness varying accordingly. For the dry model, this is clearly demonstrated, with the greater total bearing stiffness at the peak of the resonance due to the greater bearing forces (see Figure 9). This does not, however, capture the change of the total bearing stiffness with speed; the average bearing stiffness does not change. The lubricated bearing is not only stiffer than the dry bearing, but this stiffness also increases with speed. This is shown in Figure 9 by the non-linear increase in the average lubricated bearing stiffness values compared to the constant values for the dry model. The combination of these two factors leads to the lubricated model having a 16.6% greater maximum total bearing stiffness at 21,000 rpm than the dry model.

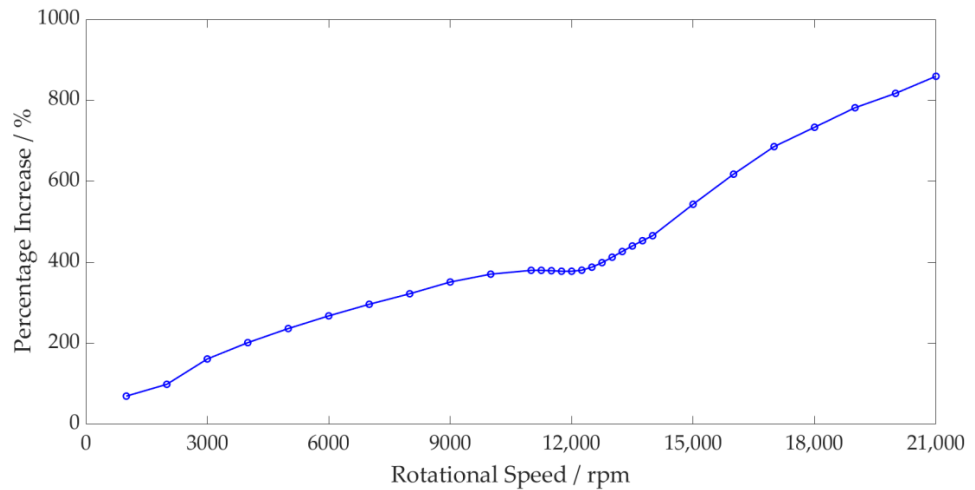


Figure 8. Rolling Element Contact Force—Dry vs. Lubricated Percentage Increase.

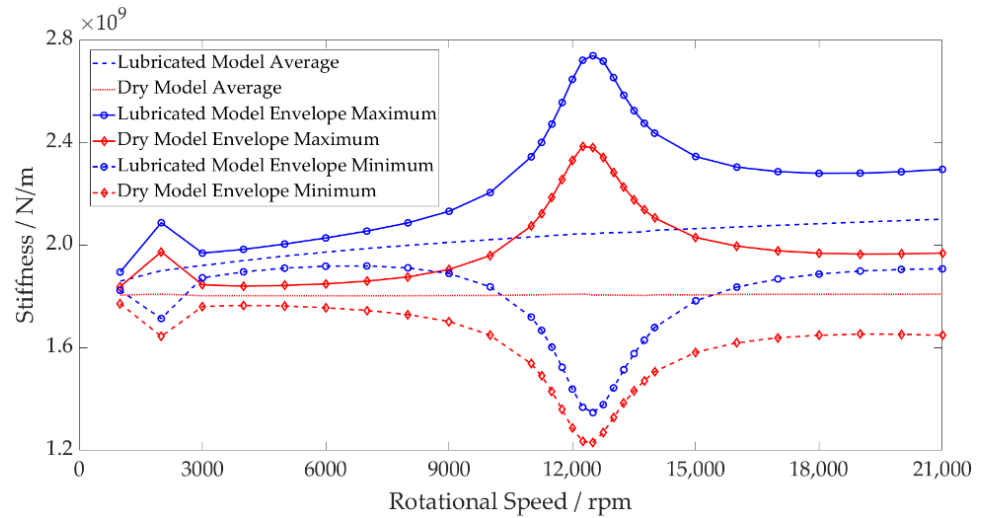


Figure 9. Inner Race Stiffness—Dry vs. Lubricated Operating Envelope.

Due to the greater total stiffness of the bearing, the shaft displacement of the lubricated model is lower both on average and peak to peak for the same applied force in comparison to the dry model (see Figure 10). Through the period of resonance, the large inner race forces result in the roller–race separation of the unloaded rollers within the dry model. This leads to greater shaft displacement as the inner race moves into this region of zero stiffness until roller–race contact is made, and a reaction force is established.

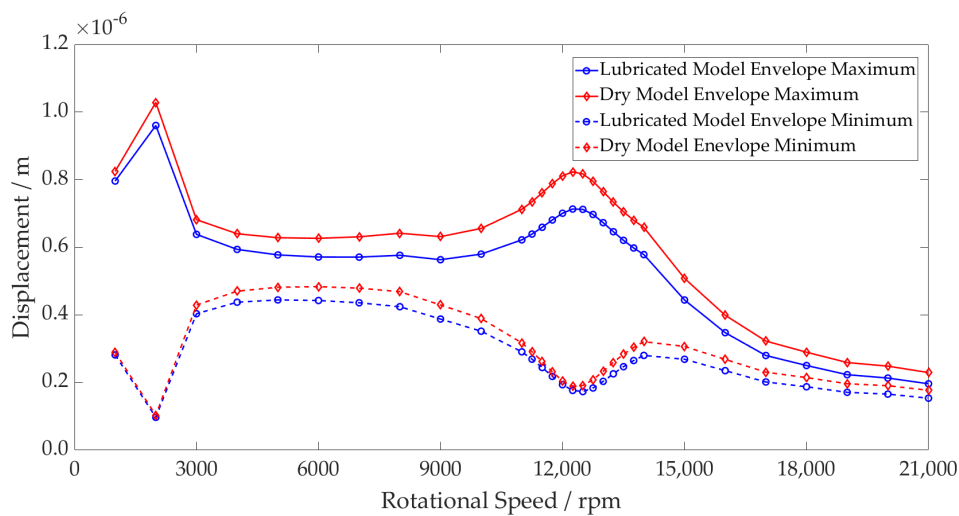


Figure 10. Inner Race Displacement—Dry vs. Lubricated Operating Envelope.

Figure 11 shows that the acceleration peak of the system resonance occurs at 12,500 rpm (3542 Hz) for the lubricated model as opposed to 12,250 rpm (3470 Hz) for the dry model. This shift in natural frequency indicates a stiffer overall system. The magnitude difference between the dry and lubricated models can also be attributed to the unloaded regions of the dry bearing. The contact deformation arising from the loading of the inner race is sufficient to cause the rollers geometrically opposite to become separated from their contacts. Contact is lost between the roller and raceway, leading to zero contact stiffness. The inner race moves into this region until it is reacted by a contact force once again. These regions of zero stiffness are shown in Figure 12, where the minimum stiffness of an individual rolling element and raceway contact in the dry model drops to zero due to separation. For the lubricated model, contact is maintained throughout.

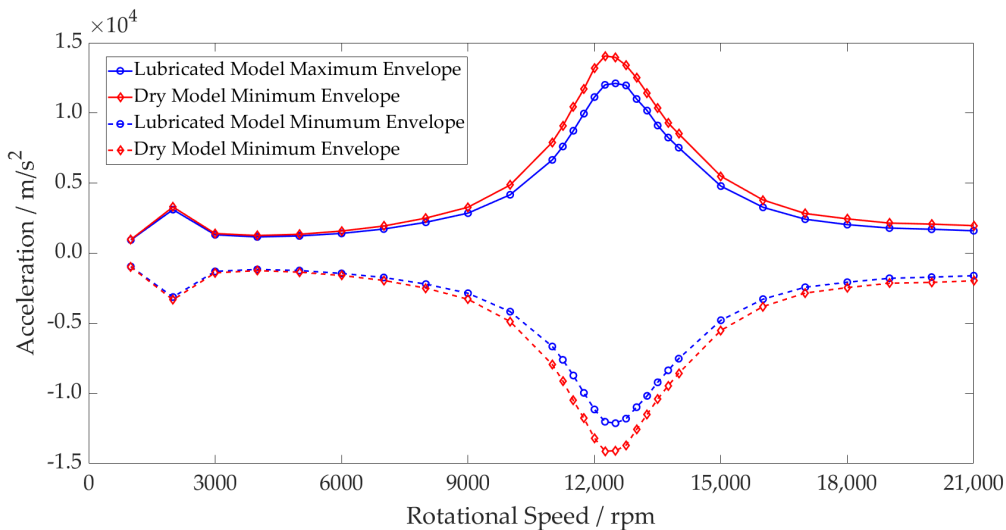


Figure 11. Inner Race Acceleration—Dry vs. Lubricated Operating Envelope.

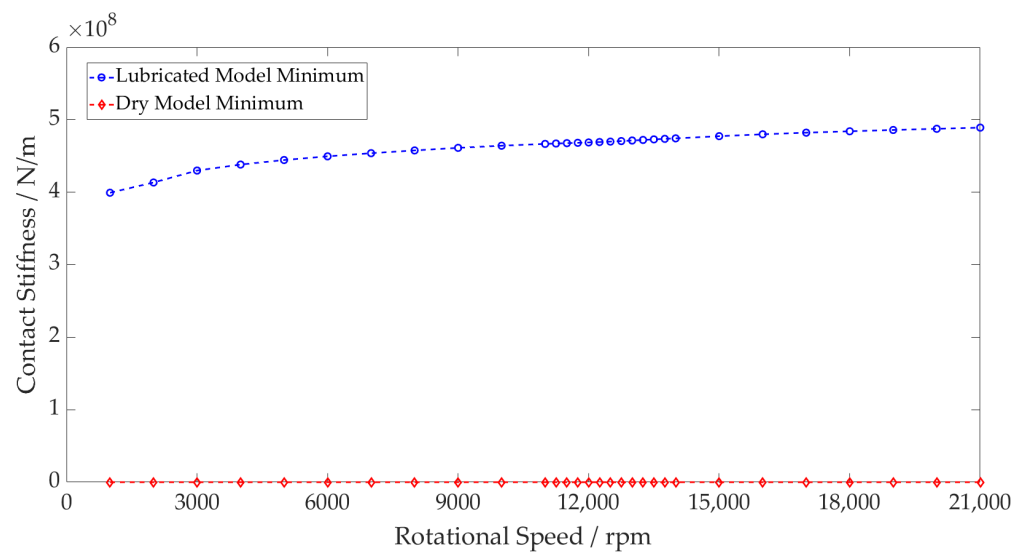


Figure 12. Rolling Element Contact Stiffness—Dry vs. Lubricated Minimum Values.

Analysing the conjunction level results from the lubricated model, the contact force due to the gear mesh frequency is shown superimposed on the ball pass frequency as an individual element passes through the loaded region of the bearings (Figures 13 and 14). The higher contact forces result in a reduction in the central film thickness, also shown when observing the variation in film thickness for both plots. At 12,500 rpm, the force and film thickness fluctuations are much larger due to the high excitation levels of the shaft during resonance. At 21,000 rpm, even with a much lower torque transfer through the gear pair, the contact forces are greater than at 12,500 rpm. This is due to the contribution of the film enhancing the total contact deflection and hence increasing the contact force.

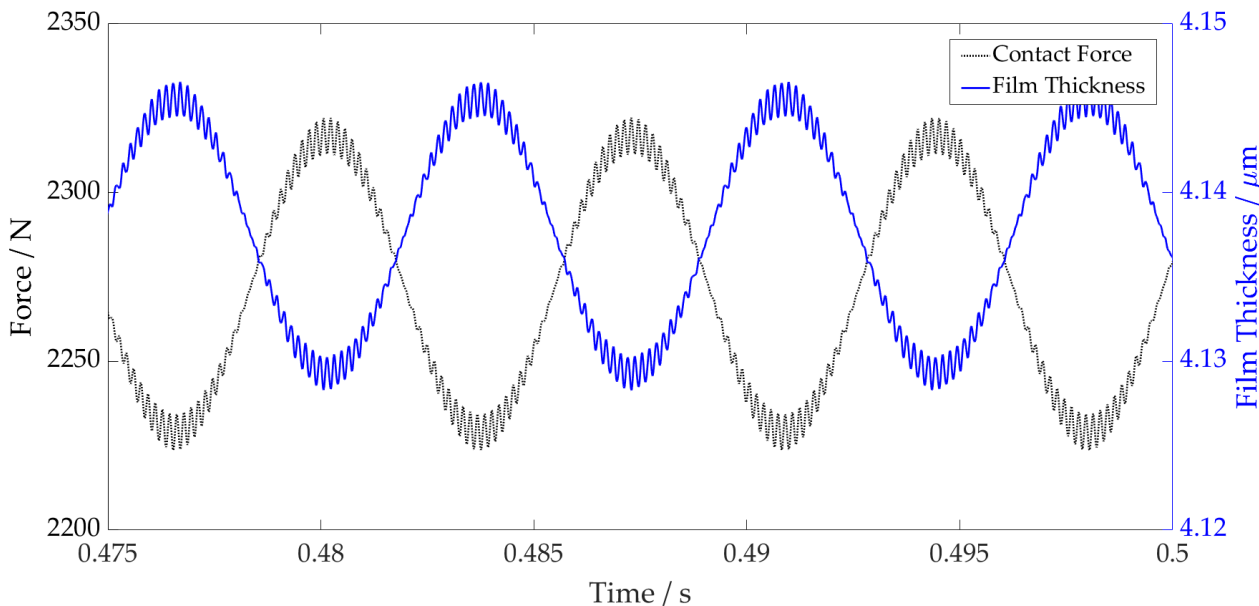


Figure 13. Film Thickness vs. Contact Force 21,000 rpm.

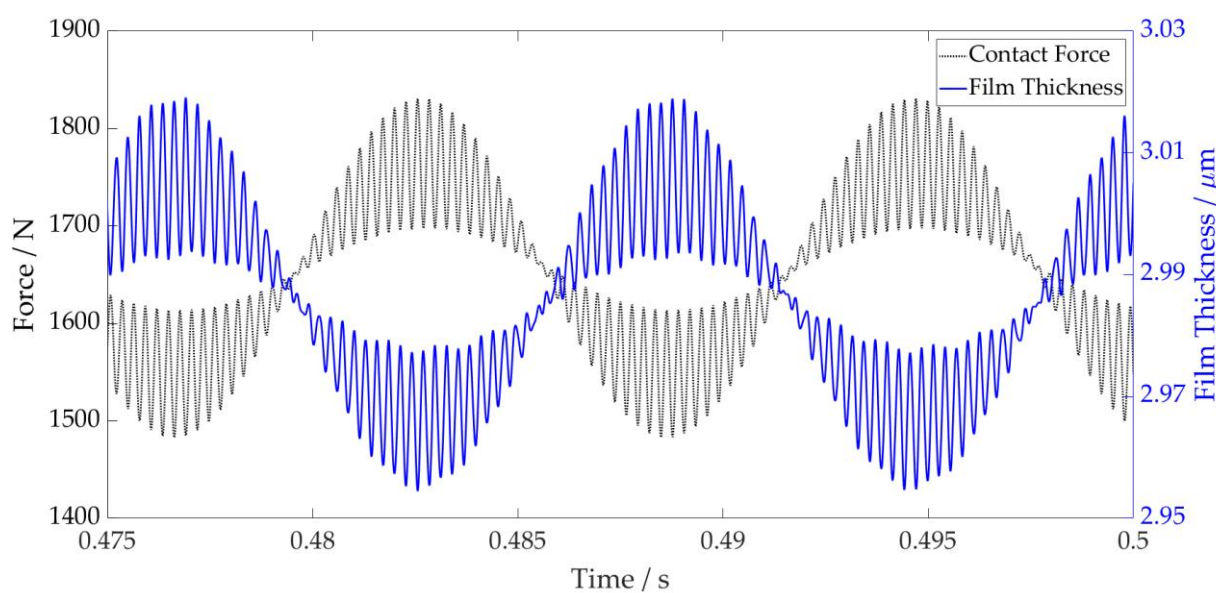


Figure 14. Film Thickness vs. Contact Force 12,500 rpm.

4. Conclusions

The new methodology presented has been developed to implement a lubricated bearing model within a flexible system level model. The model implicitly includes the lubricant film at the roller–race contact within the bearing; this is something that has not, to the authors' knowledge, been reported previously in the open literature. Simulations have been performed up to 21,000 rpm with realistic excitation forces from a first stage reduction gear pair and electric motor. The conjunction level and system level results have been analysed to compare the lubricated and conventional dry-bearing modelling techniques in a flexible multi-body dynamic (FMBD) environment.

Results show that the film thickness reaches 4.15 μm at 21,000 rpm. This leads to 9.6 times greater contact forces and hence 24.9% greater contact stiffness between the dry and lubricated models due to the lubricant entrainment and non-linear Hertzian force–deflection relationship. The contribution of all the rolling elements leads to the lubricated model having a 16.6% greater maximum total bearing stiffness at 21,000 rpm than the dry model. Moreover, this stiffness is shown to increase with speed due to the film thickness increasing with the entrainment velocity; this is something that dry models do not account for.

This increase in the total bearing stiffness leads to a change in the stiffness of the total system. By modelling the shaft as a flexible body, the influence on the natural frequency of the system is seen. The resonant peak at 12,500 rpm shifts 250 rpm higher in the lubricated model, which coincides with the higher frequency excitation from the gear meshing.

Understanding the influence of the roller bearings on the transmission stiffness is of particular importance in automotive applications, and this change shows the effect of the lubricant film on the already complex contact phenomena. Neglecting the effect of the lubricant film can lead to an underestimation of the bearing stiffness, impacting the accuracy of dynamic analyses such as noise, vibration and harshness (NVH) prediction. As transmissions operate at higher speeds with more complex interconnected structures and noise paths, it is important that these behaviours are modelled accurately. Furthermore, underestimation of the contact forces will also lead to a miscalculation of contact pressures, impacting future sub-surface stress and wear analyses for the life predictions of these critical machine elements.

Further developments of this work aim to include more complex rheological phenomena, accounting for thermal and starvation effects at high speeds. Computational efficiency

must also be maintained when embedding these models within FMBD environments, due to the iterative nature of the EHL solution.

The presented work establishes the necessity of a multi-physics approach to model the tribology and dynamics of high-speed rolling element bearings. This is essential for future powertrain modelling to ensure accurate component and system level behaviour.

Author Contributions: Conceptualisation, H.Q., M.M. and S.T.; methodology, H.Q. and M.M.; software, S.R.B. and G.O.; validation, H.Q.; formal analysis, H.Q.; investigation, H.Q.; resources, M.M., S.T., C.P.G., S.R.B. and G.O.; data curation, H.Q.; writing—original draft preparation, H.Q.; writing—review and editing, H.Q., M.M., S.T., C.P.G., S.R.B. and G.O.; visualisation, H.Q.; supervision, M.M., S.T., C.P.G., S.R.B. and G.O.; project administration, M.M.; funding acquisition, M.M. All authors have read and agreed to the published version of the manuscript.

Funding: This research received no external funding.

Informed Consent Statement: Not applicable.

Data Availability Statement: All data supporting the results are available in the paper.

Acknowledgments: The authors wish to acknowledge the support of the Loughborough University Wolfson School of Mechanical, Electrical and Manufacturing Engineering PhD Studentship Scheme and the support of AVL List GmbH.

Conflicts of Interest: The authors declare no conflict of interest.

Nomenclature

C	Radial clearance (m)
d	Body material damping ($\text{N}\cdot\text{s}\cdot\text{m}^{-1}$)
E	Elastic modulus (Pa)
E_r	Equivalent (reduced) elastic modulus (Pa)
F_d	Damping force (N)
f_{damp}	Damping factor (-)
f_F	Force vector (N)
C	Radial clearance (m)
d	Body material damping ($\text{N}\cdot\text{s}\cdot\text{m}^{-1}$)
E	Elastic modulus (Pa)
E_r	Equivalent (reduced) elastic modulus (Pa)
F_d	Damping force (N)
f_{damp}	Damping factor (-)
f_F	Force vector (N)
f_M	Moment vector ($\text{N}\cdot\text{m}$)
f	Force on partial mass (N)
f^a	External loads (N)
f^*	Non-linear excitation force (N)
G^*	Dimensionless equivalent geometry (-)
h_c	Central film thickness (m)
I_C	Inertia tensor of partial mass ($\text{kg}\cdot\text{m}^2$)
K	Body stiffness matrix ($\text{N}\cdot\text{m}^{-1}$)
k	Body material stiffness ($\text{N}\cdot\text{m}^{-1}$)
K_c	Contact stiffness ($\text{N}\cdot\text{m}^{-1}$)
K_b	Total Bearing Stiffness ($\text{N}\cdot\text{m}^{-1}$)
K_{EHL}	EHL Film Stiffness ($\text{N}\cdot\text{m}^{-1}$)
l_a	Active length of roller (m)
l	Length of roller slice (m)
m	Mass of partial mass (kg)
M	Mass matrix of body (kg)
N	Partial mass number (-)

n	Degree of freedom (-)
p^*	Non-linear inertia terms ($\text{kg}\cdot\text{m}^2$)
q	Displacement (m)
\dot{q}	Velocity ($\text{m}\cdot\text{s}^{-1}$)
\ddot{q}	Acceleration ($\text{m}\cdot\text{s}^{-2}$)
R	Bearing inner race radius (m)
r	Roller radius (m)
R_r	Equivalent radius of contact (m)
s	Slice number (-)
T	Total contact moment ($\text{N}\cdot\text{m}$)
u_t	Translational displacement of partial mass (m)
U^*	Dimensionless speed parameter (-)
W	Total contact load (N)
w	Force per unit length ($\text{N}\cdot\text{m}^{-1}$)
x	Displacement in x-direction (m)
x_c	Conjunction x-coordinate (-)
y	Displacement in y-direction (m)
y_c	Conjunction y-coordinate (-)
z	Displacement in z-direction (m)

Greek Symbols

θ	Roller angular displacement (rad)
\varnothing	Rotational displacement of partial mass (rad)
α	Pressure viscosity coefficient ($\text{m}^2\cdot\text{N}^{-1}$)
δ	Contact deformation (m)
δ_m	Material deformation (m)
η_0	Atmospheric lubricant dynamic viscosity ($\text{Pa}\cdot\text{s}$)
ρ_0	Lubricant inlet density ($\text{kg}\cdot\text{m}^{-3}$)
ω	Angular velocity of shaft (rad)

References

1. Cai, W.; Wu, X.; Zhou, M.; Liang, Y.; Wang, Y. Review and Development of Electric Motor Systems and Electric Powertrains for New Energy Vehicles. *Automot. Innov.* **2021**, *4*, 3–22. [[CrossRef](#)]
2. Stribeck, R. Ball Bearings for Various Loads. *Trans. ASME* **1907**, *29*, 420–463.
3. Palmgren, A. *Ball and Roller Bearing Engineering*; KF Industries Inc.: Philadelphia, PA, USA, 1959.
4. Jones, A.B. A general theory for elastically constrained ball and radial roller bearings under arbitrary load and speed conditions. *J. Basic Eng.* **1960**, *82*, 309–320. [[CrossRef](#)]
5. Harris, T.A. *Roller Bearing Analysis*, 3rd ed.; John Wiley and Sons: New York, NY, USA, 1984.
6. Andréason, S. Load distribution in a taper roller bearing arrangement considering misalignment. *Tribology* **1973**, *6*, 84–92. [[CrossRef](#)]
7. Liu, J.Y. Analysis of Tapered Roller Bearings Considering High Speed and Combined Loading. *J. Lubr. Technol.* **1976**, *98*, 564–572. [[CrossRef](#)]
8. De Mul, J.M.; Vree, J.M.; Maas, D.A. Equilibrium and Associated Load Distribution in Ball and Roller Bearings Loaded in Five Degrees of Freedom While Neglecting Friction—Part I: General Theory and Application to Ball Bearings. *J. Tribol.* **1989**, *111*, 142–148. [[CrossRef](#)]
9. Walters, C.T. The dynamics of ball bearings. *J. Lubr. Technol.* **1971**, *93*, 1–10. [[CrossRef](#)]
10. Meyer, L.D.; Ahlgren, F.F.; Weichbrodt, B. An Analytic Model for Ball Bearing Vibrations to Predict Vibration Response to Distributed Defects. *J. Mech. Des.* **1980**, *102*, 205–210. [[CrossRef](#)]
11. Sunnersjö, C. Varying compliance vibrations of rolling bearings. *J. Sound Vib.* **1978**, *58*, 363–373. [[CrossRef](#)]
12. Matsubara, M.; Rahnejat, H.; Gohar, R. Computational modelling of precision spindles supported by ball bearings. *Int. J. Mach. Tools Manuf.* **1988**, *28*, 429–442. [[CrossRef](#)]
13. Rahnejat, H.; Rothberg, S. *Mulit-Body Dynamics: Monitoring and Simulation Techniques III*, 1st ed.; Wiley: New York, NY, USA, 2004.
14. Gupta, P.K. Dynamics of Rolling-Element Bearings—Part I: Cylindrical Roller Bearing Analysis. *J. Lubr. Technol.* **1979**, *101*, 293–302. [[CrossRef](#)]
15. Questa, H.; Mohammadpour, M.; Theodossiades, S.; Garner, C.; Bewsher, S.; Offner, G. Tribodynamic analysis of high-speed roller bearings for electrified vehicle powertrains. *Tribol. Int.* **2020**, *154*, 106675. [[CrossRef](#)]
16. Stone, B. The State of the Art in the Measurement of the Stiffness and Damping of Rolling Element Bearings. *CIRP Ann.* **1982**, *31*, 529–538. [[CrossRef](#)]

17. Dietl, P. *Damping and Stiffness Characteristics of Rolling Element Bearings—Theory and Experiment*; TU Vienna: Vienna, Austria, 1997.
18. Bizarre, L.; Nonato, F.; Cavalca, K. Formulation of five degrees of freedom ball bearing model accounting for the nonlinear stiffness and damping of elastohydrodynamic point contacts. *Mech. Mach. Theory* **2018**, *124*, 179–196. [[CrossRef](#)]
19. Rahnejat, H.; Gohar, R. The Vibrations of Radial ball bearings. *Proc. Inst. Mech. Eng. Part C J. Mech. Eng. Sci.* **1985**, *199*, 181–193. [[CrossRef](#)]
20. Aini, R.; Rahnejat, H.; Gohar, R. Vibration modeling of rotating spindles supported by lubricated bearings. *J. Tribol.* **2000**, *124*, 158–165. [[CrossRef](#)]
21. Mohammadpour, M.; Johns-Rahnejat, P.; Rahnejat, H. Roller bearing dynamics under transient thermal-mixed non-Newtonian elastohydrodynamic regime of lubrication. *Proc. Inst. Mech. Eng. Part K J. Multi-Body Dyn.* **2015**, *229*, 407–423. [[CrossRef](#)]
22. Sopanen, J.; Mikkola, A. Dynamic model of a deep-groove ball bearing including localized and distributed defects. Part 1: Theory. *Proc. Inst. Mech. Eng. Part K J. Multi-Body Dyn.* **2003**, *217*, 201–211. [[CrossRef](#)]
23. Sopanen, J.; Mikkola, A. Dynamic model of a deep-groove ball bearing including localized and distributed defects. Part 2: Implementation and results. *Proc. Inst. Mech. Eng. Part K J. Multi-Body Dyn.* **2003**, *217*, 213–223. [[CrossRef](#)]
24. Sawalhi, N.; Randall, R. Simulating gear and bearing interactions in the presence of faults. Part I. The combined gear bearing dynamic model and the simulation of localised bearing faults. *Mech. Syst. Signal Process.* **2008**, *22*, 1924–1951. [[CrossRef](#)]
25. Liu, J.; Shao, Y. Vibration modelling of nonuniform surface waviness in a lubricated roller bearing. *J. Vib. Control* **2016**, *23*, 1115–1132. [[CrossRef](#)]
26. Nonato, F.; Cavalca, K.L. An approach for including the stiffness and damping of elastohydrodynamic point contacts in deep groove ball bearing equilibrium models. *J. Sound Vib.* **2014**, *333*, 6960–6978. [[CrossRef](#)]
27. Lundberg, G.; Yhland, E. *Cylinder Compressed between Two Plane Bodies*; SKF: Gothenburg, Sweden, 1949.
28. De Mul, J.M.; Vree, J.M.; Maas, D.A. Equilibrium and Associated Load Distribution in Ball and Roller Bearings Loaded in Five Degrees of Freedom While Neglecting Friction—Part II: Application to Roller Bearings and Experimental Verification. *J. Tribol.* **1989**, *111*, 149–155. [[CrossRef](#)]
29. Parikyan, T.; Resch, T.; Priebsch, H.H. Structured Model of Crankshaft in the Simulation of Engine Dynamics with AVL/EXCITE. In *Volume 3: Engine Systems: Lubrication, Components, Exhaust and Boosting, System Design and Simulation*; American Society of Mechanical Engineers: New York, NY, USA, 2001; Volume 67, pp. 105–114. [[CrossRef](#)]
30. Offner, G. Modelling of condensed flexible bodies considering non-linear inertia effects resulting from gross motions. *Proc. Inst. Mech. Eng. Part K J. Multi-Body Dyn.* **2011**, *225*, 204–219. [[CrossRef](#)]
31. Walford, T.L.H.; Stone, B.J. The Sources of Damping in Rolling Element Bearings under Oscillating Conditions. *Proc. Inst. Mech. Eng. Part C J. Mech. Eng. Sci.* **1983**, *197*, 225–232. [[CrossRef](#)]
32. Dareing, D.W.; Johnson, K.L. Fluid Film Damping of Rolling Contact Vibrations. *J. Mech. Eng. Sci.* **1975**, *17*, 214–218. [[CrossRef](#)]
33. Mehdigoli, H.; Rahnejat, H.; Gohar, R. Vibration response of wavy surfaced disc in elastohydrodynamic rolling contact. *Wear* **1990**, *139*, 1–15. [[CrossRef](#)]
34. Dowson, D.; Toyoda, S. A Central Film Thickness Formula for Elastohydrodynamic Line. In *Proc. Fifth Leeds-Lyon Symp. Tribol. Mech. Eng. Publ.*; Elsevier: Amsterdam, The Netherlands, 1979; pp. 60–65.
35. Nelia, D.; Bercea, I.; Paleu, V. Prediction of roller skewing in tapered roller bearings. *Tribol. Trans.* **2008**, *51*, 128–139. [[CrossRef](#)]
36. Majdoub, F.; Saunier, L.; Sidoroff-Coicaud, C.; Mevel, B. Experimental and numerical roller skew in tapered roller bearings. *Tribol. Int.* **2020**, *145*, 106142. [[CrossRef](#)]
37. Mevel, B.; Guyader, J. Routes to chaos in ball bearings. *J. Sound Vib.* **1993**, *162*, 471–487. [[CrossRef](#)]
38. Spikes, H. Basics of EHL for practical application. *Lubr. Sci.* **2014**, *27*, 45–67. [[CrossRef](#)]
39. Shi, X.; Wang, L. TEHL analysis of high-speed and heavy-load roller bearing with quasi-dynamic characteristics. *Chin. J. Aeronaut.* **2015**, *28*, 1296–1304. [[CrossRef](#)]
40. Singh, K.P.; Paul, B. Numerical Solution of Non-Hertzian Elastic Contact Problems. *J. Appl. Mech.* **1974**, *41*, 484–490. [[CrossRef](#)]
41. Harris, T.A.; Kotzales, M.N. *Advanced Concepts of Bearing Technology*, 5th ed.; Taylor and Francis Group: Boca Raton, FL, USA, 2007.
42. De Mul, J.M.; Kalker, J.J.; Fredriksson, B. The contact between arbitrarily curved bodies of finite dimensions. *J. Tribol.* **1986**, *108*, 140–148. [[CrossRef](#)]
43. Mitsuya, Y.; Sawai, H.; Shimizu, M.; Aono, Y. Damping in Vibration Transfer through Deep-Groove Ball Bearings. *Trans. Jpn. Soc. Mech. Eng. Ser. C* **1992**, *58*, 3714–3721. [[CrossRef](#)]
44. Krämer, E. *Dynamics of Rotors and Foundations*; Springer: Berlin/Heidelberg, Germany, 1993.

Disclaimer/Publisher’s Note: The statements, opinions and data contained in all publications are solely those of the individual author(s) and contributor(s) and not of MDPI and/or the editor(s). MDPI and/or the editor(s) disclaim responsibility for any injury to people or property resulting from any ideas, methods, instructions or products referred to in the content.



Application of Tribological Artificial Neural Networks in Machine Elements

J. Walker¹ · H. Questa¹ · A. Raman¹ · M. Ahmed¹ · M. Mohammadpour¹ · S. R. Bewsher² · G. Offner²

Received: 14 September 2022 / Accepted: 30 October 2022 / Published online: 23 November 2022
© The Author(s) 2022

Abstract

Traditionally, analytical equations used in tribo-dynamic modelling, such as those used for predicting central film thickness within elastohydrodynamic lubricated contacts, have led to timely computations, but tend to lack the accuracy of numerical solvers. However, it can be shown that data-driven solutions, such as machine learning, can significantly improve computational efficiency of tribo-dynamic simulations of machine elements without comprising accuracy relative to the numerical solution. During this study, artificial neural networks (ANNs) are trained using data produced via numerical solutions, which are constrained by the regimes of lubrication to ensure the quality of the training data set. Multiple ANNs are then implemented to predict EHL central film thickness, as well as viscous and boundary friction, in multiple commonly used machine elements, such as a rolling element bearing and a spur gear. The viscous and boundary friction ANN prediction are compared directly against ball-on-disc experimental measurements to validate its accuracy.

Keywords ANN · Data driven · Tribology · EHL · Friction · Bearing · Gear

List of symbols

a [m]	Hertzian half-width	W_a, W_h, W_i [N]	Newton's weight and forces
A_a, A [m^2]	Asperity/total contact area		Asperity/hydrodynamic/actual applied load
E_r [Pa]	Reduced modulus		
$F_2(\lambda), F_{5/2}(\lambda)$	Statistical functions		
f_b, f_v, f_t [N]	Boundary/viscous/total friction	α [Pa $^{-1}$]	Pressure–viscosity coefficient
G_e, G_v [-]	: Dimensionless elasticity/viscosity	γ, γ' [-]	Relaxation coefficient/performance adjustment factor
G^*, U^*, W^* [-]	Dimensionless material/speed/load parameter	$\varepsilon_p, \varepsilon_w$ [-]	Acceptable pressure/load convergence error
h_c, h_0, h [m]	Central film thickness/initial film thickness prediction/film thickness	$\zeta\beta\sigma$ [-]	Roughness parameter
L [m]	Contact length	η_0, η [Pa s]	Reference viscosity/viscosity
$N_{\text{in}}, N_{\text{hi}}, N_{\text{out}}$ [-]	Number of neurons input/hidden/output layer	λ [-]	Stribeck oil parameter
$p, p_{\text{new}}, p_{\text{old}}$ [Pa]	Pressure/ new pressure/ previous pressure	ν [-]	Poisson's ratio
R^2 [-]	Coefficient of determination	ϑ [-]	Adjustment limiting friction coefficient
R_r [-]	Reduced radius	ρ_0, ρ [kg m $^{-3}$]	Reference density/density
U_e, U_s [ms $^{-1}$]	Entrainment/sliding speed	$\sigma\beta$ [-]	Asperity slope parameter
		τ, τ_L, τ_0 , [Pa]	Limiting/Eyring shear stress
		χ [-]	Steel boundary friction coefficient

1 Introduction

Tribology plays an important role for the enhancement of sustainable design and reduction of CO₂ production, especially in mechanical power generation and transmission. Tribology is the study of three fundamental phenomena of

¹ Wolfson School of Mechanical, Electrical and Manufacturing Engineering, Loughborough University, Loughborough LE11 3TU, UK

² AVL List GmbH, Hans-List-Platz 1, 8020 Graz, Austria

interacting surfaces with relative rolling and sliding motions: friction, lubrication, and wear. Advancements in this field could reduce energy losses by up to 8.7% on a global scale over a 15-year period starting from 2019 [1]. The focus of this paper will be the time-efficient prediction of a lubricant's film thickness within mechanical component case studies, including a roller element bearing and a spur gear. The case studies are key sub-components found within automotive applications for both electric propulsion and internal combustion drivetrains alike; however, the methodology described in this work applies to many more industries and their subsequent contacting componentry. The prediction of a lubricant's film thickness is important because it ultimately describes the separation of two surfaces and whether there is partial interaction of two contiguous surfaces.

Historically, complex non-linear problems in tribology like the prediction of lubricant film thickness have been solved by one of two approaches. The first is a numerical approach [2], where systems of partial differential equations are set up to define the state of the contact and are consequently solved iteratively [3]. This method produces accurate results and is applicable to a large range of operating contact conditions. However, it is not only computationally expensive due to its iterative nature, but also there is insufficient initial conditions. The second approach is to use experimental data to create analytical equations that can be applied to specific lubrication regimes [4]. These equations provide quick estimates of certain key parameters, such as central [5] and minimum film thickness [6] and viscous [7] and boundary friction [8]. The drawback of this approach is that each equation has a limited range of applicability, a lower accuracy due to its simplified nature, and requires adequate effort to collect the experimental data. The presented workflow applies the use of Machine Learning (ML) algorithms in the form of Artificial Neural Networks (ANNs) to predict the central film thickness as well as viscous friction to compare their relative performance against analytical equations and numerical solutions. Whilst the ANN lacks the physical understanding of the numerical solution, it performs almost as fast as an analytical solution whilst benefiting from the accuracy of the numerical solution [9]. A methodology is proposed to ensure the ANN is trained within a valid range of the numerical solver.

ANNs were first utilised in tribology simulation [10] in the 1990s to model wear behaviour and predict the life of tools [11], coating materials [12], and mechanical systems [13]. Following these initial studies, they were successfully applied to the prediction of the coefficient of friction and wear rate of composite materials [14–16] and tool steels [17] to aid component design. The studies mentioned above modelled friction and wear in dry conditions, but ANNs have also been applied to lubricated contacts to model friction [9, 18, 19] and lubricant viscosity [20, 21] to aid lubricant

design. Additional work has been completed to model wear in manufacturing processes [22] including specific applications like the estimation of flank wear in drilling [23] and modelling of the surface roughness of machined parts [24]. These studies worked with fixed material properties and used process-specific inputs (i.e. speed, torque, vibration) instead of material properties as in studies [11–21].

The common feature between studies [11–24] was the use of experimental data to train ANN models, with the goal of interpolating the material behaviour between the data points for varying conditions. The limitation of this approach is that experimental data are expensive and time consuming to generate. As a result, the training dataset for the ANN is limited to approximately a hundred points [14, 15] or less [11, 12]. To develop more complex ANNs and achieve greater accuracy, it is necessary to have a sufficiently large dataset [25, 26]. Wang et al. demonstrated the capability of ANNs to predict maximum pressure in thermohydrodynamic contacts when trained on data obtained from a numerical model using Reynold's equation [27]. This modelling technique achieved an acceptable level of accuracy with lower computational expense than the numerical equivalent model. It is therefore possible to generate vast training datasets from iterative numerical models and create more accurate ANN models covering a wide range of operating conditions for dynamic simulations.

Almqvist demonstrated the use of Physics Informed Neural Networks (PINN) to solve Reynolds boundary value problem [28]; however, whilst not the purpose of the study, noted that the benefit of the method was neither accuracy nor computational efficiency, but these could improve with time and research. When simulating tribology in conjunction with dynamic simulations of machine elements, accurate and time-efficient simulation are of importance, therefore data-driven solutions currently are preferable. Marian et al. were the first to use a Finite Element Method (FEM) to generate EHL film thickness data for the purpose of training an ANN to predict an EHL film distribution [29]; the ANN was a factor of ~ 25 times more computationally efficient than the FEM solution.

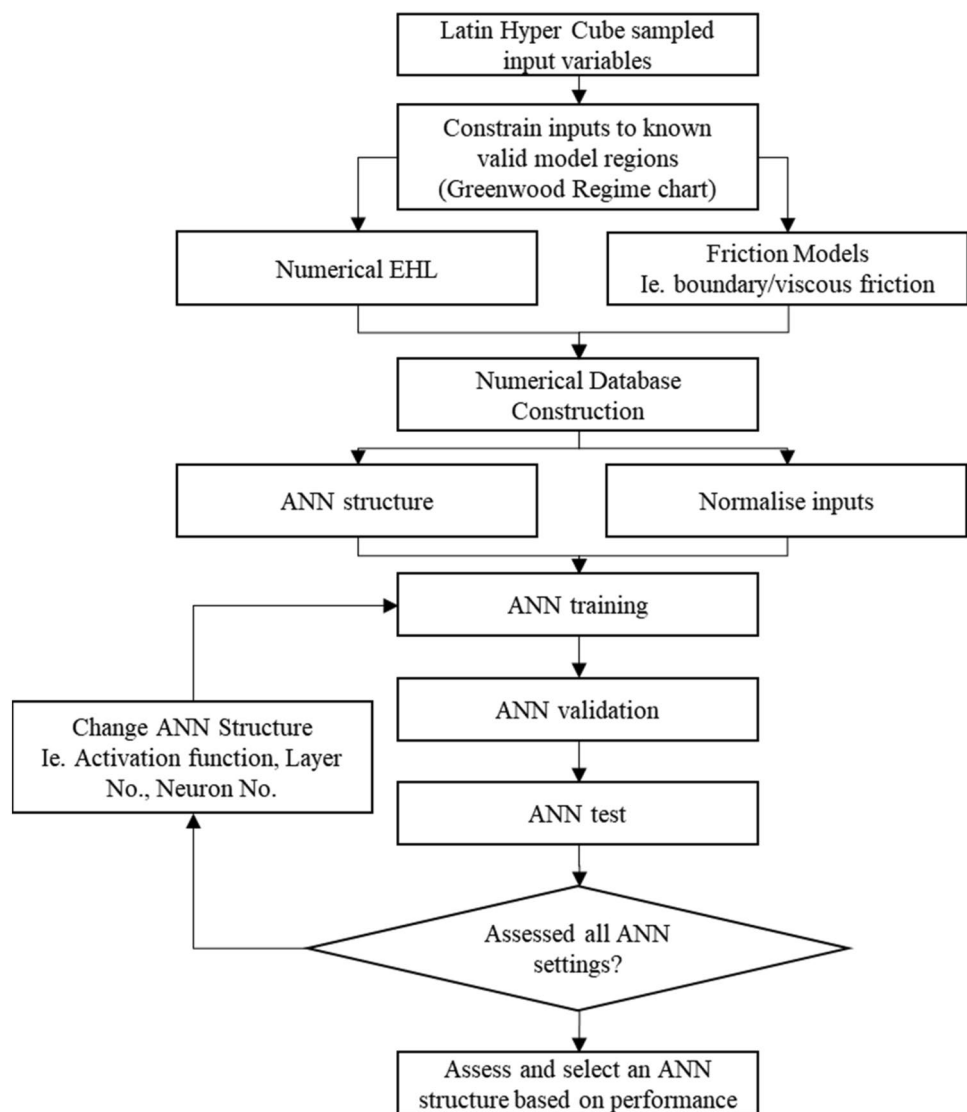
This study uses multiple tribological ANNs trained upon a numerical EHL solution, which weakly couples the elastic deformation and hydrodynamic pressure, alongside a Greenwood and Tripp deterministic asperity friction model. The outputs of the ANNs include EHL central film thickness, viscous, and boundary friction. These ANNs are used explicitly in dynamic simulations of multiple machine element applications, bearings, and gears, which has not been reported hitherto. Numerically computed EHL film thicknesses and pressure distributions are used to generate a dataset for the purpose of training the ANNs. The training data will be based on the applications of machine elements at relatively high speeds. The training data range is constrained

to lubricated steel–steel contacts to guarantee its validity and applicability within the Piezo-Rigid and predominate Piezo-Elastic EHL regime. Separate boundary and viscous ANNs will be used to compute the overall friction in boundary to mixed EHL lubrication regimes. The viscous friction ANN will be able to compute within Newtonian and Non-Newtonian regimes. The overall friction computed by the ANNs will be validated against experimentally obtained test results from a ball-on-disc tribometer. Overall friction is then predicted throughout a spur gear's meshing cycle explicitly to show the computational efficiency advantage gained by the use of data-driven ANN solutions.

2 Methodology Overview

A high-level summary flowchart of the methodology implemented in the following work is presented in Fig. 1. The numerical models for line contact film thickness were first established, alongside the numerical viscous and boundary friction models. The numerical database which includes the necessary input and outputs to be predicted structure is then constructed and assessed via statistical means and validity ranges of the models that are providing the data. The structure of the ANN model is then thoroughly assessed to find the optimum for predicting the output parameters.

Fig. 1 A flowchart to describe the implementation ANNs, data flow, and models



3 Numerical Elastohydrodynamic Lubrication

In roller raceway or gear pair conjunctions the non-conformal nature of the contact leads to high pressures under load. These pressures result in local elastic deformation of the contact and an increase in lubricant viscosity. This regime of fluid film lubrication is known EHL [30].

In roller bearings and spur gears, the contacts are often modelled as a line contact. For a line contact, the contact dimensions are much larger in the direction of side leakage than they are across the contact. Pressure along the major axis is therefore assumed to be constant, hence the analysis can be formed in one dimension.

The contacting geometries can be represented by an equivalent rigid roller, of radius R , against a semi-infinite elastic half space of equivalent elastic modulus, E_r . The analytical central film thickness is obtained from [5]:

$$h_c = R_r \left[3.06 G^{*0.56} U^{*0.69} W^{*-0.1} \right]. \quad (1)$$

The non-dimensional material, speed, and load parameters are as follows:

$$G^* = E_r \alpha, U^* = \frac{\eta_0 U_e}{E_r R_r}, W^* = \frac{W_i}{E_r R_r L}. \quad (2)$$

These types of analytical solutions for EHL are based on experimental or numerical solutions for central and minimum film thickness, some of which are based on only ten data points [31]. Whilst offering a timely solution for EHL calculations, these regressed equations were designed upon entrainments speed below 2 m/s which brings into question their validity at higher entrainment speeds. Modern electric powertrain bearings can have entrainment speed as high as 20 m/s which far exceeds the validation region of the analytical equations. Furthermore, for more sophisticated contact analysis, pressure and film thickness distribution can only be obtained from a full numerical solution. The numerical solution for the EHL problem is achieved through solution of Reynolds equation with elastic field and rheological models. The following form is used in this paper, assuming a thin film of Newtonian lubricant:

$$\frac{\partial}{\partial x} \left[\frac{\rho h^3}{\eta} \frac{\partial p}{\partial x} \right] - 6U_e \frac{\partial(\rho h)}{\partial x} = 0. \quad (3)$$

The pressure distribution across the EHL contact differs from the dry Hertzian elliptical profile due to the variation of the lubricant film. The variation of this film is computed using the following equation:

$$h = h_c + \frac{x^2}{2R_r} - \frac{2}{\pi E_r} \int_{x,\text{in}}^{x,\text{out}} p \ln(x - x')^2 dx', \quad (4)$$

where the idealised film thickness parabola, generated by the first and second term, deviates due to the localised contact deformation caused by the pressure at each computational node along the contact domain (third term).

Roelands equation [32] is used to model the increase in lubricant viscosity with pressure due to its known accuracy at higher contact EHL pressures:

$$\eta = \eta_0 \exp \left\{ (\ln(\eta_0) + 9.67) \times [-1 + (1 + 5.1 \times 10^{-9} p)^{z_0}] \right\}, \quad (5)$$

where

$$z_0 = \frac{\alpha}{5.1 \times 10^{-9} (\ln(\eta_0) + 9.67)}. \quad (6)$$

Lubricant density changes with pressure due to the compressibility of the lubricant, hence the Dowson–Higginson model [33]:

$$\rho = \rho_0 \left(1 + \frac{0.6 \times 10^{-9} p}{1 + 1.7 \times 10^{-9} p} \right). \quad (7)$$

An iterative procedure is required to solve the numerical model due to the coupled nature of the film thickness and contact pressure. The method of solution is as follows:

1. The contact load is obtained from the dynamic model of the gear pair or bearing.
2. An initial estimation of lubricant film thickness, h_0 is made.
3. The computational domain is established based on the calculated contact half-width, a . Contact inlet and outlet distances are set to $-4.5a$ to $1.5a$ to represent a fully flooded contact condition.
4. Pressure and film thickness distributions are obtained through simultaneous solutions of Eqs. (3–7). The Newton–Raphson method is used for speed and robustness of convergence [34]. The iterative solution requires pressure criteria to be satisfied at each computational node across the contact.

$$\frac{\sum_{i=1}^n |p_{\text{new}} - p_{\text{old}}|}{\sum_{i=1}^n p_{\text{old}}} \leq \varepsilon_p, \quad (8)$$

where $\varepsilon_p = 1 \times 10^{-5}$ is the pressure convergence error.

Under-relaxation is applied between successive iterations where the criterion is not met, using an under-relaxation factor typically in the region of $0.01 \leq \gamma \leq 0.8$.

$$p_{\text{new}} = (1 - \gamma)p_{\text{old}} + \gamma p_{\text{new}}. \quad (9)$$

The total reaction load from the lubricant film, W_h , should equal the total load applied to the contact, W_i . The reaction load is calculated using the integration of pressure over the computation domain.

$$W_h = L \int pdx. \quad (10)$$

Convergence criterion is applied

$$\frac{|W_i - W_h|}{W_i} \leq \varepsilon_w, \quad (11)$$

where $\varepsilon_w = 0.001$ is the load convergence error.

4 Boundary and Viscous Friction

One significant consequence of a sliding contact is the resulting friction. For a lubricated system, there can be two constituent components to the friction that occurs: viscous and boundary friction. The former component is a result of the shearing of the fluid film and the latter is from the direct contact of the bounding surfaces.

There are several analytical equations developed to compute viscous friction of sliding–rolling interfaces. These equations have been derived via tribometers such ball-on-disc [35] and twin-disc machines [36]. Evans and Johnson's formulated equations for the maximum traction coefficient that complement the traction maps for four regimes of three lubricants (HVI 650, Santovac 5 and Santotrac 50).

The regimes are given as follows:

- (1) Linear viscoelastic (Newtonian)
- (2) Non-linear viscous (Eyring)
- (3) Non-linear viscoelastic
- (4) Elastic–plastic

Bearing and gear pair traction regimes typically fall within the Newtonian and Eyring regimes. In the present study the numerical viscous friction computations are based upon these two regimes. The shear stress experienced by the lubricant across the EHL computational domain is integrated with respect to the discretised area to compute the viscous friction:

$$f_v = \int \tau dA. \quad (12)$$

The equation used for shear is dependent on the limiting shear case:

$$\tau_L = \tau_0 + \vartheta p, \quad (13)$$

where $\vartheta = 0.08$ is an adjustment coefficient for a steel on steel contact [3].

In the case where the limiting stress is exceeded by the Newtonian shear, the lubricant then exhibits a non-linear response within the Eyring regime.

Within the Newtonian regime for a line contact, the shear of the lubricants can be derived via the Reynold's equation:

$$\tau = \pm \frac{dp}{dx} \frac{h}{2} + \frac{\eta_0 U_s}{h}. \quad (14)$$

Thus, the Newtonian shear stress (Eq. 14) can be substituted into Eq. 12:

$$f_v = \int \left(\pm \frac{dp}{dx} \frac{h}{2} + \frac{\eta_0 U_s}{h} \right) dA. \quad (15)$$

The central differencing method within the numerical EHL solver resolves the film thickness and pressure distributions required in Eq. 14. As the numerical friction solution relies upon the distribution of pressure and film thickness within the contact, computation times are largely dependent on resolving Reynold's equation within the usual iterative manner. The use of an ANN methodology negates the excessive computational times of the numerical solution, whilst maintaining accuracy.

To realise any boundary interaction of the surfaces a classical *Greenwood and Tripp* model is used [8]. The surface height distributions during this study are considered to be Gaussian, and the mean radius of curvature β is assumed for the asperity summits. $F_{5/2}(\lambda)$ and $F_2(\lambda)$ are statistical functions dependent upon the Stribeck Oil Parameter λ , which can be approximated by polynomial curve fitting [37]. The roughness parameter $\zeta\beta\sigma$ of combined represented surfaces typically ranges between 0.04 and 0.07 [38]. The asperity contact load and area can be calculated using the following equations:

$$W_a = \frac{8\sqrt{2}}{15} \pi(\zeta\beta\sigma) \sqrt{\frac{\sigma}{\beta}} E_r A F_{5/2}(\lambda), \quad (16)$$

$$A_a = \pi^2 (\zeta\beta\sigma)^2 A F_2(\lambda). \quad (17)$$

The total boundary friction is obtained via

$$f_b = \tau_0 A_a + \chi W_a. \quad (18)$$

The limiting shear stress τ_0 acknowledges an adsorbed thin film on the summit of contacting asperities and thus non-Newtonian shear. χ is typically considered to be 0.17 for steel–steel contact [3].

Total friction is the summation of the boundary and viscous components:

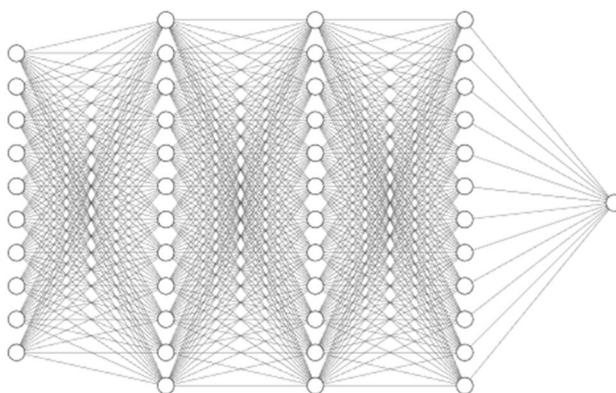


Fig. 2 ANN structure to predict EHL central film thickness $10 - [12 - 12 - 12]_3 - 1$

$$f_t = f_b + f_v. \quad (19)$$

5 Artificial Neural Network Methodology

ANNs consist of a set of interconnected neurons that can adapt to input data to approximate complex, non-linear functions. A schematic of the structure of one of the ANNs used in this work is given in Fig. 2. Previous implementations of ANNs in tribology and film thickness prediction have been limited to between one or three hidden layers [39]. This is due to increasing ANN structural complexity requiring more training time due to increased neuron and layer number. MATLAB 2022a [40] was used for the development of the ANNs.

As previously mentioned, unlike ANNs trained on limited numbers of experimental data, the production of numerical solution databases can provide vast databases in a relatively short space of time. Therefore, a decision between timely generation of an appropriately sized and valid database for any given application, training time and prediction accuracy must be made. The structure of the ANN is denoted in the following way as per [14]:

$$N_{\text{in}} - [N_{h1} - N_{h2} - N_{h3}]_t - N_{\text{out}},$$

where N represents the number of neurons in a layer. The subscripts ‘in’ and ‘out’ represent the input and output layers, whilst subscript ‘ $h1$ ’, ‘ $h2$ ’, and ‘ $h3$ ’ represent hidden layers and ‘ t ’ is the number of hidden layers.

A sensitivity study of various ANN structures, confined all by the same input ranges, was completed to evaluate their performance. This is summarised in Table 1.

The final selected structures were based on training time, coefficient of determination R^2 , and its potential for over training.

Table 1 ANN Structure Sensitivity Study

Structure variable	Value
Number of initial training data points	600–5000
Number of hidden layers	1–4
Number of neurons	10–20
Type of activation function	Hyperbolic tangent Logistic sigmoid Rectilinear

5.1 ANN Structure

The input parameters and the target values, in this case the film thickness and viscous friction, were normalised as per a standardised min–max normalisation function:

$$\tilde{x} = \frac{x - x_{\min}}{x_{\max} - x_{\min}}(u - l) + u, \quad (20)$$

where u and l , where the upper and lower normalised unit values of 1 and –1, respectively. x denotes the dimensional target input value and \tilde{x} represents the final normalised input or output parameter of the ANN. The output layer of the ANN returns a normalised value, so therefore x_{\max}, x_{\min} must be stored as a variable to dimensionalise the output later.

The input training data set was split into three categories randomly: a training set, validation set, and test set. Each set contained 70%, 15% and 15% of the training data, respectively. A limit of 1000 epochs was also implemented. During back propagation of the ANN the mean-squared error (MSE) was used to evaluate the network’s performance:

$$\text{MSE} = \frac{1}{N} \sum_{i=1}^N (t_i - y_i)^2, \quad (21)$$

where N is the number of data points being trained, validated, or tested. The coefficient of determination in line with [29], R^2 Eq. 22, was post-processed on the test data to evaluate the prediction quality of each ANN structure.

$$R^2 = 1 - \frac{\sum_{i=1}^N (t_i - y_i)^2}{\sum_{i=1}^N (y_i - \bar{y})^2}, \quad (22)$$

where t_i and y_i are the target value and the predicted value, respectively. \bar{y} is the mean of the target sample. The numerator of the fraction in Eq. 22 is the residual sum of the squares, whilst the denominator is the total sum of the squares.

As suggested per [29], suitable activation functions of hyperbolic tangent (Eq. 23) and logistic sigmoid (Log-Sig) (Eq. 24) functions were used for the hidden layers. A rectilinear (ReLU) (Eq. 25) function was also evaluated.

$$\tanh(x) = \frac{2}{1 + e^{-2x}} - 1, \quad (23)$$

$$\text{logsig}(x) = \frac{1}{1 + e^{-x}}, \quad (24)$$

$$\text{ReLU} = \begin{cases} x, & x \geq 0 \\ 0, & x \leq 0 \end{cases}. \quad (25)$$

A simple linear output activation function was used on the output. Several sizes of training data (600, 1000, 2000, and 5000) were tested to observe the influence over the prediction quality.

The ANN makes use of early stopping and regularisation in order to prevent statistical overfitting when conducting training [41]. The former improves generalisation of the trained network by observing the performance criteria of MSE of training data set relative to the validation training. Generalisation refers to the ANNs ability to adapt appropriately to previously unseen data drawn out of the training data set also known here as the validation set. If the validation set's error increases, training is stopped early. The latter technique modifies the performance criteria by accounting for the change in the mean square of the network weights and biases (MSW) (Eq. 26). A performance adjustment factor, γ' , can be applied to reduce the weights and biases (Eq. 27) for any given propagation and reduce the likelihood of overfitting.

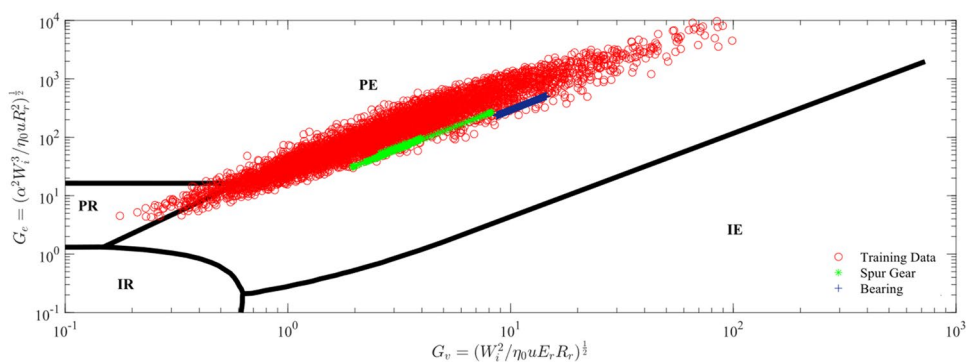
$$\text{MSW} = \frac{1}{N} \sum_{j=1}^N w_j^2, \quad (26)$$

$$\text{MSE}_{\text{reg}} = \gamma' \times \text{MSW} + (1 - \gamma') \times \text{MSE}. \quad (27)$$

5.2 Numerical Database Construction

ANNs can only perform as well as the quality and quantity of the data that it is provided, therefore the generation of a

Fig. 3 Line contact Greenwood lubrication regime chart with bearing, training data, and spur gear points plotted [4]



many quality data points for the database is of high importance. To improve the timeliness of numerical data point generation explicit parallelisation can be implemented, i.e. use of multiple computational cores of the CPU. When using MBD solvers implicitly it is not possible to exploit the use of explicit parallelisation since a particular time step is dependent on the present time step as well as on data of the same time step. The ANN functionality in turn can be embedded with an implicit MBD computation environment to significantly improve the computation times without the need of explicit parallelisation despite benefitting from it indirectly.

One previously developed EHL film thickness database constructed via a Finite Element Method (FEM) solver covered a vast range of lubricants and material properties for relatively low speed conditions (< 0.4 m/s of 2D line contacts) [29]. However, if a similar database was to be used for a numerical EHL solver, the stability and ranges of their validity may be exceeded. Therefore, training databases produced via numeric solvers should be constrained in some manner to ensure its validity. Marian et al. used Latin Hypercube Sampling (LHS) for EHL film prediction as an effective method to generate a training database to cover a vast design space with many factors [29].

In this study, LHS was used but was constrained by the Greenwood Regime chart [42] as shown in Fig. 3. The regions of the chart are Isoviscous Rigid (IR), Isoviscous Elastic (IE), Piezo-Elastic (PE), and Piezo-Rigid (PR). These bounded regions are indicational and are in fact areas of transition from one regime to another but are used here as constraints for the numeric databases. The bounding regions classifications are dependent on the geometric, material, and rheological properties of the contact. To ascertain this, dimensionless elasticity and viscosity parameters, G_e and G_v , respectively, are established.

$$G_e = \left(\frac{\alpha^2 W_i^3}{\eta_0 u R_r^2} \right)^{\frac{1}{2}}, \quad (28)$$

$$G_v = \left(\frac{W_i^2}{\eta_0 U_e E_r R_r} \right)^{\frac{1}{2}}. \quad (29)$$

The IR region can be described as a hydrodynamic region (lightly loaded contacts). Any data points generated via the LHS methodology that were found to be in this bounded region were redistributed with valid newly generated LHS EHL data points. The Piezoviscous Elastic (PE) regime prevails when the contact pressures are sufficiently high to cause elastic deformation of the bounding surfaces and a rise in lubricant viscosity. This signifies an EHL regime of lubrication and is the most prevalent regime for contact in gear pairs and sufficiently preloaded roller bearings. Piezo-rigid contacts also feature within the training dataset which refers to little to no elastic deformation of the bounding surfaces but there is a rise in lubricant viscosity.

The contacts within two commonly used machine elements, a cylindrical element roller bearing and spur gear, were superimposed on the Greenwood chart. This ensured that the training data covered their respective points of operation. This further confirmed that the lubrication regimes of both case studies were well within the PE region. Maximum and minimum ranges for the input variables were chosen to reflect the ranges over which typical high-speed gears and bearing operations would cover. Table 2 shows the initial ranges of the training data set produced that the LHS methodology was implemented with. Further constraints on the numeric database were to ensure suitable Hertzian pressures over 300 MPa and below 3.5 GPa to ensure the numeric database stayed within the PR and PE regions. Training data sets for the central film thickness are openly available from Figshare [43].

Table 2 Range of ANN input parameters *used for viscous and boundary friction ** boundary friction only

Parameter		Minimum	Maximum
Load	[N]	150	5000
Entrainment velocity	[m/s]	0.6	30
Reduced radius	[m]	0.0001	0.02
Reduced elastic modulus	[GPa]	200	250
Pressure–viscosity coefficient	[GPa ⁻¹]	10	30
Reference viscosity	[Pa.s]	0.0005	0.1
Maximum density	[kg/m ³]	7750	8050
Poisson's ratio	[–]	0.3	0.35
Contact length	[m]	0.001	0.050
*Eyring stress	[MPa]	1	5
**Roughness parameter	[–]	0.02	0.1
**RMS roughness	[μm]	0.01	1.00
**Average asperity radius	[μm]	1	50

Typically linear regression techniques can be significantly affected by multicollinearity of the input parameters. ANNs however are unaffected as it is an overparameterised methodology able to predict non-linear problems. When multicollinearity is apparent, the highly correlated input variables might require manipulation using methods to combine parameters, such as partial least squares, Principal Component Analysis (PCA), or ridge regression [44]. Figure 4 shows the absolute correlation factors between the input values for the EHL problem with the most significant bivariate correlation being between load and length with a magnitude of 0.23. This indicates a very weak correlation between the two parameters, but it must be noted that this may have been affected by the previous constraining of the input variables.

Interestingly in the study by Marian et al. [29], grouped non-dimensionalised parameters, denoted in Eq. 2 of the current study, were used as inputs and it was found to significantly impeded the ANNs ability to predict the central film thickness; the authors' of the current manuscript drew similar conclusions. ANNs can use principal component analysis similar to linear regression in an effort to reduce the dimensionality of the input space of the problem. The output of PCA conducted on the selected inputs of the present study shown in Fig. 5 shows that each of the variables provide a similar contribution to variance and therefore any reduction in input parameters may impact the ANNs ability to predict the film thickness.

5.3 Machine Element Applications

A simple shaft supported by two cylindrical roller bearings has been modelled in a flexible multi-body dynamic software. The shaft is radially loaded at the centre point between the two bearings using a static load application. The shaft is constrained to rotation about its central axis and lateral

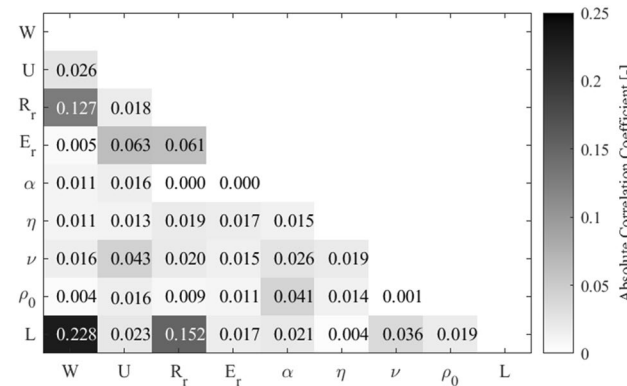


Fig. 4 Heatmap displaying multi-variate correlation values between each of the inputs of the ANN model

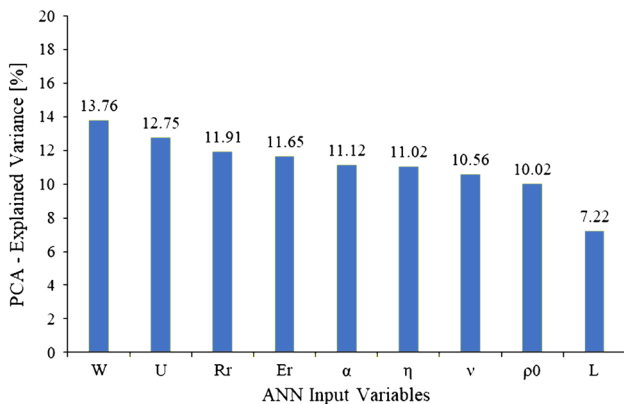


Fig. 5 Principal Component Analysis providing the explanation of variance per ANN input parameter

Table 3 Roller bearing parameters and operating conditions

Bearing parameters	
Number of rolling elements	12
Roller diameter	7.5 mm
Inner race diameter	31.5 mm
Roller length	15 mm
Radial interference	5 μ m
Young's modulus	218 GPa
Poisson's ratio	0.3
Operating conditions	
Radial force	2500 N
Rotational velocity	10,000 rpm

degrees of freedom. Bearing geometric parameters and operating conditions are shown in Table 3.

The dynamic simulation is run explicitly, and results required as inputs to the ANN are output. Results are generated for an individual rolling element in its orbit around the bearing. These include roller load per unit length, reduced radius of the roller-inner race contact, and contact entrainment velocity and are shown in Fig. 6. The bearing model accounts for the non-linear Hertzian force–deflection relationship. Peak roller loading occurs as the roller enters the lowest point in its orbit, due to the vertical direction of the radial load applied to the shaft. The loading pattern is cyclic in nature as the roller enters and exits the loaded region. Sufficient preload ensures that the roller and raceways remain in contact throughout operation, and an EHL contact is maintained throughout. The contact reduced radius and entraining velocity do not change throughout the rollers orbit as these are a function of the bearing geometry and operating speed, which remain constant.

The lubricant film prediction ANN has been embedded into an explicit workflow with a dynamic simulation of spur gear pair with microgeometry modifications. The relevant dimensions and operating conditions of the spur gear are displayed in Table 4. A common spur gear modification of a linear tip relief has been applied as it reduces mesh impact of the single to double contact during the meshing cycle [45].

Table 5 provides the lubricant parameters used in both the bearing and spur gear case study.

All the relevant input parameters required by the ANN such as reduced radius, entraining speed, and load across a meshing cycle were computed using a one degree of freedom dynamic model as shown in Fig. 7. A single meshing cycle consisted of 198 data points to be computed. The model considers tooth bending and tilt using a *Weber–Benescheck* method [47] as well as local deformations using a Hertzian model. Peak loading occurs during a period of the meshing cycle where the load is supported via a single flank pair.

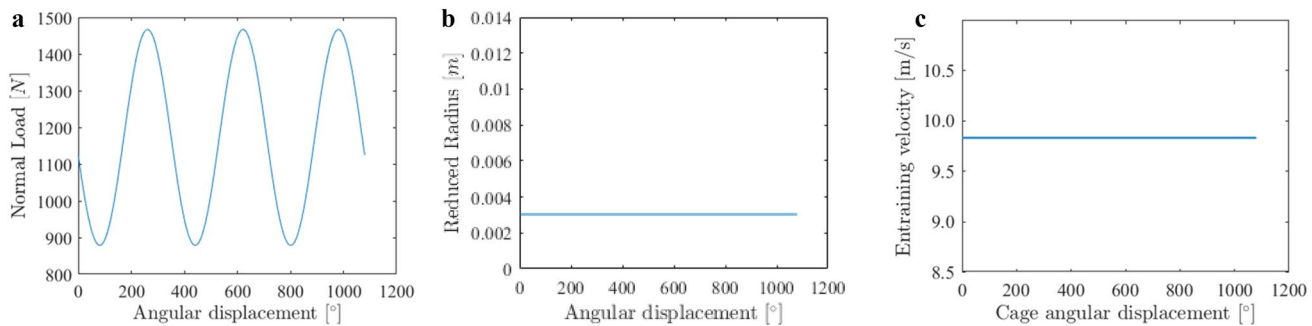


Fig. 6 Inputs to ANN for a single-rolling element of the bearing **a** load, **b** reduced radius, and **c** entrainment speed

Table 4 Spur gear parameters [46] and operating conditions

Gear parameters	
Number of teeth	50
Base radius	140.95 mm
Face width	20 mm
Module	3 mm
Centre distance	150 mm
Contact ratio	1.75
Pressure angle	20°
Tip relief	10 µm at roll angle 23.6°
Young's modulus	207 GPa
Poisson's ratio	0.3
Operating conditions	
Torque	200 Nm
Input speed	2000 rpm

Table 5 Lubricant parameters [46]

Lubricant parameters	
Viscosity	6.5 mPa s
Pressure-viscosity coefficient	$1.273e - 8 \text{ Pa}^{-1}$
Eyring stress	2 MPa

Cylindrical gears in automotive applications typically operate under a boundary to mixed EHL regime due to the contact pressures. Under mixed lubrication regimes, viscous friction is a predominate contributing factor to the overall friction.

6 Results

It is worth noting that the following results were performed on current consumer grade hardware to demonstrate the applicability of the ANN performance in

comparison to conventional numerical solutions. (Hardware used: Intel® Core™ i7-9750H CPU 6 cores @ 2.60 GHz, 32 GB RAM; GPU: NVIDIA GeForce GTX 1650).

6.1 ANN Structure Performance

The initial effort to generate a training database is of importance as the number of data points can influence the ANNs accuracy. During this study, the average time for a numerical data point to be generated was 5.88 s. This led to the database construction, using a single processor core, having a wall time between 0.98 h and 8.16 h for 600 to 5000 data points, respectively. Note the use of multiple processor cores could vastly improve the wall time over a single core.

To find the optimum structure a parameter study was completed using over 500 different ANN structures on the same input data. The number of hidden layers is varied between one and four, and the number of neurons between ten and twenty. The three documented activation functions were studied in the various hidden layer configurations including a combination of hyperbolic tangent with the final layer being a logistic tangent function. R^2 is reported only for the test data sets as this gives the best indication of the models performance and generalisation in comparison to the training and validation performances. The full training procedure completion time was also documented for each ANN structure tested.

Values for R^2 using 600 data points and different activation functions, number of layers, and neurons are presented in Tables 6, 7, 8, 9, 10, 11, and 12. The ReLU function performed significantly worse across all structures in comparison to the logistic sigmoid and hyperbolic tangent functions. However, it is worth noting that there is slight variation in the performance of a network with each new training session. The optimum number of layers was between two and three similar to tribological applications of ANNs [39].

It was found that 600 data points were sufficient to train a relatively accurate ANN for central film prediction;

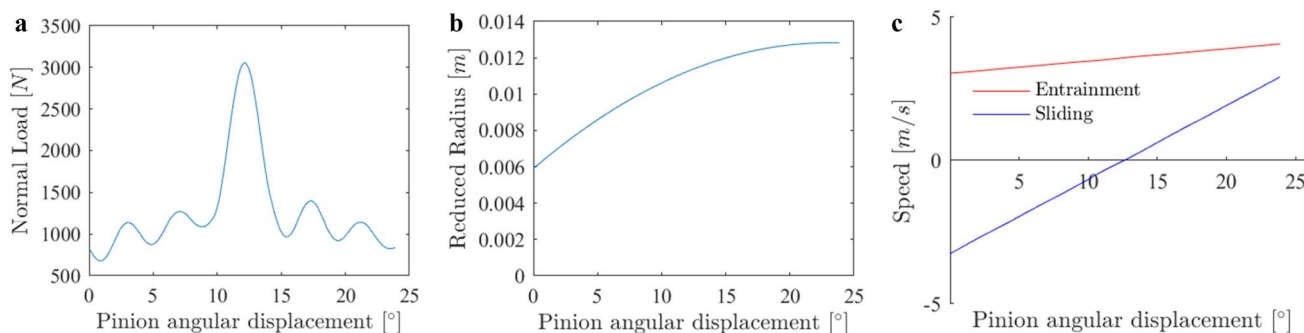
**Fig. 7** Inputs to ANN for a spur gear **a** load, **b** reduced radius, and **c** entrainment and sliding speed

Table 6 R^2 Performance of ANN structures using 600 data points, a LogSig activation function, 1 – 4 hidden layers, and 10 – 20 neurons within each layer (Color table online)

R^2		Activation function LogSig										Key R^2 [–]	
		Neuron No.											
Layers no.	1	0.997	0.995	0.998	0.998	0.999	0.999	0.999	0.998	0.998	0.995	0.999	0.990 0.993 0.997 1.000
	2	0.999	0.999	0.999	0.997	1.000	0.996	0.998	0.998	0.997	0.997	0.995	
	3	1.000	0.998	0.998	0.999	0.997	0.997	0.997	0.998	0.993	0.995	0.996	
	4	0.997	0.999	0.997	0.997	0.999	0.998	0.993	0.989	0.989	0.975	0.990	

Table 7 R^2 Performance of ANN structures using 600 data points, a Tanh activation function, 1 – 4 hidden layers, and 10 – 20 neurons within each layer (Color table online)

R^2		Activation function Tanh										Key R^2 [–]	
		Neuron No.											
Layers no.	1	0.998	0.999	0.995	0.998	0.998	0.994	0.998	0.999	0.998	0.998	0.998	0.990 0.993 0.997 1.000
	2	0.999	0.998	0.998	0.999	0.996	0.998	0.996	0.996	0.996	0.993	0.994	
	3	0.999	0.992	0.996	0.995	0.992	0.989	0.989	0.985	0.994	0.970	0.984	
	4	0.997	0.997	0.992	0.994	0.991	0.983	0.982	0.978	0.990	0.989	0.983	

Table 8 R^2 performance of ANN structures using 600 data points, a ReLU activation function, 1 – 4 hidden layers, and 10 – 20 neurons within each layer (Color table online)

R^2		Activation function ReLU										Key R^2 [–]	
		Neuron numbers											
Layers no.	1	0.985	0.991	0.994	0.993	0.993	0.994	0.992	0.994	0.995	0.987	0.990	0.990 0.993 0.997 1.000
	2	0.993	0.996	0.995	0.993	0.992	0.984	0.989	0.993	0.992	0.993	0.992	
	3	0.986	0.983	0.996	0.988	0.984	0.980	0.992	0.992	0.988	0.986	0.988	
	4	0.981	0.990	0.975	0.928	0.951	0.986	0.985	0.986	0.986	0.982	0.985	

Table 9 Training times of ANN structures using 600 data points, a LogSig activation function 1 – 4 hidden layers, and 10 – 20 neurons within each layer (Color table online)

Training time [s]		Activation function LogSig—600 data points										Key time [s]	
		Neuron numbers											
Layers no.	1	0.76	0.96	1.16	1.01	1.49	1.30	1.41	1.72	1.12	0.90	1.13	0.00 10.00 100.00 600.00
	2	1.01	2.93	1.94	1.43	1.88	1.80	1.56	1.80	1.33	2.51	1.77	
	3	2.81	1.29	2.58	2.22	2.27	1.52	1.67	2.26	2.06	1.94	3.57	
	4	1.64	5.97	2.21	2.79	6.70	2.66	4.36	2.51	2.76	2.61	2.90	

Table 10 Training times of ANN structures using 1000 data points, a LogSig activation function 1 – 4 hidden layers, and 10 – 20 neurons within each layer (Color table online)

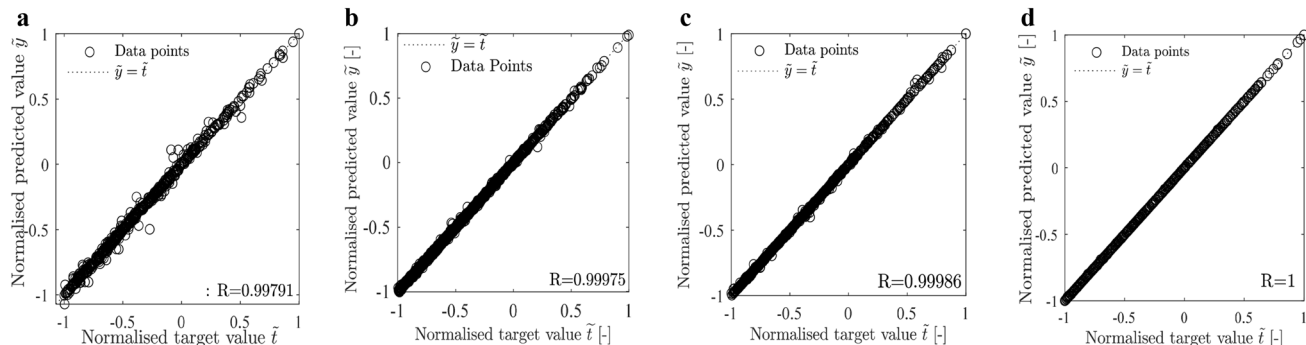
Training time [s]		Activation function LogSig—1000 data points										Key time [s]	
		Neuron numbers											
Layers no.	1	1.00	1.10	1.36	1.11	1.89	2.20	2.09	1.01	1.58	2.83	1.10	0.00 10.00 100.00 600.00
	2	3.25	1.66	2.33	2.72	4.00	3.07	2.35	2.81	5.35	1.97	3.77	
	3	2.74	6.35	4.76	5.58	4.17	2.36	4.88	7.56	7.18	6.55	5.18	
	4	2.59	2.29	8.12	6.47	7.17	3.81	7.70	11.46	19.01	12.14	8.92	

Table 11 Training times of ANN structures using 2000 data points, a LogSig activation function 1–4 hidden layers, and 10–20 neurons within each layer (Color table online)

		Activation function LogSig—2000 data points										Key time [s]	
Training time [s]		Neuron numbers											
Layers no.	1	10	11	12	13	14	15	16	17	18	19	20	Key time [s]
	2	6.06	7.19	10.66	13.38	6.20	6.54	6.76	14.61	16.32	7.86	20.32	
	3	18.72	13.45	4.55	5.19	21.54	23.88	26.00	25.44	27.50	11.66	19.71	
	4	11.49	18.79	16.06	6.69	41.55	30.72	28.04	67.86	14.78	62.17	57.13	

Table 12 Training times of ANN structures using 5000 data points, a LogSig activation function 1–4 hidden layers and 10–20 neurons within each layer (Color table online)

		Activation function LogSig—5000 data points										Key time [s]	
Training time [s]		Neuron numbers											
Layers no.	1	10	11	12	13	14	15	16	17	18	19	20	Key time [s]
	2	10.86	22.86	37.50	30.99	20.02	19.95	38.09	11.02	48.89	134.95	37.88	
	3	14.53	33.38	34.62	116.81	61.86	57.12	140.49	124.75	228.28	71.22	85.55	
	4	94.66	36.71	139.61	70.20	13.33	229.45	88.24	155.37	217.48	500.54	600.01	

**Fig. 8** R^2 performance of ANN structure 10 – [14 – 14 – 14]₃ – 1 using Hyperbolic Tangent activation function **a** 600 points, **b** 1000, **c** 2000, and **d** 5000

however, it must be noted in the current study more data points led to less variation in the R^2 values across all structures without necessarily overfitting. Although it must be noted that training times varied most significantly with increasing the number of data points rather than the network structure complexity. Figure 8a–d and Tables 9, 10, 11, and 12 demonstrate the influence of increasing the data points from 600 to 1000, 2000, and 5000 data points for a logistic sigmoid function. It was concluded during this study that 1000 to 2000 data points typically led to the ANNs ability to reliably predict the film thickness without leading to significant increases in training time. 5000 data points used with the most complex network structures exceeded five minutes with the aforementioned hardware and reached 1000 epochs.

6.2 Case Studies Overview

In order to realise the potential of ANNs to predict complex multifaceted problems they require to be demonstrated into scenarios which can benefit from their implementation. In order to assess the ANNs ability and suitability for operation in dynamic machine element modelling a few case studies are presented below. Performances of the ANNs are to be compared relative to the numerical models and experimental data.

6.3 Case Study: EHL Film Prediction for Bearings and Gears

The analytical formula from Eq. 1, the numerical solution as described in Section III, and optimum-structured ANN were

Fig. 9 Application of central film thickness computation ANN (solid blue) for **a** spur gear, **b** roller element bearing application compared against analytical (short dash green) equations and the numerical (long dash red)

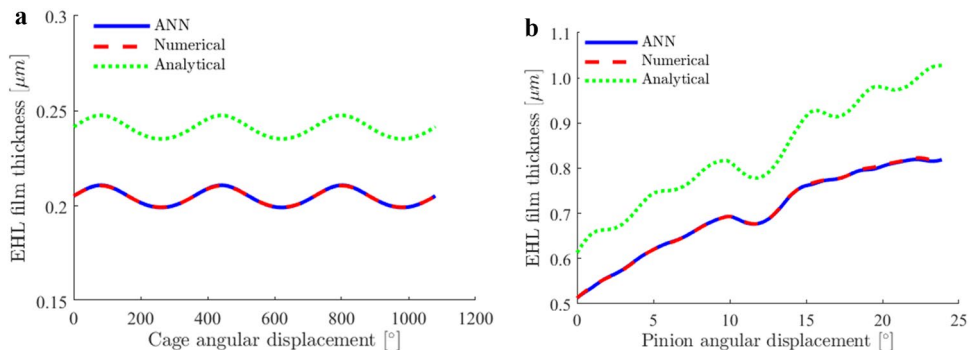


Table 13 Comparison of film thickness computation methodologies performance relative to the numerical solution

Method	Bearing		Spur Gear	
	Time per point	MSE	Time per point	MSE
	[s/#]	[μm]	[s/#]	[μm]
Numerical	4.87E+00	–	4.88E+00	–
Analytical	4.43E-05	1.32E-3	4.97E-05	1.87E-2
ANN	3.33E-03	1.46E-8	4.34E-03	2.46E-6

used to compute the EHL film thickness over a single meshing cycle of the spur gear and several cycles for the roller bearing. It is worth noting that the bearing and gear case studies operated within the range of the ANNs training dataset. The film thickness computed by each methodology for each of the machine element's angular displacement is displayed in Fig. 9a and b. For both the bearing and spur gear applications Fig. 9a and b demonstrates clearly the ANNs (solid blue) ability to predict a similar central film thickness as the numerical method (long dash red) with minimal MSE error. The analytical (short dash green) method on the other hand over predicts the film by up to 0.1 μm in the spur gear case study, in real terms this could allow for misinterpretation of little to no boundary interaction depending upon the surface roughness. Table 13 demonstrates the relative performance of the analytical and ANN against the numerical solution for the MSE. The computation time per data point was also documented for each of the case studies in Table 12

to demonstrate the timely solution of the spur gear and bearing film thickness using the analytical and ANN methods. The analytical solution is a factor of ~75 faster than the ANN but is significantly less accurate as described by the MSE. The ANN represents approx. ~1500 factor computation reduction over the numerical solution with marginal error. Despite significant computational gains, it must be noted for widespread adoption of EHL ANNs in MBD simulations and its ability to extrapolate for conditions in which the input range of the original training datasets is exceeded must be appropriately addressed. Whilst this is not the focus of the current study, it should be addressed in the future works to advance the use of this data-driven solution.

6.4 Case Study: Friction ANN Validation Against MTM

Throughout a gear meshing cycle, the contact between two flanks changes its slide-to-roll ratio (SRR). A typical maximum SRR of a spur gear is 50%. One way to experimentally explore this contact-level phenomenon in a controlled manner is to use a ball-on-disc tribometer MTM2 (PCS Instruments, London, UK), where friction can be measured. Five tests were conducted, specifically varying the entrainment speed only, using a Group III base oil with a contact pair made of AISI 52,100 steel. Each of the discs were measured using Alicona Infinite Focus microscope (Alicona, Graz, Austria) at four different locations and the topographical parameters averaged.

Table 14 MTM ½" ball and disc EHL friction study parameters

Load	Entrainment speed	SRR	Dynamic viscosity (@90 degc)	Pressure Coef	Roughness parameter	RMS roughness	Average summit radius
N	m/s	%	mPa s	Pa ⁻¹	[–]	μm	μm
75	0.6	50	6.13	1.25E-08	0.066	0.085	9.68
	1.175				0.062	0.069	13.03
	1.75				0.053	0.073	12.14
	2.325				0.064	0.071	11.68
	2.9				0.062	0.078	9.19

A reduced order 2D EHL method was used to simulate the contact in discrete slices as per [48]. Table 14 shows the inputs into the model. The numerical methodology to compute the viscous and the deterministic *Greenwood and Tripp* methodology for boundary friction, as documented in Section IV and V, were used. A training data set of 10,000 was used due to the increased number of factors to consider in the design space. Moreover, to accommodate the slice-reduced order methodology, the load and length training input parameters of Table 2 were reduced to reflect the smaller contact lengths (0.01 – 10.0 μm), whilst maintaining the similar load per unit length ratios. Separate viscous and boundary friction ANN's were trained using the following ANN network structures, respectively, using hyperbolic tangent activation functions for the hidden layers:

$$\text{Viscous : } 12_{\text{in}} - [14_{h1} - 14_{h2} - 14_{h3}]_t - 1_{\text{out}},$$

$$\text{Boundary : } 15_{\text{in}} - [14_{h1} - 14_{h2} - 14_{h3}]_t - 1_{\text{out}}.$$

Each ANNs training achieved an R^2 value of 0.9985 and 0.9993. The MTM friction results compared against the ANN, and numerical solutions are shown in Fig. 10. The Stribeck Oil Parameter is plotted to demonstrate the lubrication regimes experienced, mixed to EHL. One potential reason of both models overprediction of friction at the experiment's higher entrainment speeds at the fixed SRR of 50% could be due to shear thinning.

6.5 Case Study: ANN Friction Application for Spur Gears

The numerical and ANN viscous friction methodologies were also used in same spur gear example. As the gear flanks approach the pitch point the sliding velocity reduces towards zero. Therefore, the friction coefficient should be at its minimum. Both presented methodologies are capable of predicting this event as shown in Fig. 11. Literature has at points misused analytical lubricated friction formulas, such as those presented by Evans and Johnson [36] in gear applications where sliding–rolling motion is present. The ANN was ~ 1300 times faster at computing the friction compared the numerical solution.

7 Conclusion

Tribological ANNs have been applied to two commonly used machine elements, a roller element bearing and a spur gear with microgeometry modification, for the prediction of EHL film thickness as well as friction. During this study, the ANNs have proven to be accurate as well as a fast computation technique for explicit use in dynamic modelling. Despite ANNs shortcomings of having no physical understanding, the data-driven solution has provided similar levels of accuracy to numerical computation techniques. The ANNs numerically generated training data was produced via Latin Hypercube Sampling (LHS) and then constrained

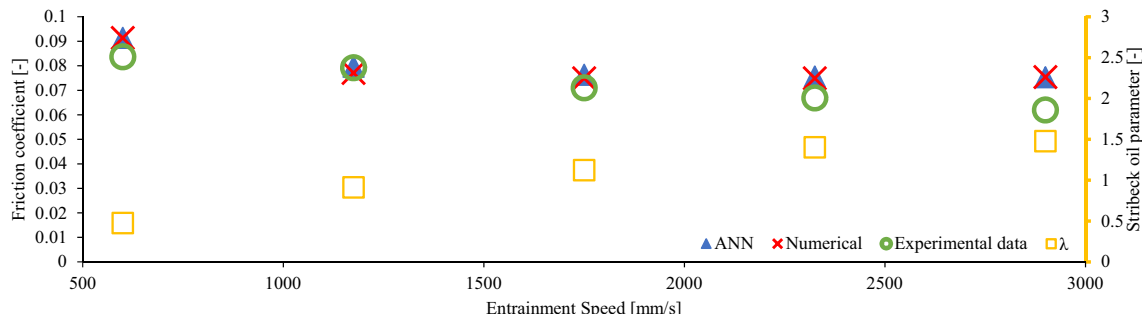
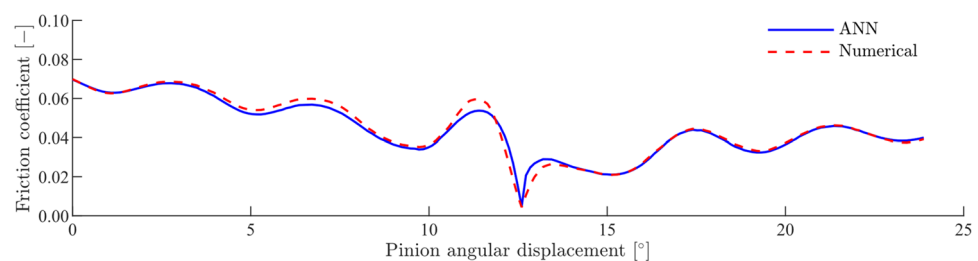


Fig. 10 Comparison between experimentally measured friction coefficient using a Mini Traction Machine (MTM), the computed friction coefficients from the numerical model, and the ANN

Fig. 11 Application of viscous friction ANN for a spur gear application compared against analytical equations and the numerical solution



via the Greenwood Regime to ensure the quality of the data, which directly affects the ANNs ability to predict with a high level of accuracy.

It was also found that at entraining velocities of the gear (~ 4 m/s) and the roller element bearing (~ 9.5 m/s) the analytical equation deviated significantly from the numerical solution for the central film thickness whilst the ANN could replicate it with very small margins of error. During these specific case studies, the ANN was shown to perform ~ 1500 times faster than the numerical solution.

Multiple regimes of friction are accounted for by the ANNs, including boundary, Newtonian, and non-Newtonian viscous friction. A numerical and ANN approach were compared directly against a lubricated ball-on-disc (MTM) study with a fixed slide-to-roll ratio and an increasing entrainment velocity. The numerical solution used a 2D-reduced order technique to replicate the contact pressure and film thickness distribution to then calculate the viscous and boundary friction. The separately trained viscous and boundary friction ANNs combined to achieve similar levels of accuracy relative to the experimental and numerical result; however, the ANN vastly outperformed the numerical solution with regards to computational efficiency. The ANN was also demonstrated to be capable of predicting a spur gear pair's changing friction coefficient throughout its meshing cycle, where the load, slide-to-roll ratio, and contact geometry varies significantly.

Future work should look to embed a tribological ANN within a dynamic co-simulation to seek the full benefits of the accuracy of a numerical solution but far faster simulation times. For this data-driven solution to be more widely adopted in MBD simulations, its ability to extrapolate beyond its training input data range needs be addressed, as this could affect the stability of the dynamic co-simulation.

Acknowledgements The authors of the current work wish to express thanks to the industrial collaborator AVL List GmbH for their financial and technical support to this research.

Author contributions JW—Methodology, Software, Validation, Investigation, Writing—Original Draft, and Visualisation. HQ—Methodology, Software, Writing—Original Draft, Investigation, and Visualisation. AR—Software, Investigation, and Writing—Original Draft. MA—Software, Investigation, and Writing—Original Draft. MM—Conceptualisation, Resources, Writing—Review & Editing, Supervision, and Project administration. SRB—Conceptualisation, Resources, Writing—Review & Editing, Supervision, and Project administration. GO—Conceptualisation, Resources, Writing—Review & Editing, Supervision, and Project administration

Funding This work was supported by undergraduate scholarships from the industrial collaborators AVL List GmbH.

Data Availability The training datasets for the EHL central film thickness are openly available in Figshare at <https://doi.org/10.6084/m9.figshare.21428088>, [43].

Declarations

Conflict of interest The authors have not disclosed any competing interests.

Open Access This article is licensed under a Creative Commons Attribution 4.0 International License, which permits use, sharing, adaptation, distribution and reproduction in any medium or format, as long as you give appropriate credit to the original author(s) and the source, provide a link to the Creative Commons licence, and indicate if changes were made. The images or other third party material in this article are included in the article's Creative Commons licence, unless indicated otherwise in a credit line to the material. If material is not included in the article's Creative Commons licence and your intended use is not permitted by statutory regulation or exceeds the permitted use, you will need to obtain permission directly from the copyright holder. To view a copy of this licence, visit <http://creativecommons.org/licenses/by/4.0/>.

References

1. Holmberg, K., Erdemir, A.: The impact of tribology on energy use and CO₂ emission globally and in combustion engine and electric cars. *Tribol. Int.* **135**(March), 389–396 (2019). <https://doi.org/10.1016/j.triboint.2019.03.024>
2. Dowson, D., Higginson, G.R.: A Numerical solution to the elastohydrodynamic problem. *J. Mech. Eng. Sci.* **1**(1), 6–15 (1959)
3. Gohar, R., Rahnejat, H.: Fundamentals of Tribology. World Scientific, Singapore (2018). <https://doi.org/10.1142/q0152>
4. ESDU, “Film thicknesses in lubricated Hertzian contacts (EHL). Part 1: two-dimensional contacts (line contacts),” *Eng. Data Sheets*, vol. 85027, no. October 1985.
5. Dowson, D., Toyoda, S.: A central film thickness formula for elastohydrodynamic line contacts. In: Proceedings of the Society of Photo Optical Instrumentation Engineering, pp. 60–65 (1979)
6. Dowson, D.: Paper 10: elastohydrodynamics. Proc. Inst. Mech. Eng. Conf. Proc. (1967). https://doi.org/10.1243/pime_conf_1967_182_014_02
7. Evans, C.R., Johnson, K.L.: The rheological properties of elastohydrodynamic lubricants. Proc. Inst. Mech. Eng. Part C J. Mech. Eng. Sci. (1986). https://doi.org/10.1243/PIME_PROC_1986_200_134_02
8. Greenwood, J.A., Tripp, J.H.: The contact of two nominally flat rough surfaces. Proc. Inst. Mech. Eng. **185**(1), 625–633 (Jun. 1970). https://doi.org/10.1243/PIME_PROC_1970_185_069_02
9. Echávarri Otero, J., et al.: Artificial neural network approach to predict the lubricated friction coefficient. *Lubr. Sci.* **26**(3), 141–162 (2014). <https://doi.org/10.1002/l.s.1238>
10. Argatov, I.: Artificial Neural Networks (ANNs) as a Novel Modeling Technique in Tribology. *Front. Mech. Eng.* **5**(May), 1–9 (2019). <https://doi.org/10.3389/fmech.2019.00030>
11. Ezugwu, E.O., Arthur, S.J., Hines, E.L.: Tool-wear prediction using artificial neural networks. *J. Mater. Process. Tech.* **49**(3–4), 255–264 (1995). [https://doi.org/10.1016/0924-0136\(94\)01351-Z](https://doi.org/10.1016/0924-0136(94)01351-Z)
12. Rutherford, K.L., Hatto, P.W., Davies, C., Hutchings, I.M.: Abrasive wear resistance of TiN/NbN multi-layers: Measurement and neural network modelling. *Surf. Coatings Technol.* **86–87**(PART 2), 472–479 (1996). [https://doi.org/10.1016/S0257-8972\(96\)02956-8](https://doi.org/10.1016/S0257-8972(96)02956-8)
13. Jones, S.P., Jansen, R., Fusaro, R.L.: Preliminary investigation of neural network techniques to predict tribological properties. *Tribol. Trans.* **40**(2), 312–320 (1997). <https://doi.org/10.1080/10402009708983660>

14. Zhang, Z., Friedrich, K., Veltén, K.: Prediction on tribological properties of short fibre composites using artificial neural networks. *Wear* **252**(1), 668–675 (2002). [https://doi.org/10.1016/0013-7952\(02\)00012-3](https://doi.org/10.1016/0013-7952(02)00012-3)
15. Hayajneh, M., Hassan, A.M., Alrashdan, A., Mayyas, A.T.: Prediction of tribological behavior of aluminum-copper based composite using artificial neural network. *J. Alloys Compd.* **470**(1–2), 584–588 (2009). <https://doi.org/10.1016/j.jallcom.2008.03.035>
16. Genel, K., Kurnaz, S.C., Durman, M.: Modeling of tribological properties of alumina fiber reinforced zinc-aluminum composites using artificial neural network. *Mater. Sci. Eng. A* **363**(1–2), 203–210 (2003). [https://doi.org/10.1016/S0921-5093\(03\)00623-3](https://doi.org/10.1016/S0921-5093(03)00623-3)
17. Cavalieri, L., Asteris, P.G., Psyllaki, P.P., Douvika, M.G., Skentou, A.D., Vaxevanidis, N.M.: Prediction of surface treatment effects on the tribological performance of tool steels using artificial neural networks. *Appl. Sci.* (2019). <https://doi.org/10.3390/app9142788>
18. Bhaumik, S., Pathak, S.D., Dey, S., Datta, S.: Artificial intelligence based design of multiple friction modifiers dispersed castor oil and evaluating its tribological properties. *Tribol. Int.* **140**(March), 105813 (2019). <https://doi.org/10.1016/j.triboint.2019.06.006>
19. Bhaumik, S., Mathew, B.R., Datta, S.: Computational intelligence-based design of lubricant with vegetable oil blend and various nano friction modifiers. *Fuel* **241**(June 2018), 733–743 (2019). <https://doi.org/10.1016/j.fuel.2018.12.094>
20. Hemmat Esfe, M., Rostamian, H., Esfandeh, S., Afrand, M.: Modeling and prediction of rheological behavior of Al_2O_3 -MWCNT/5W50 hybrid nano-lubricant by artificial neural network using experimental data. *Phys. A Stat. Mech. Appl.* **510**, 625–634 (2018). <https://doi.org/10.1016/j.physa.2018.06.041>
21. Afrand, M., et al.: Prediction of dynamic viscosity of a hybrid nano-lubricant by an optimal artificial neural network. *Int. Commun. Heat Mass Transf.* **76**, 209–214 (2016). <https://doi.org/10.1016/j.icheatmasstransfer.2016.05.023>
22. Ripa, M., Frangu, L.: A survey of artificial neural networks applications in wear and manufacturing processes. *J. Tribol.* **8**, 35–42 (2004)
23. Panda, S.S., Chakraborty, D., Pal, S.K.: Flank wear prediction in drilling using back propagation neural network and radial basis function network. *Appl. Soft Comput. J.* **8**(2), 858–871 (2008). <https://doi.org/10.1016/j.asoc.2007.07.003>
24. Asiltürk, I., Çunkaş, M.: Modeling and prediction of surface roughness in turning operations using artificial neural network and multiple regression method. *Expert Syst. Appl.* **38**(5), 5826–5832 (2011). <https://doi.org/10.1016/j.eswa.2010.11.041>
25. Barbedo, J.G.A.: Impact of dataset size and variety on the effectiveness of deep learning and transfer learning for plant disease classification. *Comput. Electron. Agric.* **153**(March), 46–53 (2018). <https://doi.org/10.1016/j.compag.2018.08.013>
26. Barbedo, J.G.A., Linjordet, T., Balog, K.: Impact of training dataset size on neural answer selection models BT—advances in information retrieval. *Comput. Electron. Agric.* **153**(March), 828–835 (2019). <https://doi.org/10.1016/j.compag.2018.08.013>
27. Wang, N., Tsai, C.M.: Assessment of artificial neural network for thermohydrodynamic lubrication analysis. *Ind. Lubr. Tribol.* **72**(10), 1233–1238 (2020). <https://doi.org/10.1108/ILT-03-2020-0109>
28. Almqvist, A.: Fundamentals of physics-informed neural networks applied to solve the Reynold's boundary value problem. *Lubricants* (2021). <https://doi.org/10.3390/lubricants9080082>
29. Marian, M., Mursak, J., Bartz, M., Profito, F.J., Rosenkranz, A., Wartzack, S.: Predicting EHL film thickness parameters by machine learning approaches. *Friction* (2022). <https://doi.org/10.1007/s40544-022-0641-6>
30. Gohar, R.: Elastohydrodynamics. Imperial College Press, London (1988)
31. Hamrock, B.J., Jacobson, B.O.: Elastohydrodynamic Lubrication of Line Contacts. *A S L E Trans.* **27**(4), 275–287 (Jan. 1984). <https://doi.org/10.1080/05698198408981572>
32. Roelands, C.J.: Correlational Aspects of the Viscosity-Temperature-Pressure Relationship of Lubricating Oils. Delft University, Delft (1966)
33. Dowson, D., Higginson, G.R.: Elasto-Hydrodynamic Lubrication. Pergamon Press, Oxford, SI (1977)
34. Okamura, H.: A contribution to the numerical analysis of isothermal elastohydrodynamic lubrication. In: Dowson, D., Taylor, C.M. (eds.) *Tribology of Reciprocating Engines*, pp. 313–320. Elsevier, Amsterdam (1993). <https://doi.org/10.1016/B978-0-408-22161-0-50048-2>
35. Björling, M., Larsson, R., Marklund, P., Kassfeldt, E.: Elastohydrodynamic lubrication friction mapping—the influence of lubricant, roughness, speed, and slide-to-roll ratio. *Proc. Inst. Mech. Eng. Part J J. Eng. Tribol.* **225**(7), 671–681 (2011). <https://doi.org/10.1177/1350650111403363>
36. Evans, C.R., Johnson, K.L.: Regimes of Traction in Elastohydrodynamic Lubrication. *Proc. Inst. Mech. Eng. Part C J. Mech. Eng. Sci.* **200**(5), 313–324 (1986). https://doi.org/10.1243/PIME_PROC_1986_200_135_02
37. Teodorescu, M., Taraza, D., Henein, N.A., Bryzik, W.: Simplified elasto-hydrodynamic friction model of the cam-tappet contact. *SAE Tech. Pap.*, no. 724 (2003). <https://doi.org/10.4271/2003-01-0985>
38. Mohammadpour, M., Theodossiades, S., Rahnejat, H., Saunders, T.: Non-Newtonian mixed elastohydrodynamics of differential hypoid gears at high loads. *Meccanica* **49**(5), 1115–1138 (2014). <https://doi.org/10.1007/s11012-013-9857-x>
39. Marian, M., Tremmel, S.: Current trends and applications of machine learning in tribology—a review. *Lubricants* **9**(9), 86 (Sep. 2021). <https://doi.org/10.3390/lubricants9090086>
40. The MathWorks Inc.: *MATLAB version 9.12.0.1956245 (R2022a)*. Natick, Massachusetts (2022)
41. The MathWorks Inc.: Improve Shallow Neural Network Generalization and Avoid Overfitting. (2022). <https://uk.mathworks.com/help/deeplearning/ug/improve-neural-network-generalization-and-avoid-overfitting.html>. Accessed 21 July 2022
42. Johnson, K.L.: Regimes of Elastohydrodynamic Lubrication. *J. Mech. Eng. Sci.* **12**(1), 9–16 (Feb. 1970). https://doi.org/10.1243/JMES_JOUR_1970_012_004_02
43. Walker, J., et al.: Application of tribological artificial neural networks in machine elements training data sets. Figshare (2022). <https://doi.org/10.6084/m9.figshare.21428088>
44. De Veaux, R.D., Ungar, L.H.: Multicollinearity: A tale of two non-parametric regressions, pp. 393–402. Springer, New York (1994). https://doi.org/10.1007/978-1-4612-2660-4_40
45. Linke, H., Börner, J., Heß, R., Linke, H., Börner, J., Heß, R.: Cylindrical Gears. Hanser Publications, Cincinnati (2016). <https://doi.org/10.3139/9781569904909.fm>
46. Kahraman, A., Blankenship, G.W.: Effect of involute contact ratio on spur gear dynamics. *J. Mech. Des. Trans. ASME* **121**(1), 112–118 (1999). <https://doi.org/10.1115/1.2829411>
47. Weber, C., Banaschek, K., Niemann, G.: Formänderung und Profilrücknahme bei-gerad und schrägverzahnten Rädern. F Vieweg, Paris (1955)
48. Walker, J., et al.: A multi-physics transient wear model for helical gear pairs. *Tribol. Int.* (2022). <https://doi.org/10.1016/j.triboint.2022.107463>

Publisher's Note Springer Nature remains neutral with regard to jurisdictional claims in published maps and institutional affiliations.